

Dipartimento di / Department of
Materials Science

Dottorato di Ricerca in / PhD program Materials Science and Nanotechnology Ciclo / Cycle XXXIV

Polymeric Water-Processable Nanoparticles towards sustainable organic photovoltaics

Cognome / Surname: DITERLIZZI Nome / Name: Marianna

Matricola / Registration number: 768261

Tutore / Tutor: Prof. Luca BEVERINA

Supervisor: Dr. Silvia DESTRI

Co-supervisor: Dr. Stefania ZAPPIA

Coordinatore / Coordinator: Prof. Marco BERNASCONI

ANNO ACCADEMICO / ACADEMIC YEAR 2020/21

Table of contents

Chapter 1

Polymer-based aqueous inks for sustainable organic solar cells: state of the art	1
1.1 Organic photovoltaic.....	2
1.2 Water-processable nanoparticles.....	6
1.2.1 Miniemulsion method.....	7
1.2.2 Nanoprecipitation.....	10
1.3 WPNP-based OPV devices.....	12
1.4 WPNPs for biological applications.....	16
1.5 Summary of WPNP-based OPV devices performances.....	17
1.6 Aim of the work.....	19
1.7 References.....	21

Chapter 2

Surfactant-free miniemulsion approach for low band gap rod-coil block copolymer water-processable nanoparticles: a proof-of-concept	29
2.1 Introduction.....	30
2.2 Results and Discussion.....	31
2.2.1 Synthesis and Characterization of the rod-coil block copolymers (BCPs).....	31
2.2.1.1 Synthesis and Characterization of BCP2 and BCP5 through a <i>Chain Growth-like</i> strategy.....	33
2.2.1.2 Synthesis and Characterization of BCP15 and BCP100 through a <i>Step Growth-like</i> strategy.....	35

2.2.2 Synthesis and optical characterization of the BCP WPNP aqueous suspensions.....	38
2.2.3 Study of the BCP bWPNP-based OPV devices.....	40
2.2.4 Morphological investigation of the BCP bWPNPs.....	43
2.2.5 Photophysical investigation of the BCP WPNP-based films.....	46
2.2.6 WPNP aqueous suspensions for bioelectronic applications.....	50
2.3 Conclusions.....	53
2.4 Experimental Section.....	54
2.4.1 Materials.....	54
2.4.2 Synthetic Procedures.....	55
2.4.2.1 <i>Chain Growth-like</i> strategy for the synthesis of BCP2 and BCP5.....	55
2.4.2.2 <i>Step Growth-like</i> strategy for the synthesis of BCP15 and BCP100.....	56
2.4.3 BCP WPNP synthesis.....	63
2.4.4 WPNP-based device fabrication.....	67
2.5 References.....	68

Chapter 3

Production of aqueous inks made from amphiphilic PTB7-based rod-coil block copolymer for organic solar cells: a case study.....	71
3.1 Introduction.....	72
3.2 Aqueous inks based on the amphiphilic rod-coil PTB7- <i>b</i> -P4VP.....	74
3.2.1 Results and Discussion.....	74
3.2.1.1 Synthesis and Characterization of the macromer PTB7.....	74
3.2.1.2 Synthesis and Characterization of the rod-coil PTB7- <i>b</i> -P4VP.....	75
3.2.1.3 WPNP aqueous suspensions: synthesis and characterization.....	83

3.2.1.4	WPNP-based films: deposition and characterization.....	86
3.2.1.5	WPNP-based OPV devices.....	90
3.3	Aqueous inks based on PC ₇₁ BM:PTB7- <i>b</i> -P4VP:PTB7 blend WPNPs	94
3.3.1	Results and Discussion.....	95
3.3.1.1	WPNP aqueous suspensions: synthesis and characterization.....	95
3.3.1.2	WPNP-based films: deposition and characterization.....	96
3.3.1.3	WPNP-based OPV devices.....	97
3.4	Aqueous inks based on the amphiphilic rod-coil PTB7- <i>b</i> -Krebs.....	98
3.4.1	Results and Discussion.....	99
3.4.1.1	Synthesis and Characterization of the rod-coil PTB7- <i>b</i> -Krebs.....	99
3.4.1.2	WPNP aqueous suspension: synthesis and characterization.....	100
3.4.1.3	Characterization of WPNP-based films.....	101
3.4.1.4	WPNP-based OPV devices.....	103
3.5	Conclusions.....	103
3.6	Experimental Section.....	105
3.6.1	Materials.....	105
3.6.2	Synthetic Procedures.....	105
3.6.2.1	Synthesis of the PTB7- <i>b</i> -P4VP.....	105
3.6.2.2	Synthesis of the PTB7- <i>b</i> -Krebs.....	111
3.6.3	BCP WPNP synthesis.....	113
3.6.4	WPNP-based device fabrication.....	116
3.7	References.....	117

Chapter 4

Investigation on two low band gap BDT-based polymers and on the middle band gap polymer PDCBT: synthesis, characterization, and perspectives.....121

4.1 Introduction.....122

4.2 Results and Discussion.....123

4.2.1 Synthesis and Characterization of PTB7-Th-F₂ and PTB7-Th-F₂-Me ester...123

4.2.2 Synthesis and Characterization of PDCBT.....129

4.3 Conclusions and Perspectives.....131

4.4 Experimental Section.....134

4.4.1 Materials.....134

4.4.2 Synthetic Procedures.....134

4.4.2.1 Synthesis of PTB7-Th-F₂.....134

4.4.2.2 Synthesis of PTB7-Th-F₂-Me ester.....135

4.4.2.3 Synthesis of poly[2,2''-bis[[2-butyl(octyl)oxy]carbonyl][2,2':5',2'':5'',2'''-quaterthiophene] -5,5'''-diyl] (PDCBT).....136

4.5 References.....142

Summary and Conclusions.....145

Acknowledgements.....149

Table of congresses, seminary, and publications.....149

Appendix

Characterization Methodologies.....151

A.1 Nuclear magnetic resonance (NMR).....152

A.2 Size exclusion chromatography (SEC).....153

A.3 Matrix assisted laser desorption/ionization time of flight mass spectroscopy (MALDI-TOF MS).....	154
A.4 Gas chromatography mass spectroscopy (GC-MS).....	155
A.5 Differential scanning calorimetry (DSC).....	155
A.6 Melting point measurements.....	155
A.7 UV-Vis spectroscopy.....	156
A.8 Fourier transform infrared spectroscopy (FTIR).....	156
A.9 Contact angle and surface energy measurements.....	156
A.10 Photoluminescence (PL).....	157
A.11 Grazing incidence wide angle X-ray scattering (GIWAXS).....	157
A.12 Dynamic light scattering (DLS).....	158
A.13 Transmission electron microscopy (TEM).....	159
A.14 Atomic force microscopy (AFM).....	159
A.15 Pump and probe.....	159
A.16 Cell cultures.....	160
A.17 Viability assay.....	160
A.18 Confocal microscopy.....	161
A.19 Staining procedure.....	161
A.20 Reactive Oxygen Species (ROS) imaging.....	162
A.21 Ca ²⁺ imaging.....	162
A.22 Current-voltage (J-V) characteristics.....	163
A.23 Cyclic Voltammetry (CV).....	163
References.....	164

Chapter 1

Polymer-based aqueous inks for sustainable organic solar cells: state of the art

1.1 Organic photovoltaic

At the beginning of the 21st century, exhaustible fossil fuels must be replaced by sustainable energy sources to satisfy growing energy needs and oppose global warming.[1] In this horizon, researchers are doing many efforts to enhance performances of photovoltaic panels and increase their life cycle in terms of energy payback time (EPBT) and environmental loads.[2] In this context, organic photovoltaic (OPV) is an appealing technology as organic solar cells (OSCs) are lightweight and flexible. Furthermore, it is possible to tune their colour and shape, and they are processable at low cost by solution with a low energy consumption. All these features make it possible to combine solar energy harvesting with architectural features (**Figure 1.1**).[3] Indeed, even though traditional inorganic silicon-based solar cells provide very high power conversion efficiencies (PCEs) and reliability, they are commonly installed in large solar power plants and on the roofs of buildings that can withstand their weight. The even higher demand for photovoltaic energy necessitates the exploitation of more and more space to install solar panels. Otherwise, OSCs can be integrated on rooftops that are unable to support heavy inorganic solar cells, such as greenhouses, or on building facades. Moreover, most organic semiconductors for light harvesting in solar cells do not incorporate rare elements, making this technology very independent of critical supply chains. Also, they are often non-toxic, allowing for end-of-life disposal without any significant challenge.[3] An OSC is composed of an active layer, which is made of at least two organic photoactive materials: an electron-donor (D) semiconductor and an electron-acceptor (A) material. The pair is accurately selected so that A has the highest occupied molecular orbital (HOMO) and the lowest unoccupied molecular orbital (LUMO) deeper than D (**Figure 1.2**). The active layer is embedded between two electrodes, one of which is transparent. An optimal photoactive layer morphology is made up of separated but interconnected domains of A and D, referred as bulk heterojunction (BHJ), depicted in **Figure 1.2**. Additionally, an electron transporting layer (ETL) and a hole transporting layer (HTL) can be inserted between the active layer and the electrode to promote the charge transport and collection.[4, 5]

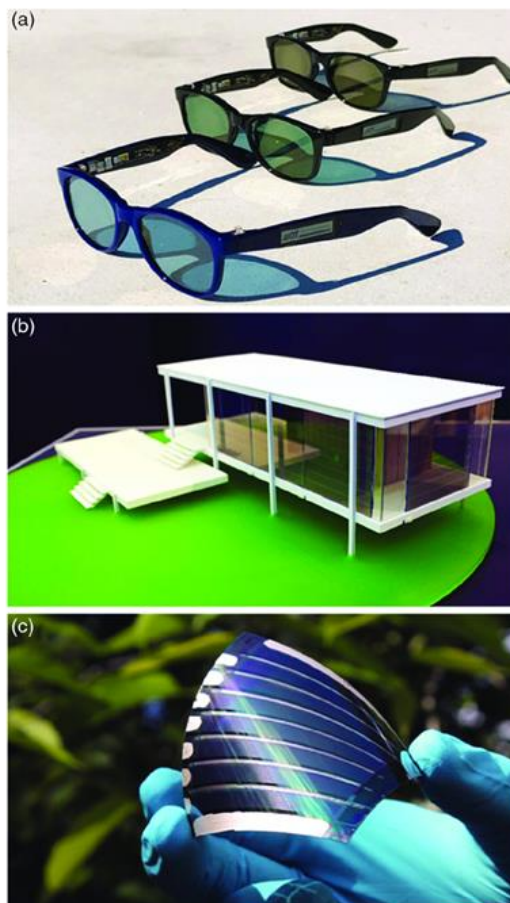


Figure 1.1 a) The Solar Glasses feature two semitransparent organic solar cells as lenses which can harvest sufficient energy, e.g., for mobile sensing applications, even under lowlight conditions (indoors). The color of the solar cells can be chosen to match the color of the chassis. b) Likewise, semitransparent solar cells can be used as shading elements in glass facades as demonstrated in this model house. c) Their mechanical flexibility, their freeform design, and their low weight render organic solar modules perfect enablers for novel applications. Adapted with permission of reference [6]. Copyright 2017, Wiley-VCH.

Upon absorption of an incident photon by the active layer, the electron is excited from the HOMO to the LUMO and a strongly bound electron-hole pair (exciton) is created. To form free charges, the exciton must encounter an interface between the D and A materials. Therefore, because of the energetic mismatch between the LUMO of D and A, the energetically more stable states of A promote the electron transfer from D to A, generating a hole on the polymer. A similar phenomenon occurs for the exciton formed in the A material. Both phenomena lead to photogenerated free charges, electrons and holes in the A and D phases, respectively. Once separated, the charges can migrate through the active layer towards their respective electrodes.[7]

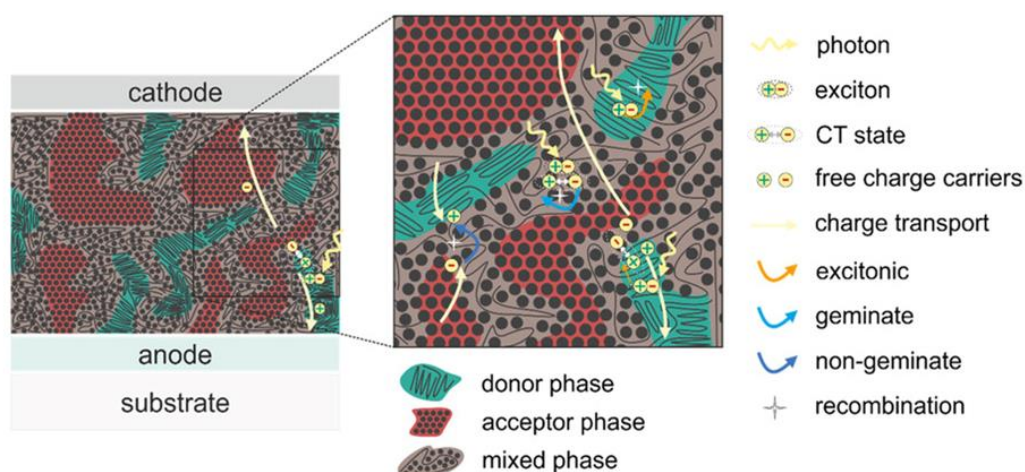


Figure 1.2 Working principle of a polymer:fullerene bulk-heterojunction. Light is absorbed on the polymer, upon which an exciton is generated. The exciton dissociates into the CT state between the polymer donor and the (fullerene) acceptor from which it further dissociates into free charge carriers. Recombination can occur from the excitonic state, from the subsequent CT state (geminatate recombination) or when two opposite charge carriers meet on their way to the electrodes (nongeminatate recombination). Adapted under the terms and conditions of the CC BY-SA 4.0 license.[3] Copyright 2019, KIT.

One of the main hindrances to replacing inorganic photovoltaic panels with organic ones is the low efficiency of OSCs compared to silicon-based cells. The benchmark A and D pair in the OPV field is constituted by [6,6]-phenyl-C₆₁-butyric acid methyl ester (PC₆₁BM) and poly(3-hexylthiophene) (P3HT), respectively, due to their availability and relatively low cost. Nevertheless, in the past few decades, the photoactive material design and the improved device layers enabled a steep rise in the PCEs of OPV devices. Originally, PCEs were improved by enhancing the overlap between the polymer absorption and the solar spectrum, and by adjusting the charge carrier transport energies of the active materials.

As displayed in **Figure 1.3**, a drastic implementation in the OPV field was provided by the design of copolymers characterized by smaller energy gaps (E_g) than homopolymers. Furthermore, the side chains of the donor polymer can be modified in order to tune energy levels of the material, to modify its solubility in organic solvent, and to control its molecular aggregation, which affects the charge carrier transport. The best performing fullerene:polymer OSC gained a PCE of ~12%. [8] A further boost in the device performance was provided by the introduction of non-fullerene acceptor (NFA) materials. Nowadays, OPV performances reach the 18% at the laboratory scale. [9]

The main factor that determines lower PCEs in organic devices compared to their inorganic counterparts is the dramatic energy losses, which occur in OPV devices, ascribable to

different contributions: the charge-transfer (CT) states,[10-13] and the non-radiative recombination mechanisms (**Figure 1.2**).[14, 15]

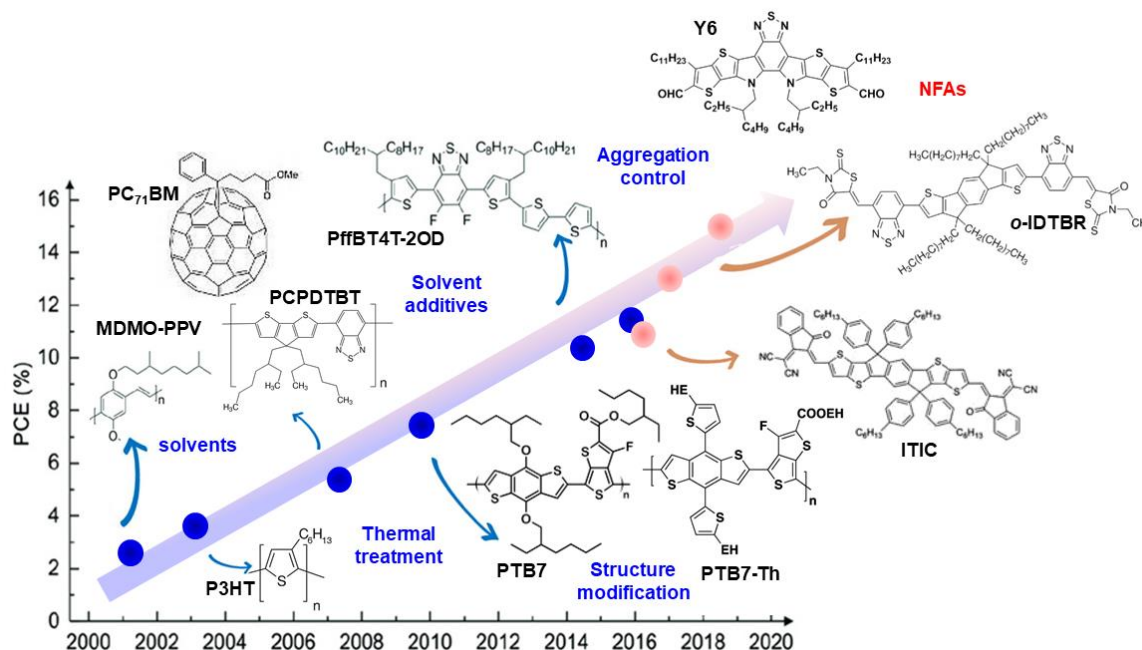


Figure 1.3 The main milestones in the conceptual development of novel light-harvesting polymer donors and, lately, acceptors for the improvement in OSCs. Gradually increasing PCEs were obtained by the development of polymer donors, which were blended with functionalized fullerene derivatives. Recently, the exploration of NFAs led to even higher PCEs. Key findings on processing conditions (choice of solvents, solvent additives, aggregation control) were as important as the development of the semiconductor materials to control the bulk-heterojunction morphology, and to yield higher efficiencies.

Therefore, the most promising concept to improve the PCE of OSCs is to reduce these losses by means of tandem architectures,[16] or using ternary blends of organic semiconductors.[17-19] Moreover, OPV devices suffer from long-term stability issues in comparison with inorganic devices.[3] What is more, another of the major issues regarding OPV is the scalability of the processes from lab to fab. In particular, to be industrially accepted, photoactive materials must fulfil two key criteria: they must be obtained through a low-cost synthesis and be solution-processable in thin films.[20] The last one is critical because most organic semiconductors are soluble in toxic halogenated solvents like dichlorobenzene, chlorobenzene, or chloroform, which are harmful to the environment and human health. In addition, they generally require a moderate temperature (above 80 °C) to be processed, producing a huge amount of hazardous vapors.[21, 22] For this reason, many efforts were done by scientist to decrease halogenated solvent waste, rendering the industrial manufacturing of OPV devices safer and more sustainable. In this regard, three main strategies were advanced.[23, 24] The first is the replacement of these hazardous

solvents by more environmentally friendly alternatives; some of them are illustrated in **Figure 1.4**. [25, 26] It is important to note that halogen-free solvents are considered "green" compared to chlorinated ones, but some of them (especially aromatics) are not without risk. The second developed approach consists in the functionalization of donor and acceptor structures with hydrophilic or polar side chains to design materials soluble in green solvents such as water or alcohol. [27, 28] The third strategy is the production of polymer-based nanoparticles processable in aqueous medium.

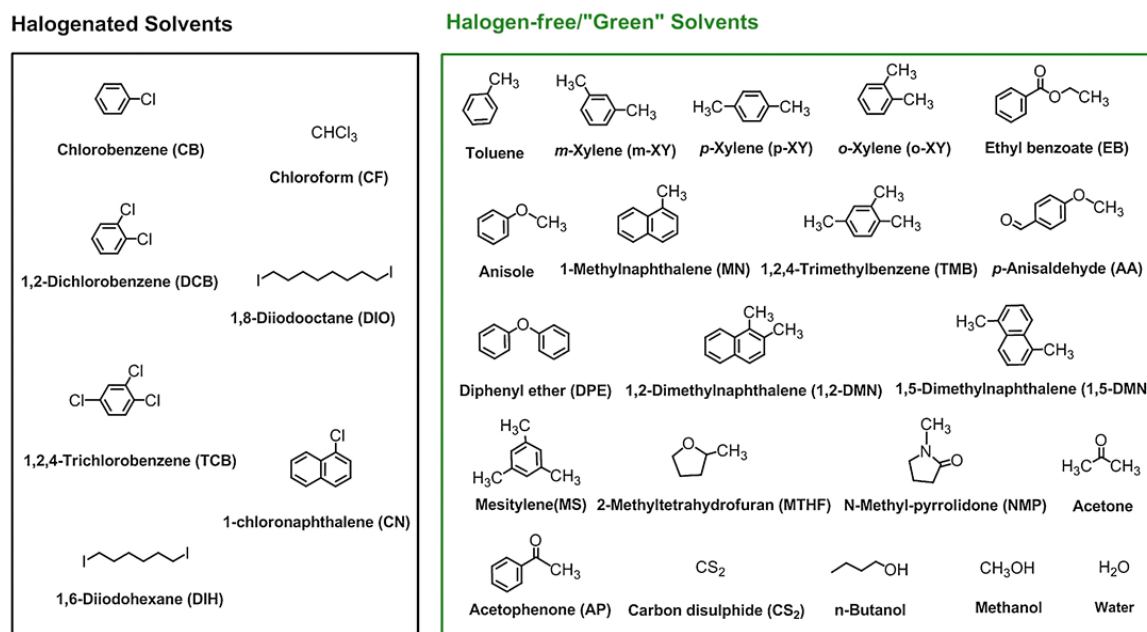


Figure 1.4 Illustration of some toxic halogenated solvents and "green" solvents used in OPV device fabrication. Reproduced with permission of reference [25] under the terms and conditions of the license. Copyright 2016, Elsevier.

1.2 Water-processable nanoparticles

Nanoparticles (NPs) are solid and colloidal objects, generally spherical but not always, with a diameter ranging from 1 to 100 nm. [29] NPs based on organic semiconductors can be prepared through a top-down or a bottom-up approach. The former corresponds to the dispersion of already synthesized polymers in the dispersed media, and the latter involves the polymerization of hydrophobic monomers in the dispersed media. [30] The top-down methodology is more versatile as allows to achieve dispersions from preformed single donor, single acceptor, or donor/acceptor blends of a wide variety of materials. Also, this approach provides the opportunity to control the morphology of the active layer thin film, and optimize the interpenetrating networks of electron-donors/acceptors, improving the final performance of the device. There is a delicate balance between two levels of

organization that contribute to the accomplishment of this condition. The first is the nanoscale, in which D and A must be sufficiently mixed to provide a large surface area of contact between both materials for an efficient exciton dissociation. The second is the mesoscale: a phase separation must occur to enable the existence of D and A domains to provide charge percolation pathways towards collecting electrodes. From these considerations it results that the ideal structure is made up of interpenetrating A and D networks, forming nanodomains with length comparable with exciton diffusion length (~20 nm). Therefore, the water-processable nanoparticles (WPNPs) approach is very attractive as it allows to module both the morphology at the molecular scale and the phase separation at the scale of the NPs. The main strategies reported in the literature to prepare single-component (containing either D or A) or composite (containing a blend of D and A) organic semiconducting NPs are the miniemulsion and the nanoprecipitation methods.[7]

1.2.1 Miniemulsion method

The miniemulsion method was firstly proposed by Landfester *et al.* in 2002 for the preparation of conjugated polymer NPs.[31] The mechanism of the NP formation is based on the immiscibility of the organic solvent and the non-solvent continuous phase (water). As depicted in **Figure 1.5**, the process involves the addition of the active materials dissolved in an appropriate solvent (organic phase) into an aqueous phase containing surfactants. Firstly, two immiscible phases are observed, and a macroemulsion is formed by conventional stirring. Therefore, a metastable miniemulsion is generated by means of ultrasonication, *i.e.* nanodroplets containing active materials and organic solvent are dispersed in the aqueous medium. At this point, the organic solvent is removed by evaporation leading to the formation of solid NPs dispersed in water. The NPs forming the dispersion have sizes on the order of 50-250 nm, depending on the experimental parameters. The dimensions can be controlled during the NP formation by varying the shear force applied during the miniemulsion process,[32, 33] the starting polymer concentration in the organic phase,[33-35] the typology of organic phase, and the surfactant nature and concentration.[33, 36, 37] The miniemulsion method is very versatile because it can be applied to a wide variety of semiconductor polymers, depending on the solvent chosen for the organic phase. Indeed, although low boiling point solvents such as chloroform are preferentially used, active materials can also be dissolved in high boiling temperature solvents (*ortho*-xylene, toluene, *ortho*-dichlorobenzene).[38, 39]

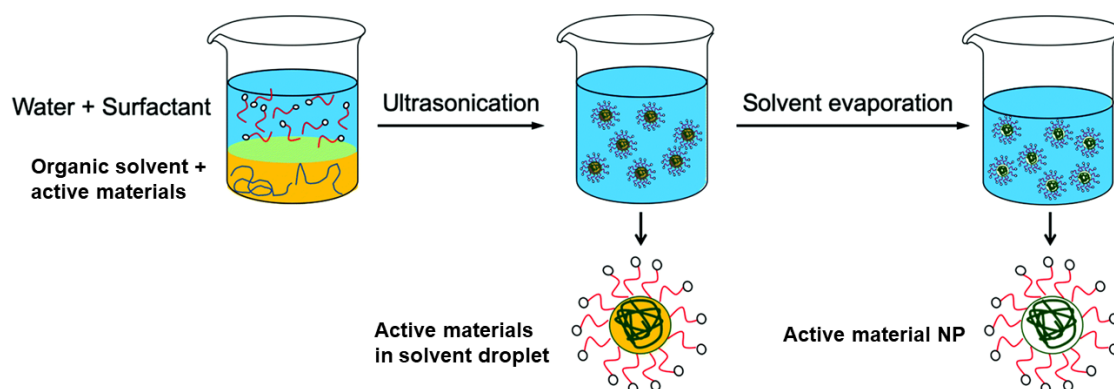


Figure 1.5 Schematic representation of NP preparation by the miniemulsion process. Reproduced with permission of reference [20]. Copyright 2020, The Royal Society of Chemistry.

In these cases, removal of the organic solvent by evaporation takes several hours, during which water is also lost and therefore it must be added regularly to the flask to compensate. The moment of organic solvent evaporation is decisive as phase separation inside NPs occurs. While the organic solvent is removed, both active materials start to rearrange to minimize unfavorable interfacial interactions, leading to a core-shell,[40] Janus,[41] or more complex nanostructures.[42] The factors that most impact the internal morphology are the miscibility of both materials and their surface energy. Typically, materials with higher surface energy segregate into the core of NPs. This is the reason why the miniemulsion approach applied to fullerene:polymer blend generally leads to the formation of core-shell NPs, with the fullerene material in the core and the semiconducting polymer in the shell.[33, 40, 43, 44] In addition, Holmes *et al.* showed that the NP morphology depends on the ratio of the two materials,[45] and they demonstrated that the phase separation and composition are affected by the nature of the active materials.[46] From these considerations it follows that the internal structure of NPs depends on the solvent chosen; varying solvent and evaporation rate, aggregation of polymer chains and phase separation change, and consequently the morphology.[20] As a matter of fact, Nagarjuna *et al.* showed that the solvent used influences the crystalline order of the aggregated phase inside the NPs.[47] Moreover, Marks *et al.* demonstrated that a rapid evaporation of the organic solvent under vacuum leads to a core-shell morphology with more intermixed phases, because of a reduced time for the materials to organize in the NPs.[48]

One of the main drawbacks of the miniemulsion approach is the use of surfactants, necessary to stabilize the aqueous/non-aqueous interfaces, assuring the colloidal

suspension stability. Nevertheless, their presence in the active layer of an OPV device is detrimental for the charge transport.[49] In fact, Han *et al.* showed that the presence of surfactants in the active layer promotes defect generation, resulting in higher charge carrier trapping.[50] Therefore, an additional step is required to remove the excess of the free surfactant before the film deposition, and also to shrink the volume of the aqueous phase, concentrating the dispersion. This goal is achieved by various washing procedures using Millipore membranes, dialysis, or centrifugation. [38, 51, 52] The most widely agent used to promote emulsification is sodium dodecyl sulfate (SDS), but a large variety of surfactants were explored over the years, either anionic (with sulfate groups), cationic (with ammonium moieties), and non-ionic (with ethoxylated chains). The chemical structures of the surfactants most investigated by the research groups are shown in **Figure 1.6**. Ionic surfactants stabilize NPs through electrostatic repulsions, while non-ionic surfactants ensure colloidal stability by steric hindering. The emulsification behavior of surfactants is also affected by the hydrophilic/lipophilic balance (HLB) that can be estimated through the Griffin's or Davies' theories.[53-55] Cho *et al.* proposed four general rules for selecting the most suitable surfactant to prepare monodisperse NP suspensions:[56] the ability to form a stable emulsion, the minimum quantity of surfactant necessary to reach the stability, the efficient removal of the excess, and the ability to generate highly crystalline domains.

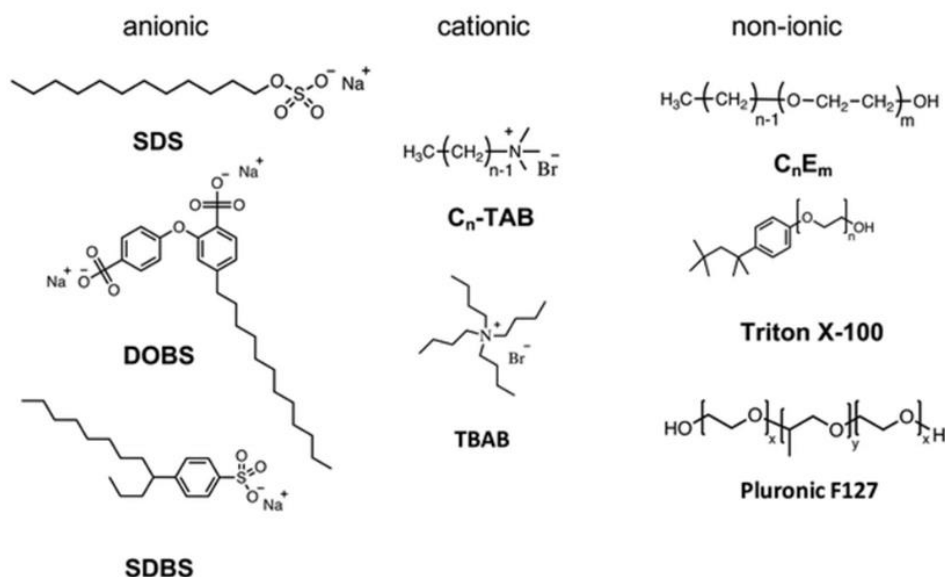


Figure 1.6 Chemical structures of surfactants mainly used in the miniemulsion approach. Reproduced with permission of reference [20]. Copyright 2020, The Royal Society of Chemistry.

By screening a wide range of candidates, the research group stated that a large aromatic tail hinders proper interaction with the polymer, while surfactants with linear alkyl chains form strong van der Waals bonds with the polymer. Specifically, by increasing the length of the alkyl tail, the packing of the polymer in the NPs becomes better, improving the charge mobility in the final active layer.[57] Furthermore, non-ionic surfactants lead to large NPs because they are not completely efficient in ensuring suspension stability. An intriguing surfactant molecule is the 2-(3-thienyl)-ethoxybutylsulfonate sodium salt (TEBS), chosen by Subianto *et al.* to prepare PC₆₁BM:P3HT NPs because of the peculiar affinity between the surfactant and both active materials. The resulting NPs were larger than ones obtained using SDS, but displayed a more homogeneous structure, different from the core-shell one, with interconnected domains of D and A materials (**Figure 1.7**), suitable for the charge percolation in the OPV device.[58]

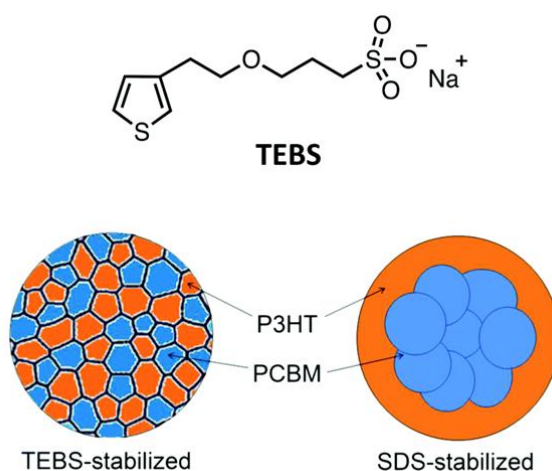


Figure 1.7 Representation of the nanostructuring of PC₆₁BM:P3HT NP stabilized by TEBS and by SDS. Adapted with permission from reference [58]. Copyright 2022 American Chemical Society.

1.2.2 Nanoprecipitation

In the nanoprecipitation technique an organic solution of the active materials is injected into a large volume of non-solvent (usually water or alcohol), miscible with the initial organic solvent (**Figure 1.8**). Therefore, the organic solvent is displaced to achieve solid NPs dispersed in water. Contrary to the miniemulsion approach, this method is quick, does not require any surfactant, and can be scaled up for the large-scale synthesis of NPs.[59]

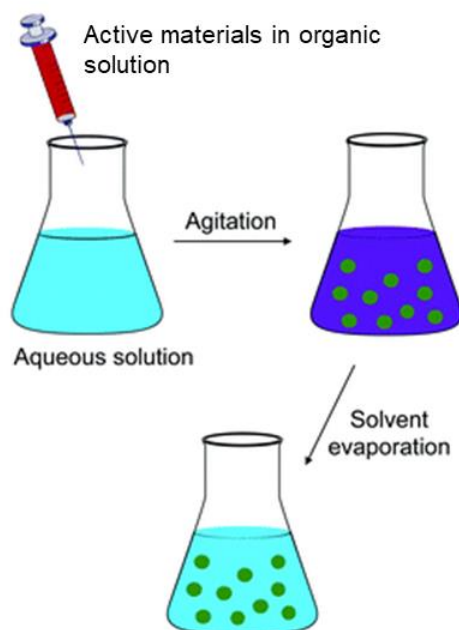


Figure 1.8 Schematic representation of the nanoprecipitation process. Reproduced with permission of reference [20]. Copyright 2020, The Royal Society of Chemistry.

Nonetheless, the aqueous suspensions suffer from long-term stability issues and exhibit low NP content in the final dispersion.[60] To overcome this problem, Xie *et al.* recently proposed a surfactant-assisted nanoprecipitation method, which combines the main advantages of the two approaches ensuring the preparation of stable aqueous suspensions and more concentrated inks.[61] Another disadvantage of this approach is the restricted array of solvents, as to achieve dispersions in water or alcohol, the organic solvent must be miscible, such as tetrahydrofuran.[62]

As for the miniemulsion method, the size and the crystallinity of NPs can be modulated through processing parameters, as the mixing speed of the two phases, the kind of solvent, the nature of the alcohol, the active material concentration, the A/D ratio, and the solvent/non-solvent ratio.[63-66] Taking advantage of this approach, no core-shell morphology is generally observed. Otherwise, NPs with uniform internal phase separation are formed (**Figure 1.9**), making the nanoprecipitation approach very attractive for OPV applications because the active layers result very close to ones obtained by casting from organic solvents.[67, 68] Darwis *et al.* ascribed this peculiar morphology to the short organic solvent removal step that “freezes” the distribution of both components in NPs, which results in highly intermixed domains.[60]

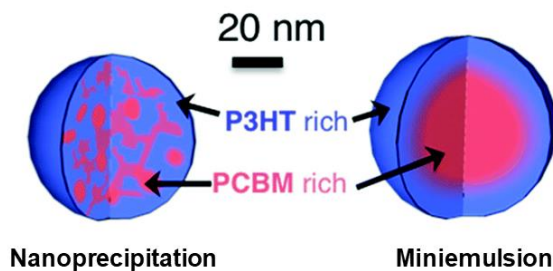


Figure 1.9 Schematic representation of the inner morphology of NPs prepared by nanoprecipitation or by miniemulsion. Adapted with permission of reference [67]. Copyright 2009, The Royal Society of Chemistry.

However, Chambon *et al.* synthesized inverted core-shell NPs *via* nanoprecipitation by means of successive solvent displacements, *i.e.* carrying out the sequential double precipitation of the A and the D materials.[69, 70]

1.3 WPNP-based OPV devices

The deposition from aqueous inks and the fabrication of the active layer is a key step in WPNP-based OPV device. In 2003, Kietzke *et al.* reported for the first time about an OSC achieved from NPs composed of the semiconducting materials poly(9,9-dioctylfluorene-*co*-benzothiadiazole) (F8BT) and poly(9,9- dioctylfluorene-*co*-*N,N'*-bis(4-buthylphenyl)-*N,N'*-diphenyl-1,4-phenylenediamine) (PFB).[71] They obtained a PCE extremely low (<0.004%) with respect to the same polymers in BHJ blend devices (~0.2%). In 2012, Stapleton *et al.* used F8BT:PFB-based NPs to fabricate a multilayered OPV device, obtaining an efficiency higher than that of the conventional blend device.[72] The improved performance was gained through the control of the surface energies of the components in the polymer NPs, and by the post-deposition thermal treatment of the active layer. As mentioned above, the ideal morphology of the film is a two phase bicontinuous structure, constituted by percolating pathways which allow the exciton dissociation at D/A interfaces and the charge transport towards the electrodes.[73] This goal is reached through the optimization of the active layer from aqueous suspensions exploiting two key steps: the NP deposition and assembly during the aqueous solvent evaporation, and the thermal annealing treatment to promote the diffusion of materials in the interparticle voids, obtaining films with higher compactness and homogeneity.[20] These two steps can be repeated several times in order to achieve multilayered films with the desired thickness and absorbance.[72]

At the laboratory scale, films by aqueous suspensions are deposited mainly through spin-coating.[74] With this technique, some tricks are needed to bypass the wettability issues of the hydrophobic substrates. Particularly, an ultraviolet ozone (UV-O₃) treatment of the poly(3,4-ethylenedioxythiophene):polystyrene sulfonate (PEDOT:PSS) layer allows a rapid and uniform deposition of NPs. Alternatively, Ghazy *et al.* reported the replacement of the PEDOT:PSS interlayer with Plexcore (25 nm).[75] Furthermore, a low surface roughness is more easily obtained if the NPs are spin-coated from a mixture of ethanol:water instead of pure water. Lastly, the deposition of a PC₆₁BM buffer ETL on the top of the photoactive layer enables a better charge extraction, reduces the surface roughness between the active layer and the electrode, and ensures the absence of short-circuits and leakage currents.[73, 76, 77]

Two main approaches can be exploited to fabricate the active layer: the use of pure NPs (single-component NPs) or the deposition of NPs combining both D and A inside the same NP (composite NPs). In the first case, the film is obtained from a binary mixture of NPs (NPs of pure D and NPs of pure A) deposited using spin-coating. A random close-packed (RCP) is generally observed, and several parameters can be modified to tune the final film morphology, as the ratio between the two types of NPs and their difference in size.[73] A post-deposition annealing treatment is required to fill the interparticle voids contained into the RCP packing, by merging the NPs and obtaining a continuous and compact film. Furthermore, in this way the contact area between D and A increases, improving the exciton dissociation, and more charge conduction pathways are generated.[41, 78] Holmes *et al.* reported that the use of single-components NPs can lead, after annealing, to a three phase microstructures: pure D domains (for efficient hole transport), pure A domains (for electron conduction), and an amorphous third phase made up of mixed D and A (**Figure 1.10**).[79] This new strongly intermixed phase allows a high exciton diffusion, resulting in an improved exciton dissociation efficiency and thus a better device performance.

On the other side, for films from composite NPs, containing a blend of D and A materials, the phase separation is different and depends on the size and inner morphology of NPs. The most common morphology is the core-shell one, but it is not the ideal nanostructuration since pathways suitable for the charge percolation in the final film are difficult to obtain. Therefore, the thermal annealing is crucial to achieve an active layer properly interconnected.[60, 80-82]

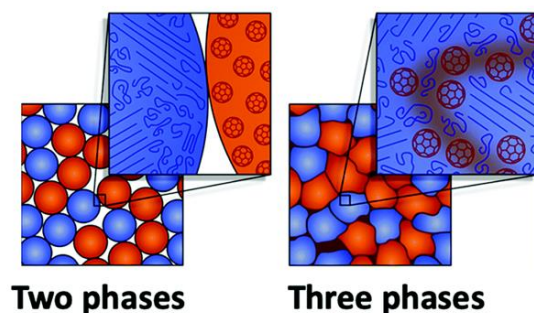


Figure 1.10 Schematic representation of the three phase film microstructures achieved by thermal annealing of the assembly of pure PC₆₁BM and pure P3HT NPs. A third intermixed phase is formed by sintering and diffusion of PC₆₁BM in the P3HT amorphous domains. Adapted with permission from reference [79].

Gärtner *et al.* deeply investigated the correlation between the thermal annealing and the final OPV device efficiency, studying the limiting recombination processes by means of intensity dependent photo-current density experiments.[83] The research group found out that the thermal treatment enhances the close packing of NPs, improving the charge transport and extraction. At the same time, they observed that the film roughness decreases, and the photovoltaic parameters increase, reaching a PCE of ~4%, very close to that of device obtained by deposition from toxic chlorinated solvents.

Spin-coating is not the appropriate deposition method at the industrial scale, where large surface area devices have to be prepared, and therefore other printing techniques are required. Printing processes allow flexible design of OSCs to meet the requisites of skilled photovoltaic applications, such as facade integration or consumer electronics.[3] For example, Bag *et al.* reported about P3HT-based NPs deposited to form a layer with thickness up to 1.5 μm by means of spray coating.[84] Other interesting techniques are the ink-jet printing, which allows the fabrication of OSCs with a designed shape, and the doctor blading, that ensures to gain large surfaces homogeneously coated.[61, 85, 86] Finally, the roll-to-roll technique allowed several research groups to deposit flexible OSC active layers from fullerene:polymer NP aqueous dispersions on PET substrate.[87-89] This last strategy is considered the most promising route to the large-scale printing of OPV devices from aqueous inks.

Generally, OPV devices made from aqueous suspensions have lower efficiencies than conventional ones. There are two main mechanisms that hamper the PCE of WPNP-based OPV devices: free charge generation, which requires exciton dissociation, and free charge extraction.[20] Al-Mudhaffer *et al.* conducted a study on PC₆₁BM:P3HT core-shell NPs

and concluded that the major limiting factor in their device was low exciton dissociation, likely due to the core-shell morphology.[90] Other research groups gained more promising results; for instance, Gärtner *et al.* fabricated an inverted OSC from ICBA:P3HT-based NPs prepared by nanoprecipitation.[83] After a proper thermal annealing on the active layer, they achieved a PCE comparable to that of the conventional solar cell, concluding that the thermal treatment decreases free charge recombination. A similar finding was accomplished by Xie *et al.* by using a non-fullerene acceptor material, namely the 5Z,5'Z)-5,5'-((7,7'-(4,4,9,9-tetraoctyl-4,9-dihydro-s-indanoceno[1,2-b:5,6.b']bithiophene-2,7-diyl)bis(benzo[c][1,2,5]thiadiazole-7,4-diyl))bis(methanylylidene))bis(3-ethyl-2-thioxothiazolidin-4-one (*o*-IDTBR)).[61]

Once exciton is dissociated and free charges are generated, the next issue concerns their extraction. One of the main methods to determine the charge extraction efficiency is to measure the charge carrier mobility.[91] Mobility can be probed along the substrate plane or in the out-of-plane direction through several layers of the device. The out-of-plane direction is perpendicular to the electrodes, and it is the preferential direction of charge transport in multilayer OSCs. This mobility can be estimated by means of time of flight (TOF) measurements,[92] and space charge limited current (SCLC) diodes.[93] Otherwise, organic field effect transistors (OFETs) allow to measure the mobility along the substrate plane.[94]

In order to implement the performance of OSCs, many parameters must be considered, such as the ratio between the D and the A materials. This ratio generally depends on the nature of the active materials and affects the morphology, the charge carrier mobilities, and thus the final PCE.[76] Noticeably, the optimal A:D ratio used in conventional photovoltaic devices should be modified when the active layer is deposited from aqueous suspensions, considering the miscibility between the two components.[45, 46] Another factor affecting OPV efficiency is the nature of the D and A materials; P3HT and PC₆₁BM continue to be the benchmark system due to their commercial availability and modest cost.[76, 95] Nevertheless, the resulting devices have PCE values limited by their optical and electronic properties. Ulum *et al.* improved the efficiency by replacing PC₆₁BM with a fullerene bisadduct, namely the indene-C₆₀-bisadduct (ICBA),[96] which has a higher LUMO level, is more soluble in organic solvents,[97] and it is more miscible in P3HT with respect to PC₆₁BM. In this case also, the post-deposition processing played a key role. Indeed, untreated NPs displayed a core-shell morphology with an enhanced ICBA concentration in the core region. After annealing, the core-shell structure was lost, and a more mixed

composition was observed. This evidence is related to the higher miscibility of ICBA in P3HT than PC₆₁BM, which results in a more efficient intermixed structure.

A significant development in the WPNP-based device field occurred with the exploration of the low band gap (LBG) polymers as donor materials,[22, 98] which are characterized by more suitable properties for photon harvesting and charge transport. The synthesis of NPs based on these materials results challenging because their poor solubility in the most common organic solvents with respect to the benchmark P3HT.[21, 99] D'Olieslaeger *et al.* exploited the miniemulsion approach to prepare NPs with a benzodithiophene- (BDT) based LBG polymer blended with phenyl-C₇₁-butyric acid methyl ester (PC₇₁BM).[38, 39] They fabricated an OPV device from these NPs dispersed in water, reaching a PCE of 3.8% after an optimized annealing step.

A further improvement was provided by NFAs, which were employed to prepare aqueous inks that led to an efficiency up to 7%.[61] In the last few years NFAs emerged as a very intriguing alternative to traditional fullerene derivatives thank to the opportunity of tuning their molecular energy levels, thus the absorption properties, and the electron mobilities. Particularly, Xie's group synthesized WPNPs from some emerging LBG polymers blended with the NFA *o*-ITBR, or 3,9-bis(2-methylene-(3-(1,1-dicyanomethylene)-indanone))-5,5,11,11-tetrakis(4-hexylphenyl)-dithieno[2,3-d':3'-d']-s-indaceno[1,2-b:5,6-b']dithiophene (ITIC). The resulting OSCs exhibited performance and stability comparable with those of BHJ devices.

1.4 WPNPs for biological applications

The possibility of obtaining nanostructures with strongly intermixed D and A material networks, and the opportunity to tune the absorption properties by selecting appropriate active materials make aqueous inks excellent scaffolds not only for the industrialization of OPV technology, but also in other emerging applications. For example, it is reported in the literature that semiconducting polymer-based NPs were exploited for biological applications.[100] Their appealing for the biological field stays in their peculiar characteristics. Indeed, not only NPs are biocompatible and have dimensions close to those of the biomolecules, but they are also soft and endowed with excellent electron transport and optical properties, such as high fluorescence, and good photostability. Thanks to these features, recent studies in which semiconducting polymer-based NPs are employed for *in vitro* and *in vivo* experiments are reported.[63, 101-103] Semiconducting polymer-based

NPs were applied as phototheranostic agents for superficial/deep-tissue cancer treatment, as activatable probes for molecular imaging.[104-106] Particularly, semiconducting NPs are able to act as photoactuators, *i.e.* they can transform light stimuli into an alteration of the physiological functions.[107-109]

Some recent study reported the exploitation of polymeric NPs as light sensitive actuators. Particularly, P3HT NPs were tested as optical transducers in HEK-293 cells; electrophysiology and Ca²⁺ imaging experiments proved that the physiological functions are fully preserved in presence of the NPs, that are uptaken in the cytosol.[103] A further experiment with the same NPs functionalized with alkyl side chains terminating with N-hydroxysuccinimidyl ester groups (NHS) demonstrated that the NPs, when administered to HEK-293 cells, stay on the top of the cell membrane, and upon illumination depolarization of the membrane potential is recorded.[110] Regarding the *in vivo* applications, optical modulation effects of P3HT NPs on *Hydra* were demonstrated: upon illumination changes in the expression of opsin proteins induced by NPs were observed.[111] In Chapter 2, the biological applications of BCP2-based WPNPs as tools to affect the human cell metabolism are discussed.

Recently, aqueous suspensions of semiconducting organic NPs were also under investigation in the hydrogen evolution photocatalysis.[112] This application is enabled by their lower toxicity with respect to the inorganic photocatalytic systems currently used, as well as their broader absorbance, and higher quantum efficiency. In this field, a great result was gained by Kosco *et al.*, who achieved aqueous suspensions using the blend consisting of the NFA EH-IDTBR and the PTB7-Th.[113] They reached an astonishing photocatalytic activity with a H₂ evolution rate up to 60000 $\mu\text{mol h}^{-1} \text{g}^{-1}$ under 350 to 800 nm illumination, which is a record never reported before.

1.5 Summary of WPNP-based OPV device performances

As summarized in **Table 1.1**, performances of WPNP-based devices reported in literature significantly increased from less than 1% up to 7%, from early 2000 to the beginning of 2020. It is evident that the main approach used by the research groups is the miniemulsion, and a strong increase in PCE was observed since 2014, with a deeper understanding of NP morphology, active layer deposition, and the influence of processing parameters on final device efficiency.

Table 1.1 Summary of photovoltaic characteristics of WPNP-based devices reported in literature.

Material (A:D)	NP synthesis technique	V_{oc} (mV)	J_{sc} (mA cm⁻²)	FF	PCE (%)	Reference
F8BT:PFB	Miniemulsion	n.d.	n.d.	n.d.	0.004	[78]
F8BT:PFB	Miniemulsion	770	1.81	0.28	0.39	[72]
F8BT:PFB	Miniemulsion	n.d.	n.d.	n.d.	1.70	[114]
PC₆₁BM:P3HT	Miniemulsion	470	4.89	0.50	1.16	[115]
PC₆₁BM:P3HT	Miniemulsion	509	6.38	0.66	2.15	[73]
PC₆₁BM:P3HT	Miniemulsion	360	5.9	0.52	0.9	[48]
PC₆₁BM:P3HT	Miniemulsion	529	4.18	0.41	0.91	[45]
PC₆₁BM:P3HT	Nanoprecipitation	634	4.84	0.36	1.09	[60]
PC₆₁BM:P3HT	Miniemulsion	510	5.84	0.65	1.94	[74]
PC₆₁BM +PEG-C₆₁:P3HT	Miniemulsion	540	10.3	0.55	2.94	[116]
PEG-C₆₁:P3HT	Miniemulsion	540	9.11	0.53	2.62	[117]
PC₆₁BM:TQ1	Miniemulsion	910	0.37	0.28	0.1	[88]
ICBA:P3HT	Miniemulsion	763	5.85	0.55	2.44	[96]
ICBA:P3HT	Nanoprecipitation	781	9.00	0.58	4.1	[83]
ICBA:P3HT	Nanoprecipitation	834	9.00	0.55	4.2	[118]
ICBA:P3HT	Nanoprecipitation	797	9.20	0.53	3.9	[68]
ICBA:P3HT	Nanoprecipitation	810	9.74	0.56	4.44	[66]
ICxBA:P3HT	Miniemulsion	500	3.64	0.36	0.67	[49]
o-IDTBR:P3HT	Surfactant-assisted nanoprecipitation	760	10.36	0.63	4.95	[61]
PC₇₁BM:PCDTBT	Nanoprecipitation	480	1.65	0.29	0.19	[65]
PC₆₁BM:PSBTBT	Miniemulsion	470	3.99	0.29	0.55	[87]
PC₇₁BM:PDPP-TNT	Miniemulsion	760	6.09	0.43	1.99	[81]
PC₇₁BM:PDPP5T	Miniemulsion	540	9.43	0.47	2.36	[52]
PC₇₁BM:PCDTBT	Miniemulsion	605	3.79	0.31	0.7	[33]
PC₇₁BM:PTNT	Miniemulsion	870	4.58	0.39	1.56	[39]
PC₇₁BM:TQ1	Miniemulsion	691	8.26	0.38	2.11	[82]
ICBA:P(TBT-DPP)	Miniemulsion	430	10.49	0.47	2.16	[119]

PC₇₁BM:PDPP5T	Miniemulsion	540	11.59	0.49	3.07	[34]
PC₇₁BM:PBDTPD	Miniemulsion	764	10.45	0.40	3.2	[38]
PC₆₁BM	Miniemulsion	720	13.6	0.55	5.29	[116]
+PEG-C₆₁:PBDTT-FTTE						
<i>o</i>-IDTBR:PCE10	Surfactant-assisted nanoprecipitation	970	12.01	0.42	4.94	[61]
<i>o</i>-IDTBR:PBQ-QF	Surfactant-assisted nanoprecipitation	950	13.09	0.48	5.96	[61]
ITIC:PBQ-QF	Surfactant-assisted nanoprecipitation	850	14.87	0.53	6.97	[61]

1.6 Aim of the work

The aim of my PhD project is the fabrication of sustainable active layers processable in water for optoelectronic applications, and in particular for OSCs. This goal was achieved through the preparation of WPNPs based on semiconducting polymers. Aqueous suspensions are generally prepared by a miniemulsion process, in which a blend of p-type and n-type semiconducting materials is dissolved into an organic solvent immiscible with water, and properly emulsified with an aqueous phase. Therefore, the organic solvent is removed by evaporation through a mild heating of the miniemulsion. This approach leads to the formation of stable aqueous suspensions of NPs consisting of the active materials making up the starting organic mixture. The further deposition and thermal annealing of the WPNPs on a properly treated substrate allows to obtain homogeneous and compact active layers. In contrast to the many papers reported in the literature on colloidal suspensions obtained *via* miniemulsion, my PhD focused on exploiting a miniemulsion approach modified such that it does not require the use of additional surfactants to stabilize the aqueous/organic solvent interfaces. Indeed, the emulsifying agents display an insulating behavior and must be removed at the end of the process. Furthermore, they generally lead to the formation of NPs with a core-shell inner morphology, that is not optimal for the proper charge percolation in the active layer of the resulting device. At this purpose, the SCITEC-CNR research group developed the preparation of polymer-based aqueous inks through an adapted miniemulsion method using amphiphilic rod-coil block copolymers (BCPs), bearing a rigid block (a p-type semiconducting polymer) and a hydrophilic flexible

segment. This coil block is able to interact with aqueous medium, assuring the colloidal suspension stability, and it is able to interact also with n-type fullerene or non-fullerene semiconducting materials. Thanks to these features, amphiphilic BCPs are able to self-assemble both neat and in blend with acceptor materials, generating pre-organized nanostructures with domains whose dimensions are suitable for the separation and the collection of the charges in the final device active layers. Finally, a mild thermal annealing of the deposited WPNPs films on different substrates (e.g. ITO, PEDOT:PSS, ZnO, etc.) provided films that were investigated as active layers in OSCs. LBG copolymers are considered as electron-donor materials in order to enhance the solar radiation absorption. Specifically, Dr. Silvia Destri and Dr. Stefania Zappia developed the synthesis of WPNPs based on four different poly[2,6-(4,4-bis-(2-ethylhexyl)-4*H*-cyclopenta[2,1-*b*;3,4-*b'*]dithiophene)-*alt*-4,7(2,1,3-benzothiadiazole)] (PCPDTBT)-based BCPs. They chose as coil a tailored segment of poly-4-vinylpyridine (P4VP) and PC₆₁BM as electron-acceptor material. Noticeably, they gained an OSC with an efficiency of ~2.5%, which is slightly lower than the efficiency of a conventional device obtained by deposition of the blend from halogenated solvents. I started my PhD studying the correlation between the coil length of the synthesized BCPs, the morphology of the resulting WPNPs in blend with PC₆₁BM, and hence the efficiency of the WPNP-based OPV devices (Chapter 2). Furthermore, I decided to explore other materials endowed of partial crystallinity, to investigate the nanoscale structural organization of the p-type material within the WPNPs. Therefore, I synthesized a new amphiphilic BCB, which bears poly[[4,8-bis[(2-ethylhexyl)oxy]benzo[1,2-*b*:4,5-*b'*]dithiophene-2,6-diyl][3-fluoro-2-[(2-ethylhexyl)carbonyl]thieno[3,4-*b*]thiophenediyl]] (PTB7) as rod, and a segment of 15 repeating units of 4-vinylpyridine (4VP) as coil. I studied the self-assembly of the PTB7-*b*-P4VP in blend with PC₇₁BM, and the so-obtained WPNPs were deeply characterized and tested as active layer of OSCs (Chapter 3). Lastly, I synthesized two new LBG semiconducting BDT-based copolymers and a middle band gap polymer. These polymers will be blended with fullerene and non-fullerene acceptor materials to prepare WPNPs using surfactants with a standard miniemulsion approach or a surfactant-assisted nanoprecipitation method.[61] The resulting aqueous inks will be deposited as active layers of optoelectronic devices (Chapter 4), in collaboration with Dr. Nadia Camaioni (ISOF-CNR, Bologna) and Dr. Nicola Gasparini (Imperial College, London).

1.7 References

- [1] I.E. Agency, World Energy Balance: An Overview, World Energy Balances 2019, 2019.
- [2] V. Muteri, M. Cellura, D. Curto, V. Franzitta, S. Longo, M. Mistretta, M.L. Parisi, Review on Life Cycle Assessment of Solar Photovoltaic Panels, *Energies* 13(1) (2020).
- [3] A. Colsmann, H. Röhm, C. Sprau, Shining Light on Organic Solar Cells, *Solar RRL* 4(6) (2020) 2000015.
- [4] Z. Hu, K. Zhang, F. Huang, Y. Cao, Water/alcohol soluble conjugated polymers for the interface engineering of highly efficient polymer light-emitting diodes and polymer solar cells, *Chemical Communications* 51(26) (2015) 5572-5585.
- [5] R. Sorrentino, E. Kozma, S. Luzzati, R. Po, Interlayers for non-fullerene based polymer solar cells: distinctive features and challenges, *Energy & Environmental Science* 14(1) (2021) 180-223.
- [6] D. Landerer, D. Bahro, H. Röhm, M. Koppitz, A. Mertens, F. Manger, F. Denk, M. Heidinger, T. Windmann, A. Colsmann, Solar Glasses: A Case Study on Semitransparent Organic Solar Cells for Self-Powered, Smart, Wearable Devices, *Energy Technology* 5(11) (2017) 1936-1945.
- [7] A. Holmes, E. Deniau, C. Lartigau-Dagron, A. Bousquet, S. Chambon, N.P. Holmes, Review of Waterborne Organic Semiconductor Colloids for Photovoltaics, *ACS Nano* 15(3) (2021) 3927-3959.
- [8] J. Zhao, Y. Li, G. Yang, K. Jiang, H. Lin, H. Ade, W. Ma, H. Yan, Efficient organic solar cells processed from hydrocarbon solvents, *Nature Energy* 1(2) (2016) 15027.
- [9] Q. Liu, Y. Jiang, K. Jin, J. Qin, J. Xu, W. Li, J. Xiong, J. Liu, Z. Xiao, K. Sun, S. Yang, X. Zhang, L. Ding, 18% Efficiency organic solar cells, *Science Bulletin* 65(4) (2020) 272-275.
- [10] W. Zhao, D. Qian, S. Zhang, S. Li, O. Inganäs, F. Gao, J. Hou, Fullerene-Free Polymer Solar Cells with over 11% Efficiency and Excellent Thermal Stability, *Advanced Materials* 28(23) (2016) 4734-4739.
- [11] J. Liu, S. Chen, D. Qian, B. Gautam, G. Yang, J. Zhao, J. Bergqvist, F. Zhang, W. Ma, H. Ade, O. Inganäs, K. Gundogdu, F. Gao, H. Yan, Fast charge separation in a non-fullerene organic solar cell with a small driving force, *Nature Energy* 1(7) (2016) 16089.
- [12] T. Linderl, T. Zechel, M. Brendel, D. Moseguí González, P. Müller-Buschbaum, J. Pflaum, W. Brütting, Energy Losses in Small-Molecule Organic Photovoltaics, *Advanced Energy Materials* 7(16) (2017) 1700237.
- [13] I. Ramirez, M. Causa, Y. Zhong, N. Banerji, M. Riede, Key Tradeoffs Limiting the Performance of Organic Photovoltaics, *Advanced Energy Materials* 8(28) (2018) 1703551.
- [14] J. Benduhn, K. Tvingstedt, F. Piersimoni, S. Ullbrich, Y. Fan, M. Tropiano, K.A. McGarry, O. Zeika, M.K. Riede, C.J. Douglas, S. Barlow, S.R. Marder, D. Neher, D. Spoltore, K. Vandewal, Intrinsic non-radiative voltage losses in fullerene-based organic solar cells, *Nature Energy* 2(6) (2017) 17053.
- [15] S. Ullbrich, J. Benduhn, X. Jia, V.C. Nikolis, K. Tvingstedt, F. Piersimoni, S. Roland, Y. Liu, J. Wu, A. Fischer, D. Neher, S. Reineke, D. Spoltore, K. Vandewal, Emissive and charge-generating donor-acceptor interfaces for organic optoelectronics with low voltage losses, *Nature Materials* 18(5) (2019) 459-464.
- [16] L. Meng, Y. Zhang, X. Wan, C. Li, X. Zhang, Y. Wang, X. Ke, Z. Xiao, L. Ding, R. Xia, H.-L. Yip, Y. Cao, Y. Chen, Organic and solution-processed tandem solar cells with 17.3% efficiency, *Science* 361(6407) (2018) 1094-1098.
- [17] M. Zhang, Z. Xiao, W. Gao, Q. Liu, K. Jin, W. Wang, Y. Mi, Q. An, X. Ma, X. Liu, C. Yang, L. Ding, F. Zhang, Over 13% Efficiency Ternary Nonfullerene Polymer Solar

Cells with Tilted Up Absorption Edge by Incorporating a Medium Bandgap Acceptor, *Advanced Energy Materials* 8(30) (2018) 1801968.

[18] R. Yu, H. Yao, J. Hou, Recent Progress in Ternary Organic Solar Cells Based on Nonfullerene Acceptors, *Advanced Energy Materials* 8(28) (2018) 1702814.

[19] T. Yan, W. Song, J. Huang, R. Peng, L. Huang, Z. Ge, 16.67% Rigid and 14.06% Flexible Organic Solar Cells Enabled by Ternary Heterojunction Strategy, *Advanced Materials* 31(39) (2019) 1902210.

[20] M. Rammal, P. Lévêque, G. Schlatter, N. Leclerc, A. Hébraud, Recent advances in the green processing of organic photovoltaic devices from nanoparticle dispersions, *Materials Chemistry Frontiers* 4(10) (2020) 2904-2931.

[21] Y. Liu, J. Zhao, Z. Li, C. Mu, W. Ma, H. Hu, K. Jiang, H. Lin, H. Ade, H. Yan, Aggregation and morphology control enables multiple cases of high-efficiency polymer solar cells, *Nature Communications* 5(1) (2014) 5293.

[22] N. Leclerc, P. Chávez, O.A. Ibraikulov, T. Heiser, P. Lévêque, Impact of Backbone Fluorination on π -Conjugated Polymers in Organic Photovoltaic Devices: A Review, *Polymers* 8(1) (2016).

[23] S. Subianto, N. Dutta, M. Andersson, N.R. Choudhury, Bulk heterojunction organic photovoltaics from water-processable nanomaterials and their facile fabrication approaches, *Advances in Colloid and Interface Science* 235 (2016) 56-69.

[24] Z. Ma, B. Zhao, Y. Gong, J. Deng, Z.a. Tan, Green-solvent-processable strategies for achieving large-scale manufacture of organic photovoltaics, *Journal of Materials Chemistry A* 7(40) (2019) 22826-22847.

[25] S. Zhang, L. Ye, H. Zhang, J. Hou, Green-solvent-processable organic solar cells, *Materials Today* 19(9) (2016) 533-543.

[26] S. Lee, D. Jeong, C. Kim, C. Lee, H. Kang, H.Y. Woo, B.J. Kim, Eco-Friendly Polymer Solar Cells: Advances in Green-Solvent Processing and Material Design, *ACS Nano* 14(11) (2020) 14493-14527.

[27] T. Tromholt, S.A. Gevorgyan, M. Jørgensen, F.C. Krebs, K.O. Sylvester-Hvid, Thermocleavable Materials for Polymer Solar Cells with High Open Circuit Voltage—A Comparative Study, *ACS Applied Materials & Interfaces* 1(12) (2009) 2768-2777.

[28] C. Duan, K. Zhang, C. Zhong, F. Huang, Y. Cao, Recent advances in water/alcohol-soluble π -conjugated materials: new materials and growing applications in solar cells, *Chemical Society Reviews* 42(23) (2013) 9071-9104.

[29] M. Vert, Y. Doi, K.-H. Hellwich, M. Hess, P. Hodge, P. Kubisa, M. Rinaudo, F. Schué, Terminology for biorelated polymers and applications (IUPAC Recommendations 2012), *Pure and Applied Chemistry* 84(2) (2012) 377-410.

[30] J. Pecher, S. Mecking, Nanoparticles of Conjugated Polymers, *Chemical Reviews* 110(10) (2010) 6260-6279.

[31] K. Landfester, R. Montenegro, U. Scherf, R. Güntner, U. Asawapirom, S. Patil, D. Neher, T. Kietzke, Semiconducting Polymer Nanospheres in Aqueous Dispersion Prepared by a Miniemulsion Process, *Advanced Materials* 14(9) (2002) 651-655.

[32] O. Pras, D. Chaussy, O. Stephan, Y. Rharbi, P. Piette, D. Beneventi, Photoluminescence of 2,7-Poly(9,9-dialkylfluorene-co-fluorenone) Nanoparticles: Effect of Particle Size and Inert Polymer Addition, *Langmuir* 26(18) (2010) 14437-14442.

[33] L. Parrenin, G. Laurans, E. Pavlopoulou, G. Fleury, G. Pecastaings, C. Brochon, L. Vignau, G. Hadziioannou, E. Cloutet, Photoactive Donor–Acceptor Composite Nanoparticles Dispersed in Water, *Langmuir* 33(6) (2017) 1507-1515.

[34] C. Xie, A. Classen, A. Späth, X. Tang, J. Min, M. Meyer, C. Zhang, N. Li, A. Osvet, R.H. Fink, C.J. Brabec, Overcoming Microstructural Limitations in Water Processed

Organic Solar Cells by Engineering Customized Nanoparticulate Inks, *Advanced Energy Materials* 8(13) (2018) 1702857.

[35] F. Almyahi, T.R. Andersen, N. Cooling, N.P. Holmes, A. Fahy, M.G. Barr, D. Kilcoyne, W. Belcher, P.C. Dastoor, Optimization, characterization and upscaling of aqueous solar nanoparticle inks for organic photovoltaics using low-cost donor:acceptor blend, *Organic Electronics* 52 (2018) 71-78.

[36] J.M. Asua, Miniemulsion polymerization, *Progress in Polymer Science* 27(7) (2002) 1283-1346.

[37] S. Satapathi, H.S. Gill, L. Li, L. Samuelson, J. Kumar, R. Mosurkal, Synthesis of nanoparticles of P3HT and PCBM for optimizing morphology in polymeric solar cells, *Applied Surface Science* 323 (2014) 13-18.

[38] L. D'Olieslaeger, M. Pfannmöller, E. Fron, I. Cardinaletti, M. Van Der Auweraer, G. Van Tendeloo, S. Bals, W. Maes, D. Vanderzande, J. Manca, A. Ethirajan, Tuning of PCDTBT:PC71BM blend nanoparticles for eco-friendly processing of polymer solar cells, *Solar Energy Materials and Solar Cells* 159 (2017) 179-188.

[39] X. Pan, A. Sharma, D. Gedefaw, R. Kroon, A. Diaz de Zerio, N.P. Holmes, A.L.D. Kilcoyne, M.G. Barr, A. Fahy, M. Marks, X. Zhou, W. Belcher, P.C. Dastoor, M.R. Andersson, Environmentally friendly preparation of nanoparticles for organic photovoltaics, *Organic Electronics* 59 (2018) 432-440.

[40] N.P. Holmes, K.B. Burke, P. Sista, M. Barr, H.D. Magurudeniya, M.C. Stefan, A.L.D. Kilcoyne, X. Zhou, P.C. Dastoor, W.J. Belcher, Nano-domain behaviour in P3HT:PCBM nanoparticles, relating material properties to morphological changes, *Solar Energy Materials and Solar Cells* 117 (2013) 437-445.

[41] T. Kietzke, D. Neher, M. Kumke, O. Ghazy, U. Ziener, K. Landfester, Phase Separation of Binary Blends in Polymer Nanoparticles, *Small* 3(6) (2007) 1041-1048.

[42] J.J. Richards, C.L. Whittle, G. Shao, L.D. Pozzo, Correlating Structure and Photocurrent for Composite Semiconducting Nanoparticles with Contrast Variation Small-Angle Neutron Scattering and Photoconductive Atomic Force Microscopy, *ACS Nano* 8(5) (2014) 4313-4324.

[43] C.M. Björström, A. Bernasik, J. Rysz, A. Budkowski, S. Nilsson, M. Svensson, M.R. Andersson, K.O. Magnusson, E. Moons, Multilayer formation in spin-coated thin films of low-bandgap polyfluorene:PCBM blends, *Journal of Physics: Condensed Matter* 17(50) (2005) L529-L534.

[44] X. Wang, T. Ederth, O. Inganäs, In Situ Wilhelmy Balance Surface Energy Determination of Poly(3-hexylthiophene) and Poly(3,4-ethylenedioxythiophene) during Electrochemical Doping–Dedoping, *Langmuir* 22(22) (2006) 9287-9294.

[45] N.P. Holmes, N. Nicolaidis, K. Feron, M. Barr, K.B. Burke, M. Al-Mudhaffer, P. Sista, A.L.D. Kilcoyne, M.C. Stefan, X. Zhou, P.C. Dastoor, W.J. Belcher, Probing the origin of photocurrent in nanoparticulate organic photovoltaics, *Solar Energy Materials and Solar Cells* 140 (2015) 412-421.

[46] H.F. Dam, N.P. Holmes, T.R. Andersen, T.T. Larsen-Olsen, M. Barr, A.L.D. Kilcoyne, X. Zhou, P.C. Dastoor, F.C. Krebs, W.J. Belcher, The effect of mesomorphology upon the performance of nanoparticulate organic photovoltaic devices, *Solar Energy Materials and Solar Cells* 138 (2015) 102-108.

[47] G. Nagarjuna, M. Baghgar, J.A. Labastide, D.D. Algaier, M.D. Barnes, D. Venkataraman, Tuning Aggregation of Poly(3-hexylthiophene) within Nanoparticles, *ACS Nano* 6(12) (2012) 10750-10758.

[48] M. Marks, N.P. Holmes, A. Sharma, X. Pan, R. Chowdhury, M.G. Barr, C. Fenn, M.J. Griffith, K. Feron, A.L.D. Kilcoyne, D.A. Lewis, M.R. Andersson, W.J. Belcher, P.C.

Dastoor, Building intermixed donor–acceptor architectures for water-processable organic photovoltaics, *Physical Chemistry Chemical Physics* 21(10) (2019) 5705-5715.

[49] F. Almyahi, T.R. Andersen, N.A. Cooling, N.P. Holmes, M.J. Griffith, K. Feron, X. Zhou, W.J. Belcher, P.C. Dastoor, Optimisation of purification techniques for the preparation of large-volume aqueous solar nanoparticle inks for organic photovoltaics, *Beilstein Journal of Nanotechnology* 9 (2018) 649-659.

[50] X. Han, M. Bag, T.S. Gehan, D. Venkataraman, D. Maroudas, Analysis of hole transport in thin films and nanoparticle assemblies of poly(3-hexylthiophene), *Chemical Physics Letters* 610-611 (2014) 273-277.

[51] B. Vaughan, A. Stapleton, E. Sesa, N.P. Holmes, X. Zhou, P.C. Dastoor, W.J. Belcher, Engineering vertical morphology with nanoparticulate organic photovoltaic devices, *Organic Electronics* 32 (2016) 250-257.

[52] F.J.M. Colberts, M.M. Wienk, R.A.J. Janssen, Aqueous Nanoparticle Polymer Solar Cells: Effects of Surfactant Concentration and Processing on Device Performance, *ACS Applied Materials & Interfaces* 9(15) (2017) 13380-13389.

[53] W.C. Griffin, Classification of surface-active agents by "HLB", *J. Soc. Cosmet. Chem.* 1 (1949) 311-326.

[54] J.T. Davies, A quantitative kinetic theory of emulsion type. I. Physical chemistry of the emulsifying agent., in: G.L.a.L.L. Interfaces (Ed.) Proceedings of 2nd International Congress Surface Activity, Butterworths, London, 1957, pp. 426-438.

[55] M. Nollet, H. Boulghobra, E. Calligaro, J.D. Rodier, An efficient method to determine the Hydrophile-Lipophile Balance of surfactants using the phase inversion temperature deviation of CiEj/n-octane/water emulsions, *International Journal of Cosmetic Science* 41(2) (2019) 99-108.

[56] J. Cho, S. Yoon, K. Min Sim, Y. Jin Jeong, C. Eon Park, S.-K. Kwon, Y.-H. Kim, D.S. Chung, Universal selection rule for surfactants used in miniemulsion processes for eco-friendly and high performance polymer semiconductors, *Energy & Environmental Science* 10(11) (2017) 2324-2333.

[57] B. Tan, Y. Li, M.F. Palacios, J. Therrien, M.J. Sobkowicz, Effect of surfactant conjugation on structure and properties of poly(3-hexylthiophene) colloids and field effect transistors, *Colloids and Surfaces A: Physicochemical and Engineering Aspects* 488 (2016) 7-14.

[58] S. Subianto, R. Balu, L. de Campo, A. Sokolova, N.K. Dutta, N.R. Choudhury, Sulfonated Thiophene Derivative Stabilized Aqueous Poly(3-hexylthiophene):Phenyl-C61-butyric Acid Methyl Ester Nanoparticle Dispersion for Organic Solar Cell Applications, *ACS Applied Materials & Interfaces* 10(50) (2018) 44116-44125.

[59] X. Zhou, W. Belcher, P. Dastoor, Solar Paint: From Synthesis to Printing, *Polymers* 6(11) (2014).

[60] D. Darwis, N. Holmes, D. Elkington, A.L. David Kilcoyne, G. Bryant, X. Zhou, P. Dastoor, W. Belcher, Surfactant-free nanoparticulate organic photovoltaics, *Solar Energy Materials and Solar Cells* 121 (2014) 99-107.

[61] C. Xie, T. Heumüller, W. Gruber, X. Tang, A. Classen, I. Schuldes, M. Bidwell, A. Späth, R.H. Fink, T. Unruh, I. McCulloch, N. Li, C.J. Brabec, Overcoming efficiency and stability limits in water-processing nanoparticulate organic photovoltaics by minimizing microstructure defects, *Nature Communications* 9(1) (2018) 5335.

[62] F. Wang, M.-Y. Han, K.Y. Mya, Y. Wang, Y.-H. Lai, Aggregation-Driven Growth of Size-Tunable Organic Nanoparticles Using Electronically Altered Conjugated Polymers, *Journal of the American Chemical Society* 127(29) (2005) 10350-10355.

[63] J.E. Millstone, D.F.J. Kavulak, C.H. Woo, T.W. Holcombe, E.J. Westling, A.L. Briseno, M.F. Toney, J.M.J. Fréchet, Synthesis, Properties, and Electronic Applications of

- Size-Controlled Poly(3-hexylthiophene) Nanoparticles, *Langmuir* 26(16) (2010) 13056-13061.
- [64] S.N. Clifton, D.M. Huang, W.R. Massey, T.W. Kee, Femtosecond Dynamics of Excitons and Hole-Polarons in Composite P3HT/PCBM Nanoparticles, *The Journal of Physical Chemistry B* 117(16) (2013) 4626-4633.
- [65] G. Prunet, L. Parrenin, E. Pavlopoulou, G. Pecastaings, C. Brochon, G. Hadziioannou, E. Cloutet, Aqueous PCDTBT:PC71BM Photovoltaic Inks Made by Nanoprecipitation, *Macromolecular Rapid Communications* 39(2) (2018) 1700504.
- [66] C. Xie, X. Tang, M. Berlinghof, S. Langner, S. Chen, A. Späth, N. Li, R.H. Fink, T. Unruh, C.J. Brabec, Robot-Based High-Throughput Engineering of Alcoholic Polymer: Fullerene Nanoparticle Inks for an Eco-Friendly Processing of Organic Solar Cells, *ACS Applied Materials & Interfaces* 10(27) (2018) 23225-23234.
- [67] K.N. Schwarz, S.B. Farley, T.A. Smith, K.P. Ghiggino, Charge generation and morphology in P3HT : PCBM nanoparticles prepared by mini-emulsion and reprecipitation methods, *Nanoscale* 7(47) (2015) 19899-19904.
- [68] S. Gärtner, A.J. Clulow, I.A. Howard, E.P. Gilbert, P.L. Burn, I.R. Gentle, A. Colsmann, Relating Structure to Efficiency in Surfactant-Free Polymer/Fullerene Nanoparticle-Based Organic Solar Cells, *ACS Applied Materials & Interfaces* 9(49) (2017) 42986-42995.
- [69] S. Chambon, C. Schatz, V. Sébire, B. Pavageau, G. Wantz, L. Hirsch, Organic semiconductor core-shell nanoparticles designed through successive solvent displacements, *Materials Horizons* 1(4) (2014) 431-438.
- [70] A. Palacio Valera, C. Schatz, E. Ibarboure, T. Kubo, H. Segawa, S. Chambon, Elaboration of PCBM Coated P3HT Nanoparticles: Understanding the Shell Formation, *Frontiers in Energy Research* 6 (2019) 146.
- [71] T. Kietzke, D. Neher, K. Landfester, R. Montenegro, R. Güntner, U. Scherf, Novel approaches to polymer blends based on polymer nanoparticles, *Nature Materials* 2(6) (2003) 408-412.
- [72] A. Stapleton, B. Vaughan, B. Xue, E. Sesa, K. Burke, X. Zhou, G. Bryant, O. Werzer, A. Nelson, A.L. David Kilcoyne, L. Thomsen, E. Wanless, W. Belcher, P. Dastoor, A multilayered approach to polyfluorene water-based organic photovoltaics, *Solar Energy Materials and Solar Cells* 102 (2012) 114-124.
- [73] T.S. Gehan, M. Bag, L.A. Renna, X. Shen, D.D. Algaier, P.M. Lahti, T.P. Russell, D. Venkataraman, Multiscale Active Layer Morphologies for Organic Photovoltaics Through Self-Assembly of Nanospheres, *Nano Letters* 14(9) (2014) 5238-5243.
- [74] M. Bag, T.S. Gehan, L.A. Renna, D.D. Algaier, P.M. Lahti, D. Venkataraman, Fabrication conditions for efficient organic photovoltaic cells from aqueous dispersions of nanoparticles, *RSC Advances* 4(85) (2014) 45325-45331.
- [75] O. Ghazy, B. Freisinger, I. Lieberwith, K. Landfester, Tuning the size and morphology of P3HT/PCBM composite nanoparticles: towards optimized water-processable organic solar cells, *Nanoscale* 12(44) (2020) 22798-22807.
- [76] M.T. Dang, L. Hirsch, G. Wantz, P3HT:PCBM, Best Seller in Polymer Photovoltaic Research, *Advanced Materials* 23(31) (2011) 3597-3602.
- [77] X. Han, M. Bag, T.S. Gehan, D. Venkataraman, D. Maroudas, Analysis of Charge Transport and Device Performance in Organic Photovoltaic Devices with Active Layers of Self-Assembled Nanospheres, *The Journal of Physical Chemistry C* 119(46) (2015) 25826-25839.
- [78] T. Kietzke, D. Neher, M. Kumke, R. Montenegro, K. Landfester, U. Scherf, A Nanoparticle Approach To Control the Phase Separation in Polyfluorene Photovoltaic Devices, *Macromolecules* 37(13) (2004) 4882-4890.

- [79] N.P. Holmes, M. Marks, J.M. Cave, K. Feron, M.G. Barr, A. Fahy, A. Sharma, X. Pan, D.A.L. Kilcoyne, X. Zhou, D.A. Lewis, M.R. Andersson, J. van Stam, A.B. Walker, E. Moons, W.J. Belcher, P.C. Dastoor, Engineering Two-Phase and Three-Phase Microstructures from Water-Based Dispersions of Nanoparticles for Eco-Friendly Polymer Solar Cell Applications, *Chemistry of Materials* 30(18) (2018) 6521-6531.
- [80] S. Ulum, N. Holmes, D. Darwis, K. Burke, A.L. David Kilcoyne, X. Zhou, W. Belcher, P. Dastoor, Determining the structural motif of P3HT:PCBM nanoparticulate organic photovoltaic devices, *Solar Energy Materials and Solar Cells* 110 (2013) 43-48.
- [81] B. Vaughan, E.L. Williams, N.P. Holmes, P. Sonar, A. Dodabalapur, P.C. Dastoor, W.J. Belcher, Water-based nanoparticulate solar cells using a diketopyrrolopyrrole donor polymer, *Physical Chemistry Chemical Physics* 16(6) (2014) 2647-2653.
- [82] N.P. Holmes, M. Marks, P. Kumar, R. Kroon, M.G. Barr, N. Nicolaidis, K. Feron, A. Pivrikas, A. Fahy, A.D.d.Z. Mendaza, A.L.D. Kilcoyne, C. Müller, X. Zhou, M.R. Andersson, P.C. Dastoor, W.J. Belcher, Nano-pathways: Bridging the divide between water-processable nanoparticulate and bulk heterojunction organic photovoltaics, *Nano Energy* 19 (2016) 495-510.
- [83] S. Gärtner, M. Christmann, S. Sankaran, H. Röhm, E.-M. Prinz, F. Pentz, A. Pütz, A.E. Türelı, B. Pentz, B. Baumstümmler, A. Colsmann, Eco-Friendly Fabrication of 4% Efficient Organic Solar Cells from Surfactant-Free P3HT:ICBA Nanoparticle Dispersions, *Advanced Materials* 26(38) (2014) 6653-6657.
- [84] M. Bag, T.S. Gehan, D.D. Algaier, F. Liu, G. Nagarjuna, P.M. Lahti, T.P. Russell, D. Venkataraman, Efficient Charge Transport in Assemblies of Surfactant-Stabilized Semiconducting Nanoparticles, *Advanced Materials* 25(44) (2013) 6411-6415.
- [85] S. Sankaran, K. Glaser, S. Gärtner, T. Rödlmeier, K. Sudau, G. Hernandez-Sosa, A. Colsmann, Fabrication of polymer solar cells from organic nanoparticle dispersions by doctor blading or ink-jet printing, *Organic Electronics* 28 (2016) 118-122.
- [86] S.K. Karunakaran, G.M. Arumugam, W. Yang, S. Ge, S.N. Khan, X. Lin, G. Yang, Recent progress in inkjet-printed solar cells, *Journal of Materials Chemistry A* 7(23) (2019) 13873-13902.
- [87] T.R. Andersen, T.T. Larsen-Olsen, B. Andreasen, A.P.L. Böttiger, J.E. Carlé, M. Helgesen, E. Bundgaard, K. Norrman, J.W. Andreasen, M. Jørgensen, F.C. Krebs, Aqueous Processing of Low-Band-Gap Polymer Solar Cells Using Roll-to-Roll Methods, *ACS Nano* 5(5) (2011) 4188-4196.
- [88] T.T. Larsen-Olsen, T.R. Andersen, B. Andreasen, A.P.L. Böttiger, E. Bundgaard, K. Norrman, J.W. Andreasen, M. Jørgensen, F.C. Krebs, Roll-to-roll processed polymer tandem solar cells partially processed from water, *Solar Energy Materials and Solar Cells* 97 (2012) 43-49.
- [89] F. Almyahi, T.R. Andersen, A. Fahy, M. Dickinson, K. Feron, W.J. Belcher, P.C. Dastoor, The role of surface energy control in organic photovoltaics based on solar paints, *Journal of Materials Chemistry A* 7(15) (2019) 9202-9214.
- [90] M.F. Al-Mudhaffer, M.J. Griffith, K. Feron, N.C. Nicolaidis, N.A. Cooling, X. Zhou, J. Holdsworth, W.J. Belcher, P.C. Dastoor, The origin of performance limitations in miniemulsion nanoparticulate organic photovoltaic devices, *Solar Energy Materials and Solar Cells* 175 (2018) 77-88.
- [91] V. Coropceanu, J. Cornil, D.A. da Silva Filho, Y. Olivier, R. Silbey, J.-L. Brédas, Charge Transport in Organic Semiconductors, *Chemical Reviews* 107(4) (2007) 926-952.
- [92] G. Bratina, E. Pavlica, Characterisation of charge carrier transport in thin organic semiconductor layers by time-of-flight photocurrent measurements, *Organic Electronics* 64 (2019) 117-130.

- [93] J.C. Blakesley, F.A. Castro, W. Kylberg, G.F.A. Dibb, C. Arantes, R. Valaski, M. Cremona, J.S. Kim, J.-S. Kim, Towards reliable charge-mobility benchmark measurements for organic semiconductors, *Organic Electronics* 15(6) (2014) 1263-1272.
- [94] H. Sirringhaus, 25th Anniversary Article: Organic Field-Effect Transistors: The Path Beyond Amorphous Silicon, *Advanced Materials* 26(9) (2014) 1319-1335.
- [95] O. Cardozo, S. Farooq, A. Stingl, N. Fraidenaich, Investigation of performance of P3HT:PCBM organic photovoltaic module under real operating conditions, *Solar Energy* 190 (2019) 543-548.
- [96] S. Ulum, N. Holmes, M. Barr, A.L.D. Kilcoyne, B.B. Gong, X. Zhou, W. Belcher, P. Dastoor, The role of miscibility in polymer:fullerene nanoparticulate organic photovoltaic devices, *Nano Energy* 2(5) (2013) 897-905.
- [97] M. Lenes, G.-J.A.H. Wetzelaer, F.B. Kooistra, S.C. Veenstra, J.C. Hummelen, P.W.M. Blom, Fullerene Bisadducts for Enhanced Open-Circuit Voltages and Efficiencies in Polymer Solar Cells, *Advanced Materials* 20(11) (2008) 2116-2119.
- [98] C. Liu, K. Wang, X. Gong, A.J. Heeger, Low bandgap semiconducting polymers for polymeric photovoltaics, *Chemical Society Reviews* 45(17) (2016) 4825-4846.
- [99] O.A. Ibraikulov, C. Ngov, P. Chávez, I. Bulut, B. Heinrich, O. Boyron, K.L. Gerasimov, D.A. Ivanov, S. Swaraj, S. Méry, N. Leclerc, P. Lévêque, T. Heiser, Face-on orientation of fluorinated polymers conveyed by long alkyl chains: a prerequisite for high photovoltaic performances, *Journal of Materials Chemistry A* 6(25) (2018) 12038-12045.
- [100] M. Zangoli, F. Di Maria, Synthesis, characterization, and biological applications of semiconducting polythiophene-based nanoparticles, *VIEW* 2(1) (2021) 20200086.
- [101] F. Di Maria, I.E. Palamà, M. Baroncini, A. Barbieri, A. Bongini, R. Bizzarri, G. Gigli, G. Barbarella, Live cell cytoplasm staining and selective labeling of intracellular proteins by non-toxic cell-permeant thiophene fluorophores, *Organic & Biomolecular Chemistry* 12(10) (2014) 1603-1610.
- [102] G. Barbarella, F. Di Maria, Supramolecular Oligothiophene Microfibers Spontaneously Assembled on Surfaces or Coassembled with Proteins inside Live Cells, *Accounts of Chemical Research* 48(8) (2015) 2230-2241.
- [103] E. Zucchetti, M. Zangoli, I. Bargigia, C. Bossio, F. Di Maria, G. Barbarella, C. D'Andrea, G. Lanzani, M.R. Antognazza, Poly(3-hexylthiophene) nanoparticles for biophotonics: study of the mutual interaction with living cells, *Journal of Materials Chemistry B* 5(3) (2017) 565-574.
- [104] Y. Jiang, P.K. Upputuri, C. Xie, Z. Zeng, A. Sharma, X. Zhen, J. Li, J. Huang, M. Pramanik, K. Pu, Metabolizable Semiconducting Polymer Nanoparticles for Second Near-Infrared Photoacoustic Imaging, *Advanced Materials* 31(11) (2019) 1808166.
- [105] Y. Jiang, J. Li, X. Zhen, C. Xie, K. Pu, Dual-Peak Absorbing Semiconducting Copolymer Nanoparticles for First and Second Near-Infrared Window Photothermal Therapy: A Comparative Study, *Advanced Materials* 30(14) (2018) 1705980.
- [106] Q. Miao, C. Xie, X. Zhen, Y. Lyu, H. Duan, X. Liu, J.V. Jokerst, K. Pu, Molecular afterglow imaging with bright, biodegradable polymer nanoparticles, *Nature Biotechnology* 35(11) (2017) 1102-1110.
- [107] F. Di Maria, F. Lodola, E. Zucchetti, F. Benfenati, G. Lanzani, The evolution of artificial light actuators in living systems: from planar to nanostructured interfaces, *Chemical Society Reviews* 47(13) (2018) 4757-4780.
- [108] C. Bossio, I. Abdel Aziz, G. Tullii, E. Zucchetti, D. Debellis, M. Zangoli, F. Di Maria, G. Lanzani, M.R. Antognazza, Photocatalytic Activity of Polymer Nanoparticles Modulates Intracellular Calcium Dynamics and Reactive Oxygen Species in HEK-293 Cells, *Frontiers in Bioengineering and Biotechnology* 6 (2018).

- [109] M. Moros, A. Lewinska, G. Onorato, M.R. Antognazza, F. Di Maria, M. Blasio, G. Lanzani, A. Tino, M. Wnuk, C. Tortiglione, Light-triggered modulation of cell antioxidant defense by polymer semiconducting nanoparticles in a model organism, *MRS Communications* 8(3) (2018) 918-925.
- [110] M. Zangoli, F. Di Maria, E. Zucchetti, C. Bossio, M.R. Antognazza, G. Lanzani, R. Mazzaro, F. Corticelli, M. Baroncini, G. Barbarella, Engineering thiophene-based nanoparticles to induce phototransduction in live cells under illumination, *Nanoscale* 9(26) (2017) 9202-9209.
- [111] C. Tortiglione, R. Antognazza Maria, A. Tino, C. Bossio, V. Marchesano, A. Bauduin, M. Zangoli, V. Morata Susana, G. Lanzani, Semiconducting polymers are light nanotransducers in eyeless animals, *Science Advances* 3(1) e1601699.
- [112] N.P. Holmes, S. Chambon, A. Holmes, X. Xu, K. Hirakawa, E. Deniau, C. Lartigau-Dagron, A. Bousquet, Organic semiconductor colloids: From the knowledge acquired in photovoltaics to the generation of solar hydrogen fuel, *Current Opinion in Colloid & Interface Science* 56 (2021) 101511.
- [113] J. Kosco, M. Bidwell, H. Cha, T. Martin, C.T. Howells, M. Sachs, D.H. Anjum, S. Gonzalez Lopez, L. Zou, A. Wadsworth, W. Zhang, L. Zhang, J. Tellam, R. Sougrat, F. Laquai, D.M. DeLongchamp, J.R. Durrant, I. McCulloch, Enhanced photocatalytic hydrogen evolution from organic semiconductor heterojunction nanoparticles, *Nature Materials* 19(5) (2020) 559-565.
- [114] B. Vaughan, A. Stapleton, B. Xue, E. Sesa, X. Zhou, G. Bryant, W. Belcher, P. Dastoor, Effect of a calcium cathode on water-based nanoparticulate solar cells, *Applied Physics Letters* 101(5) (2012) 053901.
- [115] E.B.L. Pedersen, M.C. Pedersen, S.B. Simonsen, R.G. Brandt, A.P.L. Böttiger, T.R. Andersen, W. Jiang, Z.Y. Xie, F.C. Krebs, L. Arleth, J.W. Andreasen, Structure and crystallinity of water dispersible photoactive nanoparticles for organic solar cells, *Journal of Materials Chemistry A* 3(33) (2015) 17022-17031.
- [116] Y.J. Kim, R.D. Schaller, H.C. Fry, Control of Shell Morphology in p–n Heterostructured Water-Processable Semiconductor Colloids: Toward Extremely Efficient Charge Separation, *Small* 15(2) (2019) 1803563.
- [117] Y.J. Kim, B. Lee, Unique p–n Heterostructured Water-Borne Nanoparticles Exhibiting Impressive Charge-Separation Ability, *ChemSusChem* 11(10) (2018) 1628-1638.
- [118] S. Gärtner, S. Reich, M. Bruns, J. Czolk, A. Colsmann, Organic solar cells with graded absorber layers processed from nanoparticle dispersions, *Nanoscale* 8(12) (2016) 6721-6727.
- [119] N.A.D. Yamamoto, M.E. Payne, M. Koehler, A. Facchetti, L.S. Roman, A.C. Arias, Charge transport model for photovoltaic devices based on printed polymer: Fullerene nanoparticles, *Solar Energy Materials and Solar Cells* 141 (2015) 171-177.

Chapter 2

Surfactant-free miniemulsion approach for low band gap rod-coil block copolymer water-processable nanoparticles: a proof-of-concept

*The content of this chapter is reported into three papers: Lucia Ganzer, Stefania Zappia, Mattia Russo, Anna Maria Ferretti, Varun Vohra, Marianna Diterlizzi, Maria Rosa Antognazza, Silvia Destri and Tersilla Virgili, “Ultrafast spectroscopy on water-processable PCBM:rod–coil block copolymer nanoparticles” *Phys. Chem. Chem. Phys.* **2020**, *22*, 26583-26591; Anna Maria Ferretti, Marianna Diterlizzi, William Porzio, Umberto Giovanella, Lucia Ganzer, Tersilla Virgili, Varun Vohra, Eduardo Arias, Ivana Moggio, Guido Scavia, Silvia Destri and Stefania Zappia, “Rod-coil block copolymer:fullerene blend water-processable nanoparticles: how molecular structure addresses morphology and efficiency in NP-OPVs” *Nanomaterials* **2022**, *12*, 84-101; Federico Gobbo, Marianna Diterlizzi, Anna Maria Ferretti, Silvia Destri, Stefania Zappia and Maria Rosa Antognazza, “PCPDTBT-based nanoparticles as smart photoactive transducers in cellular metabolism” in preparation.*

2.1 Introduction

The miniemulsion and nanoprecipitation methods discussed in the previous chapter are suffering from several drawbacks, which make them difficult to scale up from the laboratory to the industrial production. Namely, the miniemulsion approach involves the use of surfactant molecules to stabilize the droplets from collision and aggregation. Unfortunately, they have an electric insulating behaviour and thus additional steps aiming to remove the excess of the surfactant are required to avoid dramatic drop in the device performance. The purification step is time- and energy-consuming, and it increases the payback of the energy product by the final devices.[1] What is more, nanoparticles (NPs) formed through this technique mainly have a core-shell morphology, as a consequence of the duration of solvent evaporation.[2, 3] Thus mild thermal annealing processes, close to glass transition temperature (T_g) of the electron-donor polymer, are necessary to gain proper interconnections between donor and acceptor materials in order to achieve the interpenetrating network to facilitate charge transport and extraction, and to ensure good efficiency in organic photovoltaic (OPV) devices. Moreover, fullerene materials have surface energy noticeably higher than semiconducting polymers usually exploited in OPV device fabrication and this concurs to the formation of core-shell NPs with a PCBM-rich core. On the other hand, the absence of stabilizers expected by nanoprecipitation technique leads to stability issues of the obtained suspensions because of aggregation of the polymeric material into a non-solvent medium (mainly alcoholic medium in this case).[4]

Rod-coil block copolymers (BCPs) attracted the interest of many researchers because their self-assembly ability emerged as a powerful route to achieve the ideal morphologies in bulk heterojunction (BHJ) solar cells, which require a cocontinuous phase of donor and acceptor materials with proper nanodomains.[5-9] Amphiphilic rod-coil BCPs are materials constituted by a rigid block covalently linked to a hydrophilic flexible segment. Thanks to these features, amphiphilic BCPs are able to self-assemble in aqueous medium without the addition of any surfactant on the basis of the physical-chemical behaviour of their components to form phase separation at the nanoscale, without segregation at macroscopic level for minimizing unfavorable interfacial interactions.[10] These features attracted the interest of the researchers as good candidates for electronic and optoelectronic applications.[8]

In this chapter the aqueous processing of four amphiphilic low band gap (LBG) BCPs exploiting an adapted miniemulsion approach will be discussed. In particular, four different poly[2,6-(4,4-bis-(2-ethylhexyl)-4*H*-cyclopenta[2,1-*b*;3,4-*b'*]dithiophene)-*alt*-4,7(2,1,3-benzothiadiazole)] (PCPDTBT)-based rod-coil BCPs were synthesized. They are characterized by a standardized rod block PCPDTBT, and different tailored poly-4-vinylpyridine (P4VP)-based flexible segments with various length and molecular composition.[11, 12]. A poly(styrene-*co*-vinylpyridine) (P(Sty-*co*-4VP))

segment was chosen as coil because it was used to form nanocomposites with inorganic nanocrystals to produce hybrid solar cells, demonstrating that it coordinates the nanoclusters (NCs), improving the uniformity of NC dispersion and avoiding their aggregation.[13] We took advantage of the BCP capability to assemble into organized nanostructures suspended into aqueous medium to prepare both neat (n-) and blended with phenyl-C₆₁-butyric acid methyl ester (PC₆₁BM) (b-) water-processable nanoparticles (WPNNPs) avoiding surfactant use.[14] Finally, the bWPNNPs were exploited for the fabrication of WPNNP-based OPV devices, achieving a peculiar NP inner morphology in the case of BCP5 bearing a coil block composed by 5 repeating units of 4-vinylpyridine (4VP) that allowed to produce working devices with a relevant photocurrent and the efficiency up to 2.5%.[15] Moreover, we evaluated the effect of the BCP chemical structure and composition on the blend aggregation into the WPNNPs, correlating the morphological and compositional features of WPNNP nano-domains on BCP performances in the devices. In particular, we studied bWPNNP topology and morphology with atomic force microscopy (AFM), transmission electron microscopy (TEM), and energy filtered TEM (EFTEM) analyses, clarifying how the morphologies of the nano-domains are related to the features of the different coil molecular structures in the BCPs, and in turn how they lead to unlike device performance.[16] Furtherly, ultrafast spectroscopy study elucidated the charge separation dynamics in film obtained from bWPNNPs.[17]

What is more, nWPNNPs were exploited also in biological applications by Dr. Maria Rosa Antognazza (IIT, Milano), who evaluated how human cell metabolism can be affected by BCP2-based WPNNPs upon illumination.

2.2 Results and Discussion

2.2.1 Synthesis and Characterization of the rod-coil block copolymers

The research group in which I carried out my doctoral work developed the synthesis of four amphiphilic rod-coil BCPs constituted by a standardized LBG copolymer poly[2,6-(4,4-bis-(2-ethylhexyl)-4*H*-cyclopenta[2,1-*b*;3,4-*b'*]dithiophene)-*alt*-4,7(2,1,3-benzothiadiazole)] (PCPDTBT) covalently linked with various hydrophilic flexible coil blocks based on poly-4-vinylpyridine (P4VP), namely tailored segments constituted by 2, 5 or 15 repeating units of 4-vinylpyridine (4VP) for BCP2, BCP5 or BCP15 respectively, and a segmented random copolymer of styrene (Sty) and 4VP (with a composition of 76% of Sty and 24% of 4VP) P(Sty-*co*-4VP) for BCP100.[13, 14] The amphiphilic rod-coil BCPs studied are depicted in **Figure 2.1**.

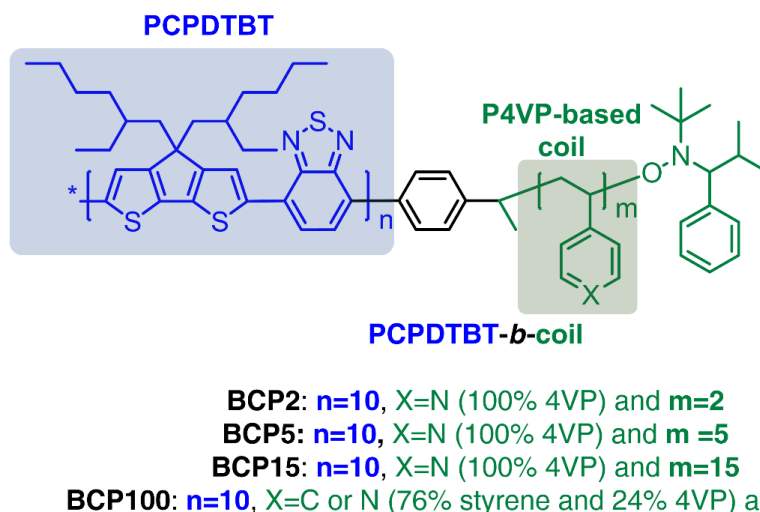
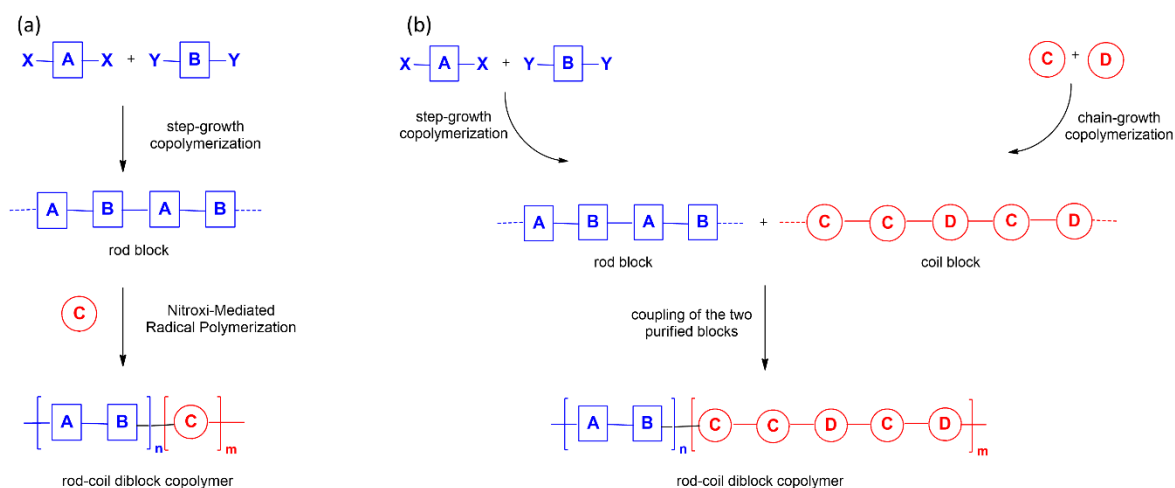


Figure 2.1 Molecular structures of the amphiphilic rod-coil block BCP2, BCP5, BCP15 and BCP100. The BCPs were synthesized by two different approaches depending on the coil length: *Chain Growth-like* and *Step Growth-like*.^[11, 18] In the first route a macroinitiator is firstly prepared by polymerization of an individual block ended with a bifunctional synthon directly capable to initiate the following polymerization or to be converted in a group doing it.^[18] Materials obtained with this method are constituted mainly by a rod longer segment. The second implies the preparation of two individual polymers properly functionalized to covalently react; this strategy gets copolymer with longer coil. The two strategies are depicted in **Scheme 2.1**.

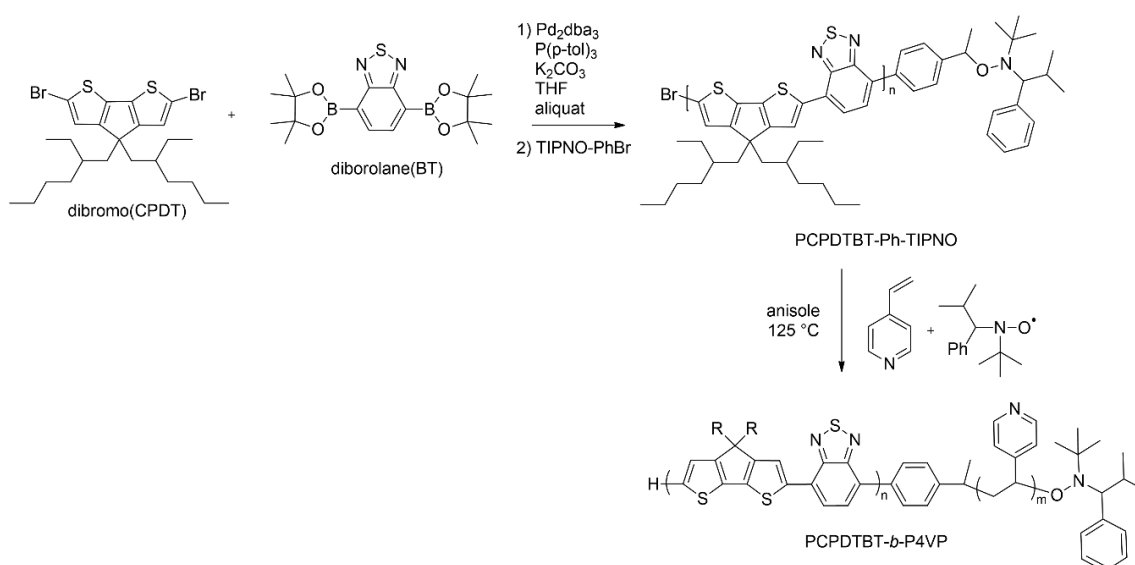


Scheme 2.1 General representation of **a)** chain growth-like and **b)** step growth-like strategies for the synthesis of PCPDTBT-*b*-P(4VP-based) copolymers.

Based on these considerations BCP2 and BCP5 were obtained through a chain growth-like approach, while BCP15 and BCP100 were synthesized through a step growth-like approach.

2.2.1.1 Synthesis and Characterization of BCP2 and BCP5 through a *Chain Growth-like* strategy

The *Chain Growth-like* approach involves the rod block synthesis through the Suzuki polycondensation and the subsequent activation with a nitroxide derivative bearing a brominated phenyl group, TIPNO-PhBr.[19] Specifically, TIPNO-PhBr is added to the reaction mixture as capping agent of borolane end groups with the aim of forming an activated macroinitiator PCPDTBT-Ph-TIPNO, which is then used for the nitroxide-mediated radical polymerization (NMRP) at 125 °C in dry conditions of the monomer 4VP (**Scheme 2.2**).



Scheme 2.2 Synthesis of the macroinitiator PCPDTBT-Ph-TIPNO and of the rod-coil BCP PCPDTBT-*b*-P(4VP-based) through a chain growth-like approach.

The macroinitiator PCPDTBT-Ph-TIPNO was purified in dry conditions to provide the mediator for the next radical polymerization of 4VP to get BCP2 and BCP5. Then the materials were characterized by comparing their proton nuclear magnetic resonance (¹H-NMR) spectra with those reported in reference.[11] There a deep characterization of macroinitiator, BCP2, and BCP5 is reported showing ¹H-NMR, size-exclusion chromatography (SEC), matrix assisted laser desorption/ionization - time of flight mass spectrometry (MALDI-TOF MS), and differential scanning calorimetry (DSC) analyses. The ¹H-NMR spectrum of PCPDTBT-Ph-TIPNO shows in the aromatic region (**Figure 2.2**) two signals at 8.1 and 7.8 ppm related to benzothiadiazole (BT) and cyclopentadithiophene (CPDT) moieties, respectively, together with the characteristic multiplets at 7.6 and 7.0 ppm typical of the TIPNO-Ph phenyl group. [19] A more detailed signal assignment for the alkoxyamine end group was avoided by the overlapping between the signals of its protons H_d and H_e and H_a of the terminal CPDT.

In addition, characteristic signals attributable to the alkyl chains of the polymeric backbone are present in the range between 0.5 and 2.0 ppm. Also, another broad multiplet is observable between 5.0 and 2.5 ppm, which multiplicity is consistent with the protons H_f , H_g and H_h , but an exhaustive assignment for the nitroxide end group was prevented both for the complexity due to the presence of asymmetric carbons and the overlap of the relative signals. All signals are listed in the Experimental Section.

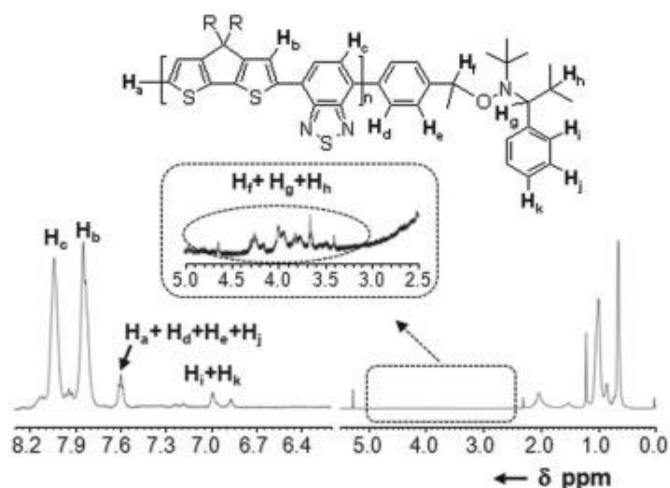


Figure 2.2 Enlarged section of $^1\text{H-NMR}$ spectrum in TCE-d_2 of the PCPDTBT-Ph-TIPNO macroinitiator. Adapted with permission of reference [11].

Comparing the $^1\text{H-NMR}$ spectrum of the PCPDTBT-Ph-TIPNO with that of the purified BCP2 and BCP5 (**Figure 2.3**) two additional signals H_m and H_n in the aromatic region can be distinguished, attributable to the aromatic protons of the P4VP moieties. Moreover, no differences between the macroinitiator and the rod-coil BCP spectra are identified in the aliphatic region in the range from 0.5 to 2.0, while an extended multiplet between 2.1 and 5.0 ppm looks modified and increased due to the overlap of the signals of the coil block aliphatic backbone. Furthermore, the multiplet at 2.6 ppm related to the proton H_f allows to confirm the effective controlled radical polymerization occurrence. Small signals corresponding to TIPNO are still visible in the spectra. It acts as a mediator in the NMRP and remains inserted into the polymeric backbone during the entire reaction mechanism to ensure the subsequent radical polymerization of 4VP.[19, 20] In addition, the reaction is quenched by cooling with liquid nitrogen and any additional capping agent is introduced into the reaction mixture. All signals are listed in the Experimental Section.

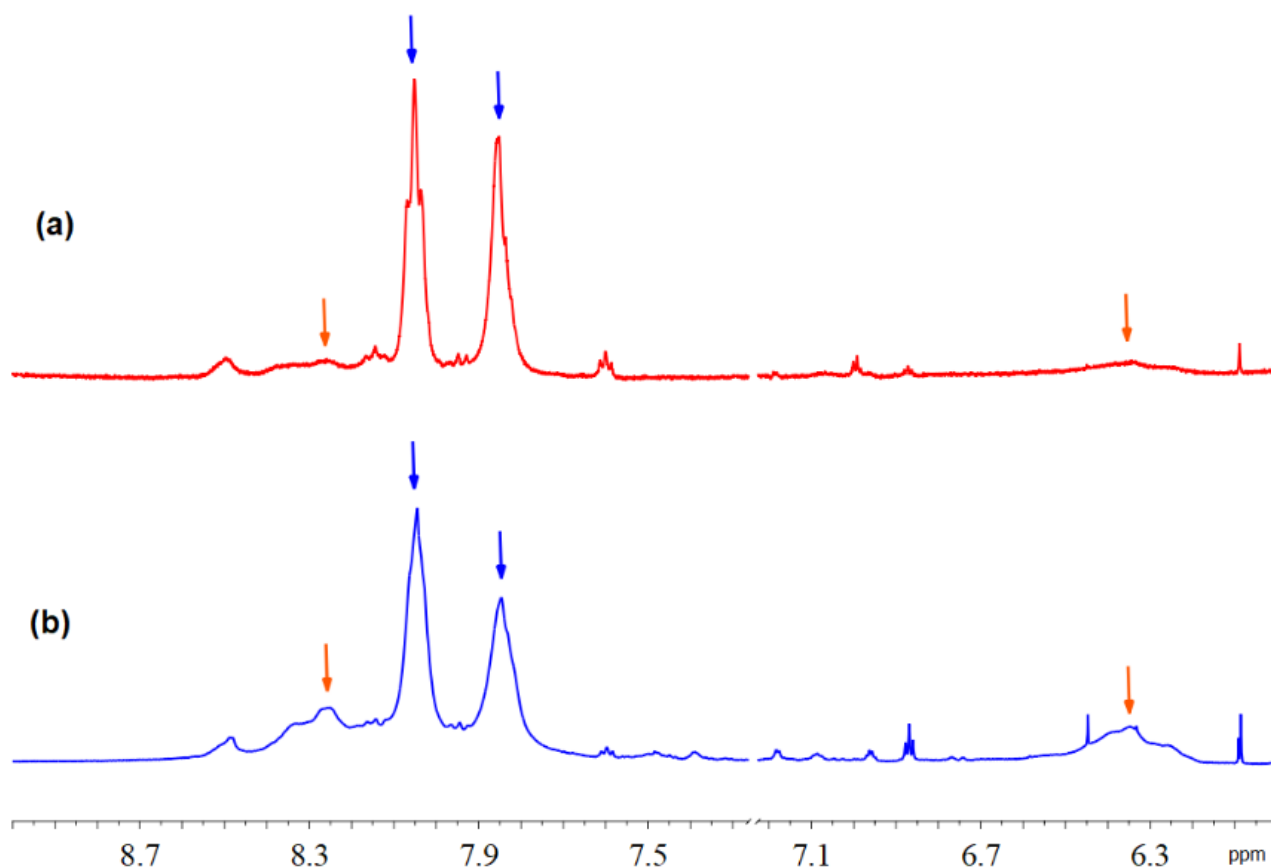


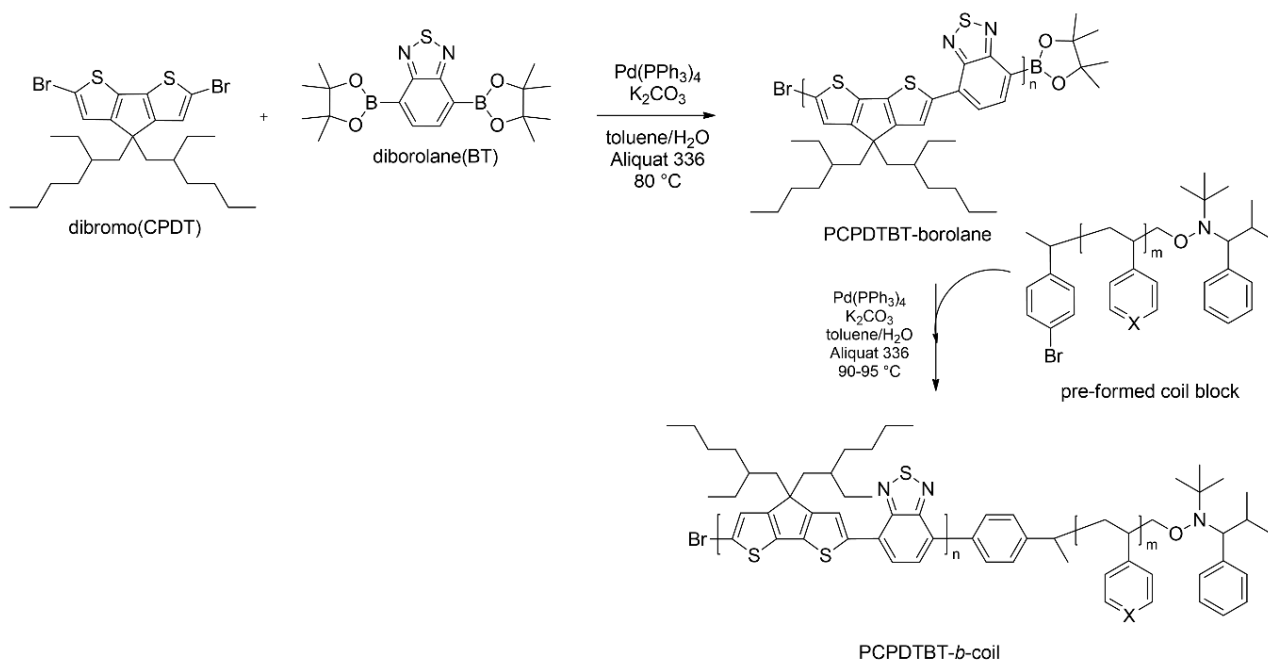
Figure 2.3 Enlarged section of ^1H -NMR spectra in TCE-d_2 (between 9.0 and 6.0 ppm) of rod-coil BCP2 (**red, a**) and BCP5 (**blue, b**). Blue arrows indicate the signals attributable to PCPDTBT-based rod blocks, orange arrows indicate the signals attributable to 4VP in the coil blocks.

The molecular weight distributions (MWDs) of the macroinitiator PCPDTBT-Ph-TIPNO and both the resulting BCP2 and BCP5 were determined by a multi-detector SEC system with a differential viscosimeter (DV) and a differential refractometer (DRI) as concentration detector (SEC-DV). A calibration of the SEC-DV chromatographic system was built using some polystyrene (PS) standards with narrow molecular weight distribution. A mixture of THF+0.25% of tetra-*n*-butylammonium bromide (TBAB) salt as mobile phase was used in order to ensure the quarterization of the pyridine units and a proper SEC elution of the samples.[21] The most important data obtained from the molecular characterization are reported in **Table 2.1**.

2.2.1.2 Synthesis and Characterization of BCP15 and BCP100 through a *Step Growth-like* strategy

Following the alternative *Step Growth-like* strategy rod and coil blocks were separately synthesized and characterized. The PCPDTBT polymer was obtained through a Suzuki coupling and the flexible coil through a NMRP using a nitroxide derivative TIPNO-PhBr exploiting the brominate phenyl group to achieve the coupling with the borolane ending group of the rod block (**Scheme 2.3**). It is

important to remark that the coupling is not quantitative because of the several purification steps necessary to remove the unreacted starting macromers before the coil attach even if they were carried out under nitrogen atmosphere to preserve borolane functionalities.



Scheme 2.3 Synthesis of the rod block through Suzuki polycondensation and of the rod-coil PCPDTBT-*b*-P(4VP-based) through a step growth-like approach.

Each block and the corresponding BCPs were deeply investigated by means of $^1\text{H-NMR}$, SEC and MALDI-TOF MS techniques in order to prove the effective covalent bond between the rod and the coil and to elucidate the composition of the obtained materials. Because the characterizations of BCP15 and BCP100 were previously reported, the collected data were compared with those in reference [11].

The $^1\text{H-NMR}$ spectra of BCP15 and BCP100 (**Figure 2.4**) show typical signals at 8.1 and 7.8 ppm related to BT and CPDT moieties, respectively, and different broad aromatic signals at about 8.2, 7.1, and 6.6 and 6.3 ppm due to the presence of the coil block. All signals are listed in the Experimental Section.

SEC analyses of the rod and the coil starting blocks, and of the final BCP15 and BCP100 were carried out by Mendichi's group with a SEC-DV system using as the solvent a mixture of THF:DMF (80:20) as THF alone is not a good solvent for the coil. The results of the molecular analyses are summarized in **Table 2.1**.

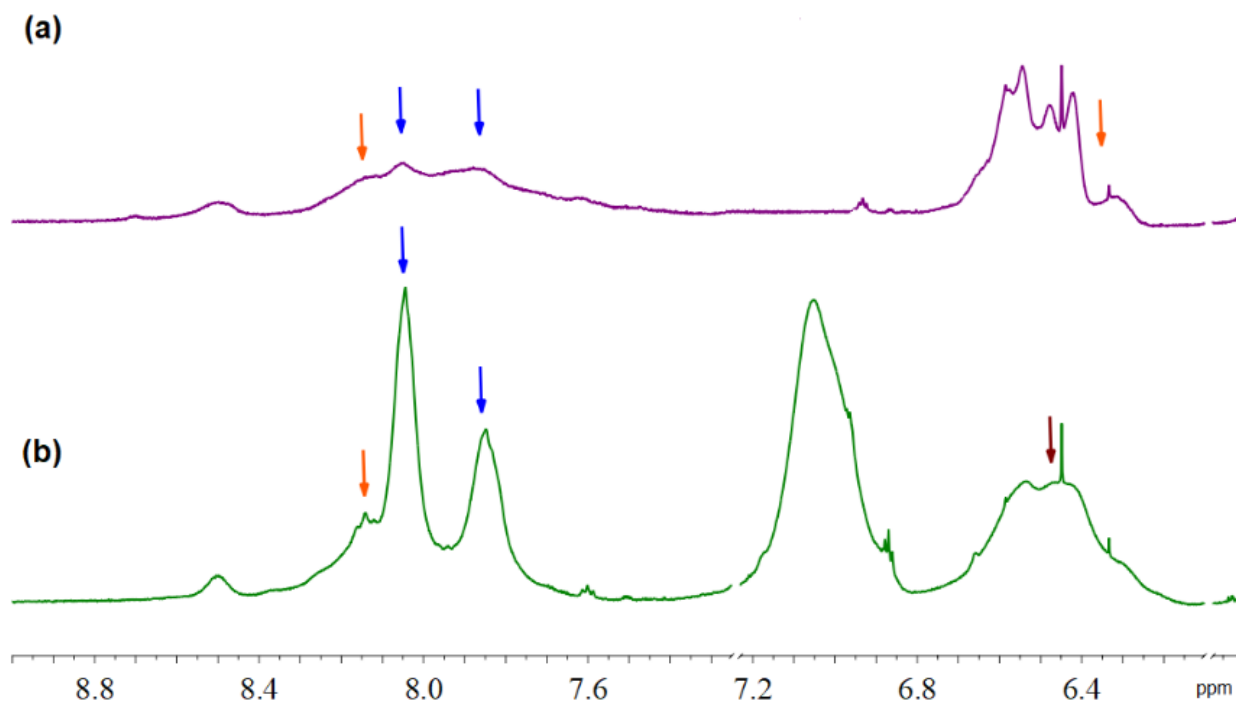


Figure 2.4 Enlarged section of $^1\text{H-NMR}$ spectra in TCE-d_2 (between 9.0 and 6.0 ppm) of rod-coil BCP15 (purple, a) and BCP100 (green, b). Blue arrows indicate the signals attributable to PCPDTBT-based rod blocks, orange arrows indicate the signals attributable to 4VP in the coil blocks, brown arrow indicate the signals attributable to overlaps between 4VP and styrene in the coil block of BCP100.

Table 2.1 MWD data of the macroinitiator PCPDTBT-Ph-TIPNO and of the related BCP2 and BCP5, and of the BCP15 and BCP100 and the related blocks. *See for MWD of P4VP(15) in **Table 3.1**. **See for MWD of Coil100 in reference [13].

Sample	M_n (KDa)	M_w/M_n
Macroinitiator PCPDTBT-Ph-TIPNO ^a	5.4	2.3
BCP2 ^b	5.6	-
BCP5 ^b	6.0	-
Macromer ^c	7.9	1.4
BCP15 ^c	16.2	1.4
Coil15 (P4VP) ^{c*}	1.10	1.0
Coil100 (P(Sty-co-4VP)) ^{c**}	13.7	1.4
BCP100 ^c	14.6	1.9

^a determined through SEC, see experimental section for the conditions; ^b determined through $^1\text{H-NMR}$ (4VP unit $M_w = 105.1 \text{ uma}$); ^c determined through SEC, see experimental section for the conditions.

2.2.2 Synthesis and optical characterization of the BCP WPNP aqueous suspensions

The rod-coil BCP2, BCP5, BCP15 and BCP100 display an amphiphilic nature as they are constituted by the hydrophobic rod block PCPDTBT and the hydrophilic P4VP-based coil block. Thanks to this peculiar feature, they are able to interact with the aqueous medium stabilizing the aqueous/non-aqueous interfaces during the WPNP preparation.[22] Therefore, we developed a modified miniemulsion approach (depicted in **Figure 2.5**), which does not involve the use of surfactants to produce WPNPs both neat (nWPNPs) and in blend with PC₆₁BM (bWPNPs). The last were used to fabricate the active layer of OPV devices, in which the photovoltaic effect was guaranteed by PCPDTBT as electron-donor material and by PC₆₁BM as electron-acceptor material.

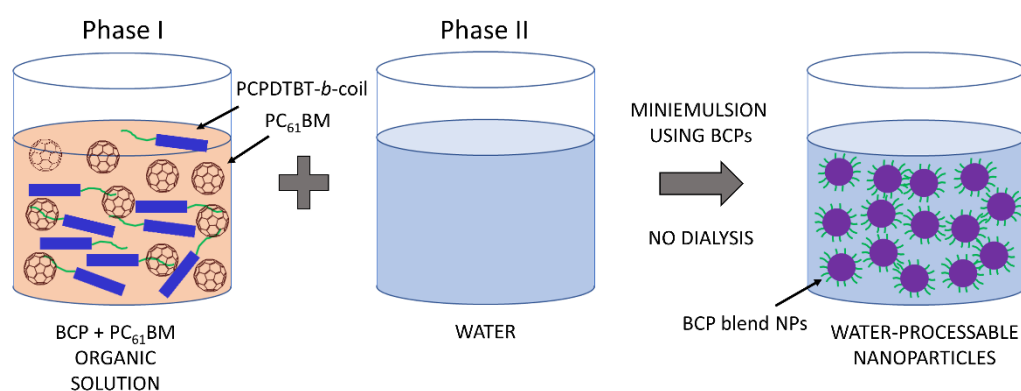


Figure 2.5 Schematic representation of the modified miniemulsion method without any surfactant.

In particular, the blend PC₆₁BM:BCP with a controlled ratio of 3:1 was dissolved into chloroform that is a good solvent for both the materials and has a low boiling point.[23] The concentration of both active materials in the organic starting solution was maintained constant in each preparation to compare the different samples. The organic solution was dropped into pure water under vigorous stirring obtaining a macroemulsion that was sonicated reducing the organic droplet dimensions and thus turning into a miniemulsion. After this, the organic solvent was removed by evaporation and a greenish/brownish stable aqueous suspension was obtained. It is important to remark that in principle in an industrial plant the removed solvent could be rescued and reused in a continuous way, improving the process sustainability.

The WPNP suspensions were characterized through UV-Vis spectroscopy (**Figure 2.6**). The absorption spectra extend over the entire visible region up to the near infrared, from 250 up to 800 nm presenting the typical profiles of the two materials composing the blends. Indeed, two peaks between 250 and 350 nm ascribable to PC₆₁BM can be observed, together with a wide peak at around 700 nm, due to the charge transfer complex into the LBG copolymer backbone, and a shoulder at 410 nm, related to the cyclopentadithiophene fused system of PCPDTBT. All these signals appear

broadened with respect to neat BCP and PC₆₁BM spectra in chloroform because of scattering and their aggregation into the suspended nanostructures. This effect is even stronger in the case of films deposited from WPNP aqueous inks onto a glass substrate.

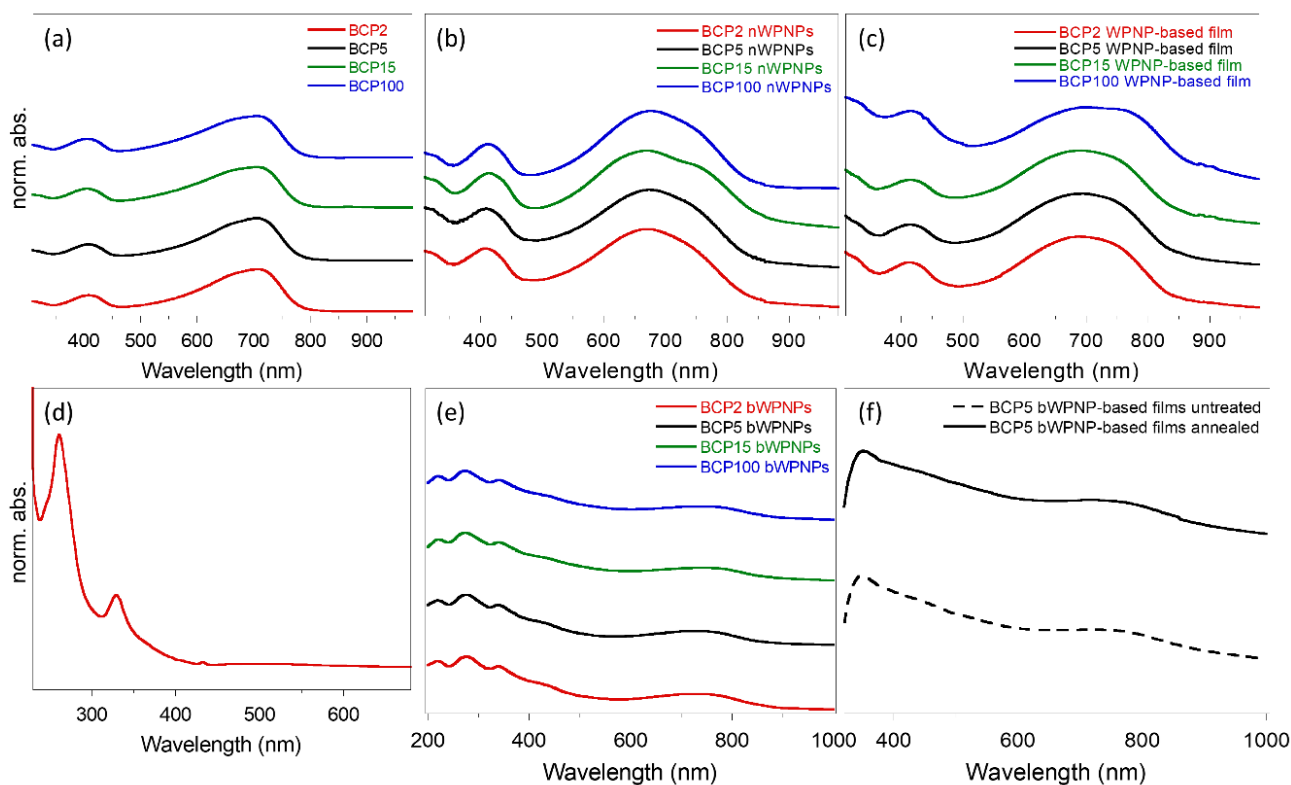


Figure 2.6 Normalized absorption UV-Vis spectra of (a) BCPs dissolved in chloroform; (b) BCP nWPNNP aqueous dispersions; (c) BCP nWPNNP-based films casted on glass substrates; (d) PC₆₁BM dissolved in chloroform; (e) BCP bWPNNP aqueous dispersions; (f) BCP5 bWPNNP-based films obtained through drop-casting on glass substrates before and after thermal treatment.

The photoluminescence (PL) spectra were acquired for samples of rod-coil BCP solutions in chloroform and BCP WPNNPs in water, prepared maintaining constant the BCP concentration (0.6 mg ml⁻¹). As an example, in **Figure 2.7** the comparison between PL spectra referred to BCP5 is reported. The PL spectrum of BCP5 in chloroform shows a significant emission peak at 807 nm. The PL spectrum of the neat BCP-based WPNNPs shows a strong quenching connected to both water presence and an increased interchain interactions among the semiconducting rigid backbones during the NP formation. Furthermore, the complete PL quenching in BCP5 bWPNNPs suggests an efficient photoinduced charge transfer from the rod electron-donor material to the fullerene derivative electron-acceptor material, as reported in the literature.[24] This behaviour indicates that BCP5 bWPNNPs are good candidates for OPV applications, hence the ultrafast spectroscopy was used to better investigate the photo-physics of BCP-base bWPNNPs (section 2.2.5).

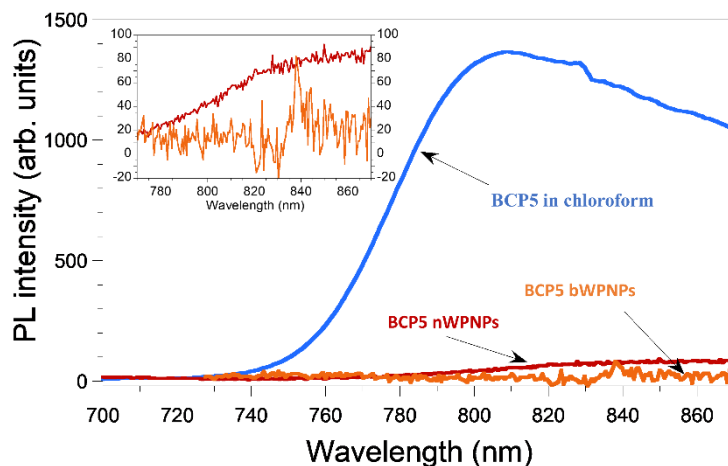


Figure 2.7 PL spectra of BCP5 dissolved into chloroform, nBCP5 and bBCP5 in water. The spectra were collected with a 380 nm exciting radiation.

2.2.3 Study of the BCP bWPNP-based OPV devices

Taking into account the promising morphological and topological features of BCP5, which will be discussed in the following paragraphs,[14] Zappia *et al.* firstly exploited PC₆₁BM:BCP5 (3:1) bWPNPs to deposit an active layer of an OSC.[15] They adopted a direct device architecture, in which commonly the active layer is deposited on a properly treated poly(3,4-ethylenedioxythiophene):polystyrene sulfonate (PEDOT:PSS) hole transporting layer on an indium tin oxide (ITO) substrate. Therefore, the WPNP-based active layer was spin-coated at 500 rpm for 60 seconds. Lastly, they deposited on the top of the active layer a thin PC₆₁BM film (~20 nm) dissolved in dichloromethane (~20 μ l) to totally exclude the presence of leak points and short-circuits. Thanks to these arrangements, they gained an OPV device with a power conversion efficiency (PCE) value of 2.53%, which is ~75% of a conventional BHJ device, obtained by deposition from halogenated solvents.[15, 23, 24]

When I joined the research group, I aimed to correlate the different coil length and structure of the BCPs with the device performances. Therefore, I repeated the synthesis of BCP2, BCP5, BCP15, BCP100, and the respective aqueous inks in order to prepare active layers after suitable pre-deposition treatments.[15, 25] A thin buffer layer of PC₆₁BM deposited from dichloromethane to seal the active layer was dropped before the thermal treatment of the devices. For each blend suspension, four devices were fabricated and characterized in collaboration with Prof. Varun Vohra (University of Electro-Communications, Tokyo). The PCEs and other photovoltaic parameters, summarized in **Table 2.2**, correspond to an average of the performances of these devices. The related current density-voltage (J-V) characteristics are depicted in **Figure 2.8**. Our purpose was to find a correlation between the length and composition of the coil, and the performance of the resulting device.[16] In the case

of BCP2 the device displays an efficiency lower than 1%, while for BCP15 and BCP100 the efficiency is even lowered by two orders of magnitude.

Table 2.2 Photovoltaic characteristics of the devices obtained with PC₆₁BM:BCP=3:1 bWPNP active layers.

Sample	J _{sc} (mA cm ⁻²)	V _{oc} (mV)	FF (%)	PCE (%)
BCP2 bWPNNPs	4.56	593	27.5	0.74
BCP5 bWPNNPs	10.61	634	37.0	2.49
BCP15 bWPNNPs	0.056	92	21.8	0.0011
BCP100 bWPNNPs	0.053	81	23.0	0.0010

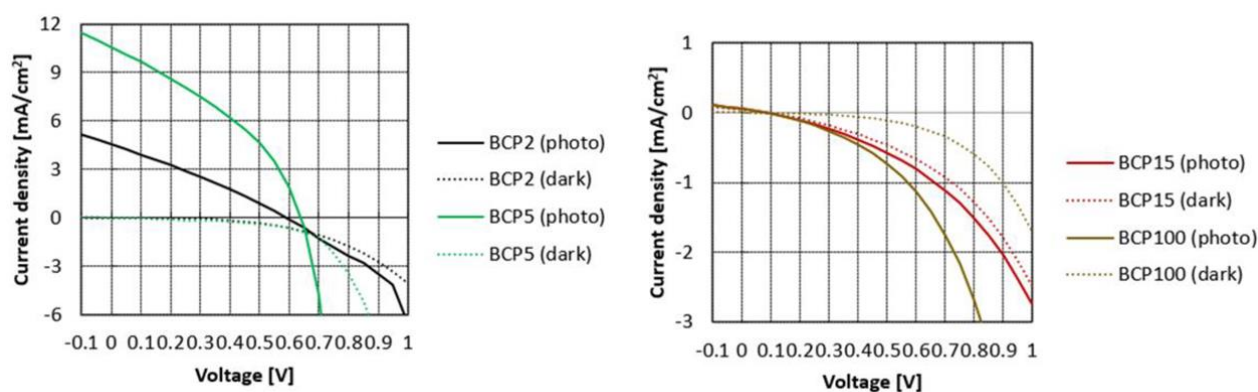


Figure 2.8 J-V curves of the devices based on BCP2 and BCP5 bWPNP dispersions (**left**), and on BCP15 and BCP100 bWPNP dispersions (**right**). Adapted from reference [16].

The active layers prepared using PC₆₁BM:BCP (3:1) blend WPNNPs annealed at 90 °C for 20 minutes were characterized through AFM by Dr. Guido Scavia (SCITEC-CNR, Milano), to explain the different performances of the samples relating to the surface morphology. All films present a distribution of spherical particles, highly clustered in the layers obtained from BCP2 and BCP100 bWPNP dispersions (**Figure 2.9a-d** and **Figure 2.9p-s**, respectively). On the other hand, in the case of BCP5 bWPNNPs (**Figure 2.9e-h**) and, in a lesser extent, in the case of BCP15 bWPNNPs (**Figure 2.9i-o**), the polymeric NPs exhibit a more homogeneous distribution on the substrate and thus a more compact layer. This trend is confirmed by root mean square (RMS) values (**Table 2.3**), which show a minimum for the layer obtained from BCP5 bWPNP dispersions (1.3 nm) with respect to the values measured for BCP2, BCP15 and BCP100 bWPNP-based films (14.5 nm, 9.6 nm, and 17.0 nm, respectively). These results denoted that the layer obtained from deposition of BCP5 bWPNNPs is more homogeneous and compact compared to the other films.

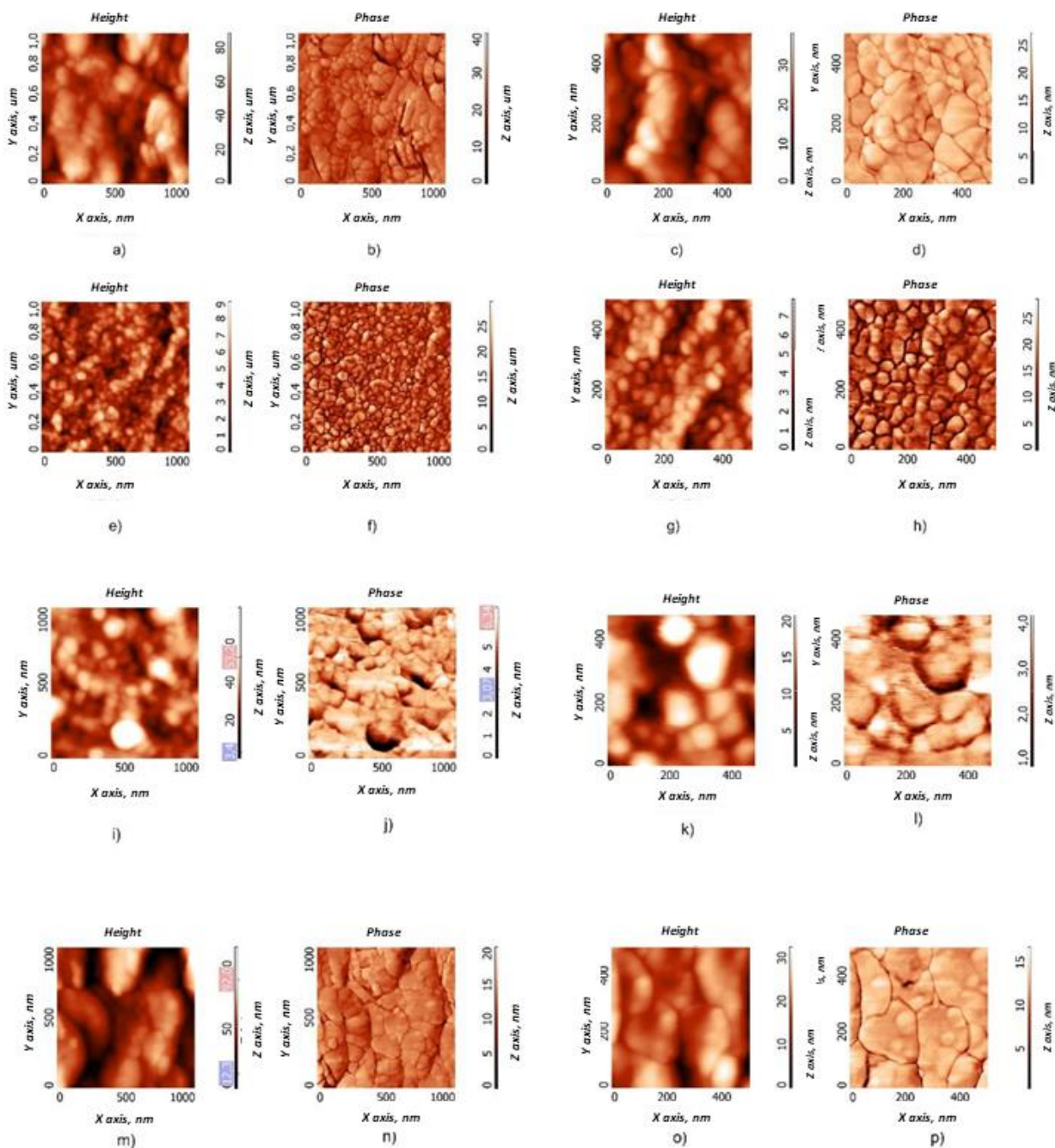


Figure 2.9 AFM images of films obtained from the aqueous dispersions, with two different magnifications, of BCP2 bWPNPs (a–d), BCP5 bWPNPs (e–h), BCP15 bWPNPs (i–l) and BCP100 WPNPs (m–p). Adapted from reference [16].

Table 2.3 RMS values correlated to the BCP2, BCP5, BCP15 and BCP100 bWPNP-based films (**Figure 2.9a,e,i,p**).

Sample	RMS (nm)
BCP2 bWPNNPs	14.5
BCP5 bWPNNPs	1.3
BCP15 bWPNNPs	9.6
BCP100 bWPNNPs	17.0

2.2.4 Morphological investigation of the BCP bWPNNPs

The drastic drop of the efficiency and of the other photovoltaic parameters of the BCP2, BCP15 and BCP100-based devices with respect to BCP5-based one could be related to the morphology of the WPNNPs at the nanoscale level. It means that, considering the chemical composition of the rod-coil BCPs, it is possible to investigate how the length and the structure of the coil block influence the formation of suitable donor/acceptor domains inside the WPNNPs. Indeed, the 4VP-based coil interacts with water during NP formation, minimizing the interaction of the hydrophobic rod with aqueous medium, and leading to the formation of nanostructures that have a semiconducting polymer-rich core and a coil block-rich shell. Notably, in this mechanism the structural and compositional features of the coil play a crucial role in addressing the assembly of the BCP WPNNPs suspended in water and in determining their stability. Firstly, dynamic light scattering (DLS) was performed to obtain information on the size and stability of nanostructure suspensions. All the nWPNNP and bWPNNP suspensions are stable as denoted by ζ -potential values. Indeed, suspensions with ζ -potential from ± 11 to ± 20 where close to the threshold of agglomeration, while the emulsions with values of ± 41 to ± 50 are considered stable. The actual stability of the aqueous suspensions was verified over the time by subsequent DLS measurements. The hydrodynamic diameter (d_H) and the ζ -potential at pH 7 of the BCP bWPNNPs were reported in **Table 2.4**. For comparison, also nWPNNPs size data are listed.

Therefore, the BCP bWPNNP suspensions were characterized through an accurate TEM characterization in collaboration with Dr. Anna Maria Ferretti (SCITEC-CNR, Milano). TEM images of bWPNNPs are depicted in **Figure 2.10a,d,g,j**, and reveal that all the bWPNNPs have a spherical shape, like the nWPNNPs (**Figure 2.29** in Experimental Section).[14] The mean diameters of the bWPNNP samples, measured from TEM micrographs, result larger than the corresponding nWPNNP samples (**Table 2.4**) because of the presence of PC₆₁BM in the blend. Indeed, PC₆₁BM has a surface energy value higher than BCP (45.8 and 40.5 mJ M⁻², respectively) and thus it prefers to stay in the core,

increasing the size of the WPNPs. Particularly, for BCP5 bWPNNs the diameter distribution ranges from 17.9 nm to 176.4 nm, and the NPs are divided in two populations: the former has a mean diameter of around 26 nm, and the latter of about 50 nm. Also, there is a small number of NPs with diameters larger than 100–120 nm surrounded by the smaller NPs, sometimes leading to the formation of tail-like nanostructures.

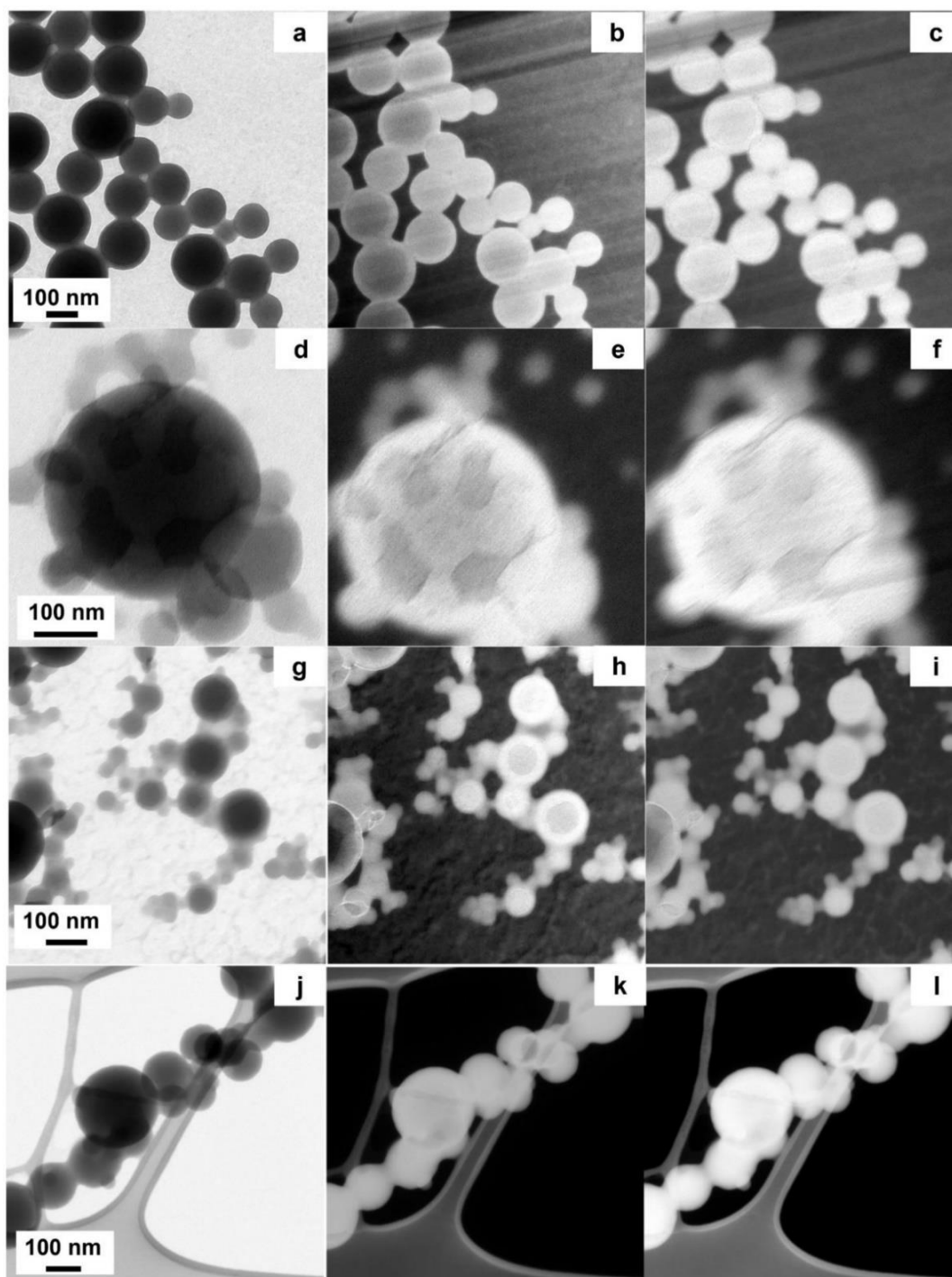


Figure 2.10 TEM and EFTEM images of bWPNNs are reported: (a,d,g,j) show the conventional TEM image, (b,e,h,k) are the EFTEM images recorded at 20 eV, (c,f,i,l) are the EFTEM images collected at 30 eV. Adapted from reference [16].

Table 2.4 Comparison of mean diameter (d_m), determined through TEM, hydrodynamic diameters (d_H), determined through DLS expressed in number, and ζ -potential (mean values) of the nWPNP and bWPNP suspensions.

Sample	d_m (nm)	d_H (nm)	ζ -potential (mV)
BCP2 nWPNPs	35.9±21.3	64.6±1.5	-31.33±0.37
BCP5 nWPNPs	51.5±36.7	90.2±22.7	-19.05±1.47
BCP15 nWPNPs	68.8±31.9	110.7±1.2	-31.23±1.14
BCP100 nWPNPs	48.7±23.7 87.1±30.0	92.3±1.2	-26.58±0.55
BCP2 bWPNPs	149.4±44.8	187.0±2.5	-45.90±0.60
BCP5 bWPNPs	58.2±21.4	133.8±9.2	-14.75±4.11
BCP15 bWPNPs	99.2±48.7	146.1±2.2	-38.40±1.14
BCP100 bWPNPs	202.2±81.7	129.6±1.7	-34.33±0.42

Differently from the morphology of nWPNPs, which could be defined by TEM and STEM-EDX line scan analyses to determine the compositional constitution of the core-shell NPs (**Figure 2.30** in Experimental Section), with the brightfield TEM (BFTEM) imaging only, it is not possible appreciate the compositional inhomogeneity inside bWPNPs. Therefore, for a more in-depth investigation inside the NPs, we take advantage of electron energy loss spectroscopy (EELS), a technique which allows to identify different organic components and thus it can help in our aim to distinguish the shape and the distribution of the nanodomains inside the bWPNPs. EELS analysis gives information about the plasmon peak of materials, and in particular the BCP we used has the plasmon peak maximum at about 22 eV, like almost every carbonaceous polymer, while PC₆₁BM plasmon peak has the maximum at 30 eV.[15, 26] The low-loss region of EELS spectra provides important information about the dielectric properties of the studied nanostructures, and to correlate this compositional information with the spatial resolution we employed the EFTEM imaging, that exploits a small energy window to collect images using only electrons that have a loss at specific energy in order to obtain more accurate data about the WPNP composition. In this kind of images, the contrast is influenced also by the local material electronic distribution, not only by the material density.[27] Based on all these considerations, with the aim to identify the size and the distribution of the PC₆₁BM nanodomains inside the bWPNPs, EFTEM zero-loss images at 22 eV and 30 eV were acquired. In the micrographs collected at 22 eV the areas enriched in BCP are white while the PC₆₁BM-rich zones result darker (**Figure 2.10b,e,h,k**). These darker areas turn into bright in the images acquired at 30 eV (**Figure 2.10c,f,i,l**). Observing the collected images, it is clear that BCP5 bWPNPs (**Figure**

2.10d,e,f) have more than one PC₆₁BM-rich zones, while BCP2 (**Figure 2.10a,b,c**) and BCP15 (**Figure 2.10g,h,i**) bWPNNPs are characterized by a similar unique and large size core, enriched in PC₆₁BM, and a BCP-based shell. To explain these different patterns, a hypothesis based on the amphiphilic behaviour of the rod-coil BCP5 is proposed: the coil blocks, composed of pyridine moieties, coordinate PC₆₁BM during the miniemulsion process and thus the BCP chains enter the water, aggregating because of the hydrophobicity of the rods. During their aggregation, the rods of PCPDTBT include also some PC₆₁BM molecules among them, while the P4VP coil blocks maintain the nanoaggregates suspended in water. The blended NPs grow until they push each other away, after that they collapse forming a new larger nanoobject. The shells of the pristine smaller NPs, composed of P4VP coordinating the PC₆₁BM, go inside the new larger NPs forming the internal pattern we observed with different PC₆₁BM-rich zones. Similar internal nanostructures are reported in literature for water-dispersed NPs composed of a blend of PC₆₁BM:PAT.[28] This process does not occur in the BCP2 and BCP15 WPNNP formation and as a consequence a core/shell structure, with large and regular core rich in PC₆₁BM, is achieved. Moreover, the thickness of the shell increases as the length of the coil, passing from 25.7 ± 11.9 nm for BCP2 bWPNNPs to 37.5 ± 21.4 for BCP15 sample (**Figure 2.32** in Experimental Section). That morphology, in which the core is a single domain that is too large to be active and the shell is so thick that does not help the interface contact of the domains, justifies the low efficiency of the BCP2 and BCP15 corresponding devices with respect to BCP5-based one. On the other hand, the BCP100 bWPNNPs do not show any PC₆₁BM-rich zones (**Figure 2.10j,k,l**). In fact, the presence of C atoms instead of N inside the coil backbone makes it more hydrophobic thus improving the homogeneity of the WPNNPs, and therefore the fullerene derivative molecules are uniformly distributed. Lastly, the several small PC₆₁BM-rich zones inside BCP5 bWPNNPs (**Figure 2.10d,e,f**) create interconnections between donor and acceptor materials suitable for an efficient charge percolation to the electrodes. This inner morphology with nanodomain size comparable with the exciton diffusion contributes to the higher efficiency of the BCP5 bWPNNP-based device with respect to the other samples.[15]

2.2.5 Photophysical investigation of the BCP WPNNP-based films

In collaboration with Dr. Lucia Ganzer and Dr. Tersilla Virgili (IFN-CNR, Politecnico di Milano), the ultrafast spectroscopy was exploited to investigate the photo-physic of the BCP bWPNNPs, that is the topic of the paper of reference [17]. Particularly, we aimed to correlate the molecular structure of the BCP with the formation of charge transfer states (CTSs) at the interfaces between the electron-donor and acceptor materials, in order to validate the impact of the coil length on the organization at the nanoscale level inside the NPs and on the charge separation efficiency.[29-31] CTSs are defined

as Coulombically bounded charge pairs where the hole is firstly placed on the highest occupied molecular orbital (HOMO) of the donor and the electron is on the lowest unoccupied molecular orbital (LUMO) of the acceptor. Hence, having information about them is mandatory as the ratio between full ionization and geminate recombination of CTS is crucial for the photovoltaic performances.[32, 33] Ultrafast transient absorption spectroscopy (TA) measurements were performed on thin films spin-coated from chloroform solution as control (CTRL) reference and from aqueous suspensions using samples based on the aqueous suspensions containing BCP-based nWPNNPs and bWPNNPs.

The TA spectra (**Figure 2.11**) at different pump-probe delays of neat CTRL were compared with the spectra obtained in the same conditions of BCP2 and BCP100 nWPNNP-based films in order to primarily investigate the influence of the coil length on the mechanism of the formation of the CTSs in the WPNNP-based films. We observed in the visible region a broad positive band centred at ~ 680 nm related to a ground state photobleaching (GSB). Moreover, a negative photoinduced absorption (PA) band centred at ~ 500 nm is present (hereafter PA₁). GSB and PA₁ bands have the same temporal decays, meaning that they both refer to the same photoexcited population, namely the excitons.

In the NIR region there is a second PA (PA₂) assigned to other charged species, as indicated from the different dynamic, whose intensity decreases as coil length of nWPNNPs increases, suggesting a reduction in the charge formation.

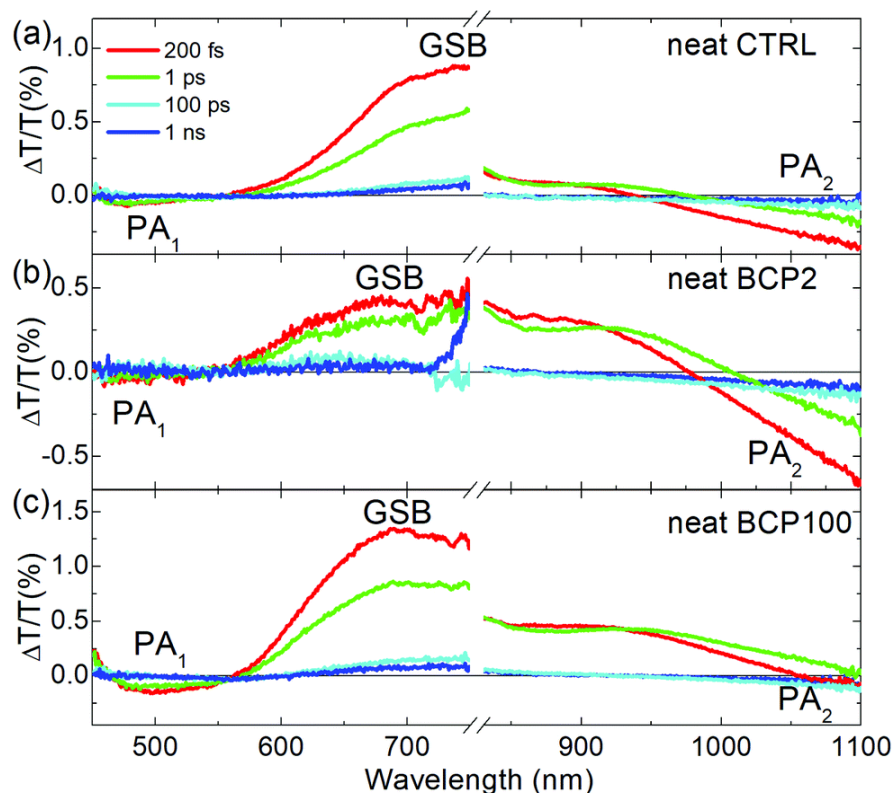


Figure 2.11 TA spectra of (a) neat CTRL, (b) BCP2 nWPNNPs and (c) BCP100 nWPNNP-based films collected with a 400 nm excitation at different time delays between pump and probe beams. TA visible spectra of BCP2 nWPNNPs were multiplied by 5. Reported from reference [17].

Some differences are expected when TA measurements are performed in presence of the fullerene derivative PC₆₁BM, both in blend film deposited from organic solvent (CTRL) and in the BCP bWPNP-based films (**Figure 2.12**). Noticeably, PA₁ band undergoes a red-shifts and a second GSB at ~470 nm appears. Furthermore, a new PA band (PA₃) becomes visible increasing the probe delay, ascribed to the electron transfer from the donor to the acceptor material. This band, at around 620-680 nm, is highlighted if we compare TA spectra at an early probe delay (200 fs) and at a long one (100 ps) (**Figure 2.13**). The BCP100-based bWPNPs displayed also CTSs at ~525 nm with a growing time of around 4 ps. This evidence suggests that the charges, created by exciton separation at the donor/acceptor interface, behave in a different manner in BCP2 and BCP100 bWPNPs. Namely, in the BCP100 bWPNPs, not only photo-induced excitons can dissociate generating free charges in around 20 ps, but also, they can form CTSs at a PCPDTBT/PC₆₁BM interface in around 4 ps. This last mechanism implies that in BCP100 bWPNPs there are more CTSs forming interfaces with respect to free charge generating ones. On the other hand, in BCP2 bWPNPs only charge generating interfaces are present. Therefore, a clear correlation between the length and composition of the coil block and the free charge generation is demonstrated. Indeed, increasing the coil length (as for BCP100 bWPNPs), an improvement in the formation of long-living CTSs occurs, negatively affecting the exciton separation mechanism, and thus impacting the proper working of the WPNP-based photovoltaic device.

The WPNP-based OPV device obtained from BCP5 bWPNPs resulted the most efficient because of the relatively short coil segment (5 repeating units), which hinders the CTS formation at the donor/acceptor interfaces, detrimental for an efficient exciton dissociation into free charges. In **Figure 2.14** TA spectra of BCP5 bWPNP-based sample are depicted. Similarly to other samples, a PA band at 550 nm, attributed to the PCPDTBT, and two GSB bands at ~680 nm and ~470 nm were detected. What is more, also in these spectra the PA band at ~650 nm due to the electron transfer from donor to acceptor material is observable and there is no CTS at 525 nm, indicating that no adverse mechanism affects the proper free charge formation, leading to higher performances of the photovoltaic devices.

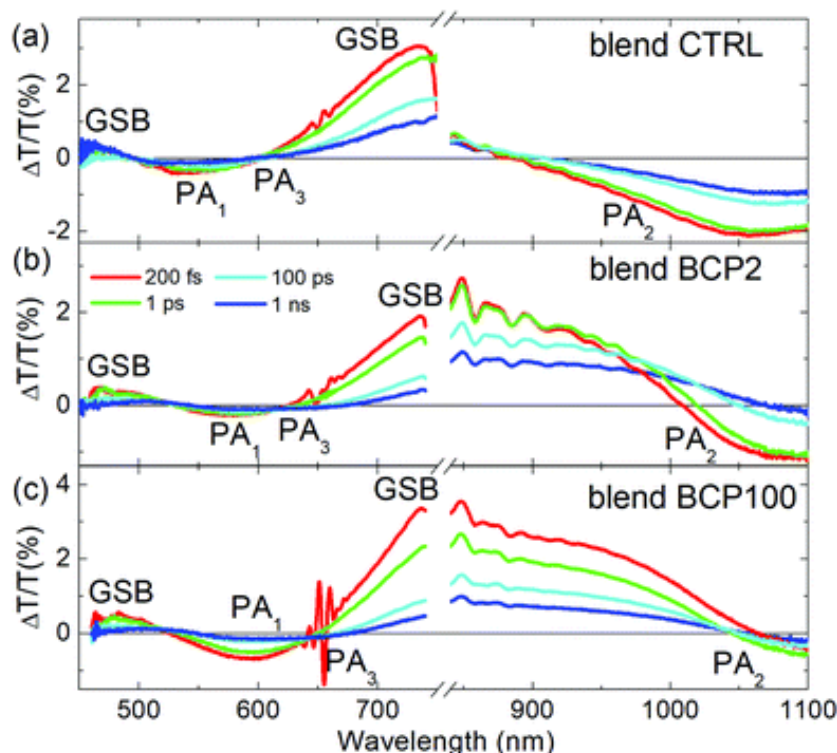


Figure 2.12 TA spectra of (a) commercial blend CTRL, (b) BCP2 bWPNP-based and (c) BCP100 bWPNP-based films collected with a 650 nm excitation to selectively excite PCPDTBT outside of the PCBM absorption range at different time delays between pump and probe beams. NIR TA spectra of BCP2 bWPNPs were divided by 2. Reported from reference [17].

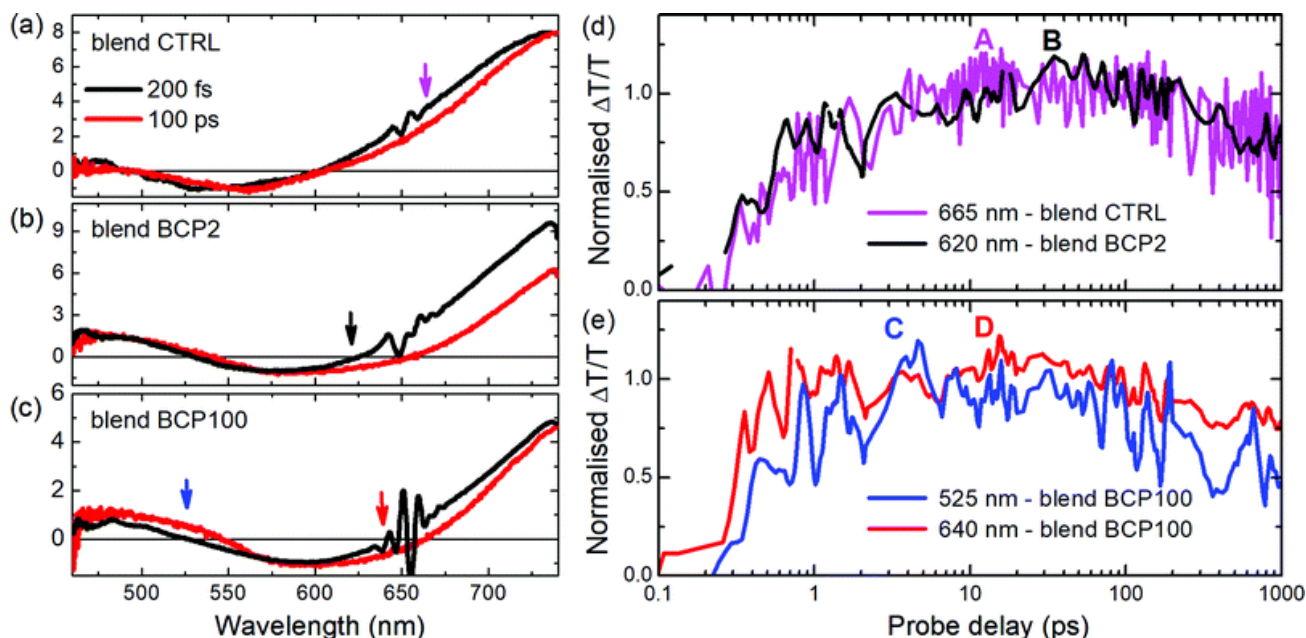


Figure 2.13 TA spectra in blend CTRL (a), BCP2 (b) and BCP100 (c) films at two different pump-probe delays; spectra were normalized at the minimum of the photo-induced band around 600 nm to compare the temporal evolution of the bands. Inset: TA *normalized* spectra in blend CTRL. In (d) and (e) *normalized* temporal dynamics at different probe wavelengths in blend CTRL, BCP2 and BCP100 films. Arrows in (a–c) indicate the probe wavelengths shown in (d) and (e). Pump excitation: 650 nm. The spectra were normalized at the minimum of the PA₁ bands. Reported from reference [17].

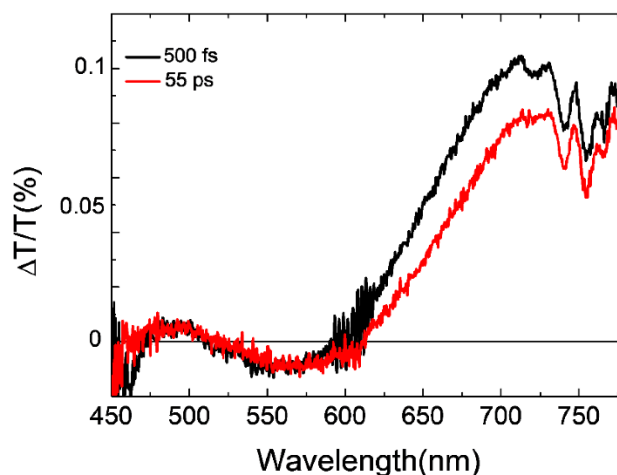


Figure 2.14 TA spectra at two different pump-probe delays for the BPC5 bWPNPs. Adapted from reference [16].

2.2.6 WPNP aqueous suspensions for bioelectronic applications

Polymer-based NPs were widely reported in the biotechnology field as intriguing tools to modulate living cell activity by means of light. Indeed, since cells are basically transparent and do not directly respond to light, scientists tried to enhance or even induce light sensitivity in living organisms to obtain light control of physiological functions by transducing the optical signal in a biological (bioelectrical, biochemical, or biomechanical) one. Particularly, NPs based on organic semiconductors (especially π -conjugated polymers) emerged as very intriguing candidates for photoactuators in biological systems, due to their excellent biocompatibility and their high degree of mechanical conformability, that can be exploited in the realization of different architectures in biointerfaces.[34]

In this context, WPNPs based on PCPDTBT-*b*-P4VP, and in particular BCP2, attracted the interest of Dr. Maria Rosa Antognazza (Italian Institute of Technology, Milano) because the emission and absorption spectra of these NPs are in the far-red region of the visible spectrum and in the near infrared (NIR), respectively. At these wavelengths the autofluorescence of biological matter is low, and tissue penetration is high,[35] so these NPs are highly attractive for potential *in vivo* applications. Preliminary studies were performed to verify that no alteration in the absorption spectrum occurs if the NPs are dispersed in extracellular media instead of water. Therefore, the biophysical interface between NPs and living cells was investigated by IIT. The cells that they used belong to the Human Embryonic Kidney -293 (HEK-293) cell line.

Firstly, viability assay with Alamar Blue, a fluorescent probe that is reduced by cellular respiration, was carried out to verify that these NPs are not toxic to the cells. Fluorescence records were conducted the day after (Day 0) and 4 days after (Day 4) the NP administration, on treated and untreated (control) samples. Both samples exhibit a good viability, as highlighted by results reported in **Figure 2.15**.

Furthermore, proliferation is not affected by the presence of the NPs since the fluorescence value at Day 4 is comparable between the two cases.

At this point, they verified the NP internalization exploiting confocal fluorescence imaging on fixed samples. Because cells do not show any fluorescent behavior, they were treated with specific fluorescent dyes, namely DAPI (4',6-diamidino-2-phenylindole) and phalloidine-FITC (conjugated with a FITC green fluorophore). The NPs exhibit the main absorption peak in the red region of the visible spectrum, thus they were excited with the 640 nm laser, where their optical density is not negligible. **Figure 2.15** reports a representative image captured, in which the fluorescence of NPs, DAPI and phalloidine are colored as red, blue and green, respectively. In the majority of cells, many red spots associated to WPNP presence are displayed in the cell cytoskeleton, indicating a successful uptake of NPs by HEK-293 cells.

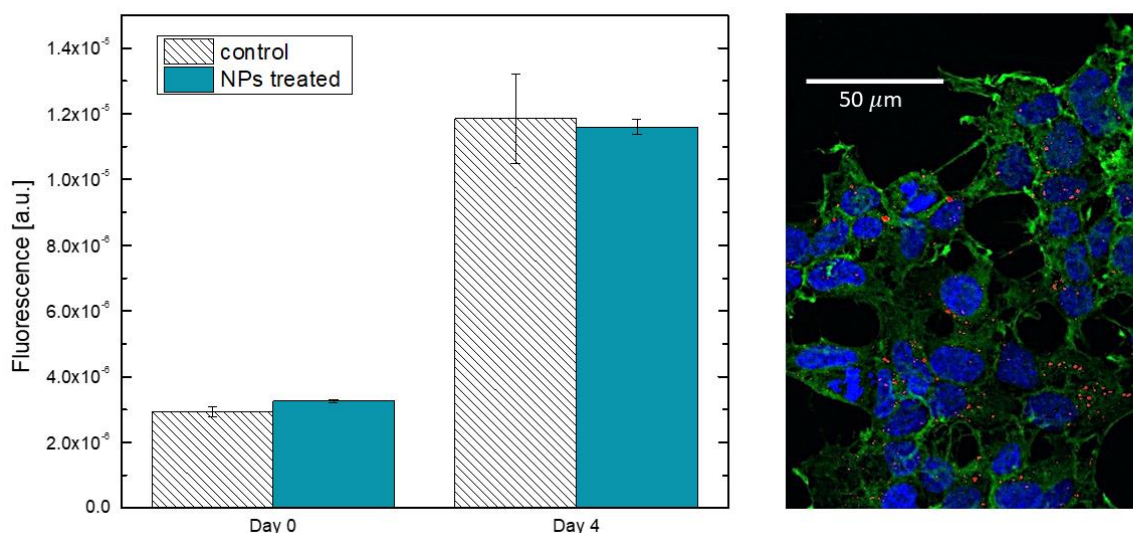


Figure 2.15 (Left) Histogram representing the average fluorescence in the viability assay for control (grey) and WPNP-treated (blue) HEK-293 cells at Day 0 and at Day 4. Error bars represent the standard error; each column of the histogram reports the average over 3 samples. **(Right)** Confocal image of fixed HEK-293 cells treated with WPNPs. Cells nuclei were stained with DAPI (blue emission); cell cytoskeleton with phalloidine (green); WPNPs were observed through their intrinsic photoluminescence, in red. Blue channel: 405/450 nm (excitation/emission wavelength). Green channel: 488/525 nm. Red channel: 640/700 nm. Objective used: 20x.

The final aim of the research group was to evaluate the functionalities that these NPs can induce upon illumination in HEK-293 cells; in particular, they focused on cell metabolism, analyzing the production of Reactive Oxygen Species (ROS), and on the intracellular Ca^{2+} dynamics. ROS are the radical species (reactive ions and free radicals, as for example hydrogen peroxide H_2O_2) generated by successive reduction of oxygen and are involved in physiological and pathological processes.[36, 37] Experiments regarding the intracellular production of ROS were performed by means of a fluorescence microscope. Control and NP treated cells were incubated with DCF, a fluorescent probe

that binds to the radical species present in the cytosol. Images both before and after the illumination at 660 nm were collected and noticeably, they observed a significant difference in the case of WPNP-treated samples after illumination with respect to all the other cases (**Figure 2.16**), denoting a remarkably production of ROS by the photocatalytic effect ascribed to WPNP presence. The model proposed to explain the ROS production in the cytosol compartment within living cells is represented in **Figure 2.17**. The specie O^{2-} is expected to be an intermediate toward the formation of other ROS species; the final product of this chain is mainly H_2O_2 .

Ca^{2+} fluxes play a fundamental role in cell metabolism and inter-cell communication processes because they influence the activity of other secondary messengers. They are released in the cytoplasm by mitochondria and by endoplasmic reticulum. Their variation triggers many cellular functions, as muscular contraction, secretion, or gene expression.[38] Entrusting in fluorescence microscopy, Ca^{2+} imaging experiments were also conducted on both treated and untreated samples. In this case, they did not distinguish any difference between the two cases (**Figure 2.16**), suggesting that the ROS species produced by the photo-stimulation of the polymer-based WPNPs do not affect the dynamics of Ca^{2+} ions.

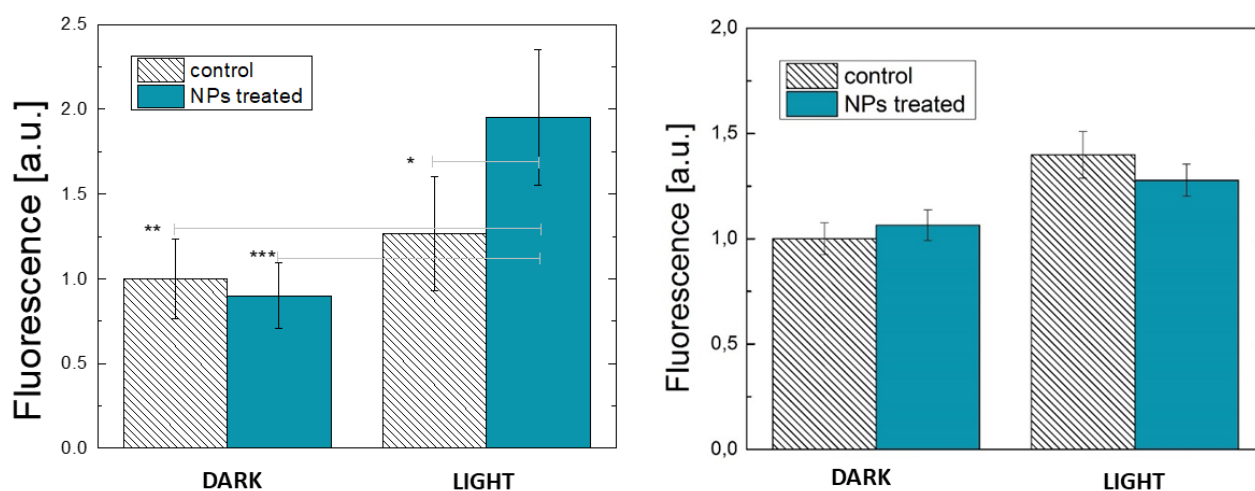


Figure 2.16 (Left) Histograms representing the average fluorescence of DCF for control (grey) and WPNP-treated (blue) HEK-293 cells in dark and light conditions. Bars represent the standard error. Data were normalized to the dark control fluorescence value. **(Right)** Average amplitude of the Ca^{2+} signals for control (grey) and NPs treated (blue) HEK-293 cells in dark and light conditions. NPs administered 24 hours after the plating phase. Bars represent the standard errors. Data were normalized to the dark control value.

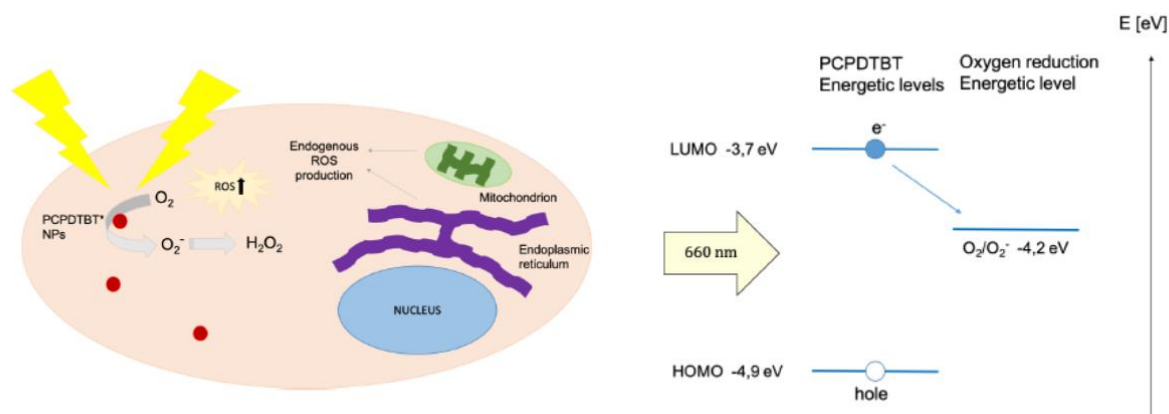


Figure 2.17 Schematic representation of the mechanism activated by WPNP photo-stimulation inside HEK-293 cells (**left**) and energetic levels of the HOMO and LUMO of PCPDTBT and of the oxygen reduction, with respect to an Ag/AgCl electrode (**right**).

Basing on these results, we can conclude that the BCP-based WPNPs are biocompatible, and their optical excitation may pave the way to novel therapeutic strategies, based on non-invasive, spatially controlled and reversible modulation of intracellular ROS. On the other hand, further studies are needed to gain the possibility to modulate Ca²⁺ fluxes, and it is necessary to evaluate if sizable effects can be observed by changing parameters, as power intensity and time duration of the excitation.

2.3 Conclusions

In summary, four amphiphilic rod-coil BCPs, bearing a standard rigid block constituted by the LBG polymer PCPDTBT, and tailored flexible blocks differing in length and chemical composition, were synthesized and characterized. ¹H-NMR, SEC, MALDI-TOF MS techniques were employed to prove the formation of the BCPs. In particular, BCP2 and BCP5 were achieved through a chain growth-like approach, which allows to obtain copolymers with a short coil. On the other hand, a step growth-like approach was adopted to gain copolymers with a longer flexible moiety, namely BCP15 and BCP100. BCP2, BCP5 and BCP15 include short segments of 4VP repeating units (2, 5, and 15, respectively), while BCP100 consists of a long coil block of 76% Sty and 24% 4VP. The BCPs were used for the preparation of bWPNPs with PC₆₁BM as the acceptor material through an adapted miniemulsion approach, without using any other surfactant. The resulting aqueous suspensions were stable and were exploited for the deposition of active layers of sustainable OPV devices. Noticeably, the final performance was deeply affected by the coil length and structure. Therefore, the morphology of the bWPNPs was investigated by means of TEM, EFTEM and EELS to shed the light on the internal morphology of the nanostructures, and to correlate the dimensions of the donor/acceptor nanodomains with the efficiency of the devices. Furthermore, the photo-physics of the bWPNP deposited on thin

films was studied to elucidate the charge generation processes in the bWPNP-based active layers. The best performance was reached using the BCP5 bWPNP-based aqueous ink. This sample enabled us to gain working devices with efficiencies close to those of the devices obtained by deposition from halogenated solvents. We ascribed this behavior to the relatively short coil block that leads to the formation of many small PC₆₁BM-rich regions inside each bWPNP. As a consequence, the exciton separation mechanism at the donor/acceptor interfaces is very efficient, allowing a good charge generation and collection at the electrodes. Moreover, we observed that a shorter coil block, as in the case of BCP2 bWPNPs, generated a core-shell morphology with PC₆₁BM-rich large cores. Also in this case, the exciton separation was efficient, but the low quality of the obtained films led to low device performance. Otherwise, longer coil segments, as for BCP15 and BCP100, produced longer-lived charge transfer states that justified the poor efficiencies achieved, together with the inefficient morphology of the nanodomains in the bWPNPs. Particularly, in the BCP100-based samples, the presence of Sty in the coils with its insulating behavior was detrimental to the device's efficiency. In conclusion, we demonstrated that a careful molecular design is crucial to optimize the BCP molecular structures, enabling the morphology control in the WPNP-based OPV active layer fabrication.

To further implement the effectiveness of this approach, I will aim to synthesize new amphiphilic BCPs, characterized by a rod block consisting in a polymer with a higher degree of crystallinity and that leads to high efficiencies.

2.4 Experimental Section

2.4.1 Materials

All reagents, unless otherwise specified, were purchased from Sigma-Aldrich and used as received. 2,6-dibromo-4,4-di-(2-ethylhexyl)-4H-cyclopenta[2,1-b;3,4-b']dithiophene, referred as dibromo-CPDT, was obtained from Lumtec-Luminescence Technology Corp. Commercially available Sty, 4VP, and anisole used to prepare the coil block were previously distilled on calcium hydride under reduced pressure and stored at -20 °C under nitrogen. 2,2,5-Trimethyl-4-phenyl-3-azahexane-3-nitroxide (TIPNO) was purchased from Sigma-Aldrich and handled under nitrogen atmosphere, whilst brominated *tert*-butyl isopropyl phenyl nitroxide (TIPNO-PhBr) was synthesized as reported in reference [19]. All other solvents used for the chemical reactions were dried by standard procedures. All manipulations involving air-sensitive reagents were performed under dry nitrogen atmosphere. 1,2-Dideutero-1,1,2,2-tetrachloroethane (TCE-d₂) is a TCI Chemicals product.

For the BCP WPNP production through the miniemulsion approach MilliQ water grade ultrapure was used (resistivity of ~18 and pH~7 at 25 °C).

PEDOT:PSS and PC₆₁BM were purchased from Lumtec-Luminescence Technology Corp, from Heraeus Clevios AI 4083, and from Solenne BV respectively and used as received.

2.4.2 Synthetic Procedures

2.4.2.1 Chain Growth-like strategy for the synthesis of BCP2 and BCP5

Synthesis of the macroinitiator PCPDTBT-Ph-TIPNO. To a Schlenk tube dibromo-CPDT (250 mg, 0.446 mmol) and 2,1,3-benzothiadiazole-4,7-bis(boronic acid pinacol ester) (referred thereafter as diborolane-BT) (173 mg, 0.446 mmol) were dissolved in 10 ml of anhydrous THF. The catalytic system Pd₂(dba)₃ (4.1 mg, 4.46 mmol, 1% eq) and P(*p*-tol)₃ (5.4 mg, 17.8 mmol, 4% eq), 1 ml of a degassed solution of K₂CO₃ 4.2 M and a drop of Aliquat 336 were added to the solution. The reaction mixture was stirred at 70 °C for 9 hours. After this, an excess of TIPNO-Ph-Br (270 mg, 1.5 eq) was added to cap the borolane end groups and the mixture was left under stirring for 16 hours. Then, it was cooled at room temperature and poured into methanol. The crude polymer was filtered, recovered, and poured again in methanol. The so-obtained precipitate was collected (198 mg, 50%).

¹H-NMR (TCE-d₂, 600 MHz, 315 K, ppm) δ: 8.04 (br, 2H, phenyl), 7.85 (br, 2H, thienyl), 2.04 (br, 4H, CH₂ alkyl chain), 1.26-0.81 (br, 18H, CH and CH₂ alkyl chain), 0.71-0.56 (br, 12H, CH₃ alkyl chain) related to the PCPDTBT backbone and consistent with that reported in literature;[39] 7.60 (m, 6H, phenyl), 6.99 (m, 3H, phenyl), 4.3-3.5 (m, 3H, CH-N, CH-O, CH *i*-propyl TIPNO) related to the TIPNO end group and consistent with that reported in literature.[19]

Chain Growth-like strategy - general procedure. The macroinitiator PCPDTBT-Ph-TIPN and 4VP were dissolved in dry anisole. After this, the radical TIPNO (5% with respect to the macroinitiator) dissolved in the same solvent, was added. Three freeze-pump-thaw cycles were repeated to remove any oxygen traces and the reaction mixture was heated at 125 °C for 20 or 45 minutes (in the case of BCP2 or BCP5, respectively). Subsequently, the reaction was stopped immersing the reaction flask in liquid nitrogen. The crude product was purified through consecutive precipitation in selective solvents. A typical procedure consisted first in a precipitation of the cold anisole solution in hexane (selective for the rod), followed by a dissolution in THF of the recovered solid which was precipitated again in methanol (selective for the homopolymer P4VP). This precipitate is the rod-coil BCP.

¹H-NMR (TCE.d₂, 600 MHz, 315 K, ppm) δ: 8.26 (br, 2H, 4VP), 8.05 (br, 2H, phenyl PCPDTBT), 7.85 (br, 2H, thienyl PCPDTBT), 7.60 (m, 6H, phenyl TIPNO), 6.99 (m, 3H, phenyl TIPNO), 6.34 (br, 2H, 4VP), 2.04 (br, 4H, CH₂ alkyl chain PCPDTBT), 1.29-0.75 (br, 18H CH and CH₂ alkyl chain

PCPDTBT and 9H CH₃ t-butyl TIPNO), 0.66 (br, 12H CH₃ alkyl chain PCPDTBT and 6H CH₃ *i*-propyl TIPNO).

The ratio of the integrals of H_m and H_b or H_m and H_c allows the determination of the ratio between the block molar masses. Thus, the length of the coil moiety, indicated as number of P4VP units, was calculated considering the M_n value of the macroinitiator PCPDTBT-Ph-TIPNO determined by SEC [11] and the molecular weight of 4VP (105.1 uma).

2.4.2.2 Step Growth-like strategy for the synthesis of BCP15 and BCP100

Synthesis of the rod block PCPDTBT-borolane. The two monomers (1 eq each), dibromo-CPDT and diborolane-BT were introduced into a dry, oxygen-free Schlenk tube and undergone to three vacuum/nitrogen cycles. They were dissolved into anhydrous THF, then sequentially K₂CO₃ aq. 4 M (10 eq), a drop of Aliquat 336, Pd₂(dba)₃ (1% eq) and P(*p*-tol)₃ (4% eq) were added. The reaction mixture was heated at 70 °C for 8 hours and 5-methylthiophene-2-boronic acid pinacol ester (3 eq) was added to quench the polycondensation. Subsequently the reaction mixture was kept under stirring overnight. After this it was cooled at room temperature and filtered through Celite® to completely remove any trace of the metal catalyst, washing with chloroform. The recovered crude was poured into methanol and recovered through filtration. Finally, the so-obtained product was extracted in Soxhlet apparatus using sequentially acetone, ethyl acetate, chloroform.

¹H-NMR (TCE-d₂, 600 MHz, ppm) δ: 8.05 (br, 2H, phenyl); 7.86 (br, 2H, thienyl), 2.04 (br, 4H, CH₂ alkyl chain), 1.16-0.89 (br, 18H, CH and CH₂ alkyl chain), 0.70-0.58 (br, 12H, CH₃ alkyl chain). The spectrum was consistent with that reported in literature.[39]

Synthesis of Coil100 (P(Sty-*co*-4VP)).[13] A Schlenk tube was conditioned with three vacuum/nitrogen cycles, then Sty, 4VP (20% of distilled 4VP and 80% of Sty), TIPNO-PhBr, TIPNO, and dry anisole were introduced. The mixture was degassed by several freeze-pump-thaw cycles and subsequently the tube was heated at 125 °C for 15 hours. The polymerization was quenched through cooling at room temperature, diluting with THF and precipitated twice in hexane to obtain a whitish solid.

¹H-NMR (TCE-d₂, 400 MHz, ppm) δ: 8.11 (br, 2H, 4VP), 7.01 (br, 3H, Sty), 6.49-6.11 (br, 2H 4VP and 2H Sty), 2.05-0.92 (br, 6H, CH and CH₂ alkyl chain). The actual percentage of the two components (24% of 4VP and 76% of Sty random insertion) was determined through the comparison between the normalized integral of the signal at 8.11 ppm corresponding to two aromatic protons of the 4VP and the normalized integral of the signal at 7.01 ppm corresponding to three aromatic signals of the Sty unit.

Synthesis of Coil15 (P4VP).[13] A Schlenk tube was conditioned with three vacuum/nitrogen cycles and 205 μl of distilled 4VP (199 mg, 1.89 mmol) and 140 μl of anisole were introduced and seven freeze-pump-thaw cycles were performed to remove any remaining oxygen. After that, 70 mg of TIPNO-PhBr and 2 μl of TIPNO (2,2,5-Trimethyl-4-phenyl-3-azahexane-3-nitroxide) (1.87 mg, 8.5×10^{-3} mmol) dissolved in 120 μl of anisole were added and seven freeze-pump-thaw cycles were repeated. The reaction was heated at 125 $^{\circ}\text{C}$ for 45 minutes and the colour changes from light yellow to dark yellow. The reaction was quenched in liquid nitrogen, diluted with anisole and precipitated in hexane. The precipitated was filtered yielding to 38 mg of polymer.

$^1\text{H-NMR}$ (TCE- d_2 , 600 MHz, ppm) δ : 8.6-8.0 (br, 2H, 4VP), 7.0-6.9 (br, 4H Ph-Br and 5H Ph TIPNO), 6.7-6.2 (br, 2H, 4VP), 3.3-3.0 (m, 1H, CH-N TIPNO), 2.0-0.9 (br, 6H, CH and CH_2 alkyl chain). The number of repeated units of 4VP in the coil block was calculated as the ratio between the normalized integral of the signal at 8.6-8.0 ppm (2H aromatic of the 4VP) and the normalized integral of the signal at 3.3-3.0 ppm (1H of CH-N of TIPNO-PhBr backbone).

Step Growth-like strategy - general procedure. The two degassed rod and coil blocks (1:1 eq) were dissolved into distilled toluene in a Schlenk tube conditioned with three vacuum/nitrogen cycles. A degassed aqueous solution of K_2CO_3 1M (17 eq), catalyst $\text{Pd}(\text{PPh}_3)_4$ (5% eq) dissolved into dry toluene, and one drop of Aliquat 336 were added. The reaction mixture was stirred for 3 days at 95 $^{\circ}\text{C}$, then cooled at room temperature and filtered through Celite® to completely remove any trace of the metal catalyst, washing with toluene and chloroform. The filtrate was concentrated in vacuum and poured into methanol. The product was dissolved in a small quantity of solvent and poured again into hexane to obtain a blue solid.

BCP15: $^1\text{H-NMR}$ (TCE- d_2 , 600 MHz, ppm) δ : 8.5 (br, 2H, 4VP), 8.1-7.5 (br, 2H, phenyl PCPDTBT, 2H, thienyl PCPDTBT, 9H Ph TIPNO), 6.6-6.3 (br, 2H, 4VP), 2.1 (br, 4H, CH_2 alkyl chain PCPDTBT), 1.3-0.7 (br, 18H CH and CH_2 alkyl chain PCPDTBT and 9H CH_3 *t*-butyl TIPNO), 0.7 (br, 12H CH_3 alkyl chain PCPDTBT and 6H CH_3 *i*-propyl TIPNO).

BCP100: $^1\text{H-NMR}$ (TCE- d_2 , 600 MHz, ppm) δ : 8.17 (br, 2H, 4VP), 8.04 (br, 2H, phenyl PCPDTBT), 7.85 (br, 2H, thienyl PCPDTBT), 7.60 (m, 6H, Ph TIPNO), 7.18-6.83 (br, 3H, styrene), 6.82-6.10 (br, 2H 4VP and 2H styrene), 2.03 (br, 4H, CH_2 alkyl chain PCPDTBT), 1.12-0.87 (br, 18H, CH and CH_2 alkyl chain PCPDTBT and 9H CH_3 *t*-butyl TIPNO), 0.71-0.56 (br, 12H CH_3 alkyl chain PCPDTBT and 6H CH_3 *i*-propyl TIPNO).

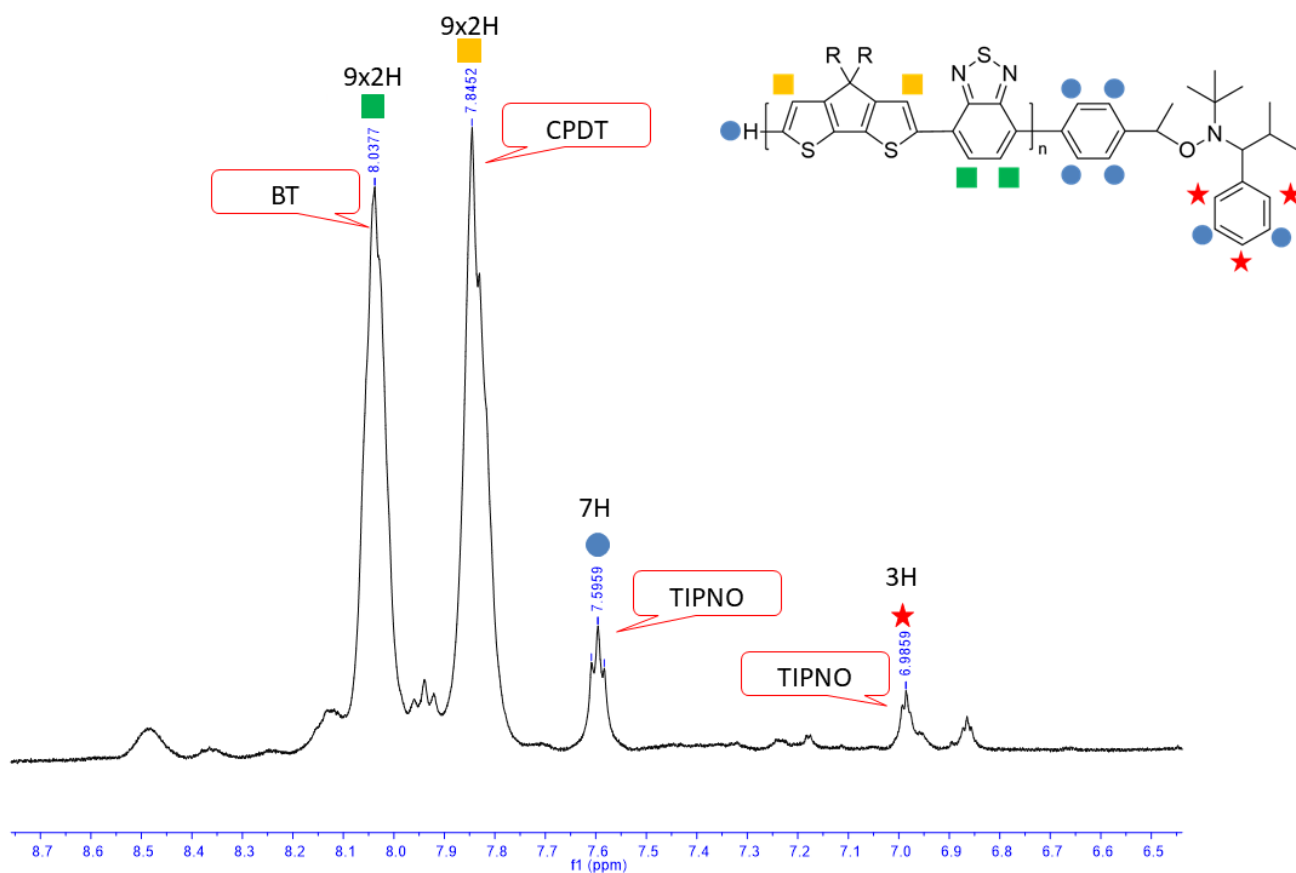


Figure 2.18 Assigned $^1\text{H-NMR}$ spectrum of the PCPDTBT-Ph-TIPNO macroinitiator.

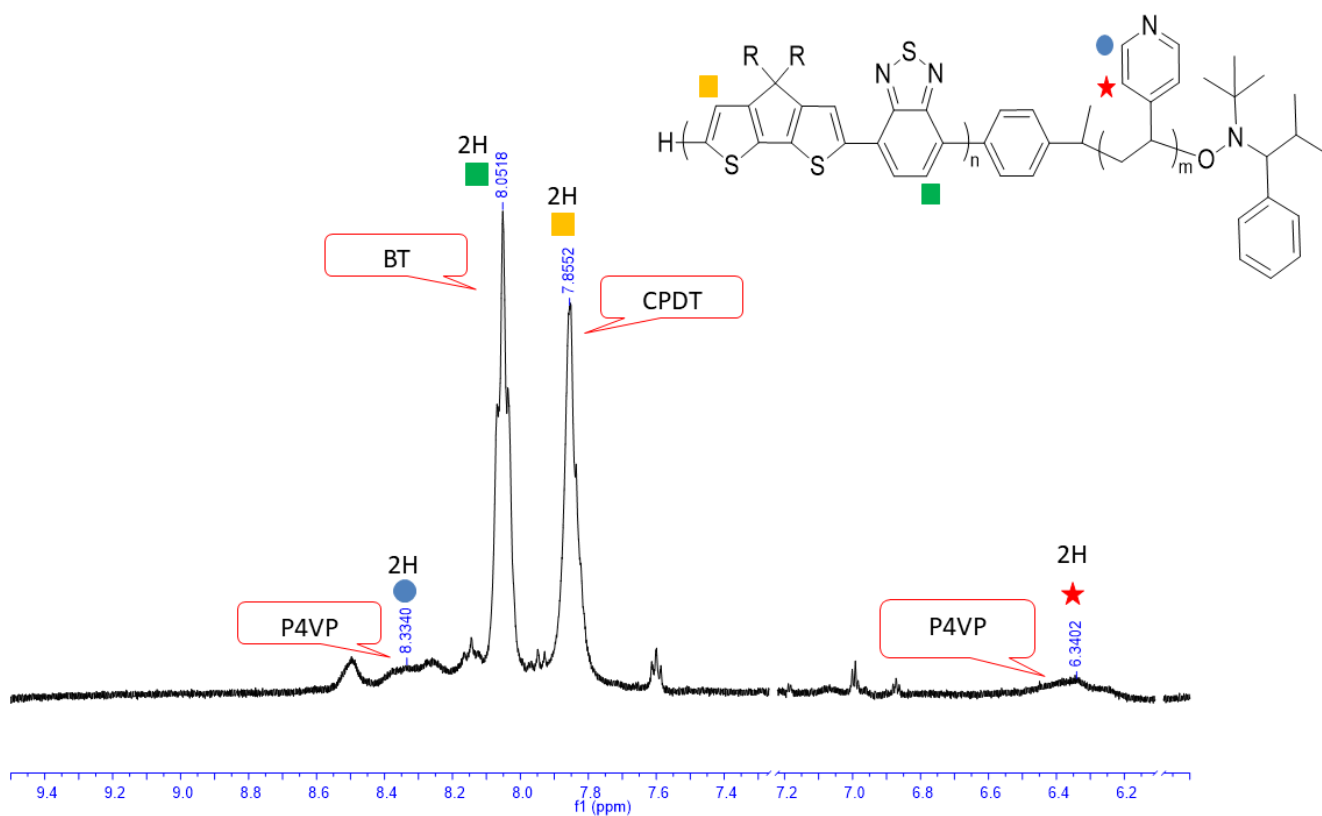


Figure 2.19 Assigned $^1\text{H-NMR}$ spectrum of the BCP2.

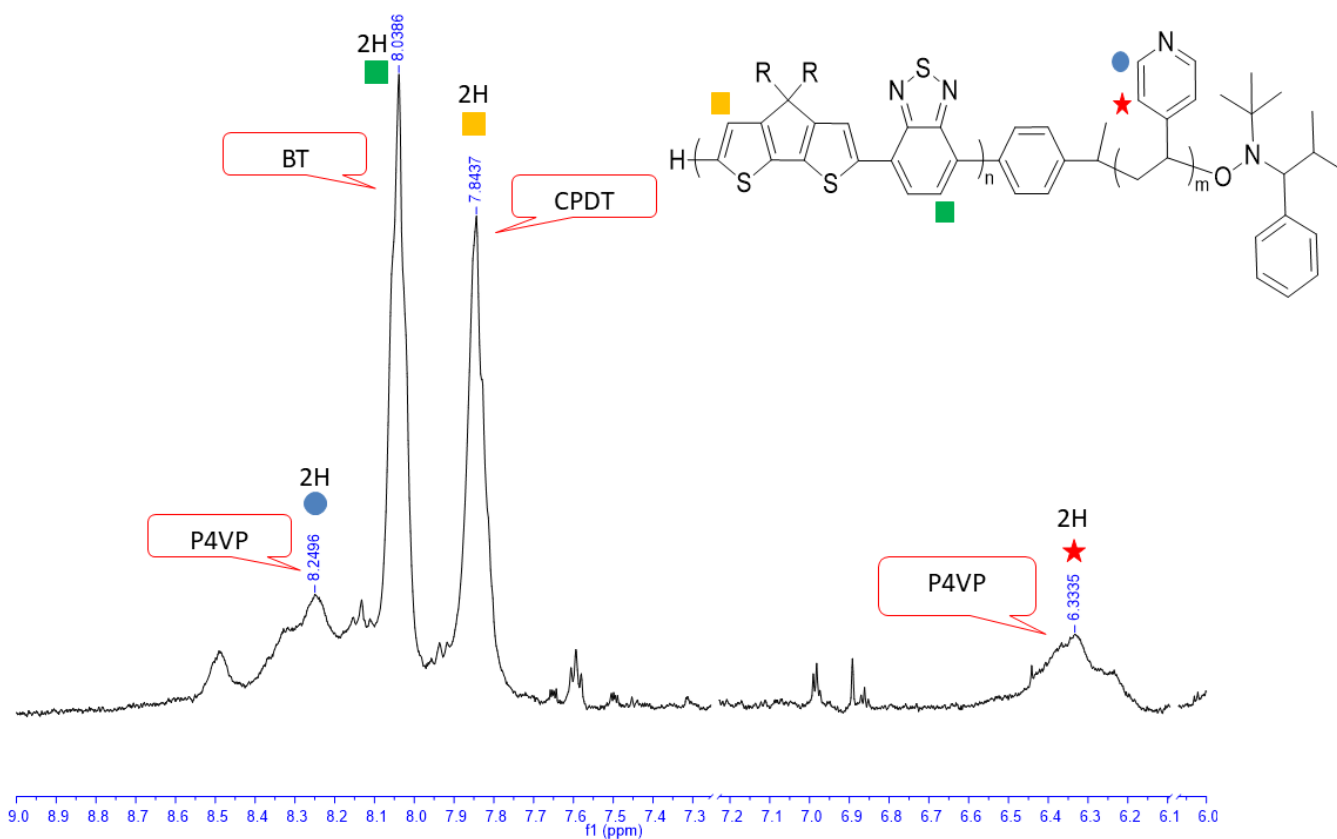


Figure 2.20 Assigned $^1\text{H-NMR}$ spectrum of the BCP5.

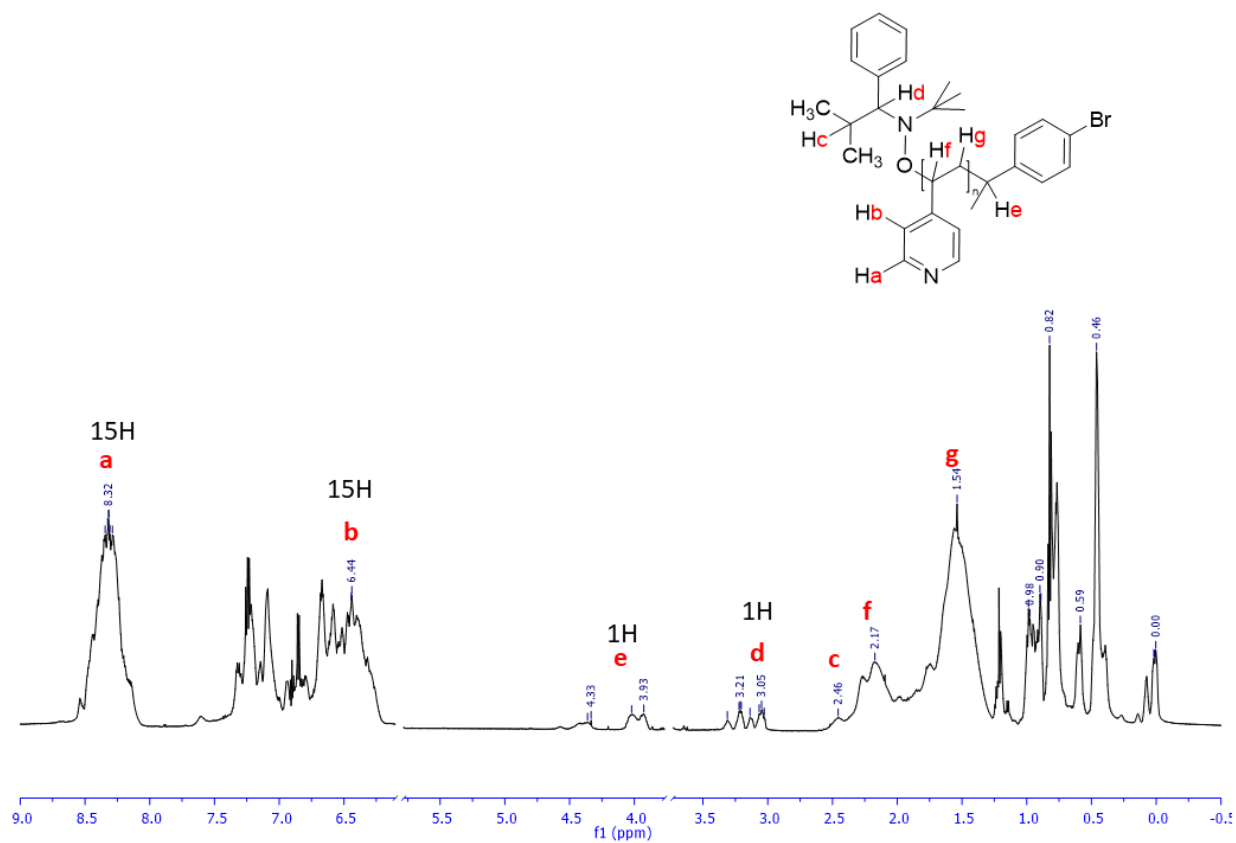


Figure 2.21 Assigned $^1\text{H-NMR}$ spectrum of the Coil15.

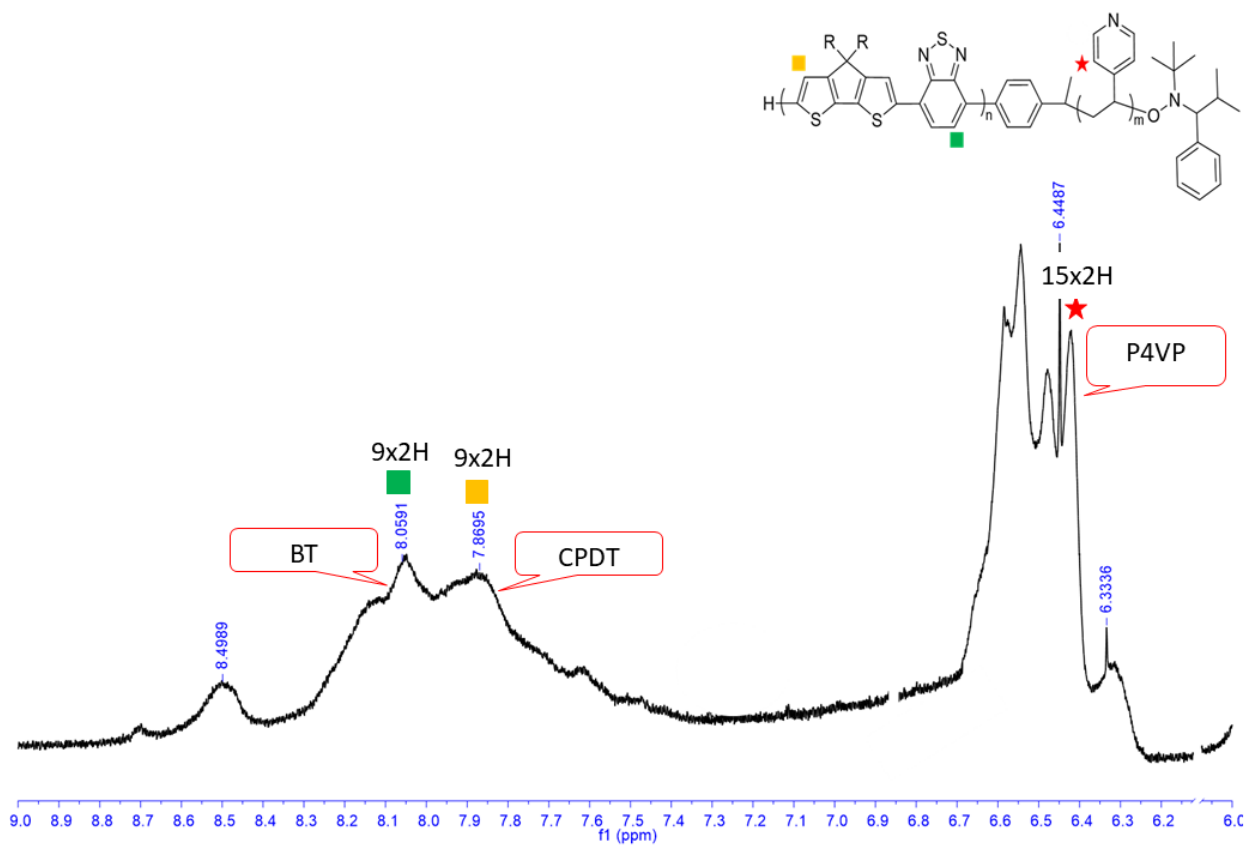


Figure 2.22 Assigned ¹H-NMR spectrum of the BCP15.

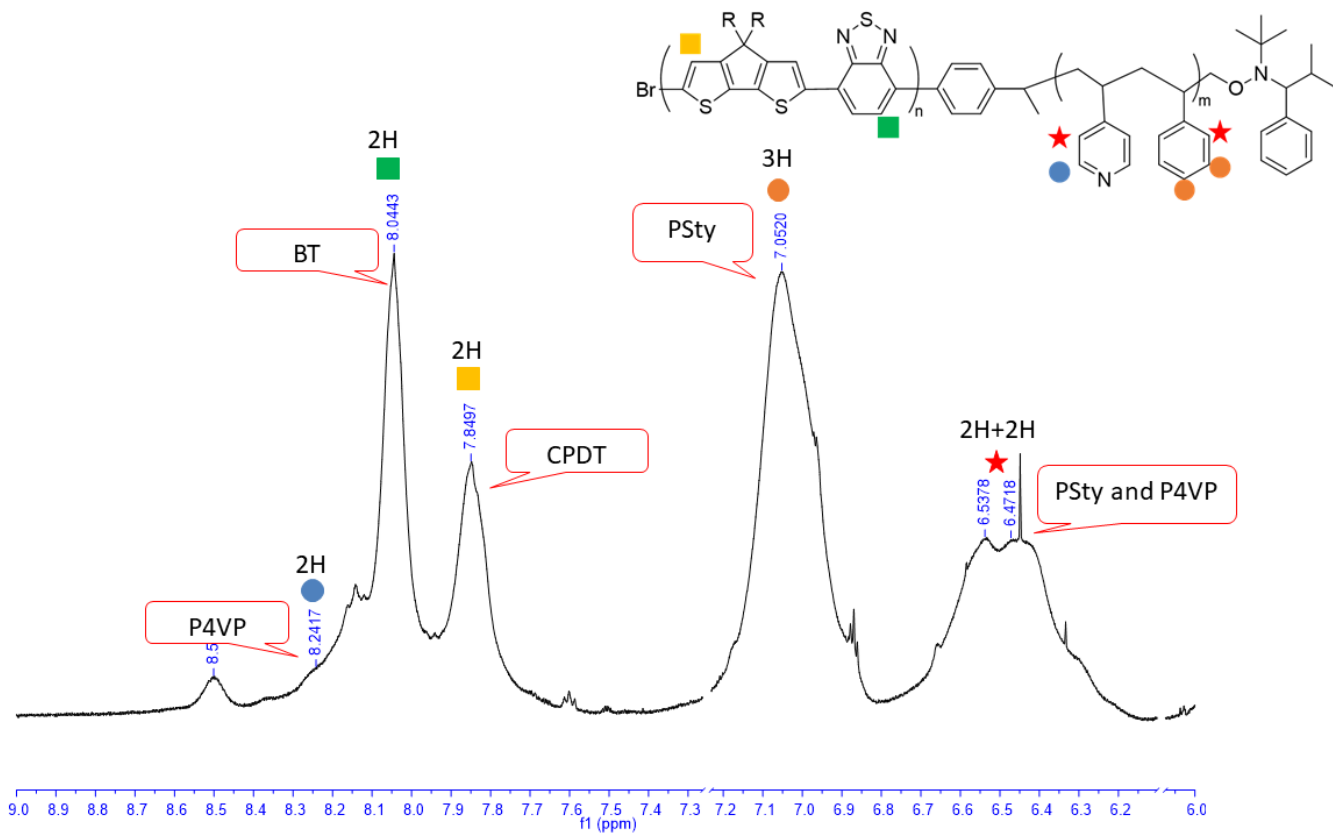


Figure 2.23 Assigned ¹H-NMR spectrum of the BCP100.

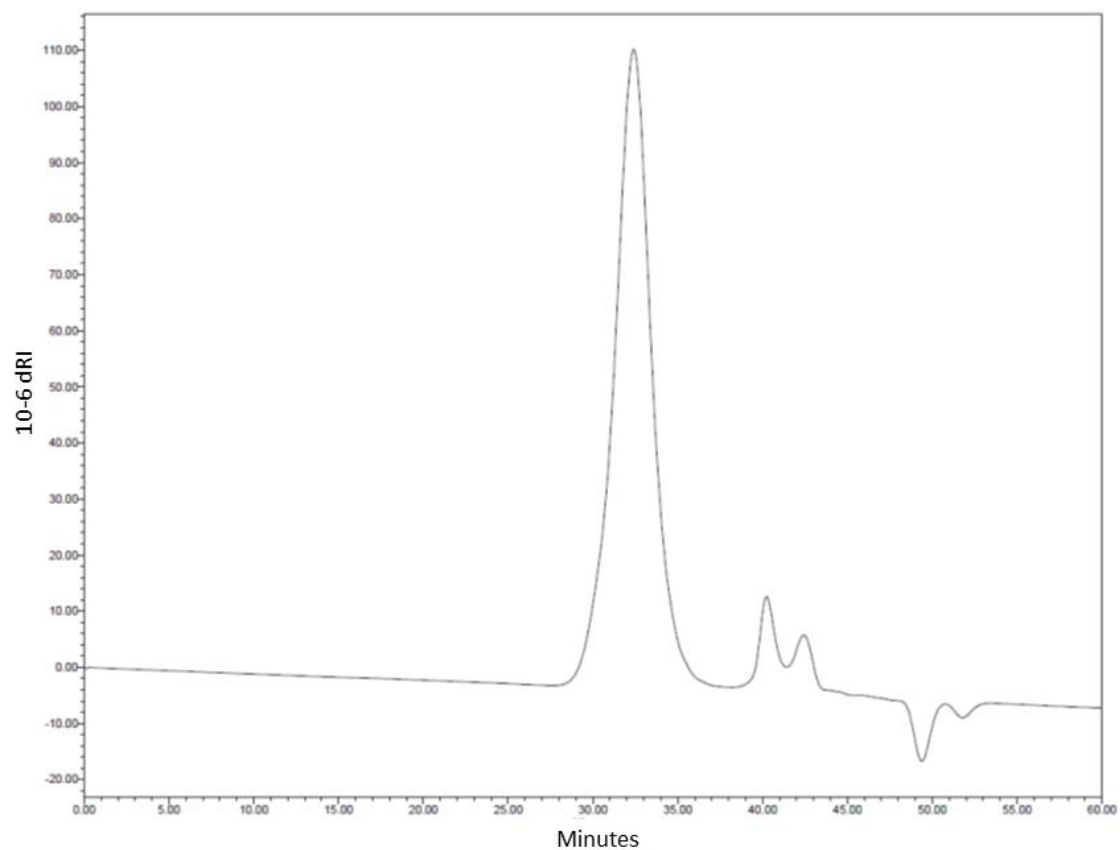


Figure 2.24 SEC chromatogram of the PCPDTBT-Ph-TIPNO macroinitiator.

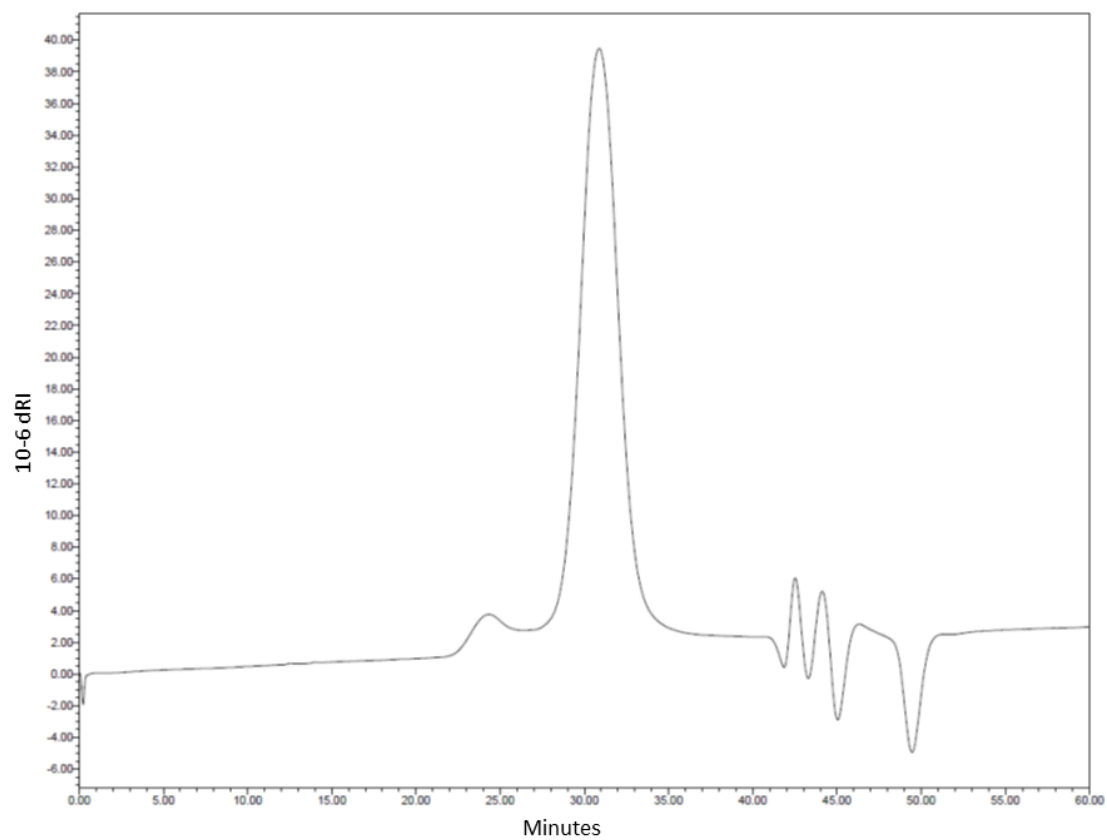


Figure 2.25 SEC chromatogram of the BCP15.

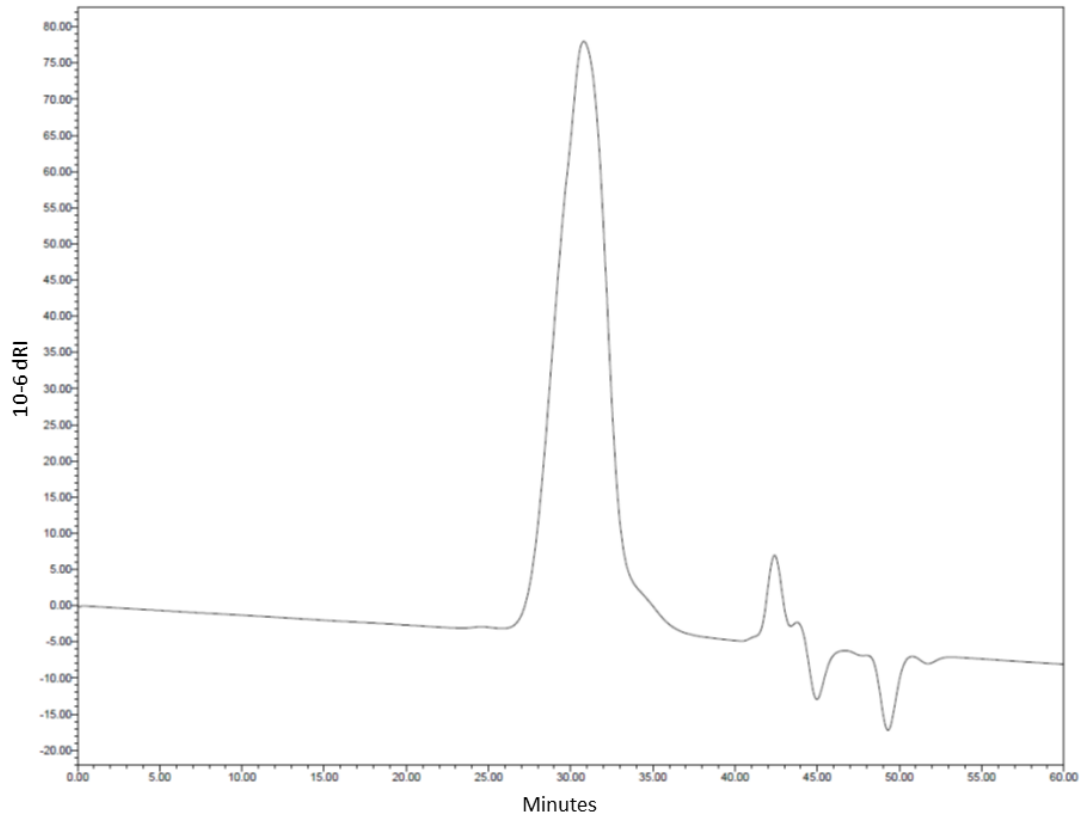


Figure 2.26 SEC chromatogram of the BCP100.

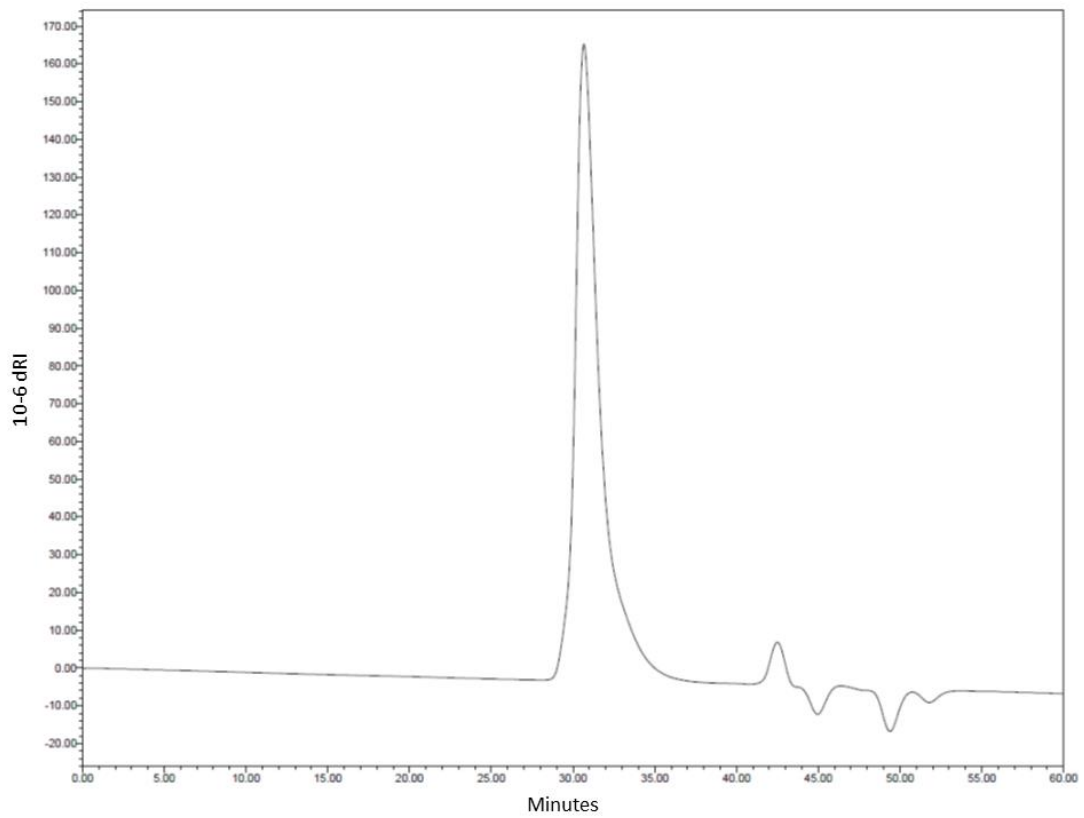


Figure 2.27 SEC chromatogram of the Coil100.

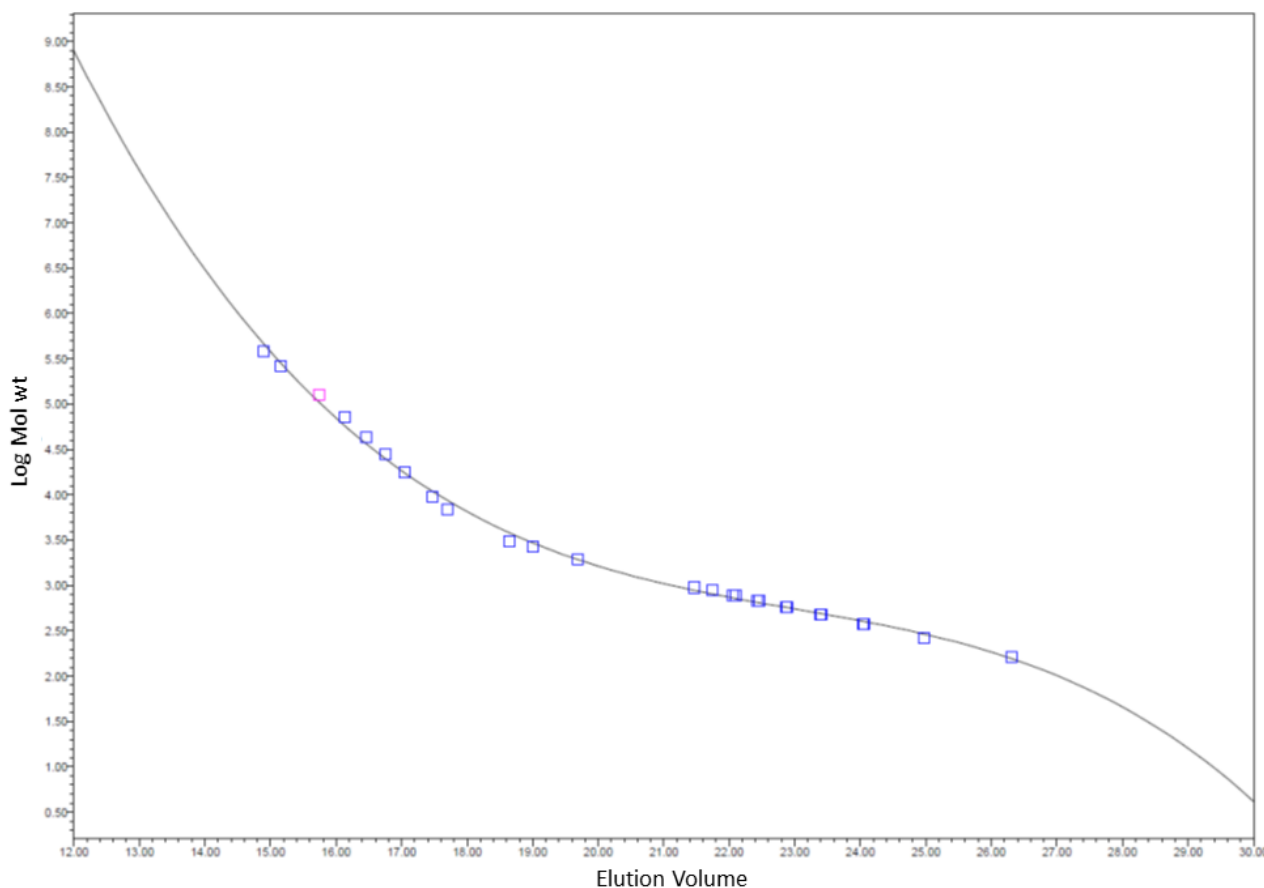


Figure 2.28 Calibration curve of SEC analyses. (Elution Volume = $-0.0036 V^3 + 0.248 V^2 - 5.83 V + 49.29$; $R^2 = 0.9986$).

2.4.3 BCP WPNP synthesis

Synthesis of nWPNPs.[14] In a typical procedure, the organic starting solutions of BCP in chloroform was prepared with a standard concentration of 10 mg ml^{-1} . Each BCP macroemulsion was obtained slowly pouring under vigorous stirring $60 \mu\text{l}$ of the organic starting solution into 1 ml of pure MilliQ water, preheated at $40 \text{ }^\circ\text{C}$. After 1 hour the macroemulsion was sonicated in an ultrasonic bath for 10 minutes at room temperature to obtain a miniemulsion, which was then heated at $70 \text{ }^\circ\text{C}$ under stirring to remove all the chloroform. Stable dark-blue WPNP aqueous suspensions were achieved. All the preparations were performed in air. The suspensions were obtained with a concentration of 0.6 mg ml^{-1} , and they are stable for several weeks in the dark at $25 \text{ }^\circ\text{C}$. The deposited films are stable at the same conditions for months.

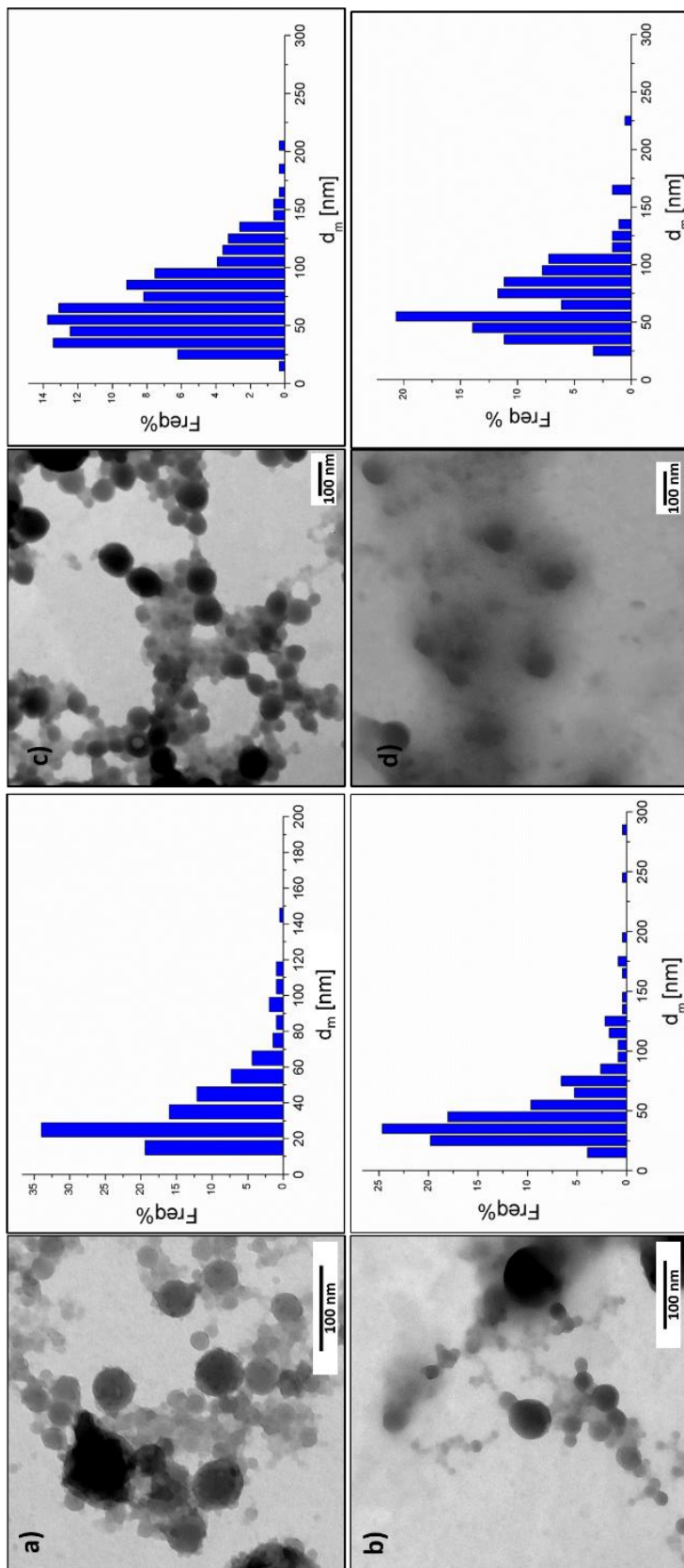


Figure 2.29 TEM images and size distributions of **a)** BCP2- **b)** BCP5- **c)** BCP15- **d)** BCP100-based nWPNTs deposited from the original aqueous suspensions. Reported with permission from Elsevier from reference [14].

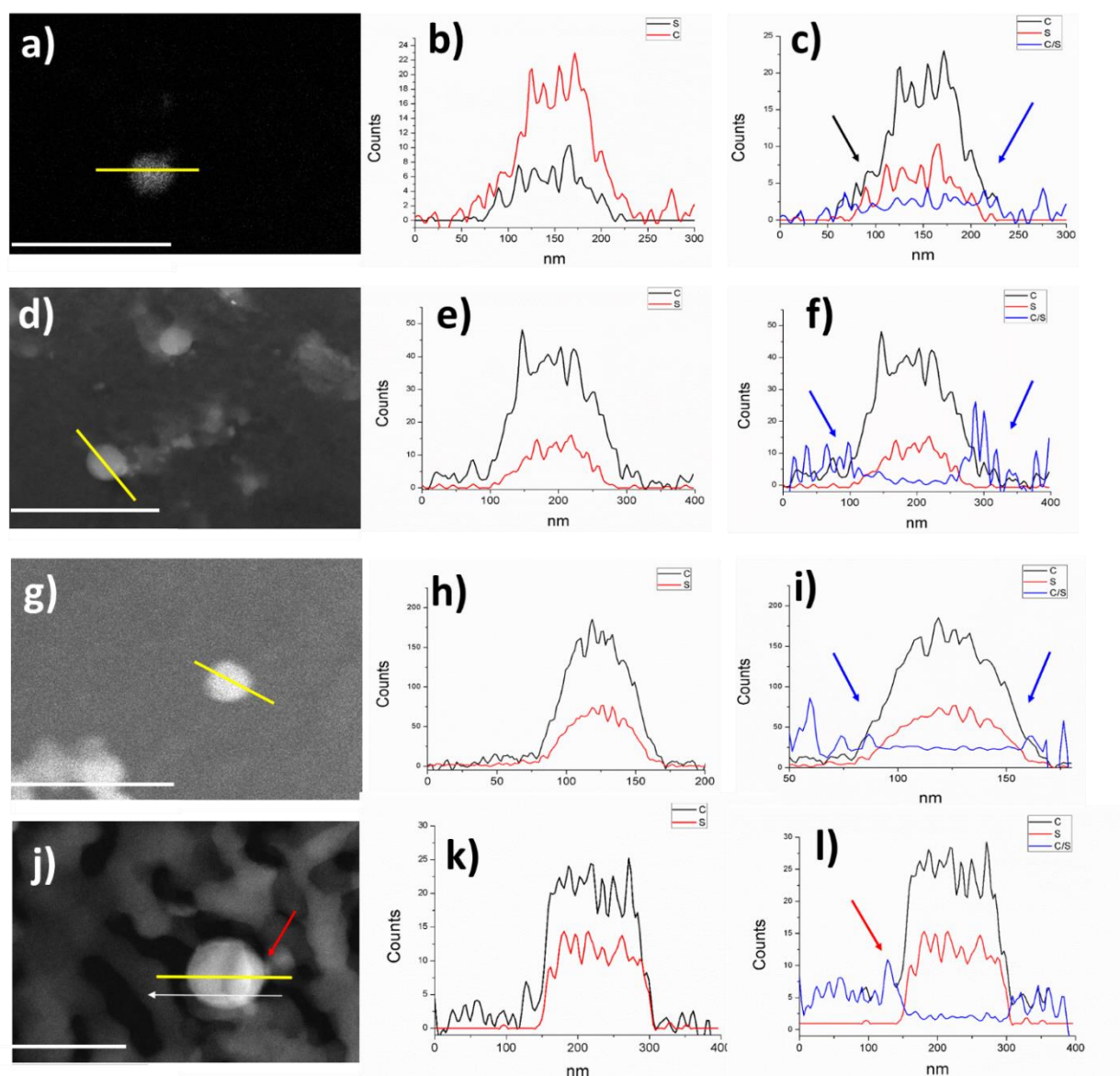


Figure 2.30 a) STEM image of BCP2 WPNP sample; the yellow line shows the position of the line scan analysis (bar 400 nm); b) line scan elemental profile in the BCP2 WPNP: black line is carbon, red line is sulfur; c) the blue line is the carbon/sulfur atomic ratio in the BCP2 WPNP; blue arrows indicate that the C/S ratio is higher on the edge of the NPs. d) STEM image of BCP5 sample; the yellow line shows the position of the line scan analysis (bar 600 nm); e) line scan elemental profile in the BCP5 WPNP: black line is carbon, red line is sulfur; f) the blue line is the carbon/sulfur atomic ratio in the BCP5 WPNP; blue arrows indicate that the C/S ratio is higher on the edge of the NPs. g) STEM image of BCP15 sample (bar 300 nm); the yellow line the position of the line scan analysis; h) line scan elemental profile in the BCP15 WPNP: black line is carbon, red line is sulfur; i) the blue line is the carbon/sulfur atomic ratio in the BCP15 WPNP; blue arrows indicate that the C/S ratio is higher on the edge of the NPs. j) STEM image of BCP100 sample; the yellow line shows the position of the line scan analysis, the white arrow indicates the direction of the scan and the red arrow the carbon aggregation on the WPNP surface (bar 300 nm); k) line scan elemental profile in the BCP100 WPNP: black line is carbon, red line is sulfur; l) the blue line is the carbon/sulfur atomic ratio in the BCP100 WPNP; red arrow indicates where the C/S ratio is higher corresponding to the carbon aggregation on the edge of the WPNP analyzed. Reported with permission from Elsevier from ref [14].

Synthesis of bWPNNPs. In a typical experiment, PC₆₁BM and BCP were dissolved into chloroform to achieve two starting solutions with standard concentrations, 25 mg ml⁻¹ and 10 mg ml⁻¹, respectively. A proper quantity of each starting organic solution was mixed up to obtain a blend organic solution with a ratio of PC₆₁BM:BCP = 3:1. Therefore, 200 μ l of the blend organic solution was sonicated, warmed at 40 °C, and slowly poured under vigorous stirring into 1 ml of pure MilliQ water, preheated at 40 °C. After 1 hour the macroemulsion was sonicated for 10 minutes at 40 °C in an ultrasonic bath to obtain a stable miniemulsion, which was heated up to 70 °C under gentle stirring to completely remove the chloroform. Finally, a brown-greenish stable aqueous suspension of bWPNNPs was gained with a concentration of 2.4 mg ml⁻¹. All steps of the preparation were performed under air.

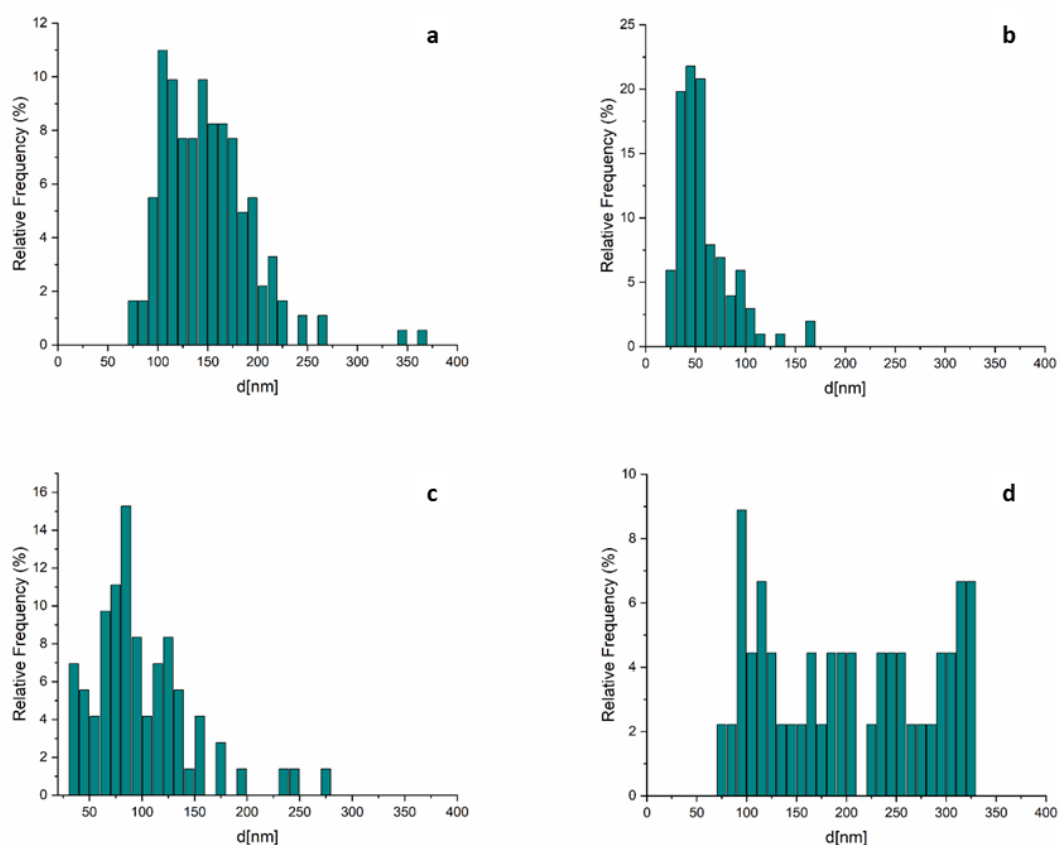


Figure 2.31 Size distribution of the **a)** BCP2 bWPNNPs **b)** BCP5 bWPNNPs **c)** BCP15 bWPNNPs **d)** BCP100 bWPNNPs. Adapted from reference [16].

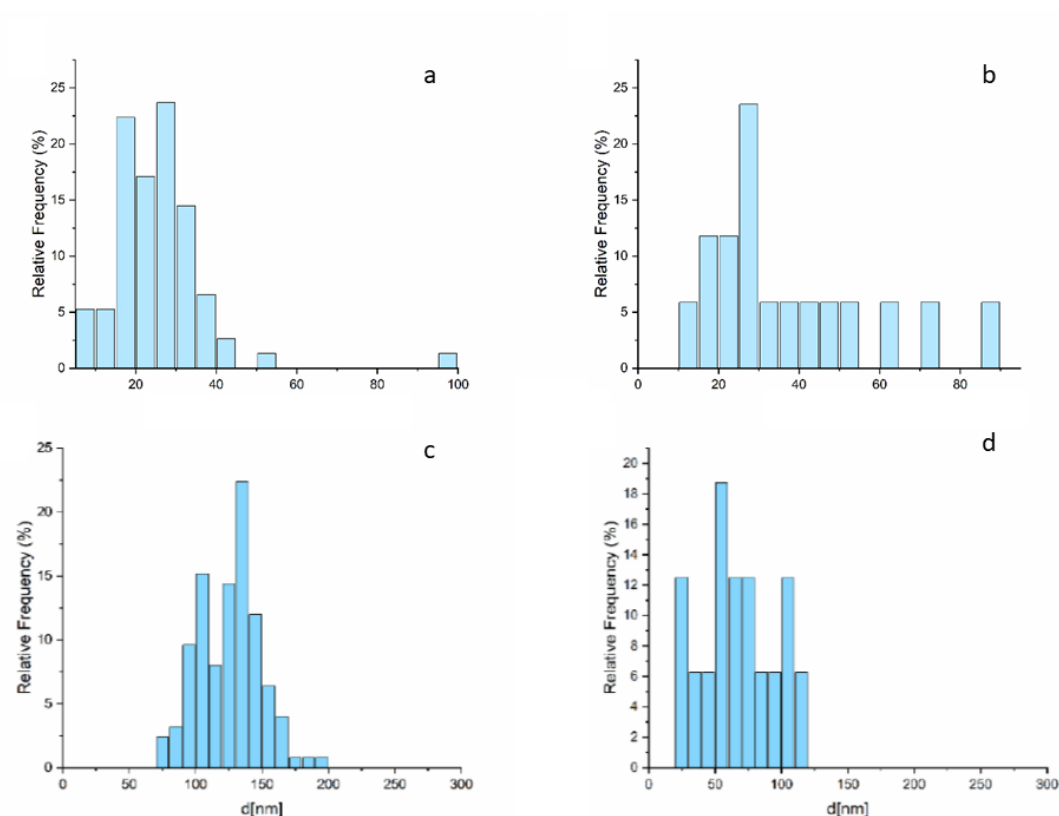


Figure 2.32 Size distribution of the shell thickness measured for the **a)** BCP2 bWPNPs and **b)** BCP15 bWPNPs. Size distribution of the PC₆₁BM rich cores measured for the **c)** BCP2 bWPNPs and **d)** BCP15 bWPNPs. Adapted from reference [16].

2.4.4 WPNP-based device fabrication

Patterned ITO substrates were purchased from Atsugi Micro. The ITO substrates were cleaned using standard procedure by sequential ultrasonication in acetone, detergent, ultrapure water, isopropanol and hot isopropanol. After exposure to ultraviolet ozone (UV-O₃) treatment for 5 minutes, the substrates were coated with PEDOT:PSS by spin-coating at 5000 rpm for 30 seconds, followed by annealing at 150 °C for 20 minutes, and the PC₆₁BM:BCP WPNP suspension was spin-coated onto UV-O₃ treated ITO/PEDOT:PSS substrates at 500 rpm for 90 seconds. The samples were then dried at 60 °C for 30 minutes in air prior to spin-coating a PC₆₁BM solution (10 mg ml⁻¹ in dichloromethane) at 4000 rpm for 10 seconds on top of the multilayer. After drying the active layer at 90 °C for 20 minutes, the substrates were placed in a high vacuum overnight prior to the sequential thermal evaporation of bathocuproine (10 nm) and Ag (65 nm) to finalize the devices. The device area, defined by the cross-section of the ITO and Ag electrodes, was of 0.02 cm².

2.5 References

- [1] D. Darwis, N. Holmes, D. Elkington, A.L. David Kilcoyne, G. Bryant, X. Zhou, P. Dastoor, W. Belcher, Surfactant-free nanoparticulate organic photovoltaics, *Solar Energy Materials and Solar Cells* 121 (2014) 99-107.
- [2] K.B. Burke, A.J. Stapleton, B. Vaughan, X.J. Zhou, A.L.D. Kilcoyne, W.J. Belcher, P.C. Dastoor, Scanning transmission x-ray microscopy of polymer nanoparticles: probing morphology on sub-10 nm length scales, *NANOTECHNOLOGY* 22(26) (2011).
- [3] J.J. Richards, C.L. Whittle, G.Z. Shao, L.D. Pozzo, Correlating Structure and Photocurrent for Composite Semiconducting Nanoparticles with Contrast Variation Small-Angle Neutron Scattering and Photoconductive Atomic Force Microscopy, *ACS NANO* 8(5) (2014) 4313-4324.
- [4] A. Holmes, E. Deniau, C. Lartigau-Dagron, A. Bousquet, S. Chambon, N.P. Holmes, Review of Waterborne Organic Semiconductor Colloids for Photovoltaics, (2021).
- [5] J.A. Osaheni, S.A. Jenekhe, ELECTROACTIVE AND PHOTOACTIVE ROD-COIL COPOLYMERS - DESIGN, SYNTHESIS, AND SUPRAMOLECULAR REGULATION OF PHOTOPHYSICAL PROPERTIES, *JOURNAL OF THE AMERICAN CHEMICAL SOCIETY* 117(28) (1995) 7389-7398.
- [6] M. Sommer, A.S. Lang, M. Thelakkat, Crystalline-crystalline donor-acceptor block copolymers, *Angewandte Chemie - International Edition* 47(41) (2008) 7901-7904.
- [7] J. Peet, M.L. Senatore, A.J. Heeger, G.C. Bazan, The Role of Processing in the Fabrication and Optimization of Plastic Solar Cells, *ADVANCED MATERIALS* 21(14-15) (2009) 1521-1527.
- [8] R.A. Segalman, B. McCulloch, S. Kirmayer, J.J. Urban, Block Copolymers for Organic Optoelectronics, *MACROMOLECULES* 42(23) (2009) 9205-9216.
- [9] M. He, F. Qiu, Z.Q. Lin, Conjugated rod-coil and rod-rod block copolymers for photovoltaic applications, *JOURNAL OF MATERIALS CHEMISTRY* 21(43) (2011) 17039-17048.
- [10] B.D. Olsen, R.A. Segalman, Self-assembly of rod-coil block copolymers, *Materials Science and Engineering: R: Reports* 62(2) (2008) 37-66.
- [11] S. Zappia, R. Mendichi, S. Battiato, G. Scavia, R. Mastria, F. Samperi, S. Destri, Characterization of amphiphilic block-copolymers constituted of a low band gap rigid segment (PCPDTBT) and P4VP based coil block synthesized by two different strategies, *Polymer* 80 (2015) 245-258.
- [12] S. Zappia, A.E. Di Mauro, R. Mastria, A. Rizzo, M.L. Curri, M. Striccoli, S. Destri, Rod-coil block copolymer as nanostructuring compatibilizer for efficient CdSe NCs/PCPDTBT hybrid solar cells, *European Polymer Journal* 78 (2016) 352-363.
- [13] A.E. Di Mauro, M. Toscanini, D. Piovani, F. Samperi, M.L. Curri, M. Corricelli, L. De Caro, D. Siliqi, R. Comparelli, A. Agostiano, S. Destri, M. Striccoli, Segmented poly(styrene-co-vinylpyridine) as multivalent host for CdSe nanocrystal based nanocomposites, *European Polymer Journal* 60 (2014) 222-234.
- [14] A.M. Ferretti, S. Zappia, G. Scavia, U. Giovanella, F. Villafiorita-Monteleone, S. Destri, Surfactant-free miniemulsion approach for low band gap rod-coil block copolymer water-processable nanoparticle fabrication: Film preparation and morphological characterization, *Polymer* 174 (2019) 61-69.
- [15] S. Zappia, G. Scavia, A.M. Ferretti, U. Giovanella, V. Vohra, S. Destri, Water-Processable Amphiphilic Low Band Gap Block Copolymer: Fullerene Blend Nanoparticles as Alternative Sustainable Approach for Organic Solar Cells, *Advanced Sustainable Systems* 2(3) (2018) 10.
- [16] A.M. Ferretti, M. Diterlizzi, W. Porzio, U. Giovanella, L. Ganzer, T. Virgili, V. Vohra, E. Arias, I. Moggio, G. Scavia, S. Destri, S. Zappia, Rod-Coil Block Copolymer: Fullerene Blend Water-Processable Nanoparticles: How Molecular Structure Addresses Morphology and Efficiency in NP-OPVs, *Nanomaterials* 12(1) (2022).
- [17] L. Ganzer, S. Zappia, M. Russo, A.M. Ferretti, V. Vohra, M. Diterlizzi, M.R. Antognazza, S. Destri, T. Virgili, Ultrafast spectroscopy on water-processable PCBM: rod-coil block copolymer nanoparticles, *Physical Chemistry Chemical Physics* 22(45) (2020) 26583-26591.

- [18] P.D. Topham, A.J. Parnell, R.C. Hiorns, Block copolymer strategies for solar cell technology, *Journal of Polymer Science Part B: Polymer Physics* 49(16) (2011) 1131-1156.
- [19] D. Benoit, V. Chaplinski, R. Braslau, C.J. Hawker, Development of a universal alkoxyamine for "living" free radical polymerizations, *JOURNAL OF THE AMERICAN CHEMICAL SOCIETY* 121(16) (1999) 3904-3920.
- [20] W.A. Braunecker, K. Matyjaszewski, Controlled/living radical polymerization: Features, developments, and perspectives, *Progress in Polymer Science* 32(1) (2007) 93-146.
- [21] R.H. Lohwasser, M. Thelakkat, Synthesis of Amphiphilic Rod-Coil P3HT-b-P4VP Carrying a Long Conjugated Block Using NMRP and Click Chemistry, *Macromolecules* 45(7) (2012) 3070-3077.
- [22] K. Landfester, R. Montenegro, U. Scherf, R. Güntner, U. Asawapirom, S. Patil, D. Neher, T. Kietzke, Semiconducting polymer nanospheres in aqueous dispersion prepared by a miniemulsion process, *Advanced Materials* 14(9) (2002) 651-655.
- [23] D. Muhlbacher, M. Scharber, M. Morana, Z.G. Zhu, D. Waller, R. Gaudiana, C. Brabec, High photovoltaic performance of a low-bandgap polymer, *ADVANCED MATERIALS* 18(21) (2006) 2884-+.
- [24] M. Morana, M. Wegscheider, A. Bonanni, N. Kopidakis, S. Shaheen, M. Scharber, Z. Zhu, D. Waller, R. Gaudiana, C. Brabec, Bipolar Charge Transport in PCPDTBT-PCBM Bulk-Heterojunctions for Photovoltaic Applications, *Advanced Functional Materials* 18(12) (2008) 1757-1766.
- [25] M. Bag, T.S. Gehan, L.A. Renna, D.D. Algaier, P.M. Lahti, D. Venkataraman, Fabrication conditions for efficient organic photovoltaic cells from aqueous dispersions of nanoparticles, *RSC Advances* 4(85) (2014) 45325-45331.
- [26] O. Dyck, S. Hu, S. Das, J. Keum, K. Xiao, B. Khomami, G. Duscher, Quantitative Phase Fraction Detection in Organic Photovoltaic Materials through EELS Imaging, *Polymers* 7(11) (2015).
- [27] L.F. Drummy, R.J. Davis, D.L. Moore, M. Durstock, R.A. Vaia, J.W.P. Hsu, Molecular-Scale and Nanoscale Morphology of P3HT:PCBM Bulk Heterojunctions: Energy-Filtered TEM and Low-Dose HREM, *Chemistry of Materials* 23(3) (2011) 907-912.
- [28] E.B.L. Pedersen, M.C. Pedersen, S.B. Simonsen, R.G. Brandt, A.P.L. Böttiger, T.R. Andersen, W. Jiang, Z.Y. Xie, F.C. Krebs, L. Arleth, J.W. Andreasen, Structure and crystallinity of water dispersible photoactive nanoparticles for organic solar cells, *Journal of Materials Chemistry A* 3(33) (2015) 17022-17031.
- [29] T. Virgili, G. Grancini, E. Molotokaite, I. Suarez-Lopez, S.K. Rajendran, A. Liscio, V. Palermo, G. Lanzani, D. Polli, G. Cerullo, Confocal ultrafast pump-probe spectroscopy: a new technique to explore nanoscale composites, *Nanoscale* 4(7) (2012) 2219-2226.
- [30] M. Scarongella, J. De Jonghe-Risse, E. Buchaca-Domingo, M. Causa', Z. Fei, M. Heeney, J.-E. Moser, N. Stingelin, N. Banerji, A Close Look at Charge Generation in Polymer:Fullerene Blends with Microstructure Control, *Journal of the American Chemical Society* 137(8) (2015) 2908-2918.
- [31] B. Jana, A. Ghosh, A. Patra, Photon Harvesting in Conjugated Polymer-Based Functional Nanoparticles, *The Journal of Physical Chemistry Letters* 8(18) (2017) 4608-4620.
- [32] C.R. McNeill, S. Westenhoff, C. Groves, R.H. Friend, N.C. Greenham, Influence of Nanoscale Phase Separation on the Charge Generation Dynamics and Photovoltaic Performance of Conjugated Polymer Blends: Balancing Charge Generation and Separation, *The Journal of Physical Chemistry C* 111(51) (2007) 19153-19160.
- [33] I.A. Howard, R. Mauer, M. Meister, F. Laquai, Effect of Morphology on Ultrafast Free Carrier Generation in Polythiophene:Fullerene Organic Solar Cells, *Journal of the American Chemical Society* 132(42) (2010) 14866-14876.
- [34] F. Di Maria, F. Lodola, E. Zucchetti, F. Benfenati, G. Lanzani, The evolution of artificial light actuators in living systems: from planar to nanostructured interfaces, *Chemical Society Reviews* 47(13) (2018) 4757-4780.

- [35] X. Feng, F. Lv, L. Liu, H. Tang, C. Xing, Q. Yang, S. Wang, Conjugated Polymer Nanoparticles for Drug Delivery and Imaging, *ACS Applied Materials & Interfaces* 2(8) (2010) 2429-2435.
- [36] T. Finkel, N.J. Holbrook, Oxidants, oxidative stress and the biology of ageing, *Nature* 408(6809) (2000) 239-247.
- [37] J.L. Martindale, N.J. Holbrook, Cellular response to oxidative stress: Signaling for suicide and survival*, *Journal of Cellular Physiology* 192(1) (2002) 1-15.
- [38] B. Alberts, *Molecular biology of the cells*, Sixth edition, Garland Science, Taylor and Francis Group, New York, 2015.
- [39] J. Kettle, M. Horie, L.A. Majewski, B.R. Saunders, S. Tuladhar, J. Nelson, M.L. Turner, Optimisation of PCPDTBT solar cells using polymer synthesis with Suzuki coupling, *SOLAR ENERGY MATERIALS AND SOLAR CELLS* 95(8) (2011) 2186-2193.

Chapter 3

Production of aqueous inks made from amphiphilic PTB7-based rod-coil block copolymer for organic solar cells: a case study

*The content of this chapter is reported into one paper: **Marianna Diterlizzi**, Anna Maria Ferretti, Guido Scavia, Roberto Sorrentino, Silvia Luzzati, Antonella Boccia, Riccardo Po, Eleonora Quadrivi, Stefania Zappia, Silvia Destri, “Amphiphilic PTB7-based rod-coil block copolymer for water-processable nanoparticles as active layer for sustainable organic photovoltaic: a case study” **Polymers** **2022**, **14**, **1588**, <https://doi.org/10.3390/polym14081588>, and presented at subsequent development levels at three congresses: Macrogiovani 2019, Napoli, 1-2.07.2019 (oral communication); CIS2019 (Chemistry Meets Industry and Society), Salerno, 28-30.08.2019 (poster contribution); Nanoday IV, Milano, 11-14.12.2019 (poster contribution); ENERCHEM_2, Padova, 12-14.02.2020 (poster contribution) and to the International School of Chemistry (organized by SCI), 1-6.09.2020 (book of Abstracts).*

3.1 Introduction

In the previous chapter I described how my research group obtained organic photovoltaic (OPV) devices fabricated from polymer aqueous inks.[1] The water processable nanoparticles (WPNPs) were prepared through an adapted miniemulsion approach,[2] using a blend of phenyl-C₆₁-butyric acid methyl ester (PC₆₁BM) and an amphiphilic rod-coil block copolymer (BCP), bearing the semiconducting polymer poly[2,6-(4,4-bis-(2-ethylhexyl)-4*H*-cyclopenta[2,1-*b*;3,4-*b'*]dithiophene)-*alt*-4,7(2,1,3-benzothiadiazole)] (PCPDTBT) as rigid polymer, and a tailored poly(4-vinylpyridine) (P4VP)-based segment as coil. The hydrophilic flexible block acts as surfactant, interacting with water and ensuring the colloidal stability of the aqueous suspension, without the requirement of any additional emulsifying agent. Noticeably, using the coil with length of 5 repeating units of 4VP, namely the BCP5, Zappia *et al.* gained an organic solar cell (OSC) with a power conversion efficiency (PCE) of ~2.5%, which is quite comparable with the efficiency of the devices obtained by deposition from halogenated solvents.[3]

In this chapter our attempt to further implement the effectiveness of our approach by synthesizing new amphiphilic BCPs will be discussed. Particularly, we chose to investigate BCPs characterized by a rod block consisting in a polymer with a higher degree of crystallinity. Indeed, it is reported in literature that a higher polymer crystallinity generally leads to better charge transport properties,[4, 5] and thus to enhanced performances of the OPV device. Therefore, we selected the low band gap (LBG) poly[[4,8-bis[(2-ethylhexyl)oxy]benzo[1,2-*b*:4,5-*b'*]dithiophene-2,6-diyl][3-fluoro-2-[(2-ethylhexyl)carbonyl]thieno[3,4-*b*]thiophenediyl]] (PTB7) as electron-donor material. PTB7 is semicrystalline and it is stiffer than PCPDTBT.[6] Moreover, this LBG polymer is well known in the OPV field as it leads to efficiencies up to 7% when blended with phenyl-C₇₁-butyric acid methyl ester (PC₇₁BM).[7-9]

On the other hand, the segment of P4VP used as coil in this chapter is tailored to be made up of around 15 repeating units on the base of the results found for the previous LBG polymer.[1] In addition to this structural consideration, in designing the rod-coil PTB7-*b*-P4VP, we took into account the process feasibility, as to obtain a shorter coil a *Chain-Growth like* approach is needed, that means a harder synthetic procedure. In fact, it involves the synthesis of a very rigid macroinitiator, and the subsequent radical controlled polymerization of the 4VP which becomes more difficult as the macroinitiator PTB7 hindrance is increased with respect to the PCPDTBT one.[10] What is more, it was

demonstrated that by increasing the length of the alkyl tail of the surfactant the packing of the polymer in the resulting nanoparticles (NPs) becomes better, improving the charge mobility in the final active layer.[11] Thus, the rod-coil PTB7-*b*-P4VP was synthesized through the *Step-Growth like* approach, and it was deeply characterized with UV-Visible (UV-Vis), photoluminescence (PL), and Fourier transform infrared (FTIR) spectroscopies, proton nuclear magnetic resonance ($^1\text{H-NMR}$) spectroscopy, bidimensional NMR (2D-NMR), size exclusion chromatography (SEC), matrix assisted laser desorption/ionization time of flight mass spectroscopy (MALDI-TOF MS), differential scanning calorimetry (DSC), and contact angles and surface energy were measured. Furthermore, we investigated its ability to form WPNPs in blend with PC₇₁BM, and the achieved suspensions were analyzed through dynamic light scattering (DLS) and transmission electron microscopy (TEM). The collected TEM images revealed a Janus-like WPNP morphology, which prompts the exciton splitting, and the free charge generation and collection.[12] Finally, achieved aqueous inks were employed to realize WPNP-based films, studied with atomic force microscopy (AFM) and grazing-incidence wide-angle X-ray scattering (GIWAXS), which were subsequently tested as active layer in sustainable OSCs, in which the photovoltaic activity was guaranteed by the combination of PTB7 as donor material with PC₇₁BM as acceptor material. We reached a PCE of 0.85%, which is still very far from the benchmark, but it is higher than the efficiency obtained depositing the same designed rod-coil from chlorinated solvents. This result was ascribed to the P4VP, and thus we tried to reduce the overall quantity of P4VP in the active layer by adding a certain amount of unbound PTB7. Furthermore, we attempted the same approach with another PTB7-base BCP, bearing a thiophene endowed with an ester group of an alcohol with polar moieties as coil. However, even these attempts did not lead to any progress in the photovoltaic parameters of OSCs.

3.2 Aqueous inks based on the amphiphilic rod-coil PTB7-*b*-P4VP

3.2.1 Results and Discussion

3.2.1.1 Synthesis and Characterization of the macromer PTB7

The rigid block, constituted by the LBG polymer poly[[4,8-bis[(2-ethylhexyl)oxy]benzo[1,2-*b*:4,5-*b'*]dithiophene-2,6-diyl][3-fluoro-2-[(2-ethylhexyl)carbonyl]thieno[3,4-*b*]thiophenediyl]] (PTB7), was obtained through a Stille coupling (**Scheme 3.1**) between the electron-rich monomer 4,8-bis[(2-ethylhexyl)oxy]-2,6-bis(trimethylstannyl)benzo[1,2-*b*:4,5-*b'*]dithiophene (hereafter BDTOEHSn) (**1**) and the electron-poor 2-ethylhexyl 4,6-dibromo-3-fluorothieno[3,4-*b*]thiophene-2-carboxylate (FTThBr) (**2**),^[13] using the complex Pd₂(dba)₃/P(*o*-tol)₃ as catalytic system. The achieved macromer PTB7 was fully characterized from molecular, thermal, and spectroscopic points of view. The ¹H-NMR spectrum (**Figure 3.4**) and the FTIR one (**Figure 3.3a**) are in agreement with the data reported in literature.^[13-15] What is more, the numerical molecular weight (M_n) and weighted molecular weight (M_w) values are 14380 g mol⁻¹ and 56350 g mol⁻¹, respectively, determined by SEC, and corresponding to about 13-15 repeating units. The M_n value was confirmed by MALDI-TOF MS analysis carried out by Dr. Filippo Samperi (IPCB-CNR, Catania) using as a matrix 2-methyl-2-propenylidene]malononitrile (DCTB). Determination of the ending groups carried out through MALDI analysis (**Figure 3.1**) could not identify all the stannyl derivatives of PTB7 growing chains because their hydrolysis during the waiting time. However, hydroxyl derivatives and some chain containing tin could be recognized. It is important to remark that these analyses were performed on non-extracted sample. Indeed, the macromer cannot be extracted before the coil attachment because reactive stannyl end-groups must remain there without being exposed to air. Therefore, we settled for such a relatively low molecular weight to reach a satisfying compromise between the rod length and its polydispersity (PDI=M_w/M_n) value. As a matter of fact, a narrow PDI is required to have homogeneous aqueous suspensions. Furthermore, the polymer should not be too long to have NPs with dimensions suitable for the OPV active layer deposition.

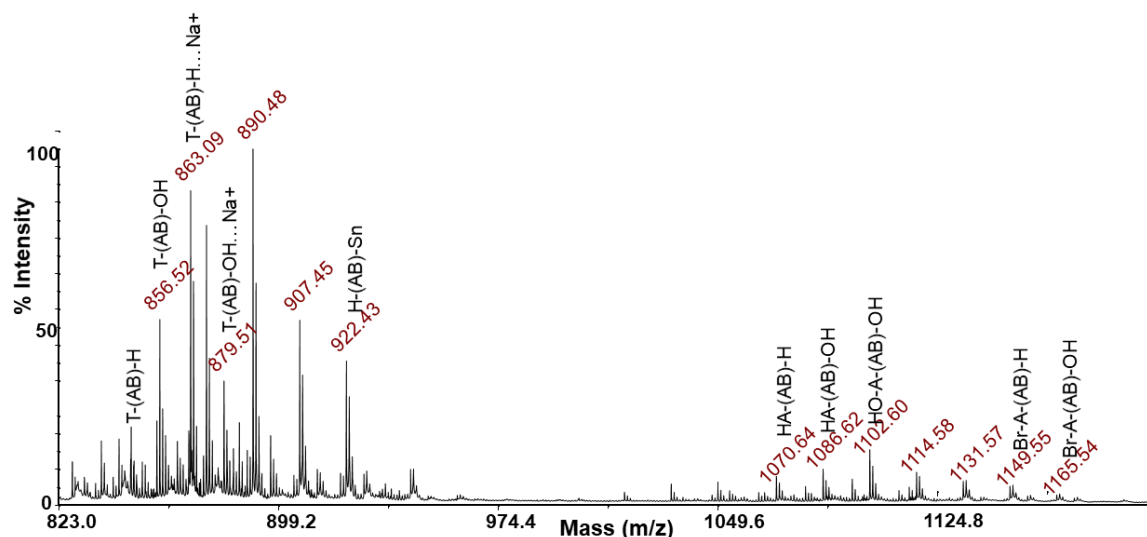
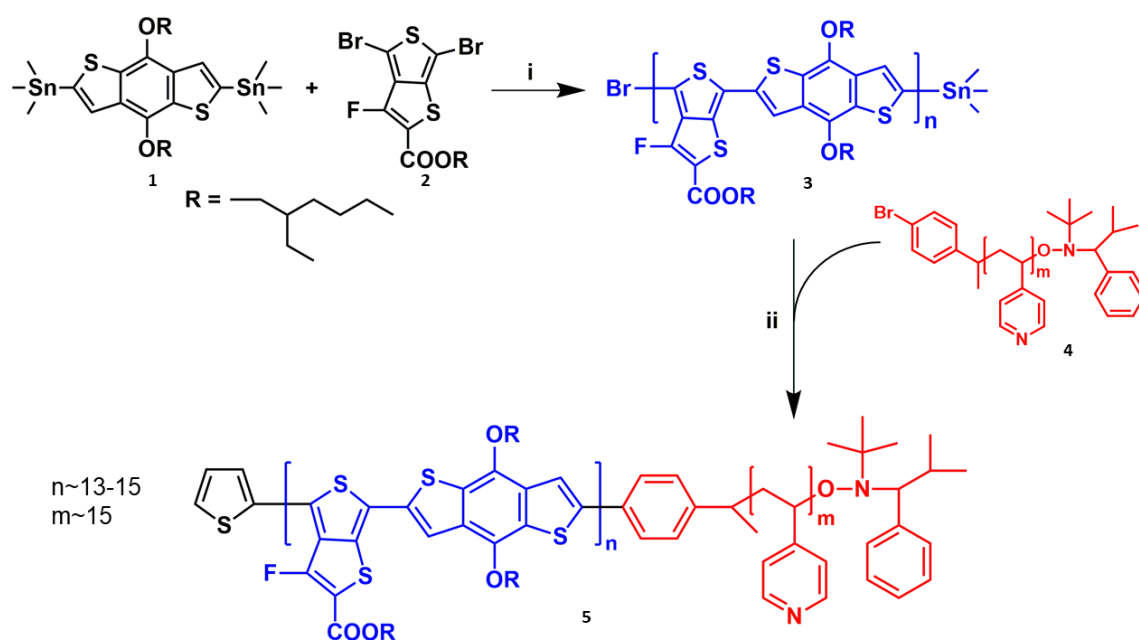


Figure 3.1 Enlarged section of the positive ions MALDI-TOF mass spectrum of the macromer PTB7 sample recorded in reflectron mode using DCTB as matrix. Br-A-(AB)-H and Br-A-(AB)-OH species are detected, denoting direct arylation reaction occurrence.

3.2.1.2 Synthesis and Characterization of the rod-coil PTB7-*b*-P4VP

The PTB7-*b*-P4VP was obtained using a *Step Growth-like* approach, namely synthesizing the two individual polymeric blocks properly functionalized to covalently react.[10] The segment of P4VP (**4**) was achieved through nitroxide mediated radical polymerization (NMRP) using a bromo derivative of the radical TIPNO as mediator, as reported in literature.[16] The coil length was confirmed by $^1\text{H-NMR}$ analysis, in agreement with the molecular weight determined by SEC, even if the found out repeating unit number should be considered as an average value. The P4VP segment was linked to the previously synthesized macromer through a Stille coupling (**Scheme 3.1**), and the resulting PTB7-*b*-P4VP (**5**) was fully characterized, from molecular, thermal, and spectroscopic points of view, and compared with the two individual blocks. All the characterizations were preceded by a careful material cleaning through reprecipitations in methanol and hexane, and extractions in a Soxhlet apparatus with different solvents to remove all the unlinked P4VP and some of the unbonded macromer PTB7.



Scheme 3.1 Synthetic route for **i**) the macromer PTB7 and **ii**) the PTB7-*b*-P4VP. Reaction conditions: i) Pd₂(dba)₃, P(*o*-tol)₃, 120 °C, 24 h; ii) Pd₂(dba)₃, P(*o*-tol)₃, 120 °C, 24 h.

The UV-Vis absorption and the PL properties of the PTB7-*b*-P4VP were compared with a previously homemade PTB7 ($M_n=9470$, $M_w=31540$, $M_w/M_n=3.3$). In the UV-Vis spectra depicted in **Figure 3.2a,b** it is possible to notice that the PTB7-*b*-P4VP retains the PTB7 shape,^[13, 17] showing a broad absorption band with a maximum at ~600 nm typical of PTB7. However, the peak of the rod-coil is slightly displaced towards shorter wavelengths. This blue-shift is less evident in the solid-state absorption spectrum, while in the on-glass normalized PL spectrum a red shift of the peaks of the rod-coil with respect to the PTB7 one was observed (**Figure 3.2b** and **c**). Specifically, PL spectra, obtained exciting samples at 380 nm, reveal a partially quenched emission at ~879 nm in the rod-coil with respect to the macromer, which also shifts to ~884 nm, and the peak at ~703 nm moves to ~710 nm. The blue shift in the absorption spectrum is due to the different molecular weights of the samples. The features evidenced in solid state absorption and PL spectra could be correlated to the added coil moiety that could act, for example, as a fluorescence quencher, reducing PL emission. On the other hand, the red-shift might be signatures of more H-aggregate behavior of the PTB7-*b*-P4VP, and of a π -packing of PTB7 chains improved by the coil. The different attitude of the PTB7-*b*-P4VP compared to the macromer PTB7 also emerged in FTIR and NMR analysis. Indeed, FTIR spectrum of PTB7-*b*-P4VP includes altered and additional peaks due to the coil block (**Figure 3.3**);^[16] in particular, signals between 1400 and 1500 cm⁻¹ become more extended because in this area there are P4VP contributes at

1558 cm^{-1} and 1417 cm^{-1} , assigned to C=C and C=N vibrations, and at 1597 cm^{-1} and 1493 cm^{-1} , ascribable to the C=C modes of the aromatic rings, which overlap with PTB7 signals. In addition, at $\sim 800 \text{ cm}^{-1}$ a signal due to C-H vibrations of P4VP is distinguished.

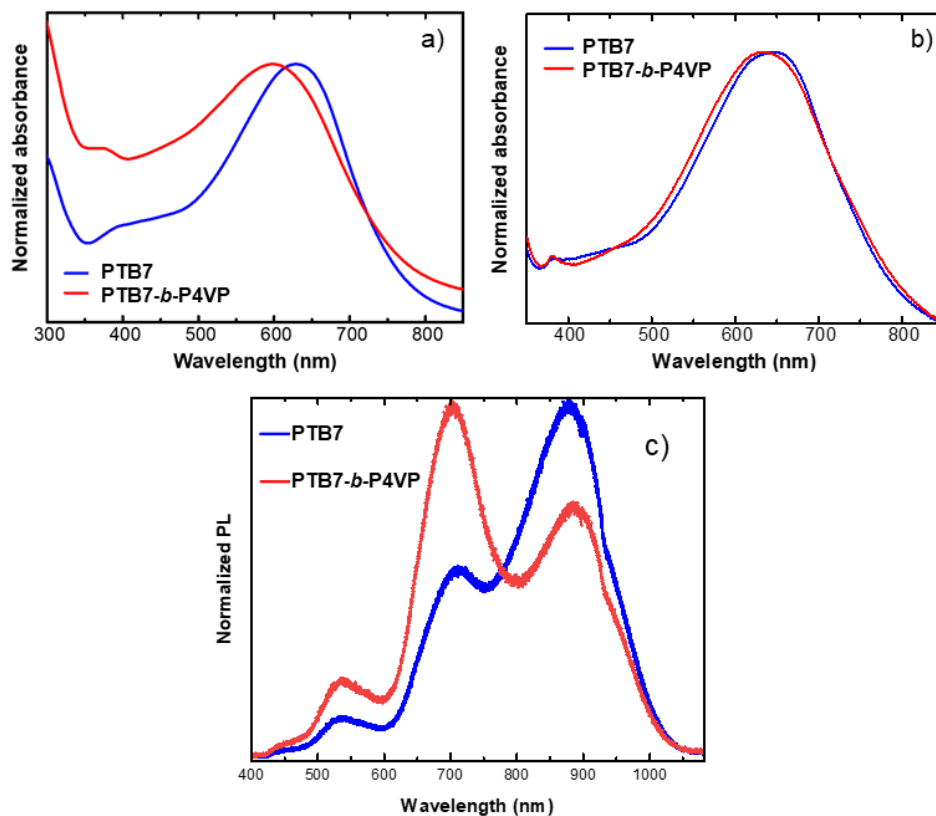


Figure 3.2 Comparison between **a)** the normalized absorption spectra of the homemade PTB7 and the PTB7-*b*-P4VP dissolved in chloroform; **b)** the normalized absorption spectra of the homemade PTB7 and the PTB7-*b*-P4VP on glass substrate and **c)** normalized PL spectra of the homemade PTB7 and the PTB7-*b*-P4VP on glass substrate exciting at 380 nm. PL measurements were performed by Dr. Laura Ciammaruchi (ENI, Novara).

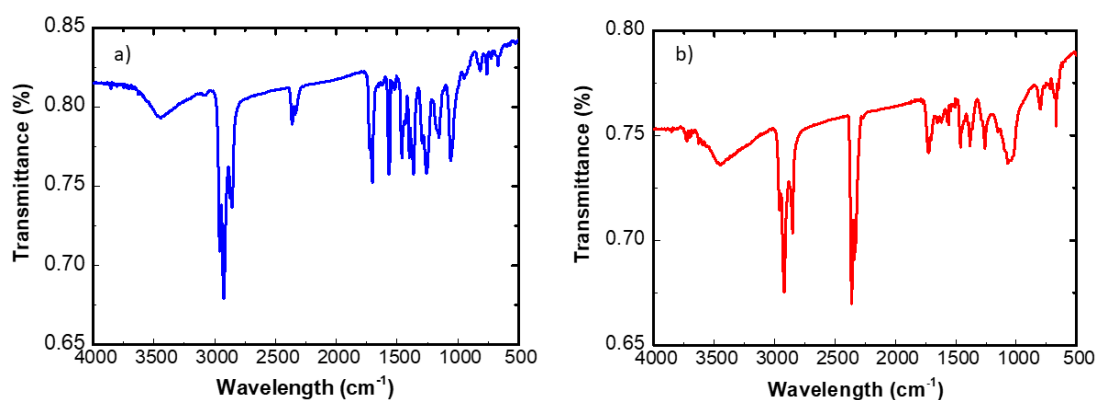


Figure 3.3 FTIR spectra of **a)** the macromer PTB7 and **b)** the rod-coil PTB7-*b*-P4VP.

In **Figure 3.4** $^1\text{H-NMR}$ spectra of the macromer PTB7 and of the PTB7-*b*-P4VP are depicted. As reported above, the signals related to the macromer PTB7 are in agreement with the spectrum described in literature,[13-15] while the PTB7-*b*-P4VP one presents some differences. Indeed, as we can observe in the insertion corresponding to the enlarged aromatic region, there are several differences marked by green arrows, ascribed to the presence of the coil segment and TIPNO. Particularly, a new broadened peak appears at 6.58 ppm while the signals in the range 7.00-7.20 ppm, and 7.55-7.70 ppm appear with modified shape and intensity. This remark evidences the actual presence of the coil block into the analyzed sample, but to demonstrate the effective coupling with the rod, we needed to entrust in other techniques. Specifically, two 2D-NMR experiments contributed in a synergistic way to provide additional clues about the formation of the PTB7-*b*-P4VP. Namely, diffusion ordered spectroscopy (DOSY) and total correlation spectroscopy (TOCSY) experiments were performed by Dr. Antonella Boccia (SCITEC-CNR, Milano). The former technique allows to resolve a mixture of compounds basing on their diffusion coefficients that are dependent on the size and shape of the molecules. DOSY experiments are generally used to analyze mixtures of small molecules and the oligomeric state of biomolecules, but recent studies reported their exploitation also for the polymer investigation.[18] Further discussion on the technique can be found in the Appendix. The DOSY spectrum of the PTB7-*b*-P4VP (**Figure 3.5a**) shows distinct signals associated to aliphatic fragments, which diffuse together, reinforcing the hypothesis that the two blocks are covalently bounded. The latter technique highlights the correlations between all protons within a given spin system. In **Figure 3.5b,c** two portions of TOCSY spectrum of the PTB7-*b*-P4VP are displayed and signals due to typical phenyl correlation are indicated by red narrows, while other signals ascribable to the aromatic protons adjacent to N-atom of the 4VP units are circled. Interestingly, the signals are split because the sample is composed of coil segments with lengths slightly different; indeed, as we discussed above, the number of repeating 4VP units must be considered as an average value.

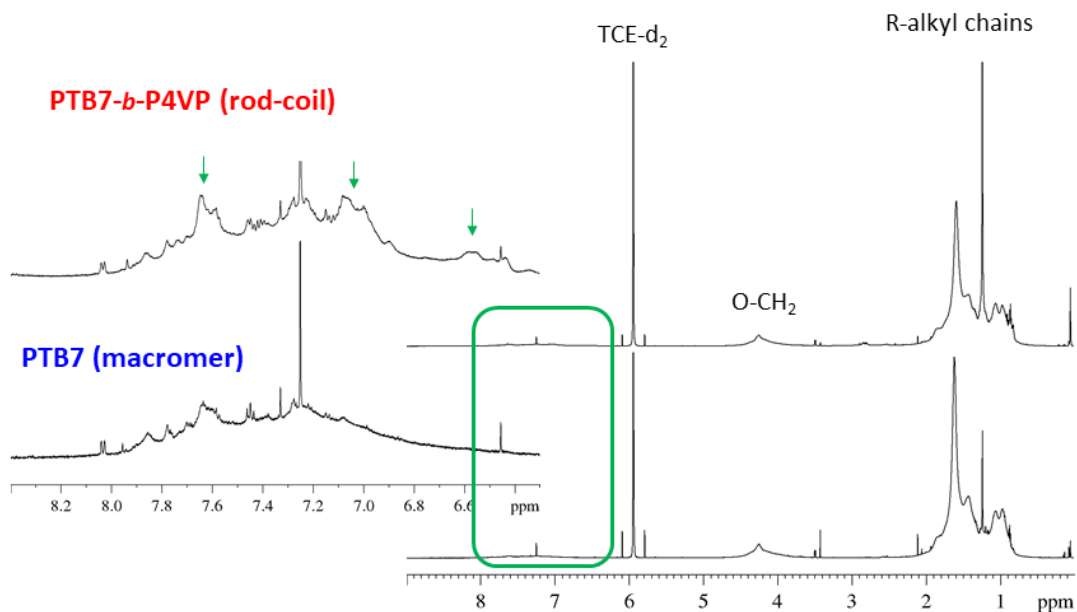


Figure 3.4 ^1H -NMR spectra of the macromer PTB7 (**down**) and of the rod-coil PTB7-*b*-P4VP (**up**) in TCE- d_2 . The most relevant dissimilarities are in the aromatic region. The narrow and well-defined peak at 7.26 ppm is due to chloroform residual in the analyzed sample, not coming from deuterated solvent.

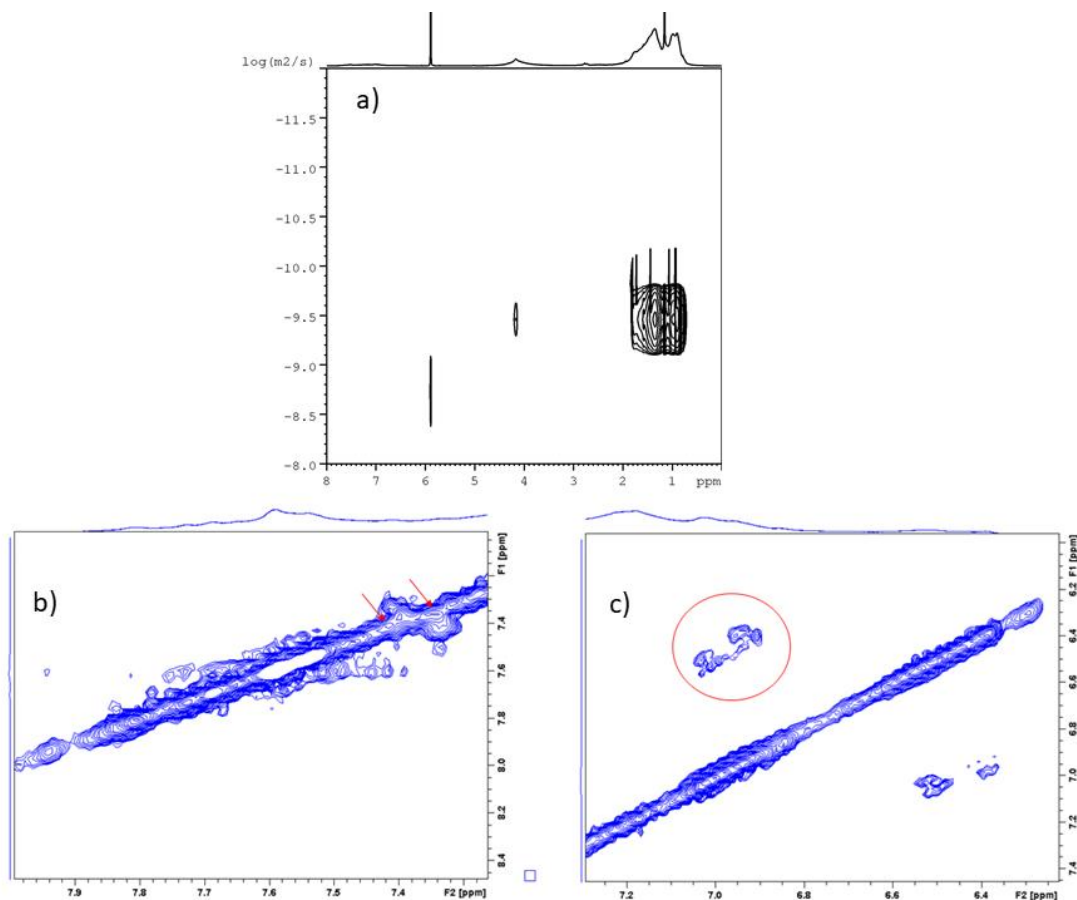


Figure 3.5 a) DOSY spectrum and b,c) sections of TOCSY spectrum of the PTB7-*b*-P4VP.

SEC analyses were carried out by Mendichi's group (SCITEC-CNR, Milano) to determine the block copolymer molecular weight using a differential refractometer (DRI) as concentration detector and a differential viscosimeter (DV) as additional detector. The found-out molecular weight values using the DRI are not absolute but relative to a specific calibration: PTB7-*b*-P4VP and PTB7 molecular weights are relative to polystyrene (PS), and P4VP molecular weight is relative to poly(methyl methacrylate) (PMMA). Because of their different solubility, the samples were characterized using the mixture 80% THF+20% (DMF+ 0.05M LiBr) as mobile phase (see Appendix for further details) for comparing the molecular weight of the macromer PTB7 with that of the PTB7-*b*-P4VP. The main molecular weight distribution (MWD) data are summarized in **Table 3.1**.

Table 3.1 MWD data of the macromer PTB7, the P4VP and the rod-coil PTB7-*b*-P4VP.

Sample	Mobile phase	M_n (g mol ⁻¹)	M_w (g mol ⁻¹)	M_w/M_n
PTB7 (macromer)	80% THF+20% (DMF+0.05M LiBr)	14380	56350	3.92
P4VP (coil)	DMF+0.05M LiBr	1100	1130	1.03
PTB7-<i>b</i>-P4VP (rod-coil)	80%THF+20% (DMF+0.05M LiBr)	15140	62280	4.11

Comparing the data reported in **Table 3.1**, we noticed a difference of ~10% between PTB7 and PTB7-*b*-P4VP molecular weight values. This variation is very small since the segment of P4VP has a low molecular weight, and therefore it negligently contributes to the rod-coil final molecular weight. SEC measurement was performed using a viscosimeter as detector, too. The intrinsic viscosity is an intrinsic measure of the properties of a macromolecule in solution. The intrinsic viscosity as measured from a dilute solution of macromolecules contains information on the macromolecular shape, flexibility, and (for non-spherical particles) molecular weight of macromolecules.[19] The Mark-Houwink-Sakurada (MHS) equation ($[\eta]=kM^a$, where $[\eta]$ is the intrinsic viscosity and a is the MHS coefficient) correlates the intrinsic viscosity with the molecular weight.[20, 21] Therefore, the MHS plot is a decisive tool in evaluating the polymer conformations. Indeed, the comparison between the MHS plots of the macromer PTB7 and the PTB7-*b*-P4VP (**Figure 3.6**) proves a rigid conformation for the macromer and a slightly higher viscosity for the rod-coil. From this comparison it is possible to assume that the rod-coil PTB7-*b*-P4VP conformation is less compact than that of the macromer PTB7 alone. In fact, the difference

between the two plots is ~8% and is due to the coil presence, which interacts better with the mobile phase with respect to the unbound macromer, reducing the aggregation degree.

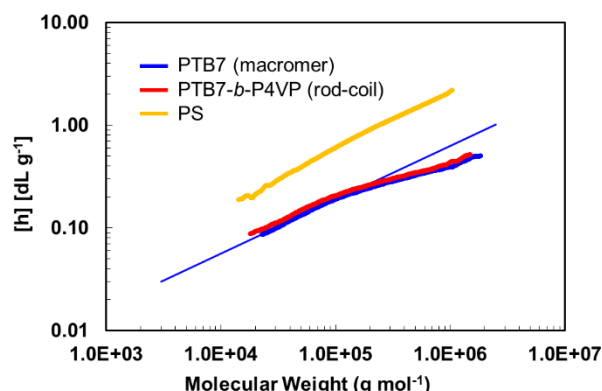


Figure 3.6 MHS plots determined by DV. $[\eta]=kM^a$, where $[\eta]$ is the intrinsic viscosity and a is the MHS coefficient.

Furthermore, DSC was exploited to determine thermal transitions of the PTB7-*b*-P4VP. The experiments were performed by Samperi's group (IPCB-CNR, Catania). The achieved thermogram (**Figure 3.29** in Experimental Section) exhibits two distinct transitions: one at ~120 °C, related to the coil block,[22, 23] and another one at ~170 °C due to the rod segment.[24-26] This evidence represents a clear-cut proof about the actual covalent bond formation between the PTB7 and the P4VP, because the measurement was performed on extracted sample, thus without any not-bounded P4VP segments thank to the accuracy of cleaning procedure.

The formation of the rod-coil also influences the polymeric interactions with substrates. As a matter of fact, contact angle and surface energy measurements on both the macromer PTB7 and the PTB7-*b*-P4VP films revealed some differences, as shown in **Table 3.2**. Contact angles and surface energy measurements were conducted by Dr. Eleonora Quadrivi (ENI, Novara). Contact angles were detected using diiodomethane (DIM) ($\gamma^D = 50.8 \text{ mN m}^{-1}$; $\gamma^P = 0$),[27] and acetonitrile (ACN) ($\gamma^D = 20.8 \text{ mN m}^{-1}$; $\gamma^P = 8.5 \text{ mN m}^{-1}$) as test liquids (**Figure 3.7**).[28] The determined values were used for the calculation of the dispersive and the polar components of the surface energy, according to the Fowkes model.[29] The PTB7 surface energy is 33.1 mN m^{-1} , in accordance with data reported in the literature ($20\text{-}35 \text{ mN m}^{-1}$) for other similar materials with a very low polar contribution, employed for OPV applications.[30-32]

The attachment of the short hydrophilic P4VP block (corresponding to about 10% of variation of M_n , according to SEC data) leads to a slight increase of the polar component

of the surface energy from 0.06 mN m^{-1} to 0.5 mN m^{-1} . The mean values and the standard deviation of the DIM and the ACN contact angles on the macromer PTB7 and the PTB7-*b*-P4VP are summarized in **Table 3.3**.

Table 3.2 Contact angles of DIM and ACN on the macromer PTB7 and the PTB7-*b*-P4VP films, dispersive component (γ^D), polar component (γ^P) and total surface energy (γ) for the two samples.

Sample	$\theta_{\text{DIM}} (^{\circ})$	$\theta_{\text{ACN}} (^{\circ})$	$\gamma^D (\text{mN m}^{-1})$	$\gamma^P (\text{mN m}^{-1})$	$\gamma (\text{mN m}^{-1})$
PTB7 (macromer)	52.2	33.0	33.0	0.06	33.1
PTBT-<i>b</i>-P4VP (rod-coil)	45.4	41.5	36.8	0.5	37.3

Table 3.3 Mean values and standard deviation of DIM and ACN contact angles on the macromer PTB7 and the PTB7-*b*-P4VP films, calculated from about 10 contact angles values.

	PTB7 (macromer)	PTB7-<i>b</i>-P4VP (rod-coil)
DIM [$^{\circ}$]	52.2 ± 0.9	45.4 ± 0.4
ACN [$^{\circ}$]	33.0 ± 0.9	41.5 ± 1.2

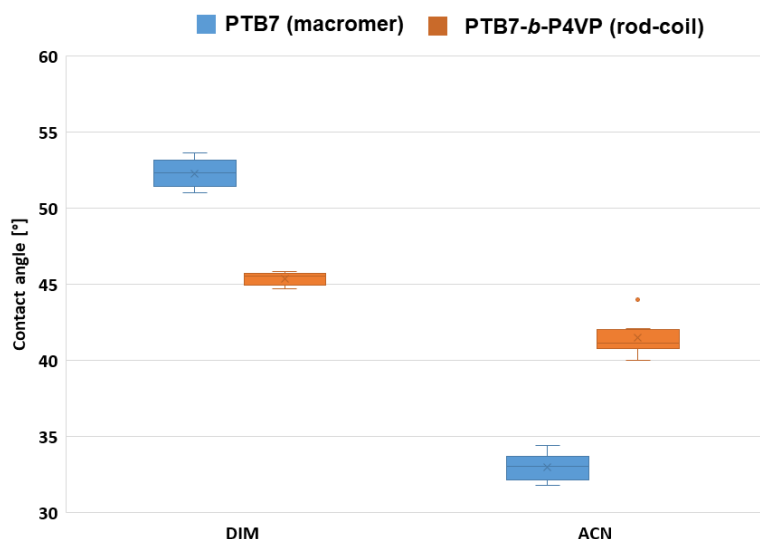


Figure 3.7 Distribution of contact angles of DIM and ACN on the macromer PTB7 and the PTB7-*b*-P4VP films.

3.2.1.3 WPNP aqueous suspensions: synthesis and characterization

To avoid the use of halogenated solvents in the solar cell device fabrication also during the NP preparation step, WPNP aqueous suspensions were obtained through the modified miniemulsion procedure deeply described in the Chapter 2. A blend of PC₇₁BM and PTB7-*b*-P4VP in ratio 1.1:1 was dissolved in a mixture of toluene and *o*-xylene (in ratio 50:50). Not only the proper removal of chlorinated solvents during the WPNP production improves the whole process sustainability, but also the employment of xylene and toluene as organic phase supports the process scale-up from lab to fab. About that, it is important to remark that a controlled evaporation of the hazardous organic solvents could be performed using a proper circular industrial plant equipped with condenser systems to recover and recycle the utilized solvent. The mixture toluene/*o*-xylene was chosen as organic phase with the aim to gain a great amount of WPNPs in the aqueous suspensions. In fact, with the pure toluene the resulting suspensions were poorly concentrated, as deduced from the absorbance, which is much lower than that of WPNPs obtained using the mixture to dissolve active materials (**Figure 3.8**).

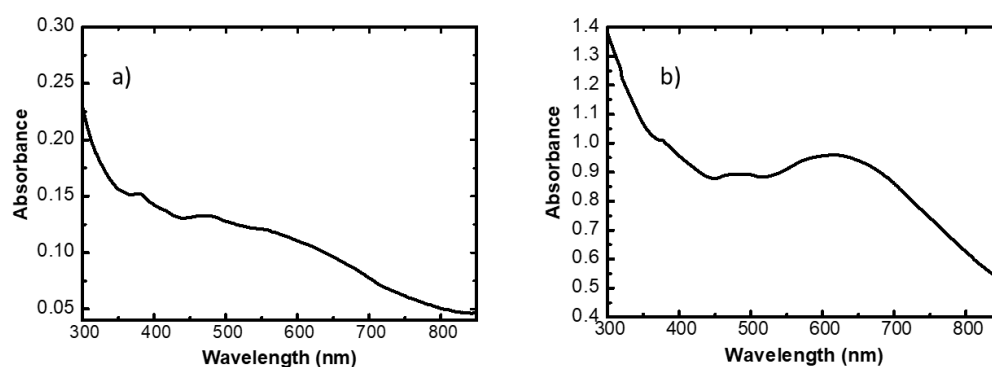


Figure 3.8 UV-Vis absorption spectra of PC₇₁BM:PTB7-*b*-P4VP (1.1:1) blend WPNP aqueous suspensions obtained dissolving both active materials in **a)** toluene and **b)** a mixture of toluene/*o*-xylene (50:50).

The UV-Vis absorption spectrum, depicted in **Figure 3.8b**, exhibits the typical profiles of the two materials constituting the blend, and shows a wide and pronounced peak at ~600 nm typical of PTB7. All the peaks are broadened and slightly shifted with respect to PTB7-*b*-P4VP and PC₇₁BM organic solutions because of the nanoaggregation which occurs inside NPs during the miniemulsion process.

DLS was carried out on PC₇₁BM:PTB7-*b*-P4VP blend WPNPs to determine their size and to establish the colloidal stability in aqueous medium. The mean diameter of NPs,

extrapolated by lognormal in number, is 79.2 ± 1.3 nm. We considered data expressed by number because our aqueous suspensions are quite complex samples, and size by number is more comparable to size calculated from TEM micrographs. In actual fact, multimodal size distribution (MSD) denotes the presence of two main populations in the aqueous suspension: the first centered at ~ 50 nm and the second at ~ 200 nm (**Figure 3.37a** in the Experimental Section). Moreover, the colloidal stability is very high as the measured ζ -potential at pH 7 value is -46.91 ± 0.68 mV.

With the purpose of more in-depth investigation of the inner morphology of WPNPs and to examine their internal composition, TEM experiments were performed by Dr. Anna Maria Ferretti (SCITEC-CNR, Milano). Even though the images appeared covered by an extra layer carbon-based, probably coming from the *o*-xylene residual that made the NP contours blurred, they reveal a quasi-spherical shape (**Figure 3.9**). These micrographs also show the presence of NP aggregates; in particular, there are larger NPs surrounded by smaller nanostructures, in agreement with DLS results. The size data of the WPNPs measured from conventional TEM images are reported in **Table 3.4**.

To study more thoroughly the internal composition, it was demanded energy-filtered TEM (EFTEM) experiments.

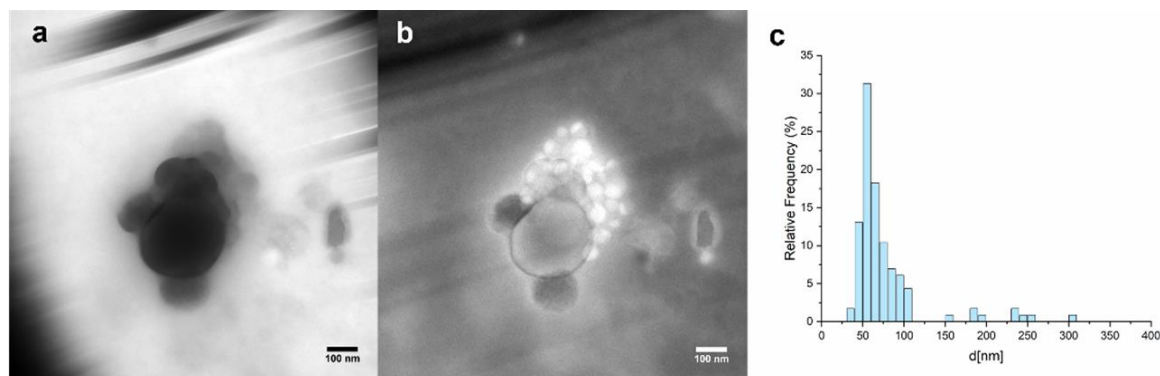


Figure 3.9 a) Conventional TEM images, b) EFTEM images recorded at 30 eV, and c) size distribution of PC₇₁BM:PTB7-*b*-P4VP (1.1:1) blend WPNPs.

Table 3.4 Mean diameter (d_m), calculated from TEM, standard deviation (st. dev), and minimum and maximum size observed in the micrographs.

Sample	d_m (nm)	st. dev. (nm)	Min (nm)	Max (nm)
PC ₇₁ BM:PTB7- <i>b</i> -P4VP (1.1:1) blend WPNPs	77.1	47.1	37.1	303.7

The size distribution is polydisperse (**Figure 3.9c**), as the standard deviation and the large difference between the minimum and the maximum of the measured data confirm. The image acquired with EFTEM is related to the electrons with specific and selected energy loss; performing electron energy loss spectroscopy (EELS) of each component of the sample is mandatory to select the proper energy loss. In this specific case, the WPNPs were synthesized starting from a blend of PTB7-*b*-P4VP and PC₇₁BM, and it is known that these two components have different Low Loss EELS spectra.[1, 3, 23, 33] In particular, the plasmon signals of the PTB7 and the PC₇₁BM have their maximum at ~22 eV and ~30 eV, [3, 34, 35] respectively, and in the case of the blend the maximum of the plasmon is ~ 23 eV (reported in **Figure 3.10**). In order to elucidate how the donor and acceptor components were distributed inside each nanostructure, the EFTEM images at four different energy loss were collected. In **Figure 3.10** the study of the PC₇₁BM:PTB7-*b*-P4VP (1.1:1) blend WPNP sample is reported. The EFTEM images were collected at 17 eV, 22 eV, and 30 eV. As expected, the PTB7-enriched area resulted lighter at 17 eV, and darker at 30 eV and, *vice versa* the PC₇₁BM-enriched one. We selected these two energies to better separate the contribute of each component to the plasmon peak, in fact at 23 eV the two components result to be similar, and it is difficult cut off correctly the contribution of each component. It is evident that the acceptor segregates on one side of the NPs, resulting lighter in images collected at 30 eV and darker in the images taken at 17 eV, while PTB7-*b*-P4VP is evidenced on the other way round. Comparing the EFTEM images in **Figure 3.10** collected at 17 eV and 30 eV it is highlighted the presence of the PTB7-*b*-P4VP-rich region at one side of the NP, while the PC₇₁BM-rich segregates to the other side of the NP. This nano-organization is typical of NPs with a Janus-like inner morphology.[36]

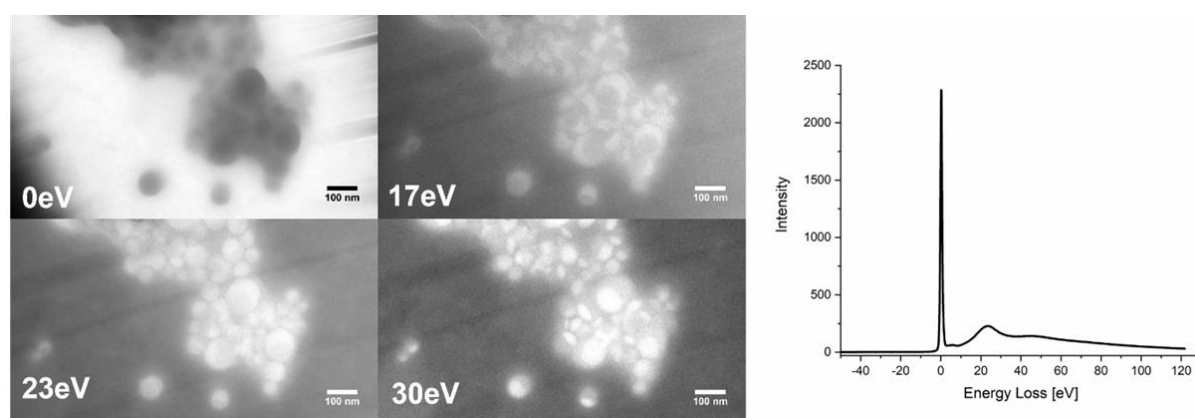


Figure 3.10 EFTEM images of PC₇₁BM:PTB7-*b*-P4VP (1.1:1) blend WPNPs at different energy loss (0 eV, 17 eV, 23 eV, and 30 eV), and EELS spectrum of the blend.

The mean size of the PC₇₁BM-enriched domain was estimated, and the size distribution is reported in **Figure 3.11**.

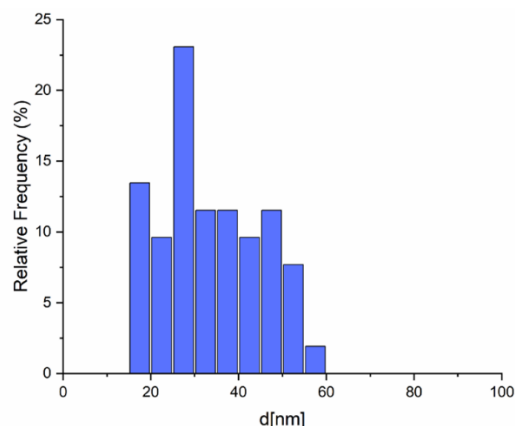


Figure 3.11 PC₇₁BM:PTB7-*b*-P4VP (1.1:1) blend WPNP core size distribution.

To confirm that there is a segregation of the PTB7-*b*-P4VP with respect to the PC₇₁BM the scanning transmission electron microscopy-energy dispersive X-ray spectroscopy (STEM-EDX) analysis was performed, too. The local distribution of sulfur was used as marker to identify the rod block location. In **Figure 3.12** the elemental distribution of carbon and sulfur are reported, and it is evident that the sulfur segregate inside the WPNPs. This result, together with the EFTEM images, support the Janus-like nanostructure of the sample.

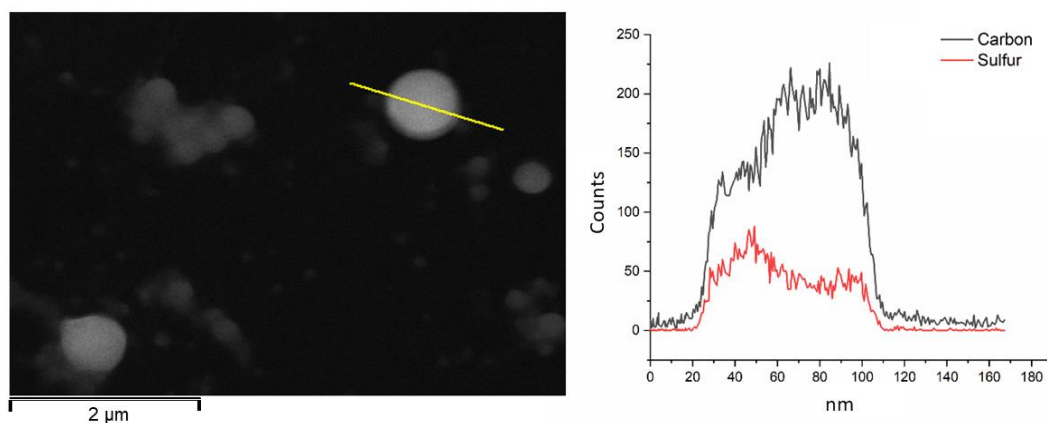


Figure 3.12. STEM image, with line scan reference (**right**), and profile of the elemental (carbon in black and sulfur in red) concentration along the line scan (**left**) of the PC₇₁BM:PTB7-*b*-P4VP (1.1:1) blend WPNP sample.

3.2.1.4 WPNP-based films: deposition and characterization

A preliminary optimization of the stable aqueous suspension deposition was required since PC₇₁BM:PTB7-*b*-P4VP blend WPNPs were consequently employed to fabricate OPV

device active layers. After multiple trials, it was found that several consecutive depositions are required to obtain an active layer with a reasonably absorbance (at least 0.2), which allows the subsequent operation of the device. Specifically, a poly(3,4-ethylenedioxythiophene):polystyrene sulfonate (PEDOT:PSS) layer (as a hole transport layer) was deposited on a suitably treated indium tin oxide (ITO) substrate, and annealed at 200 °C for 15 minutes. Next, the PEDOT:PSS layer was exposed to ultraviolet ozone (UV-O₃) treatment for more uniform coverage, increasing its wettability with aqueous suspension. [23.50,51] A topological study of the film as deposited was conducted by Dr. Guido Scavia (SCITEC-CNR, Milano) using AFM. The resulting images, shown in **Figure 3.13**, disclose that the film is compact, but not quite homogeneous, as denoted by the roughness value. Therefore, thermal annealing at 90 °C for 20 minutes was necessary to improve the film quality. Indeed, the root mean square (RMS) value decreased from 44 nm (before annealing) to 27 nm (after annealing), while the thickness (including PEDOT:PSS layer) decreased from 90 nm to 80 nm.

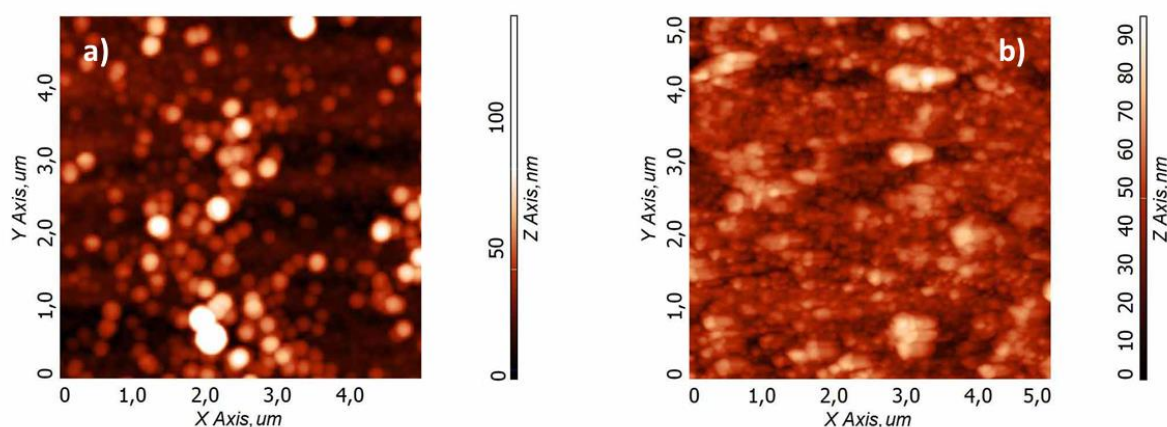


Figure 3.13 AFM images of the layer obtained by 8 consequent depositions of PC₇₁BM:PTB7-*b*-P4VP (1.1:1) blend WPNPs, **a)** before and **b)** after annealing.

This film was also examined by GIWAXS by Dr. William Porzio (SCITEC-CNR, Milano) to inquire into its degree of order, and it was compared with a film obtained by drop-casting a chloroform solution of homemade PTB7 (with molecular weight close to the macromer PTB7 and already used for UV-Vis absorption spectrum collection). The comparison of the drop-casted sample with the same polymer spin-coated reported by Hoefler *et al.* denotes a more crystalline film, preferably oriented "flat" on the substrate, although a significant amount of "edge-on" crystallites are evident as in the OP profile the interlayer spacing is noted and the π -stacking is diminished, as we can infer from the data reported in **Table 3.5**. [37]

Table 3.5 GIWAXS data of the film obtained by drop-casting of homemade PTB7 (with molecular weight close to the macromer PTB7) dissolved into chloroform (film a), and the PC₇₁BM:PTB7-*b*-P4VP WPNP-based film (film b).

Sample	OP peaks position (Å)			IP peaks position (Å)		
PTB7 film (a)	18.93	3.85	3.85	20.35	7.40	3.89
WPNP-based film (b)	19.37	4.86	3.86	20.21		4.90

The comparison between the 2D images (**Figure 3.14**) acquired at an incidence angle near 0.0° and at 0.15° denotes higher order near the substrate, as often observed for polymeric materials.[38]

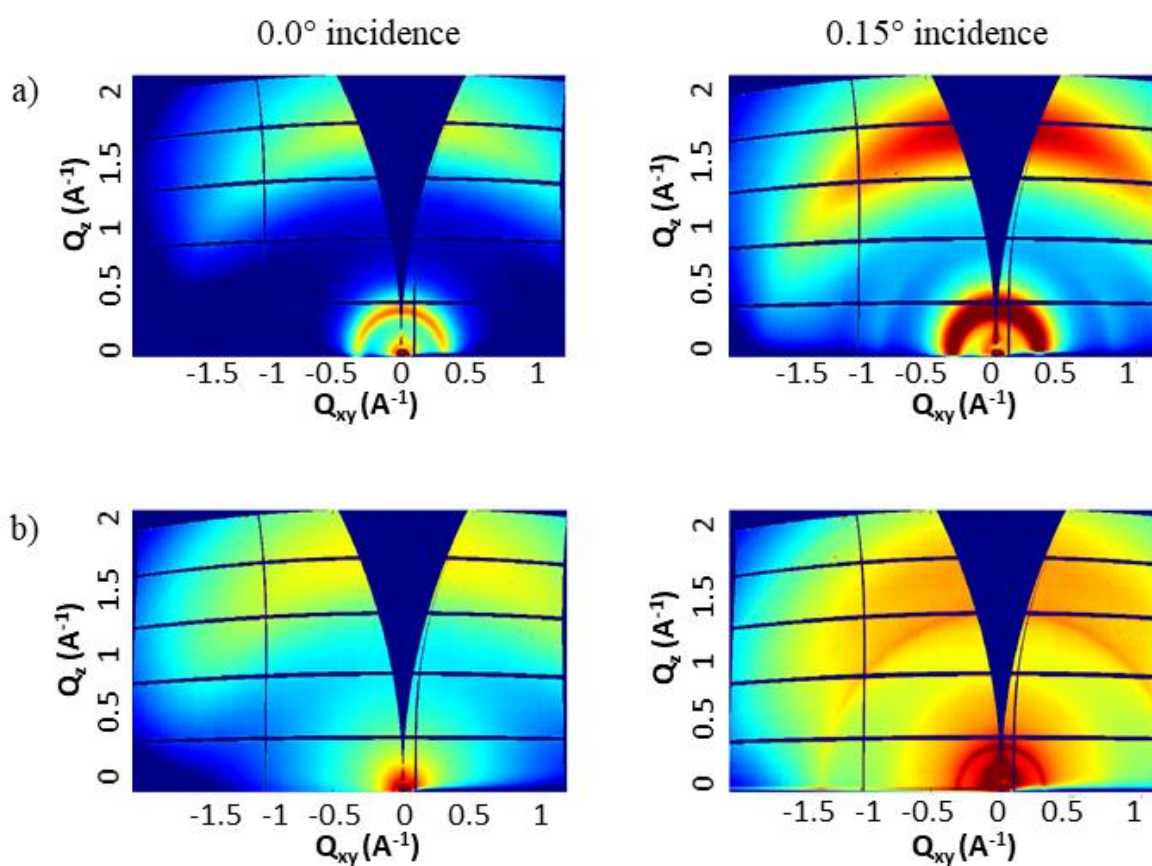


Figure 3.14 2D images from synchrotron radiation diffraction, at the incidence angle of 0.0° (**right**) and 0.15° (**left**) of **a**) a drop-casted film of homemade PTB7 (with molecular weight close to the macromer PTB7) dissolved into chloroform and **b**) PC₇₁BM:PTB7-*b*-P4VP WPNP-based film.

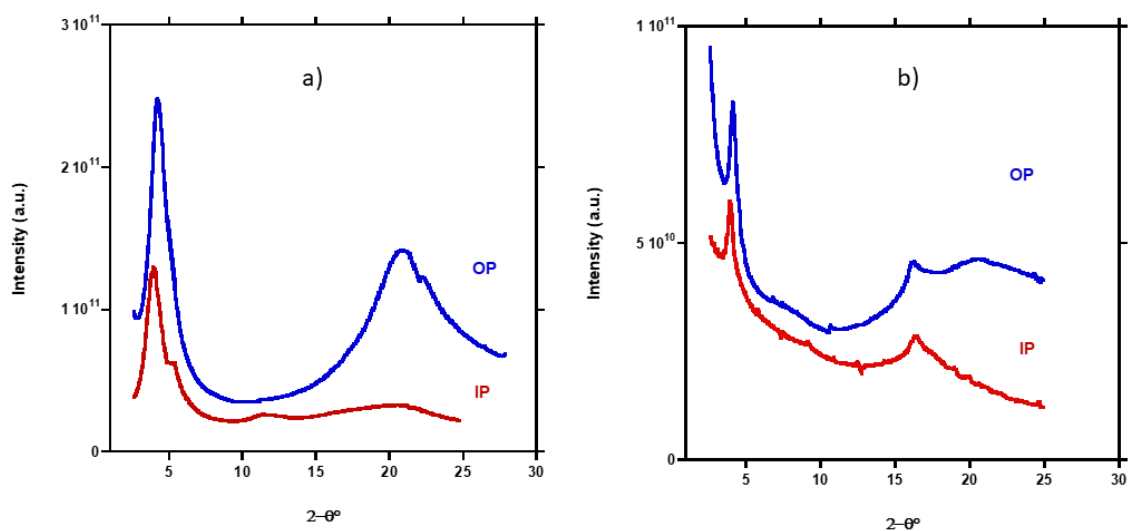


Figure 3.15 XRD profiles extracted from 2D images acquired at an incident angle of 0.15° of **a)** a film obtained by drop-casting homemade PTB7 (with molecular weight close to the macromer PTB7) dissolved into chloroform and **b)** $\text{PC}_{71}\text{BM}:\text{PTB7-}b\text{-P4VP}$ WPNP-based film.

All films are distinguished by long spacing at about 2 nm, while dissimilarities are observed at medium and short spacing. Specifically, film (a) exhibits wide peaks centered at 0.74 nm and 0.39 nm (mainly in IP), while film (b) shows peaks at 0.49 nm along with 0.39 nm (in OP). The 0.74 nm spacing in the IP profile of film (a) could be ascribable to a partial lateral stacking of edge-on oriented crystallites. In film (b), the typical peak assigned to PC_{71}BM at 0.95 nm is barely observed in the OP profile, indicating a fairly disordered pattern in the blend. The increase in long spacing in film (b) is due to the presence of flexible P4VP segment. We note the presence of a relatively sharp peak at 0.486 nm, fourth order of the long spacing, mapping to a significant degree of order achieved primarily along the interlayer direction.

By contrast, the second order close to 0.95 nm ($\sim 10 \text{ \AA}$) is totally covered by the broad spacing of PC_{71}BM . On the other hand, no periodic repetition is observed for the fullerene material. Hence, we can presume that $\text{PTB7-}b\text{-P4VP}$ preserves its semicrystalline nature even if deposited by aqueous suspension, while PC_{71}BM does not aggregate in a coherent manner (as instead PC_{61}BM does); this is caused by the shape of PC_{71}BM , which is not as spherical as PC_{61}BM , and thus prompting it to aggregate results challenging, even including thermal annealing.

3.2.1.5 WPNP-based OPV devices

To research the sustainable fabrication of the OSC, we prepared devices based on WPNPs with a direct configuration in collaboration with Dr. Silvia Luzzati (SCITEC-CNR, Milano). The active layer was processed by eight consecutive spin-coated depositions of PC₇₁BM:PTB7-*b*-P4VP (1.1:1) blend WPNPs above an ITO/PEDOT:PSS anode electrode, by using the previously described operative conditions. Lastly, a Ca/Al cathode electrode was evaporated on top. The resulting devices are under short-circuit, as the current density-voltage (J-V) characteristics reported in **Figure 3.16a** disclose. This behavior implicates that even after thermal treatments, the active layer is still not enough compact/homogeneous to prevent shunts. With the goal of minimizing electrical leakages, the device architecture was adjusted by depositing a thin layer of fullerene molecules on top of the WPNP blend film. This approach was already adopted as an effective tool to lower electric shunts in WPNP-based devices, and it was discussed in the previous chapter.[3, 39] Aiming to totally eliminate halogenated solvents in the whole device fabrication process, the deposition of an alcohol-soluble, polyethylene glycol-modified fullerene, PC₆₁BM-peg, was initially explored. This fullerene derivative was reported to perform as a successful solution-processable cathode interlayer for polymer solar cells.[40] Nevertheless, as shown in **Figure 3.16b** and **c**, the devices fabricated with PC₆₁BM-peg were short-circuited. With a small volume of dichloromethane, PC₇₁BM and PC₆₁BM were next tested in sequence; there was a modest enhancement with PC₇₁BM, but a high number of shunts still affected the device (**Figure 3.16d**). A substantial upgrade was gained using PC₆₁BM and **Figure 3.16e**, **Figure 3.17a**, and **Table 3.6** show the photovoltaic characteristics of the optimized ITO/PEDOT:PSS/WPNP/PC₆₁BM/Ca/Al devices. Further details about the device fabrication are reported in the Experimental Section.

The J-V characteristics (**Figure 3.16e** and **Figure 3.17**) highlight a significant mitigation of electric shorts/losses, suggesting that PC₆₁BM can fill the gaps generated by NPs in the active layer to avoid shunts. Moreover, relatively uniform photovoltaic curves were achieved, as displayed in **Figure 3.16e**, in agreement with AFM images, reported in **Figure 3.18**, which reveal a more homogeneous and smoother surface after PC₆₁BM deposition, with a remarkably reduction in roughness value that becomes 5.6 nm.

The same rod-coil PTB7-*b*-P4VP designed to act as donor material in the prepared water processable acceptor:donor WPNPs under investigation, was also employed for comparison in a conventional polymer bulk heterojunction (BHJ) solar cell, *i.e.* fabricating

the active layer by spin-coating the PTB7-*b*-P4VP in blend with PC₇₁BM (in ratio 1.5:1), both dissolved in chlorobenzene. The comparison between the device obtained from the aqueous suspension (device 1) and the conventional BHJ solar cell (device 2) reveals that device 1 has higher performance than device 2 (**Figure 3.17a** and **Table 3.6**). In fact, the PCEs of device 1 and device 2 reach values of 0.85% and 0.63%, respectively. Precisely, the WPNP-based device shows higher fill factor (FF) and short-circuit current density (J_{sc}) parameters, but it exhibits a lower open-circuit voltage (V_{oc}), probably because both PC₇₁BM and PC₆₁BM could operate as electron-acceptor materials.[41] The higher FF parameter suggests that charge separation and collection to the electrodes are improved in the device obtained using aqueous suspensions. This hypothesis is supported by plotting the photocurrent densities (J_{ph}) versus the effective applied voltage (V_{eff}), where J_{ph} is defined as $J_{light}-J_{dark}$, and V_{eff} is V_0-V (being V_0 the voltage where $J_{light}=J_{dark}$ and V the applied voltage).[58] The graph, depicted in **Figure 3.17b**, shows that the conventional device, unlike to the WPNP-based device, has the photocurrent that does not saturate going to high V_{eff} . This sign is related to the presence of a marked hindrance to charge dissociation and collection that occurs in the conventional PTB7-*b*-P4VP-based device. [59] Given these circumstances, it is possible to conclude that the rod-coil PTB7-*b*-P4VP, designed as donor active material in an OSC, performs better if deposited from water in the form of WPNPs instead of dissolved in chlorinated organic solvents.

Table 3.6 Photovoltaic parameters of the device from PC₇₁BM:PTB7-*b*-P4VP (1.1:1) blend WPNPs (device 1), the device from PC₇₁BM:PTB7-*b*-P4VP (1.5:1) blend in chlorobenzene (device 2), and a reference device obtained from PC₇₁BM:PTB7 (1.5:1) blend in chlorobenzene. For each parameter the best obtained value is reported with the mean value and the standard deviation between brackets.

Sample	V_{oc} (V)	FF	J_{sc} (mA cm ⁻²)	PCE (%)
Device from PC₇₁BM:PTB7-<i>b</i>-P4VP (1.1:1) blend WPNPs (device 1)	0.67 (0.60±0.07)	0.52 (0.54±0.02)	2.46 (2.30±0.10)	0.85 (0.81±0.05)
Device from PC₇₁BM:PTB7-<i>b</i>-P4VP (1.5:1) blend in chlorobenzene (device 2)	0.73 (0.70±0.10)	0.47 (0.44±0.04)	1.83 (1.60±0.10)	0.63 (0.50±0.10)
Device from PC₇₁BM:PTB7 (1.5:1) blend in chlorobenzene (reference)[42]	0.72 (0.70±0.01)	0.67 (0.70±0.01)	12.25 (12.30±0.10)	5.90 (6.0±0.30)

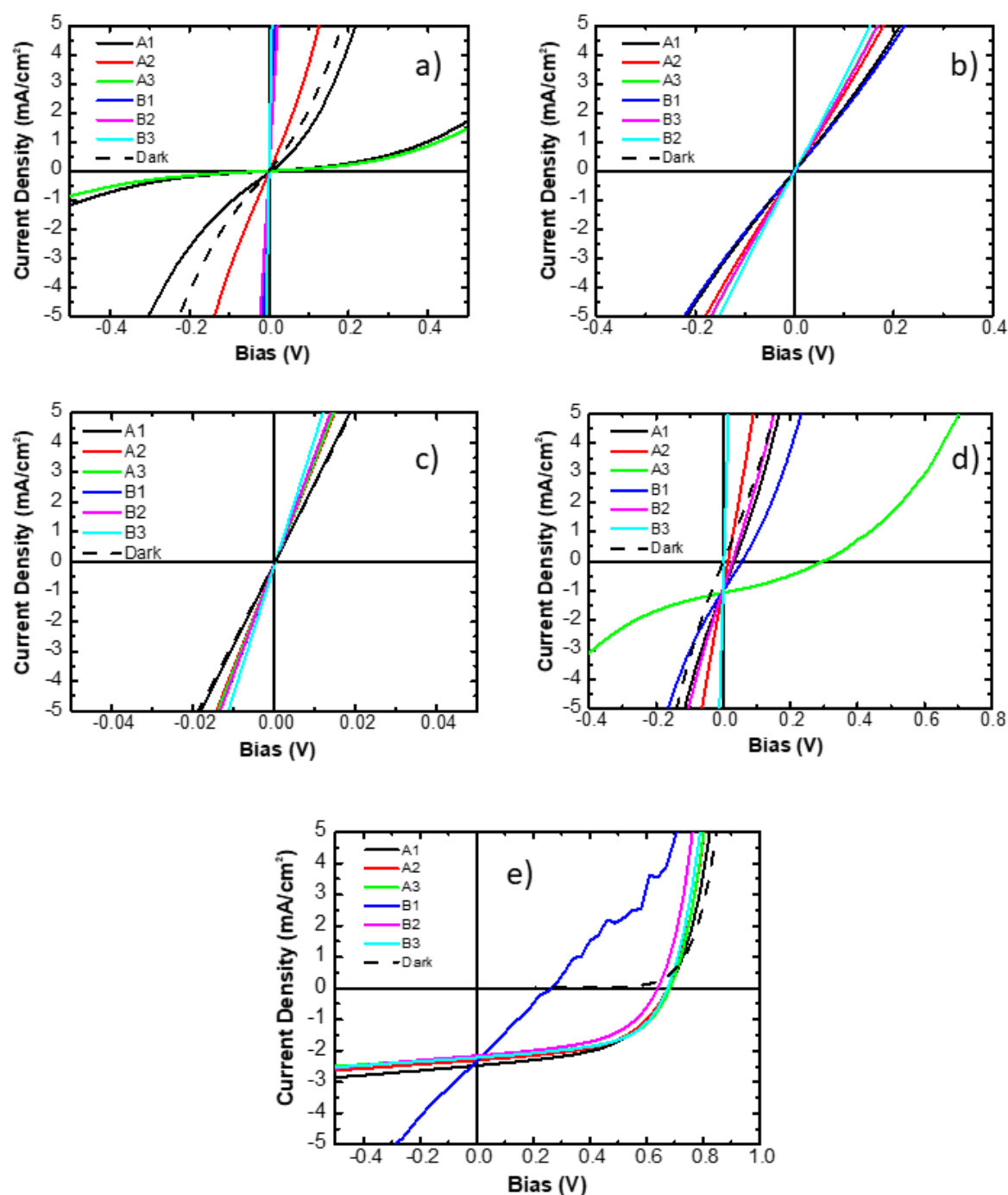


Figure 3.16 J-V curves of the device from PC₇₁BM:PTB7-*b*-P4VP (1.1:1) blend WPNPs with **a)** no interlayer on top; **b)** PC₆₁BM-peg as interlayer (deposited from ethanol); **c)** PC₆₁BM:PC₆₁BM-peg (50:50) as interlayer (deposited from ethanol); **d)** PC₇₁BM as interlayer (deposited from dichloromethane), and **e)** PC₆₁BM as interlayer (deposited from dichloromethane).

It is notable that the AFM images of device 2 (**Figure 3.18d**) reveal a non-optimal morphology, with large macrodomains of 300-600 nm, which can explain the charge recombination promotion, and the charge dissociation and extraction prevention. On the other hand, as revealed by EFTEM images (**Figure 3.10**), WPNPs have a Janus

morphology, which probably allows to limit charge recombination and aids charge separation. In addition, the presence of PC₆₁BM may also be beneficial in selectively collecting charges to electrodes.

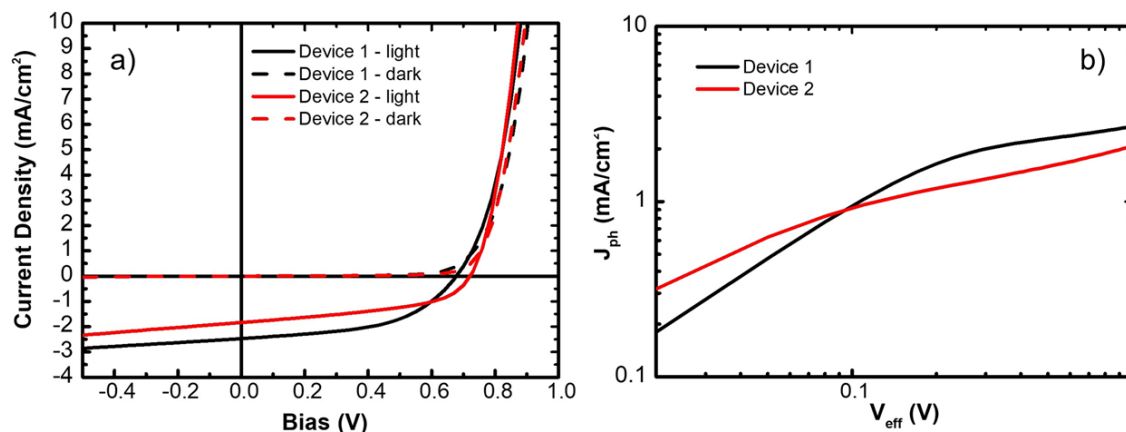


Figure 3.17 a) J-V characteristics and b) J_{ph} - V_{eff} plot of the optimized device from PC₇₁BM:PTB7-*b*-P4VP (1.1:1) blend WPNPs (device 1), and of the device from PC₇₁BM:PTB7-*b*-P4VP (1.5:1) blend in chlorobenzene (device 2).

To conclude this comparative case study, we also considered a reference OPV device obtained from PC₇₁BM:PTB7 (1.5:1) blend in chlorobenzene, using the benchmark PTB7 donor polymer. From the data listed in **Table 3.6** for the reference device, we can observe that with a commercial PTB7 much better performances in conventional blend devices with PC₇₁BM are gained, and the PCE is about one order of magnitude higher with respect to the conventional BHJ device from the PTB7-*b*-P4VP. This finding is in accordance with AFM images (**Figure 3.18d** and **e**), where it is evident that the active layer of device 2 is less interconnected than reference layer as it is featured by macrodomains, leading to the implications discussed above. Otherwise, the reference active layer displays smaller and more interconnected domains.

Such different morphology could be only partly explained by the lower molecular weight of the PTB7-*b*-P4VP in comparison with the commercial PTB7 used in reference (with $M_w=50000-60000$ g mol⁻¹), as it is reported that PTB7 performance in photovoltaic devices is dependent on its molecular weight.[43, 44] Also, PTB7 in the rod-coil has a lower polydispersity value than commercial one, and thus it tends to aggregate in diverse and more crystalline domains. Furthermore, the rod-coil used in this work presents the polar group P4VP that can negatively interfere with the proper device operation,[45] acting as an electron trap, and thus hindering charge extraction.

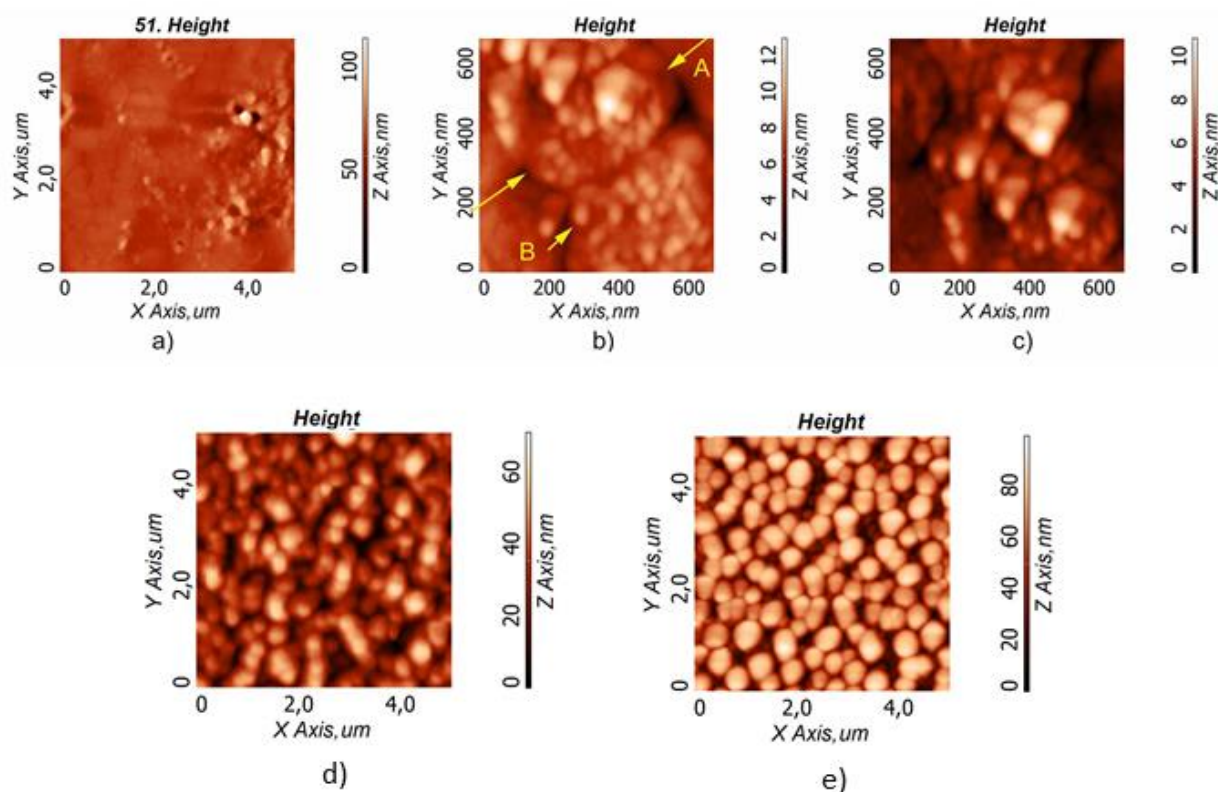


Figure 3.18 AFM images of **a,b,c**) the device from PC₇₁BM:PTB7-*b*-P4VP (1.1:1) blend WPNPs (device 1); **d**) the device from PC₇₁BM:PTB7 (1.5:1) blend in chlorobenzene (commercial PTB7) (reference), and **e**) the device from PC₇₁BM:PTB7-*b*-P4VP (1.5:1) blend in chlorobenzene (device 2).

3.3 Aqueous inks based on PC₇₁BM:PTB7-*b*-P4VP:PTB7 blend WPNPs

In the previous paragraph we hypothesized that one of the reasons why the WPNP-based OPV device shows a low efficiency is the presence of a too long P4VP segment as coil block, which can negatively affect the proper charge extraction, reducing the final device performance.[45] We tried to get around this issue reducing the overall ratio between the rod and the coil P4VP (with 15 repeating units) by introducing a certain amount of homemade PTB7 (without any flexible segment attached and with a molecular weight close to the macromer, already used for UV-Vis absorption spectrum collection) to the active material mixture during the miniemulsion process. In this way we maintained the ratio between the acceptor material (PC₇₁BM) and the donor (PTB7) in the blend equal to 1.1:1, decreasing the coil amount, probably responsible of the drastic drop in the OSC efficiency.

3.3.1 Results and Discussion

3.3.1.1 WPNP aqueous suspensions: synthesis and characterization

The PC₇₁BM:PTB7-*b*-P4VP:PTB7 blend aqueous suspension was prepared by following the modified miniemulsion approach already outlined. A first attempt was carried out using a ratio between the rod-coil PTB7-*b*-P4VP and the homemade PTB7 of 50:50. Hence, PC₇₁BM, PTB7-*b*-P4VP and PTB7 (in ratio 1.1:50:50) were dissolved in the organic solvents (toluene and *o*-xylene in ratio 50:50) and injected into pure water under vigorous stirring to form a macroemulsion. After the formation of the miniemulsion by ultrasonication, the organic solvents were removed by evaporation, but unfortunately a stable aqueous suspension was not obtained. We assumed that this failure was due to an insufficient coil amount to ensure colloidal stability, thus we next attempted to increase the PTB7-*b*-P4VP:PTB7 ratio to 70:30. By adopting the same preparation conditions, we succeeded in achieving WPNPs stably dispersed in water, and the corresponding UV-Vis absorption curve is shown in **Figure 3.20a**. The absorption spectrum is affected by a strong scattering, as if there is in the sample a huge quantity of aggregates. This hypothesis is supported by the results provided by DLS, which reveals the presence of a single population with the mean diameter, calculated through the lognormal by number, of 256.9±16.6 nm. These data are very far from those obtained through TEM analysis carried out by Dr. Anna Maria Ferretti (SCITEC-CNR, Milano), which instead showed that PC₇₁BM:PTB7-*b*-P4VP:PTB7 blend WPNPs had smaller size than the PC₇₁BM:PTB7-*b*-P4VP based sample, and a narrow polydispersity. This difference is likely due to the fact that DLS detects aggregates, rather than the single NP. The NP aggregates are distinguishable in the images collected by conventional TEM and EFTEM recorded at 30 eV. The size distribution calculated from the micrographs is depicted in **Figure 3.19**, and the size data of the WPNPs measured from conventional TEM images are reported in **Table 3.7**.

Table 3.7 Mean diameter (d_m), calculated from TEM, standard deviation (st. dev), and minimum and maximum size observed in the micrographs.

Sample	d_m (nm)	st. dev. (nm)	Min (nm)	Max (nm)
PC ₇₁ BM:PTB7- <i>b</i> -P4VP:PTB7 (1.1:0.70:0.30) blend WPNPs	24.8	8.1	11.9	61.1

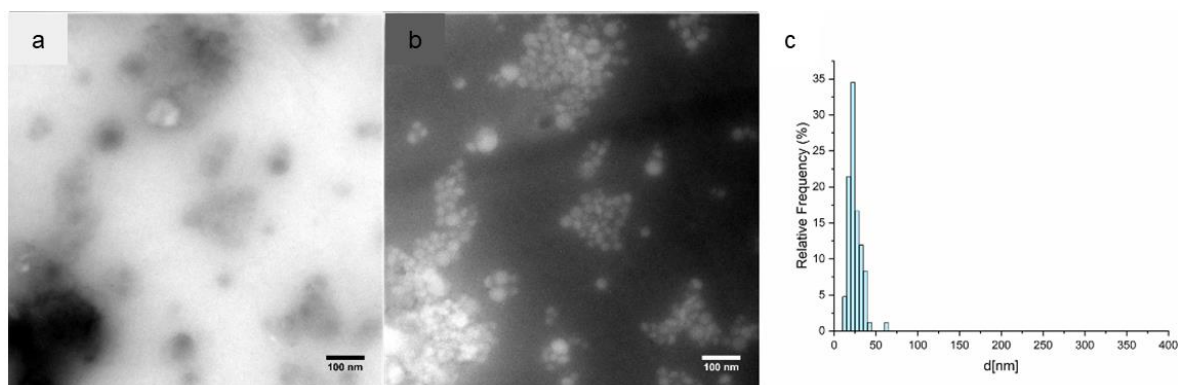


Figure 3.19 a) Conventional TEM images, b) EFTEM images recorded at 30 eV, and c) size distribution of PC₇₁BM:PTB7-*b*-P4VP:PTB7 blend WPNPs.

3.3.1.2 WPNP-based films: deposition and characterization

We deposited the film with PC₇₁BM:PTB7-*b*-P4VP:PTB7 aqueous suspension, proceeding with the optimized methodology previously developed. Then, eight consecutive layers were spin-coated on an appropriately treated ITO/PEDOT:PSS substrate to achieve a film with an absorbance sufficiently high (the absorption spectrum is depicted in **Figure 3.20b**). Actually, the film was very inhomogeneous, as confirmed by AFM analysis (**Figure 3.21**) performed by Dr. Guido Scavia (SCITEC-CNR, Milano). This condition further worsened after heat treatment at 90 °C for 20 minutes. In fact, the RMS value before and after annealing is ~20 nm and ~48 nm, respectively. This attitude denotes an increase in the roughness of the sample, as if the annealing emphasizes the differences between the two distinct donor materials in the WPNPs, which segregated thus leading to greater inhomogeneity in the sample.

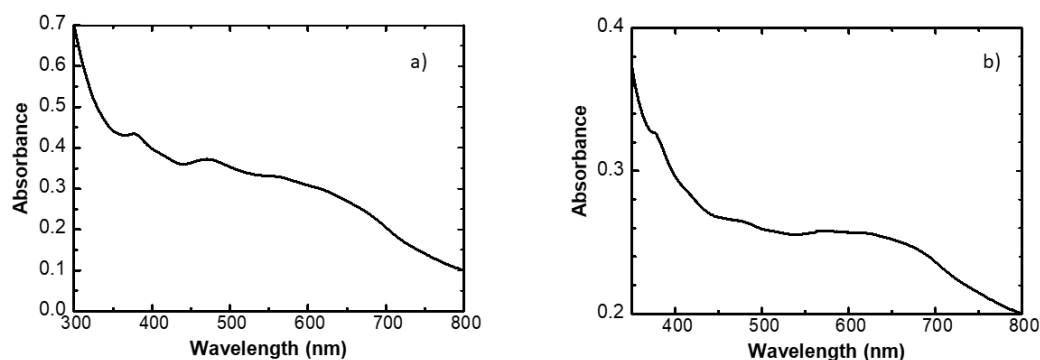


Figure 3.20 UV-Vis absorption spectra of a) PC₇₁BM:PTB7-*b*-P4VP:PTB7 (1.1:0.70:0.30) blend WPNP aqueous suspensions and b) PC₇₁BM:PTB7-*b*-P4VP:PTB7 (1.1:0.70:0.30) blend WPNP-based film.

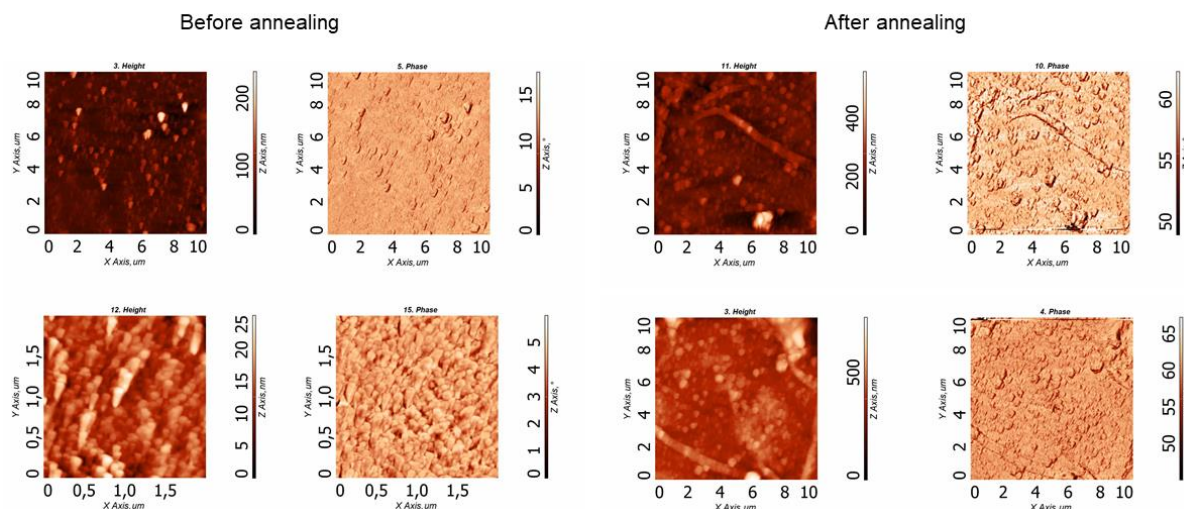


Figure 3.21 AFM images acquired at different scales of the film obtained by 8 repeated depositions of PC₇₁BM:PTB7-*b*-P4VP:PTB7 (1.1:0.70:0.30) blend WPNPs, before and after thermal annealing.

3.3.1.3 WPNP-based OPV devices

Despite the inhomogeneity of the film resulting from preliminary deposition tests, we attempted to fabricate an OSC by depositing the PC₇₁BM:PTB7-*b*-P4VP:PTB7 (1.1:0.70:0.30) aqueous suspension as active layer, in collaboration with Dr. Silvia Luzzati (SCITEC-CNR, Milano). The OPV device was fabricated with a direct configuration, in accordance with the architecture previously defined: ITO/PEDOT:PSS/WPNPs/PC₆₁BM/Ca/Al. The photovoltaic parameters were determined (**Table 3.8**), and the J-V curves were extrapolated in direct and reverse bias (**Figure 3.22**). For further details about the fabrication operating conditions of the device consult the Experimental Section.

Table 3.8 Photovoltaic parameters of the device from PC₇₁BM:PTB7-*b*-P4VP:PTB7 (1.1:0.70:0.30) blend WPNPs (device 3). For each parameter the best obtained value is reported with the mean value and the standard deviation between brackets.

Sample	V _{oc} (V)	FF	J _{sc} (mA cm ⁻²)	PCE (%)
Device from PC ₇₁ BM:PTB7- <i>b</i> -P4VP:PTB7 (1.1:0.70:0.30) blend WPNPs (device 3)	0.60 (0.23±0.10)	0.40 (0.33±0.01)	1.33 (1.28±0.02)	0.32 (0.16±0.02)

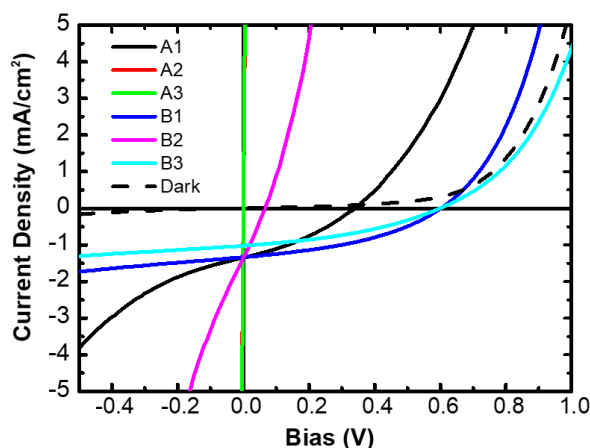


Figure 3.22 J-V curves of the device from PC₇₁BM:PTB7-*b*-P4VP:PTB7 (1.1:0.70:0.30) blend WPNPs with PC₆₁BM as interlayer (deposited from dichloromethane).

3.4 Aqueous inks based on the amphiphilic rod-coil PTB7-*b*-Krebs

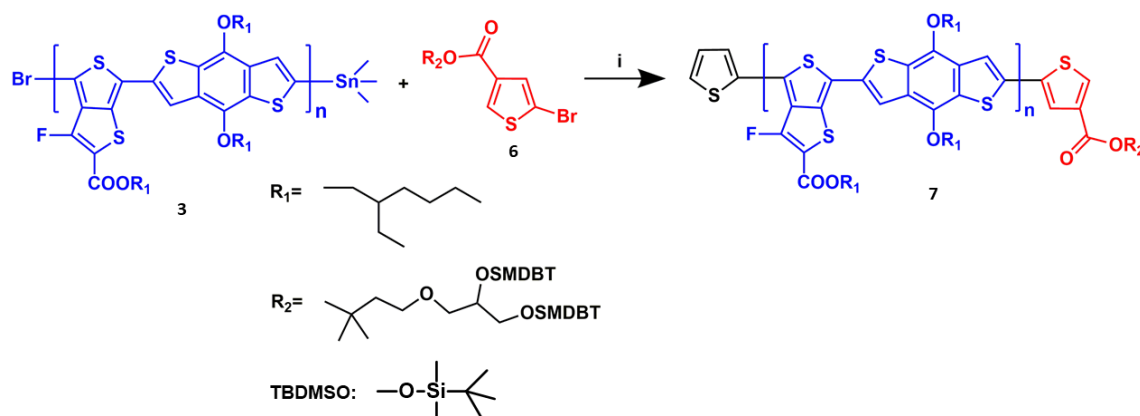
Another attempt we undertake with the goal of reducing the overall amount of coil present in the active materials blend was the synthesis of a new PTB7-based rod-coil BCP bearing a shorter coil with respect to the segment of P4VP with 15 repeating units. At this purpose we ruled out the possibility of exploiting a *Chain Growth-like* approach,[10] which involves the initial achievement of the macroinitiator PTB7-based with stannyl ending group to be activated with TIPNO-PhBr to initiate the polymerization of the 4VP. Indeed, it was already discussed in Chapter 2 that this method requires the use of the TIPNO-PhBr as capping agent to gain the desired macroinitiator, resulting too expensive to be scaled-up. Furthermore, the macroinitiator would be enough rigid to make the activation time too long. Lastly, the chain growth-like approach resulted not to be entirely reproducible and controllable, that means it is not easy to obtain a coil with exactly the aimed number of repeating units.

Basing on these reflections, we decided to introduce as coil block the molecule proposed by Krebs *et al.* (**Scheme 3.2 (6)**), hereafter will be referred as Krebs' ester),[46] which consists of a thiophene functionalized with an ester group of an alcohol bearing polar moieties able to interact with water, providing the aspired amphiphilic behaviour to the resulting rod-coil BCP, that will be referred as PTB7-*b*-Krebs.

3.4.1 Results and Discussion

3.4.1.1 Synthesis and Characterization of the rod-coil PTB7-*b*-Krebs

The new copolymer PTB7-*b*-Krebs (**7**) was achieved attaching to the macromer PTB7 the Krebs' ester (**6**),[46] functionalized with a bromide atom, as a capping agent for the stannyl end groups, as represented in **Scheme 3.2**. The detailed synthetic procedure is reported in the Experimental Section.



Scheme 3.2 Synthetic route of the rod-coil PTB7-*b*-Krebs. Reaction conditions: i) $\text{Pd}_2(\text{dba})_3$, $\text{P}(o\text{-tol})_3$, $120\text{ }^\circ\text{C}$, 24 h.

The achieved PTB7-*b*-Krebs was structurally and optically characterized through $^1\text{H-NMR}$, SEC and UV-Vis spectroscopy.

The $^1\text{H-NMR}$ spectrum (**Figure 3.36** in Experimental Section) presents the typical signals of PTB7, in accordance with literature.[13, 15] The peaks related to the Krebs' ester are not distinguishable because it is just present in a small amount with respect to the rod, and therefore its signals are completely overlapped by those of PTB7. In addition, high-temperature SEC (HT-SEC) measurements were performed by Dr. Stefania Zappia using *ortho*-dichlorobenzene as eluent, and the found out MWD was reported in **Table 3.9**

Table 3.9 MWD data of the PTB7-*b*-Krebs.

Sample	M_n (g mol^{-1})	M_w (g mol^{-1})	M_w/M_n
PTB7- <i>b</i> -Krebs	24400	100850	4.1

Lastly, UV-Vis spectroscopy was carried out on the PTB7-*b*-Krebs dissolved into chloroform. The corresponding spectrum (**Figure 3.23**) shows the absorption band with a maximum at about 600 nm typical of PTB7.[13, 17]

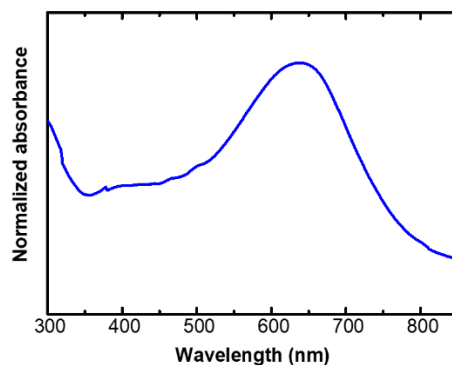


Figure 3.23 UV-Vis spectrum of the rod-coil PTB7-*b*-Krebs dissolved into chloroform.

3.4.1.2 WPNP aqueous suspension: synthesis and characterization

The rod-coil PTB7-*b*-Krebs was employed to prepare WPNP aqueous suspension in blend with PC₇₁BM (in ratio PC₇₁BM:PTB7-*b*-Krebs=1.1:1), adopting the method reported in the previous paragraph. Thus, both active materials were dissolved in the mixture of toluene and *o*-xylene (in ratio 50:50). The organic solution was injected into pure water under vigorous stirring to form a macroemulsion and, after ultrasonication, a miniemulsion. At this point the organic solvents were removed by evaporation, leading to a stable aqueous suspension of PC₇₁BM:PTB7-*b*-Krebs blend WPNPs.

The aqueous suspension was optically characterized, and DLS measurements were carried out to determine the NP size and their stability in water. The mean diameter of NPs, extrapolated by lognormal in number, is 74.0 ± 3.1 nm. Actually, like in the case of PTB7-*b*-P4VP-based WPNPs, also in this aqueous suspension the MSD denotes the presence of two main populations (**Figure 3.37c**): the former centered at ~ 60 nm and the latter at ~ 200 nm. Furthermore, the measured ζ -potential value is -45.74 ± 0.35 mV, denoting a very high colloidal stability. These results are in agreement with the data obtained by TEM experiments, performed by Dr. Anna Maria Ferretti (SCITEC-CNR, Milano). The TEM images reveal a quasi-spherical shape (**Figure 3.24**). The micrographs also verified the DLS results, showing that there are larger NPs surrounded by smaller nanostructures. The size data of the WPNPs measured from conventional TEM micrographs are reported in **Table 3.10**.

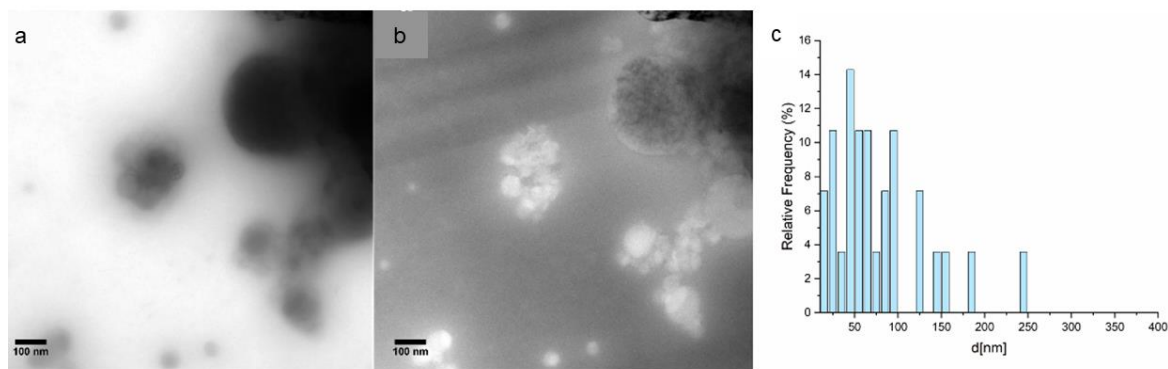


Figure 3.24 a) Conventional TEM images, b) EFTEM images recorded at 30 eV, and c) size distribution of PC₇₁BM:PTB7-*b*-Krebs blend WPNPs.

Table 3.10 Mean diameter (d_m), calculated from TEM, standard deviation (st. dev), and minimum and maximum size observed in the micrographs

Sample	d_m (nm)	st. dev. (nm)	Min (nm)	Max (nm)
PC ₇₁ BM:PTB7- <i>b</i> -Krebs (1.1:1) blend WPNPs	78.5	54.9	19.6	246.3

Lastly, in **Figure 3.25a** the UV-Vis absorption profile of the WPNPs dispersed in water is depicted.

3.4.1.3 Characterization of WPNP-based films

Films based on the WPNPs were deposited adopting the optimized method developed for PTB7-*b*-P4VP. Therefore, eight consecutive depositions were executed on a suitably treated ITO/PEDOT:PSS substrate in order to reach an absorbance sufficiently high (at least 0.2) to allow the subsequent device working. The so-obtained layer was optically characterized through UV-Vis absorption spectroscopy, and the collected spectrum is shown in **Figure 3.25b**.

Additionally, topologically studies through AFM were performed by Dr. Guido Scavia (SCITEC-CNR, Milano), before and after a mild annealing at 90 °C for 20 minutes. Also in this case, the thermal treatment induced an increment in the homogeneity of the film and a reduction of the roughness. Indeed, the RMS value decreases from 52 nm to 42 nm.

Since the OPV device was fabricated with the same architecture used for PTB7-*b*-P4VP-based OPV, a thin layer of PC₆₁BM (~20 nm) was deposited from ~20 μ l of dichloromethane on the top of PC₇₁BM:PTB7-*b*-Krebs film. Lastly, the resulted sample was annealed again at 90 °C for 20 minutes, and AFM analysis was carried out again,

revealing a rather homogeneous and flat sample, exhibiting a drastic reduction in roughness, with an RMS value reaching a value of 4 nm in certain areas. All the images acquired through AFM are depicted in **Figure 3.26**.

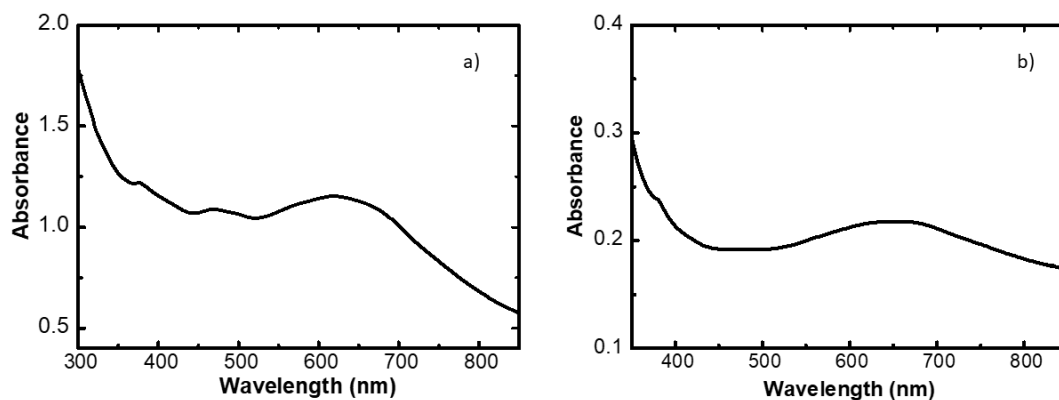


Figure 3.25 UV-Vis absorption spectra of **a)** PC₇₁BM:PTB7-*b*-Krebs (1.1:1) blend WPNP aqueous suspension and **b)** PC₇₁BM:PTB7-*b*-Krebs (1.1:1) blend WPNP-based film.

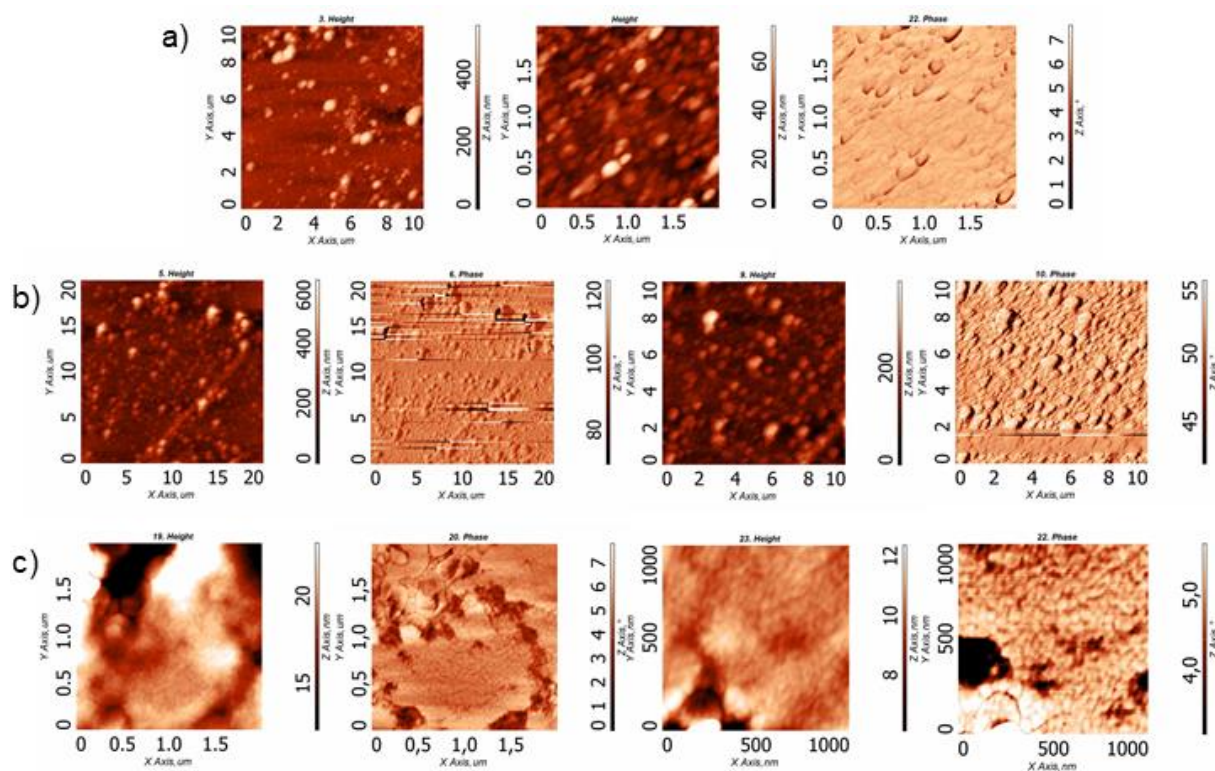


Figure 3.26 AFM images of PC₇₁BM:PTB7-*b*-Krebs (1.1:1) WPNP-based film acquired **a)** before annealing; **b)** after thermal annealing at 90 °C for 20 minutes, and **c)** after a thin layer of PC₆₁BM on the top and a further thermal treatment at 90 °C for 20 minutes.

3.4.1.4 WPNP-based OPV devices

In collaboration with Dr. Silvia Luzzati (SCITEC-CNR, Milano) we fabricated an OSC using PC₇₁BM:PTB7-*b*-Krebs blend WPNPs to deposit the active layer. The OPV device was produced with a direct configuration, following the architecture defined in the paragraph above. Therefore, an ITO/PEDOT:PSS/WPNP/PC₆₁BM/Ca/Al cell was fabricated and J-V characteristics were measured, and shown in **Figure 3.27**, while the photovoltaic parameters are summarized in **Table 3.11**. The device fabrication operative conditions are described in detail in the Experimental Section.

Table 3.11 Photovoltaic parameters of the device from PC₇₁BM:PTB7-*b*-Krebs (1.1:1) blend WPNPs (device 4). For each parameter the best obtained value is reported with the mean value and the standard deviation between brackets.

Sample	V _{oc} (V)	FF	J _{sc} (mA cm ⁻²)	PCE (%)
Device from PC ₇₁ BM:PTB7- <i>b</i> -Krebs (1.1:1) blend WPNPs (device 4)	0.60 (0.56±0.03)	0.35 (0.31±0.02)	1.62 (1.23±0.3)	0.34 (0.22±0.08)

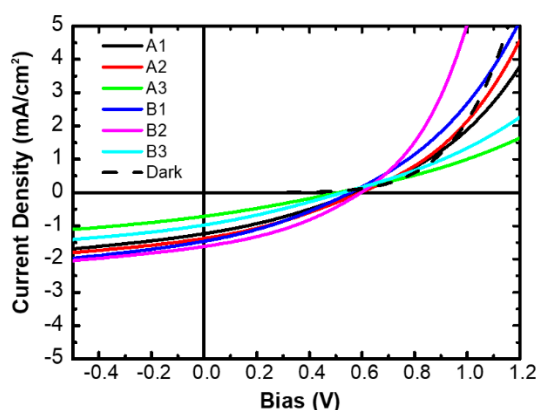


Figure 3.27 J-V curves of the device from PC₇₁BM:PTB7-*b*-Krebs (1.1:1) blend WPNPs with PC₆₁BM as interlayer (deposited from dichloromethane).

3.5 Conclusions

In summary, I synthesized new amphiphilic rod-coil BCPs based on the semiconducting polymer PTB7, covalently linked to a hydrophilic flexible coil. This last segment was tailored at 15 repeating units of 4VP. The copolymer PTB7-*b*-P4VP was fully characterized from spectroscopical and structural points of view. Firstly, the effective covalent bond formation between the coil and rod blocks was proved by trusting several advanced techniques, which synergistically allowed us to confirm the bond formation. WPNPs of

PTB7-*b*-P4VP blended with PC₇₁BM were prepared and their size together with the colloidal stability of the aqueous suspensions were determined using DLS analysis. Furthermore, TEM experiments were performed revealing a spherical shape of the NPs and, more important, EFTEM disclosed the donor material PTB7-*b*-P4VP segregated in ordered domains at one side of the NP, while PC₇₁BM-rich regions were visible to the other side of the NPs. This feature is typical of nanostructures with a Janus-like morphology (also known as biphasic),[46, 47] which enhances interfaces between donor and acceptor materials and increases the interconnections of the two networks promoting the charge mobility. This morphology was suggested by Kietzke *et al.* for PFB:F8BT NPs,[48] and proposed recently by Ghazy *et al.*[12] As a matter of fact, devices fabricated with WPNNPs of the block copolymer perform better than a BHJ device achieved by conventional deposition of PTB7-*b*-P4VP from chlorinated solvents.

A typical miniemulsion procedure implies the use of surfactants, which leads to NPs with a core-shell morphology, not totally appropriate for an optimal photovoltaic activity.

The use of amphiphilic rod-coil BCPs capable of self-assembly is an advantageous tool to obtain pre-organized nanostructures suitable for good charge dissociation, transport, and extraction. Indeed, Ghazy's research group affirmed that the Janus-like morphology suits photovoltaic applications much better than the core-shell one, which instead minimizes surface area between donor and acceptor materials, decreasing the efficiency of the WPNNP-based OSCs.[12] Unfortunately, it is very challenging to pre-determine the nanostructuration inside NPs as the inner morphology is affected by a lot of parameters and conditions, such as rod and coil block ratio in the BCP, donor and acceptor ratio, their concentration in the starting solution, surface energy of the BCP and the acceptor, and so on. Even though a more suitable NP morphology for OPV purposes was obtained, we are still very far from the performance reached by a commercial PTB7 processed by hazardous halogenated solvents. Assuming that this result was due to the presence of the polar group P4VP, that can act as a trap for the electrons and hamper the proper device working, an improvement of our approach was tried by modifying the NP composition. Particularly, we added to the active material blend a proper amount of neat homemade PTB7 to reduce the overall quantity of P4VP in the active layer. Another attempt was performed through a modification of the chemical structure of the BCP. Unfortunately, it was not possible to increase the rod PTB7 molecular weight to approximate the value of the benchmark one because longer reaction times lead to a larger polydispersity, which has a dramatic impact on the production of WPNNPs. As an alternative way to implement the device performance,

we tried to modify the hydrophilic flexible segment, using a shorter coil block. Specifically, we attached to the PTB7 rod a thiophene with an ester group of an alcohol that can interact with water. Devices fabricated following the procedures already adopted for the rod-coil PTB7-*b*-P4VP, gave no improvement in the device performance.

The use of a different vertical architecture could allow to bypass the problem caused by the orientation of the hydrophilic coil next to the cathode. The fabrication of an OPV device with an inverted configuration will be considered.

3.6 Experimental Section

3.6.1 Materials

All reagents were purchased from Sigma-Aldrich and Ossila and used as received. 4-(2,3-bis((tert-butyldimethylsilyl)oxy)propoxy)-2-methylbutan-2-ol was purchased from Sunatech and used as received. Commercially available 4VP and anisole used to prepare the coil block were distilled on calcium hydride under reduced pressure and stored at -20 °C under nitrogen. The coil block P4VP with 15 repeating units was synthesized as reported,[10] and already described in Chapter 2. All other solvents used for the chemical reactions were dried by standard procedures. All manipulations involving air-sensitive reagents were performed under dry nitrogen atmosphere. Purifications through flash chromatography were performed using Merck silica gel type 40-60 mesh. 1,2-Dideutero-1,1,2,2-tetrachloroethane (TCE-d₂) and deuteriochloroform (CDCl₃) used to collect ¹H-NMR spectra are TCI Chemicals products. For the WPNP production through miniemulsion approach MilliQ water grade ultrapure was used (resistivity of ~18 at 25 °C). Clevis AI 4083 PEDOT:PSS was purchased from Heraeus. PC₇₁BM and PC₆₁BM from Solenne BV and used as received.

3.6.2 Synthetic Procedures

3.6.2.1 Synthesis of the PTB7-*b*-P4VP

Synthesis of the macromer PTB7 (3). 4,8-Bis[(2-ethylhexyl)oxy]-2,6-bis(trimethylstannyl)benzo[1,2-*b*:4,5-*b'*]dithiophene (BDTOEHSn) (80 mg, 0.103 mmol) (1) and 2-ethylhexyl 4,6-dibromo-3-fluorothiopheno[3,4-*b*]thiophene-2-carboxylate (FTThBr) (50 mg, 0.103 mmol) (2) were dissolved in a mixture of 1 ml of toluene and 300 µl of dimethylformamide (DMF) in a dry, oxygen-free Schlenk tube. After that, Pd₂(dba)₃ (1.9

mg, 2.06×10^{-3} mmol) and $P(o\text{-tol})_3$ (2.5 mg, 8.24×10^{-3} mmol), dissolved in 170 μl of toluene, were added to the reaction mixture, and several freeze-pump-thaw cycles were performed to remove any remaining oxygen. Therefore, the mixture was heated at 120 °C under stirring. The colour turns quickly from dark red to dark blue. After 24 hours the reaction mixture was cooled at room temperature and a sample was taken, filtered through Celite® and characterized with $^1\text{H-NMR}$, SEC, MALDI-TOF MS, and FTIR. The $^1\text{H-NMR}$ spectrum was consistent with that reported in literature.[13-15]

Coupling between the macromer PTB7 and the coil P4VP. After taking a sample of the macromer PTB7 (**3**) for the characterization, the coil block of about 15 repeating units of P4VP (30 mg) (**4**), synthesized as reported, [10] was dissolved in 1 ml of toluene and 300 μl di DMF. The obtained mixture was introduced into the reaction Schlenk tube at room temperature, and 200 μl of catalytic solution was added to ensure the Stille coupling between the two blocks. The reaction mixture was heated again at 120 °C for 24 hours. After that, the Schlenk tube was cooled at room temperature, and 200 μl of degassed 2-bromothiophene was introduced to cap the residual stannyl terminal groups. After 24 hours at 120 °C, 200 μl of degassed 2-(tributylstannyl)thiophene and some catalysts were added to cap the bromide terminal groups. The mixture was warmed at 120 °C for 24 hours. At this point, ~70 mg of Scavenger resin (3-mercaptopropyl-functionalized silica gel) was added, and after about 2 hours under stirring at 120 °C the mixture was filtered through Celite®, washing with toluene and chloroform. The filtrate was poured into methanol, after concentration in vacuum, to remove the unlinked homopolymer P4VP soluble in methanol. Subsequently, the product was dissolved in a small quantity of chloroform, then poured again into hexane (solvent selective for the rod block) to obtain a blue solid. Finally, the so-obtained material was filtered and extracted with Soxhlet apparatus in acetone, hexane, and chloroform, in sequence. The final product appears as a dark blue solid (**5**) (23 mg, Yield: 19%).

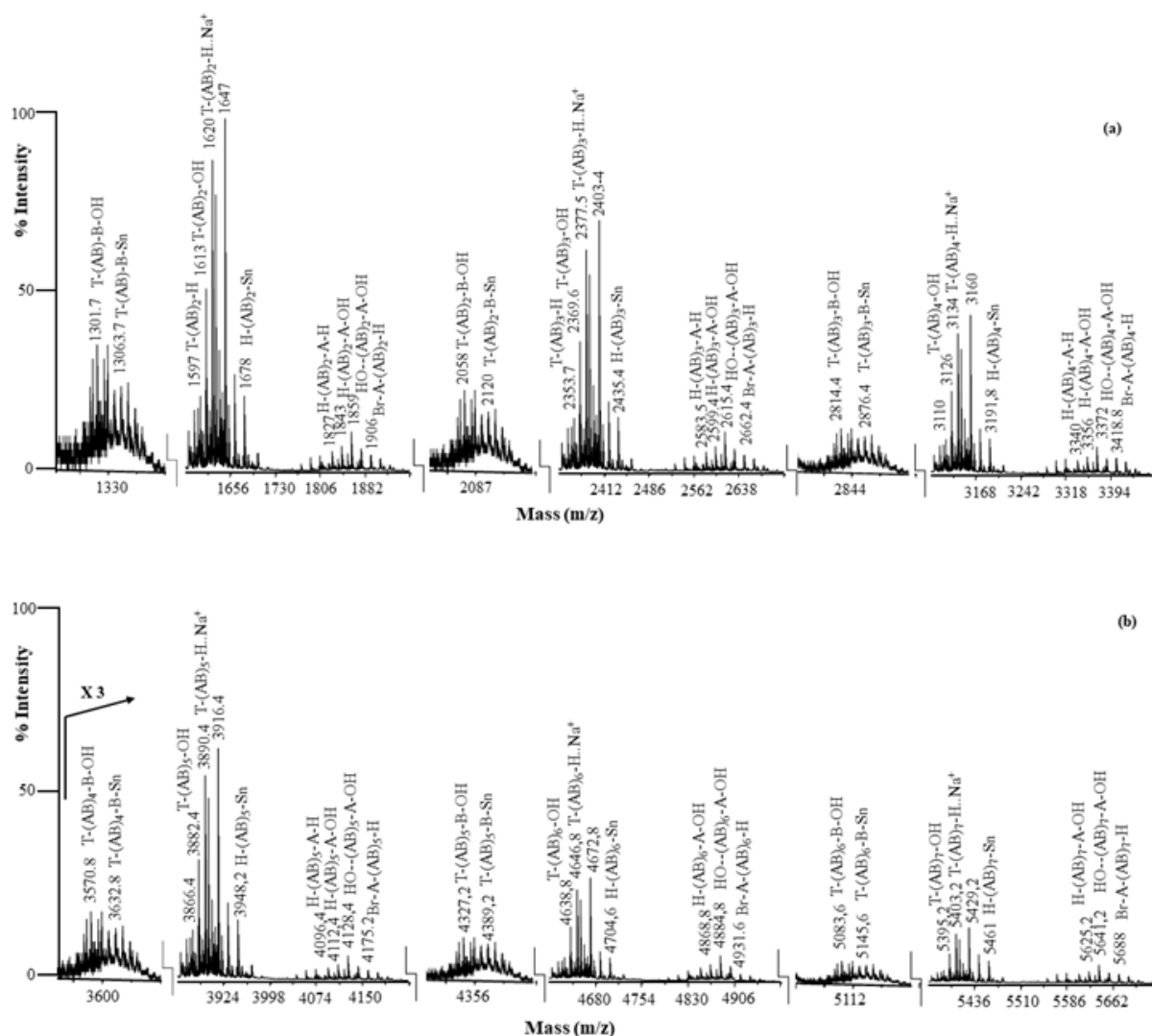


Figure 3.28 Positive ions MALDI-TOF mass spectrum of the macromer PTB7 recorded in reflectron mode using DCTB as matrix.

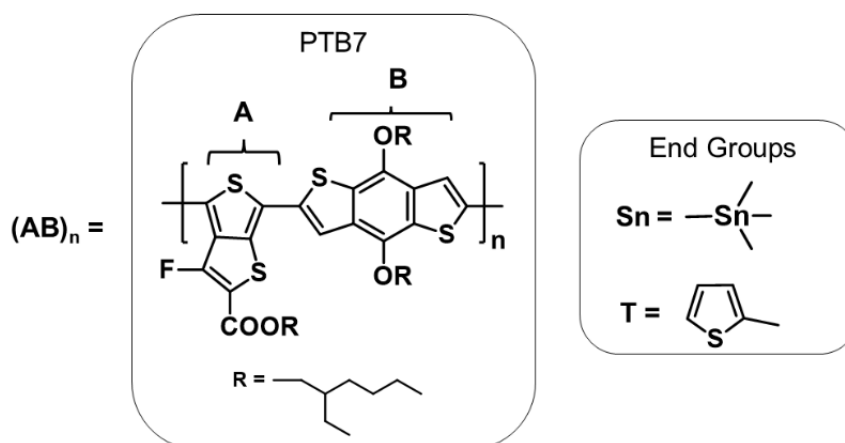


Chart 3.1 Structures of the macromer PTB7 polymer chains and of their end groups detected by MALDI TOF MS analysis.

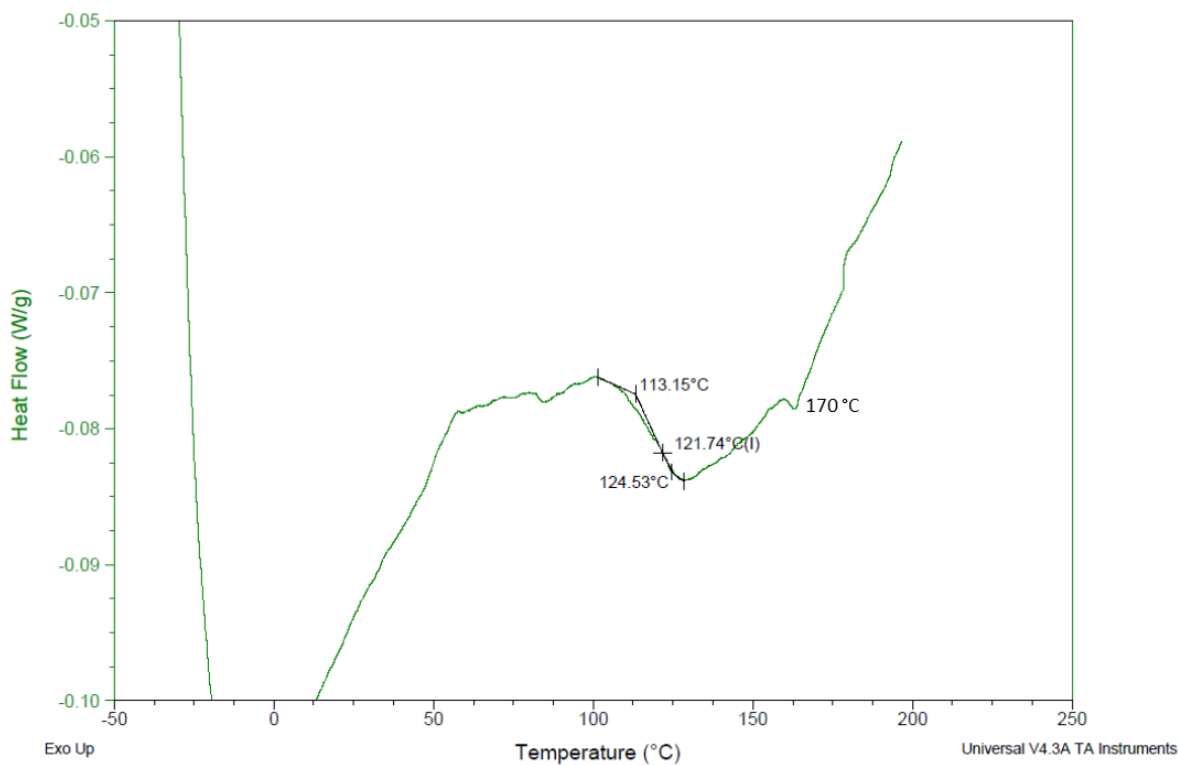


Figure 3.29 DSC thermogram of the PTB7-*b*-P4VP. Two peaks at ~120 °C and ~170 °C are distinguishable, related to the coil and the rod block, respectively.

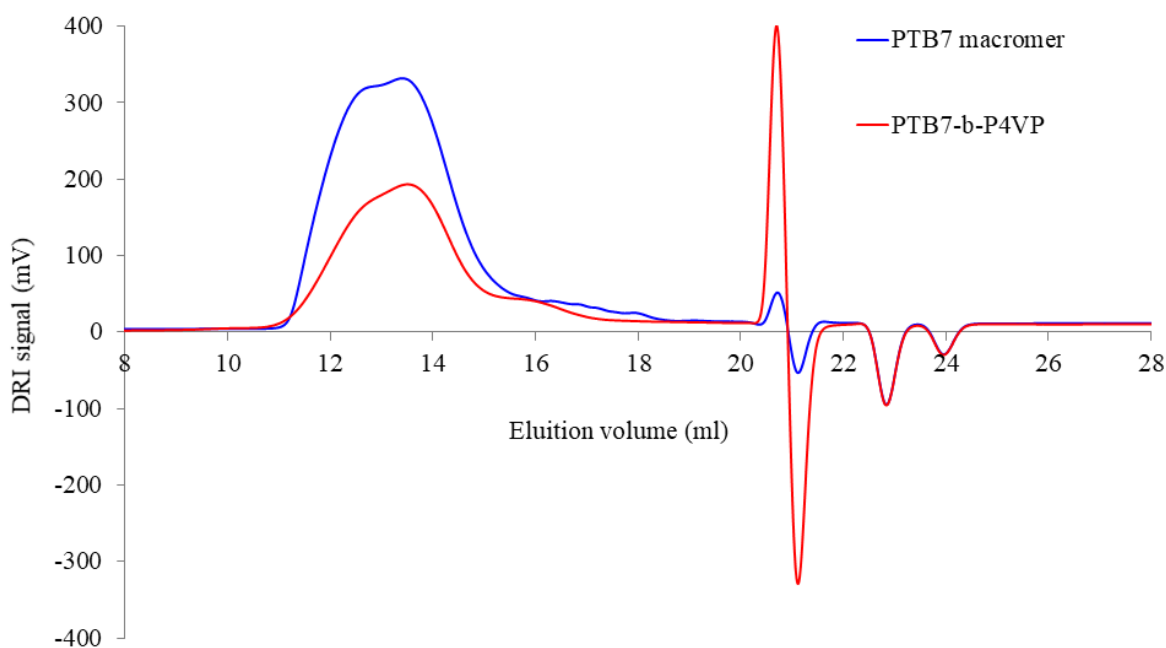


Figure 3.30 Chromatograms obtained by SEC analysis of the macromer PTB7 and the rod-coil PTB7-*b*-P4VP.

The 3D-UV spectra of the macromers PTB7 and the rod-coil PTB7-*b*-P4VP samples were shown in **Figure 3.31** and **Figure 3.33** collected with on-line Diode Array UV. From these

spectra it is possible to obtain UV spectra ($\lambda=200-800\text{ nm}$) at any retention time and then to study and correlate the structure and the conjugation length through the analysis of UV absorbance of the different conjugated component of the samples. **Figure 3.32** and **Figure 3.34** display the UV spectra ($\lambda=200-800$) of two samples extracted at different retention times (RT). The two samples showed similar conjugation and then similar length of the polymeric backbone.

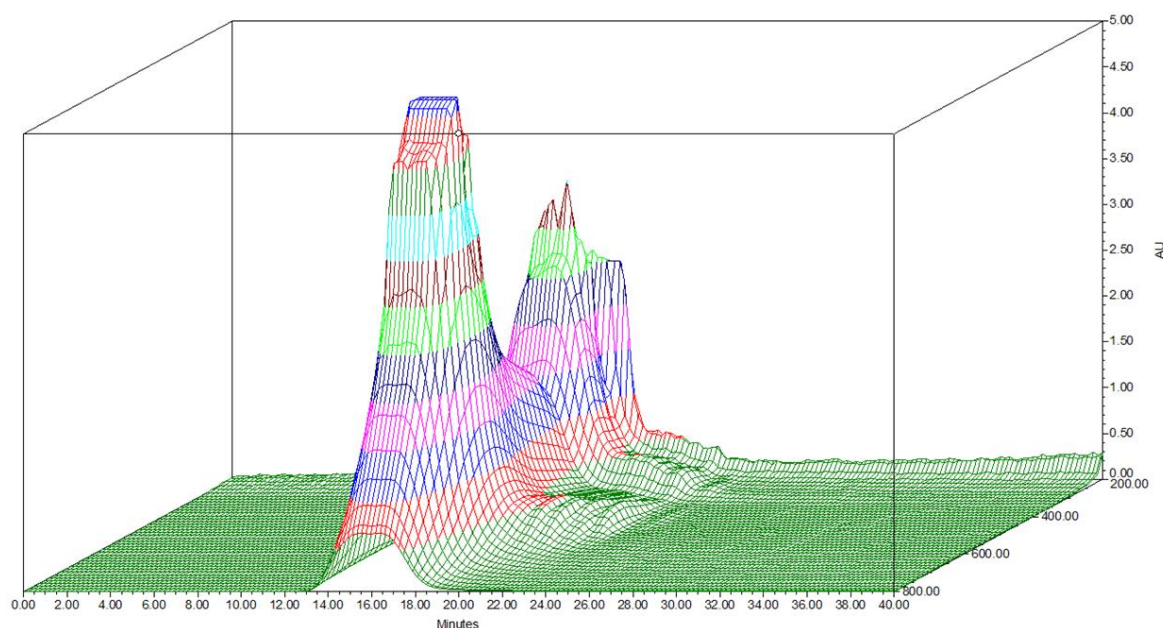


Figure 3.31 3D-UV structure of the sample PTB7 macromer.

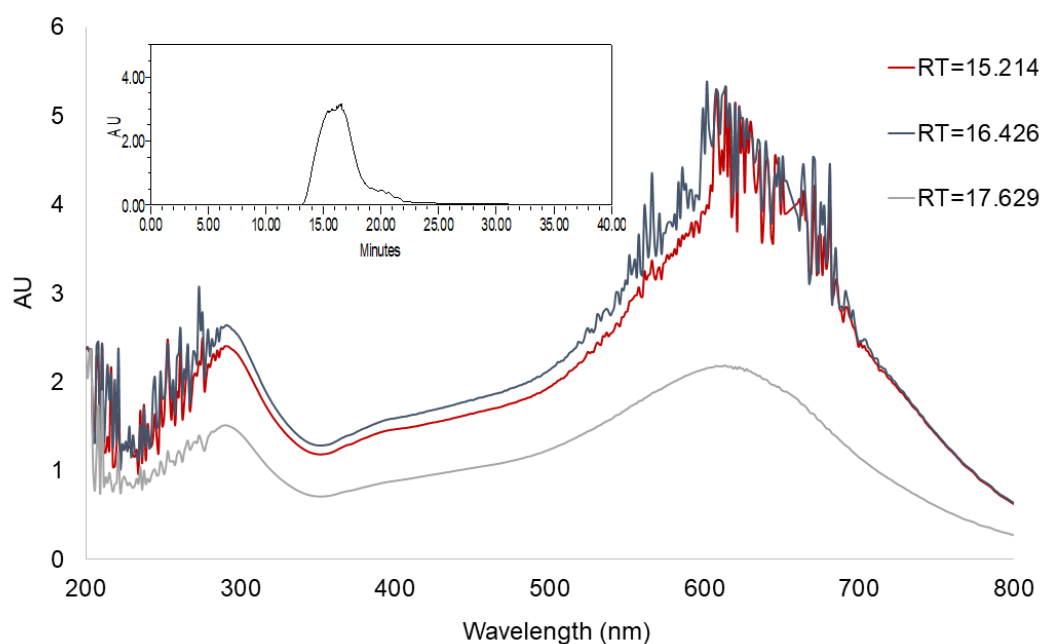


Figure 3.32 Overlay of the UV spectra of the sample PTB7 macromer. In the inset the chromatogram extracted at maximum wavelength.

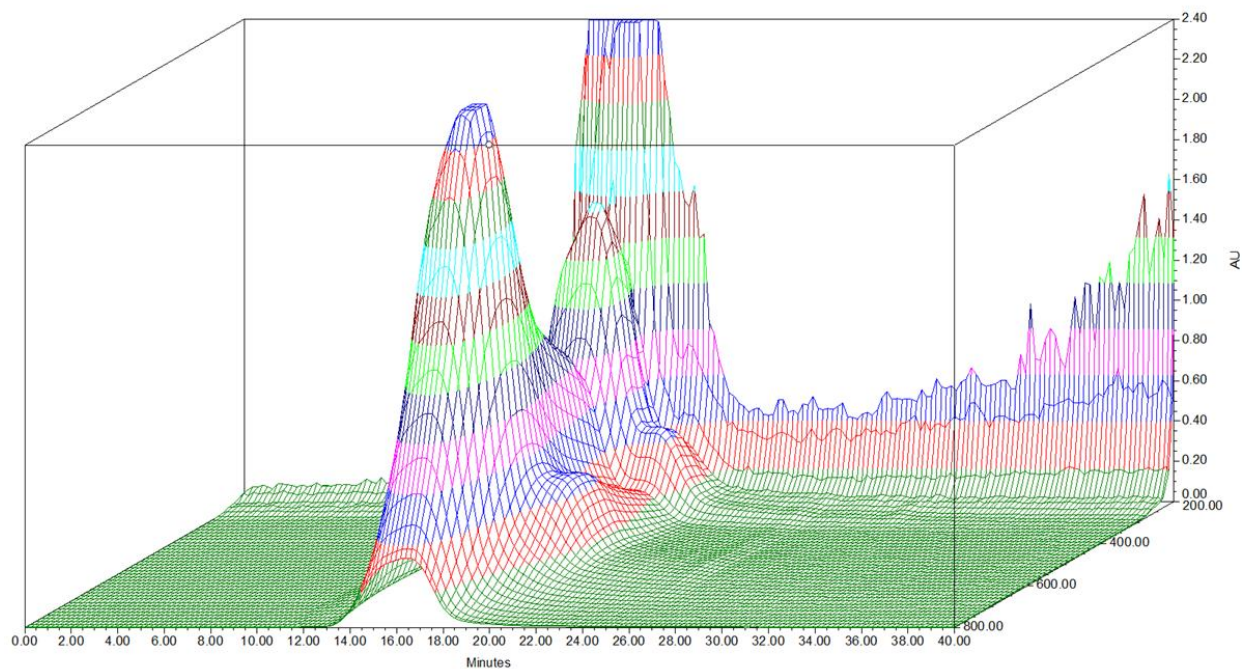


Figure 3.33 3D-UV structure of the sample PTB7-*b*-P4VP.

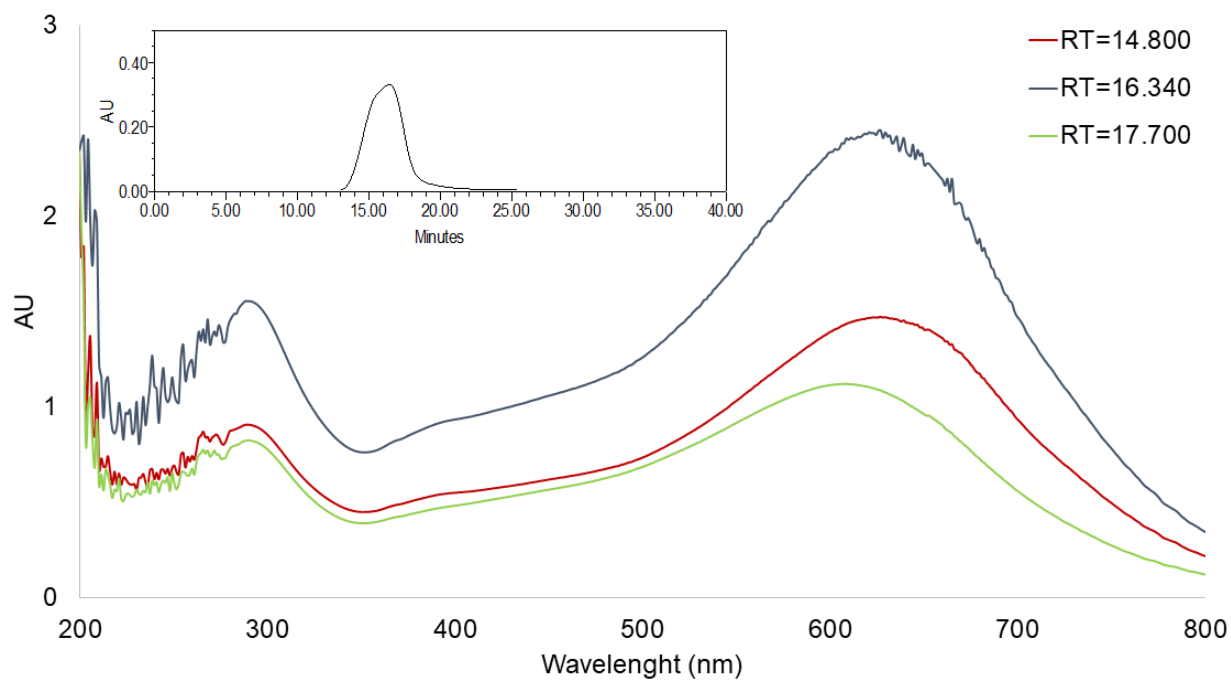
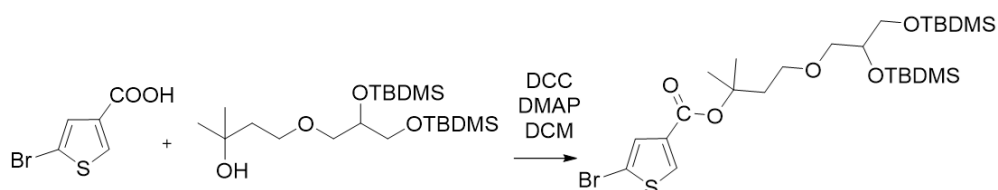


Figure 3.34 Overlay of the UV spectra of the sample PTB7-*b*-P4VP. In the inset the chromatogram extracted at maximum wavelength.

3.6.2.2 Synthesis of the PTB7-*b*-Krebs

Synthesis of the Krebs' ester (6).[46]



Scheme 3.3 Synthetic route for Krebs' ester.

5-bromo-thiophene-3-carboxylic acid (1 g, 4.83 mmol) was introduced into a Schlenk tube, and 12 ml of dichloromethane (DCM) was added. The mixture was stirred for 15 minutes, forming a whitish suspension. Therefore, 4-dimethylaminopyridine (DMAP) (681 mg, 5.57 mmol) was introduced, and the reaction mixture was stirred again for 15 minutes. 4-(2,3-bis((tert-butyl dimethylsilyl)oxy)propoxy)-2-methylbutan-2-ol (1.5 g, 3.71 mmol), dissolved in 3.8 ml of DCM, was added. Thus, the Schlenk tube was cooled at 0 °C and *N,N'*-dicyclohexylcarbodiimide (DCC) (1 g, 4.83 mmol) was introduced gradually. The reaction mixture was left under stirring at 0 °C for 30 minutes, then it was restored to room temperature, and subsequently warmed at 40 °C. After 20 hours, the reaction mixture was cooled at room temperature, diluted with DCM and filtered. Purification on a silica column using as eluent hexane:ethyl acetate (10:1) yielded the desired product as a colorless oil (1 g, Yield: 50%).

¹H-NMR (CDCl₃, 600 MHz, ppm) δ: 7.30 (d, 1H); 7.18 (d, 1H); 3.79-3.75 (m, 1H); 3.60-3.40 (m, 4H); 3.44 (dd, 2H); 2.16-2.14 (m, 2H); 1.60 (s, 6H); 0.88 (m, 18H); 0.07-0.03 (m, 2H).

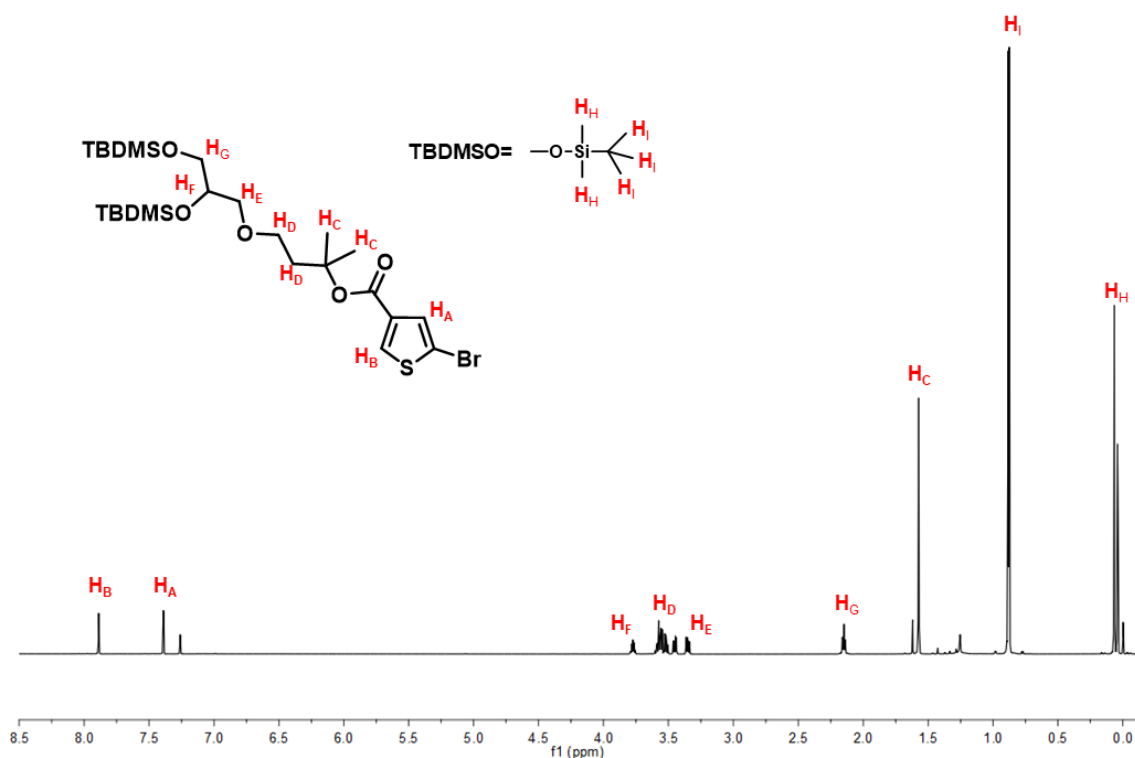


Figure 3.35 ^1H -NMR spectrum of Krebs' ester (**6**) performed in CDCl_3 .

Coupling between the macromer PTB7 and the coil Krebs' ester. After taking a sample of the macromer PTB7 (**3**) for the characterization, the Krebs' ester (490 mg, 0.82 mmol) was dissolved in 1 ml of toluene and 300 μl di DMF and introduced into the reaction Schlenk tube at room temperature, and 200 μl of catalytic solution was added to ensure the Stille coupling between the two blocks. The reaction mixture was heated again at 120 $^\circ\text{C}$ for 24 hours. After that, the Schlenk tube was cooled at room temperature, and 200 μl of degassed 2-bromothiophene was introduced to cap the residual stannyl terminal groups. After 24 hours at 120 $^\circ\text{C}$, 200 μl of degassed 2-(tributylstannyl)thiophene and some catalysts were added to cap the bromide terminal groups. The mixture was warmed at 120 $^\circ\text{C}$ for 24 hours. At this point, ~70 mg of Scavenger resin (3-mercaptopropyl-functionalized silica gel) was added, and after about 2 hours under stirring at 120 $^\circ\text{C}$ the mixture was filtered through Celite®, washing with toluene and chloroform. The filtrate was concentrated in vacuum and poured into methanol. The crude material was filtered, then extracted with Soxhlet apparatus in acetone, hexane, and chloroform, in sequence. The final product appears as a dark blue solid (**7**) (30 mg, Yield: 38%).

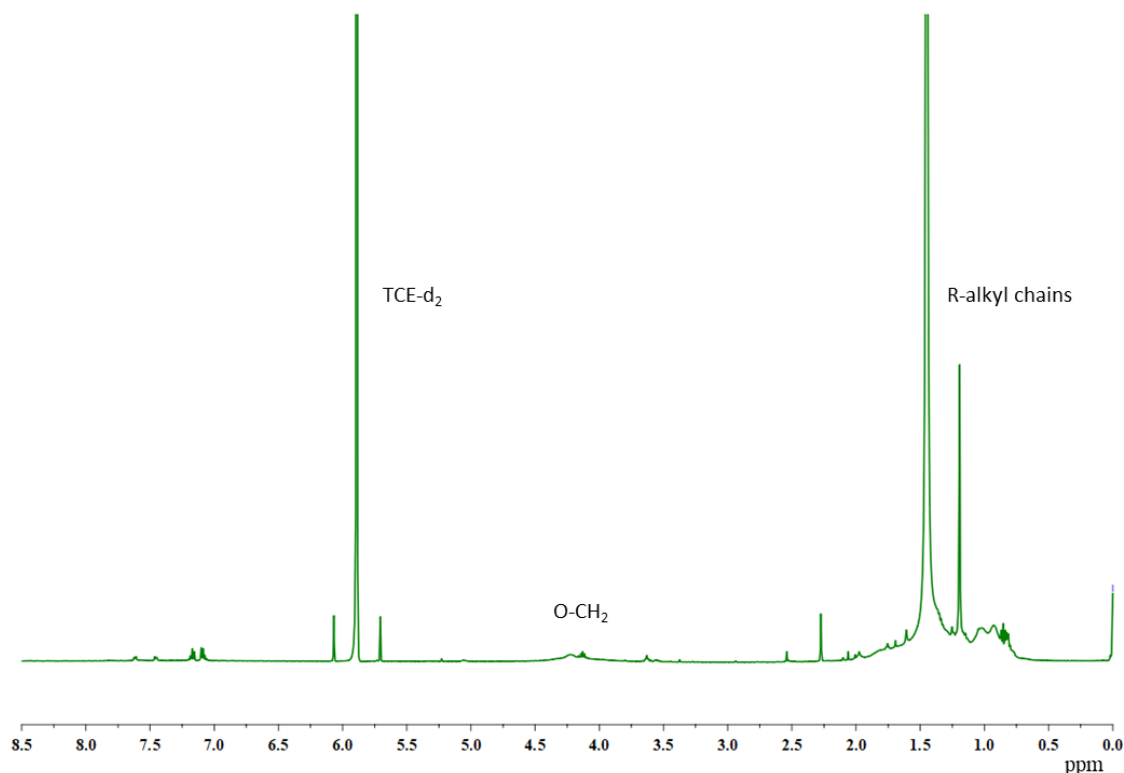


Figure 3.36 ^1H -NMR spectrum of the rod-coil PTB7-*b*-Krebs performed in TCE- d_2 .

3.6.3 BCP WPNP synthesis

The PC₇₁BM:BCP (1.1:1) blend WPNPs were prepared through a modified miniemulsion approach, based on the procedure developed by Landfester.[2] In a typical experiment, the two active materials composing the blend were dissolved into the mixture of toluene/*o*-xylene (in ratio 50:50) in order to achieve two starting solutions with standard concentrations, 20 mg ml⁻¹ and 10 mg ml⁻¹ for the PC₇₁BM and the BCP (PTB7-*b*-P4VP or PTB7-*b*-Krebs) respectively. In the case of PC₇₁BM:PTB7-*b*-P4VP:PTB7 WPNPs, a solution of pure PTB7 in toluene/*o*-xylene (10 mg ml⁻¹) was prepared, too. Therefore, a proper quantity of each starting organic solution was mixed up to obtain an active material organic solution with actual ratio of PC₇₁BM:PTB7-*b*-P4VP=1.1:1 (in the case of PC₇₁BM:PTB7-*b*-P4VP:PTB7 WPNPs, the ratio is equal to 1.1:0.70:0.30). Then 100 μl of the blend organic solution was sonicated and slowly poured into 1 ml of MilliQ water pre-heated at 50 °C, under vigorous stirring. After ~45 minutes the macroemulsion was sonicated for 40 minutes at 50 °C in an ultrasonic bath to achieve a stable miniemulsion, that was heated up to 105-110 °C to remove the solvent mixture under a gently stirring. 100 μl of MilliQ water pre-heated at 50 °C was regularly added if evaporated with the organic

solvent. After ~2 hours, a dark blue-brown aqueous suspension of WPNPs was obtained with a concentration of 1.26 mg ml^{-1} . All steps of the preparation were performed in air.

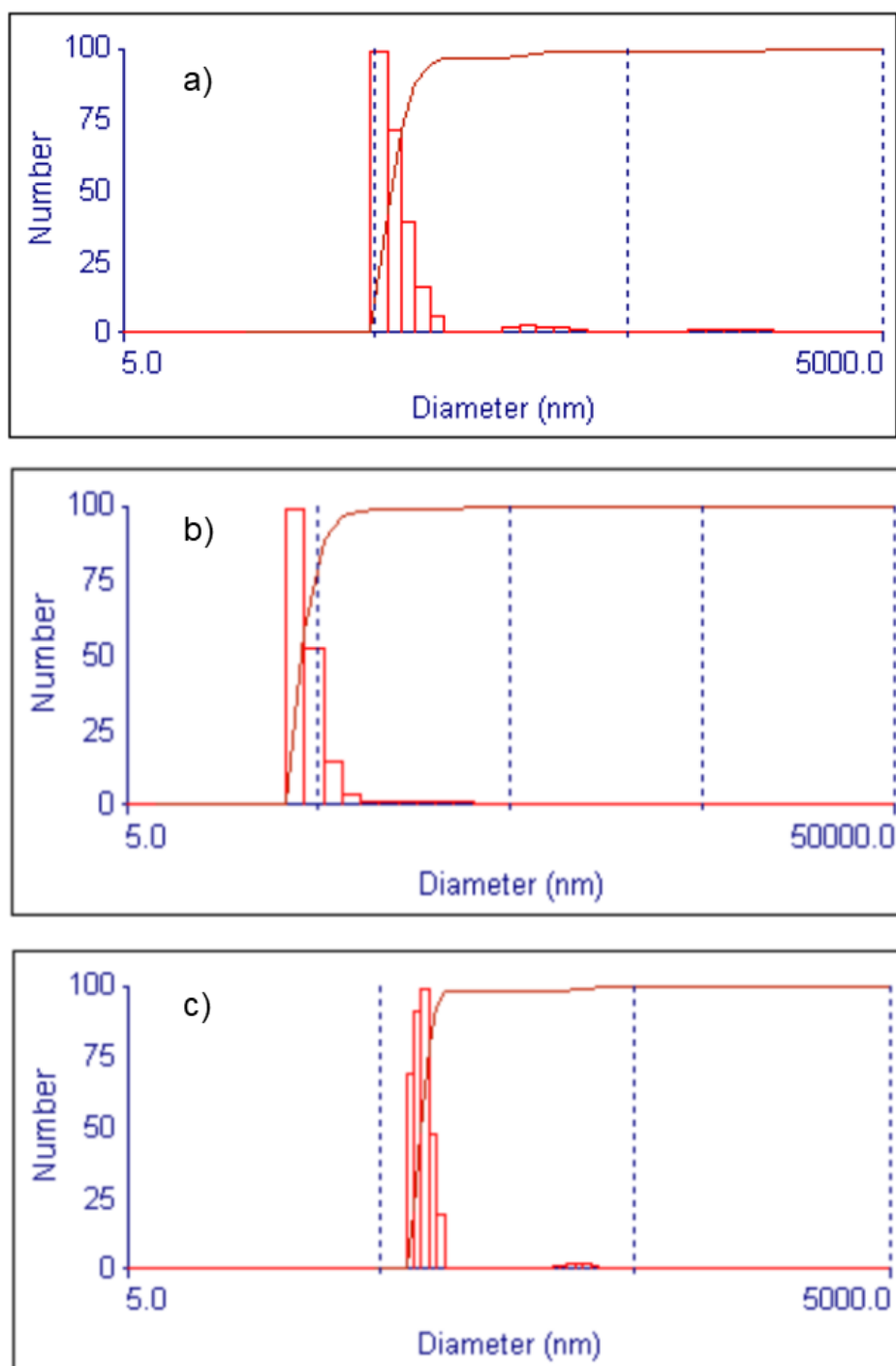


Figure 3.37 MSD distribution by number of **a)** PC₇₁BM:PTB7-*b*-P4VP (1.1:1) WPNPs, **b)** PC₇₁BM:PTB7-*b*-P4VP:PTB7 (1.1:0.70:0.30) WPNPs, and **c)** PC₇₁BM:PTB7-*b*-Krebs (1.1:1) WPNPs.

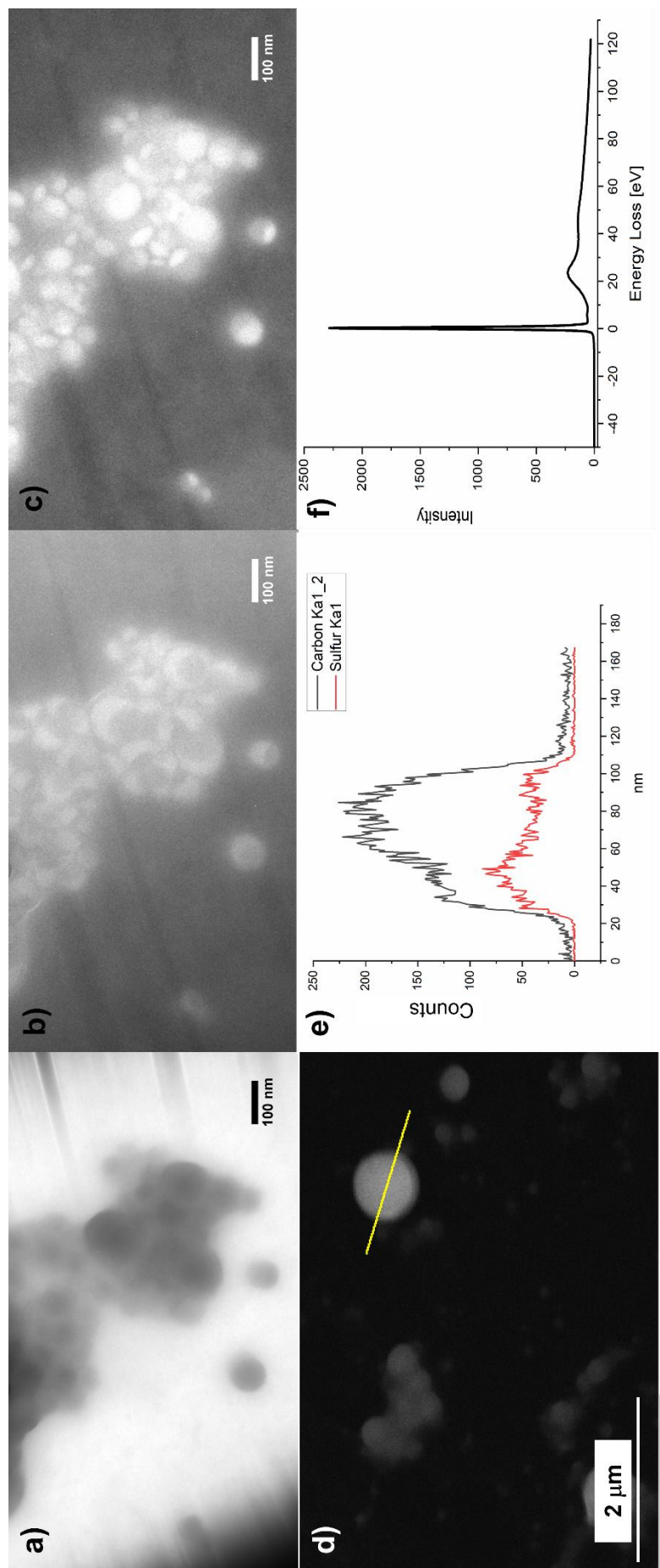


Figure 3.38 PC71BM:PTB7-b-P4VP (1.1:1) blend WPNPs images and microanalysis. a) conventional TEM image, b) EFTEM image at 17 eV. (the 521 domain containing PC71BM is darker), c) EFTEM at 30 eV (the domain containing PC71BM is lighter), and d) STEM image. The 522 yellow line indicates the line scan done to collect the EDX line scan reported in e). f) LOW LOSS EELS spectrum.

3.6.4 WPNP-based device fabrication

For the fabrication of the devices, glass substrates ($25 \times 25 \times 1.1 \text{ mm}^3$) coated with ITO with a sheet resistance of $15 \Omega \text{ sq}^{-1}$ were used. After mechanical cleaning with fibreless paper, the substrates were sonicated at $50 \text{ }^\circ\text{C}$ in water, acetone, and finally in 2-propanol for 10 minutes each step. After being dried with an N_2 gun, the substrates were subjected to plasma etching treatment for 10 minutes before a thick layer of PEDOT:PSS (~10 drops) was spin-coated at 1500 rpm for 60 seconds. The PEDOT:PSS layer was annealed at $200 \text{ }^\circ\text{C}$ for 15 minutes through a hotplate under N_2 flux. After this, it was exposed to a UV- O_3 treatment clean substrates for 10 minutes. $200 \mu\text{l}$ of ethanol were added to the WPNP suspension in order to facilitate the deposition. Therefore, WPNPs were spin-coated on the PEDOT:PSS layer at 500 rpm for 40 seconds. Eight repeated depositions of WPNP suspension were needed to have an active layer with an absorbance suitable for the device. Each layer was heated on hotplate at $60 \text{ }^\circ\text{C}$ for few minutes to completely remove water, then washed with ethanol to ease the following deposition. Finally, a thin PC_{61}BM layer (~20 nm) dissolved in dichloromethane (~20 μl) was deposited on the top of the active layer by spin-coating at 4000 rpm for 10 seconds. The finalized active layer was then annealed at $90 \text{ }^\circ\text{C}$ for 20 minutes in air.

The OPV device obtained with standard deposition of the active layer from organic solvents was fabricated into a glovebox. The blend constituted of 4 mg of PTB7-*b*-P4VP and 6 mg of PC_{71}BM was dissolved into chlorobenzene, together with 6 μl of anisaldehyde. The blend was spin-coated at 1500 rpm for 60 seconds. The active layer was annealed at $65 \text{ }^\circ\text{C}$ for 10 minutes.

All the substrates were inserted into a glovebox where 10 nm of Ca and 100 nm of Al were evaporated on top of the samples through a shadow mask under a pressure of $327.15 \times 10^{-6} \text{ mbar}$. The deposition rates were 0.7 nm s^{-1} for Al and 0.1 nm s^{-1} for Ca. On each substrate six devices were separately connected and characterized, each one with an active area of 6.1 mm^2 .

3.7 References

- [1] A.M. Ferretti, M. Diterlizzi, W. Porzio, U. Giovanella, L. Ganzer, T. Virgili, V. Vohra, E. Arias, I. Moggio, G. Scavia, S. Destri, S. Zappia, Rod-Coil Block Copolymer: Fullerene Blend Water-Processable Nanoparticles: How Molecular Structure Addresses Morphology and Efficiency in NP-OPVs, *Nanomaterials* 12(1) (2022).
- [2] K. Landfester, R. Montenegro, U. Scherf, R. Güntner, U. Asawapirom, S. Patil, D. Neher, T. Kietzke, Semiconducting Polymer Nanospheres in Aqueous Dispersion Prepared by a Miniemulsion Process, *Advanced Materials* 14(9) (2002) 651-655.
- [3] S. Zappia, G. Scavia, A.M. Ferretti, U. Giovanella, V. Vohra, S. Destri, Water-Processable Amphiphilic Low Band Gap Block Copolymer: Fullerene Blend Nanoparticles as Alternative Sustainable Approach for Organic Solar Cells, *Advanced Sustainable Systems* 2(3) (2018) 1700155.
- [4] M.C. Scharber, M. Koppe, J. Gao, F. Cordella, M.A. Loi, P. Denk, M. Morana, H.-J. Egelhaaf, K. Forberich, G. Dennler, R. Gaudiana, D. Waller, Z. Zhu, X. Shi, C.J. Brabec, Influence of the Bridging Atom on the Performance of a Low-Bandgap Bulk Heterojunction Solar Cell, *Advanced Materials* 22(3) (2010) 367-370.
- [5] M.C. Scharber, C. Lungenschmied, H.-J. Egelhaaf, G. Matt, M. Bednorz, T. Fromherz, J. Gao, D. Jarzab, M.A. Loi, Charge transfer excitons in low band gap polymer based solar cells and the role of processing additives, *Energy & Environmental Science* 4(12) (2011) 5077-5083.
- [6] M. Brinkmann, Insights into the structural complexity of semi-crystalline polymer semiconductors: electron diffraction contributions, *Materials Chemistry Frontiers* 4(7) (2020) 1916-1929.
- [7] H.-Y. Chen, J. Hou, S. Zhang, Y. Liang, G. Yang, Y. Yang, L. Yu, Y. Wu, G. Li, Polymer solar cells with enhanced open-circuit voltage and efficiency, *Nature Photonics* 3(11) (2009) 649-653.
- [8] Y. Liang, Z. Xu, J. Xia, S.-T. Tsai, Y. Wu, G. Li, C. Ray, L. Yu, For the Bright Future—Bulk Heterojunction Polymer Solar Cells with Power Conversion Efficiency of 7.4%, *Advanced Materials* 22(20) (2010) E135-E138.
- [9] S. Park, J. Jeong, G. Hyun, M. Kim, H. Lee, Y. Yi, The origin of high PCE in PTB7 based photovoltaics: proper charge neutrality level and free energy of charge separation at PTB7/PC71BM interface, *Scientific Reports* 6(1) (2016) 35262.
- [10] S. Zappia, R. Mendichi, S. Battiato, G. Scavia, R. Mastroia, F. Samperi, S. Destri, Characterization of amphiphilic block-copolymers constituted of a low band gap rigid segment (PCPDTBT) and P4VP based coil block synthesized by two different strategies, *Polymer* 80 (2015) 245-258.
- [11] B. Tan, Y. Li, M.F. Palacios, J. Therrien, M.J. Sobkowicz, Effect of surfactant conjugation on structure and properties of poly(3-hexylthiophene) colloids and field effect transistors, *Colloids and Surfaces A: Physicochemical and Engineering Aspects* 488 (2016) 7-14.
- [12] O. Ghazy, B. Freisinger, I. Lieberwith, K. Landfester, Tuning the size and morphology of P3HT/PCBM composite nanoparticles: towards optimized water-processable organic solar cells, *Nanoscale* 12(44) (2020) 22798-22807.
- [13] H.J. Son, W. Wang, T. Xu, Y. Liang, Y. Wu, G. Li, L. Yu, Synthesis of Fluorinated Polythienothiophene-co-benzodithiophenes and Effect of Fluorination on the Photovoltaic Properties, *Journal of the American Chemical Society* 133(6) (2011) 1885-1894.
- [14] Y. Liang, D. Feng, Y. Wu, S.-T. Tsai, G. Li, C. Ray, L. Yu, Highly Efficient Solar Cell Polymers Developed via Fine-Tuning of Structural and Electronic Properties, *Journal of the American Chemical Society* 131(22) (2009) 7792-7799.

- [15] L. Fernandes, H. Gaspar, J.P.C. Tomé, F. Figueira, G. Bernardo, Thermal stability of low-bandgap copolymers PTB7 and PTB7-Th and their bulk heterojunction composites, *Polymer Bulletin* 75(2) (2018) 515-532.
- [16] A.E. Di Mauro, M. Toscanini, D. Piovani, F. Samperi, M.L. Curri, M. Corricelli, L. De Caro, D. Siliqi, R. Comparelli, A. Agostiano, S. Destri, M. Striccoli, Segmented poly(styrene-co-vinylpyridine) as multivalent host for CdSe nanocrystal based nanocomposites, *European Polymer Journal* 60 (2014) 222-234.
- [17] F. Bencheikh, D. Duché, C.M. Ruiz, J.-J. Simon, L. Escoubas, Study of Optical Properties and Molecular Aggregation of Conjugated Low Band Gap Copolymers: PTB7 and PTB7-Th, *The Journal of Physical Chemistry C* 119(43) (2015) 24643-24648.
- [18] P. Groves, Diffusion ordered spectroscopy (DOSY) as applied to polymers, *Polymer Chemistry* 8(44) (2017) 6700-6708.
- [19] M.L. Huggins, The Viscosity of Dilute Solutions of Long-Chain Molecules. IV. Dependence on Concentration, *Journal of the American Chemical Society* 64(11) (1942) 2716-2718.
- [20] M. Rubinstein, R.H. Colby, *Polymer Physics*, Oxford University Press, 2003.
- [21] P.C. Hiemenz, L.P. Timothy, *Polymer Chemistry*, Second ed., Boca Rator, CRC P.2007.
- [22] D. Seo, J. Park, T.J. Shin, P.J. Yoo, J. Park, K. Kwak, Bathochromic shift in absorption spectra of conjugated polymer nanoparticles with displacement along backbones, *Macromolecular Research* 23(6) (2015) 574-577.
- [23] A.M. Ferretti, S. Zappia, G. Scavia, U. Giovanella, F. Villafiorita-Monteleone, S. Destri, Surfactant-free miniemulsion approach for low band gap rod-coil block copolymer water-processable nanoparticle fabrication: Film preparation and morphological characterization, *Polymer* 174 (2019) 61-69.
- [24] G.J. Hedley, A.J. Ward, A. Alekseev, C.T. Howells, E.R. Martins, L.A. Serrano, G. Cooke, A. Ruseckas, I.D.W. Samuel, Determining the optimum morphology in high-performance polymer-fullerene organic photovoltaic cells, *Nature Communications* 4(1) (2013) 2867.
- [25] Y.-C. Hsiao, T. Wu, M. Li, W. Qin, L. Yu, B. Hu, Revealing optically induced dipole-dipole interaction effects on charge dissociation at donor:acceptor interfaces in organic solar cells under device-operating condition, *Nano Energy* 26 (2016) 595-602.
- [26] M.R. Raj, M. Kim, H.I. Kim, G.-Y. Lee, C.W. Park, T. Park, A comparative study on the thermal- and microwave-assisted Stille coupling polymerization of a benzodithiophene-based donor-acceptor polymer (PTB7), *Journal of Materials Chemistry A* 5(7) (2017) 3330-3335.
- [27] B. Jańczuk, T. Białopiotrowicz, Surface free-energy components of liquids and low energy solids and contact angles, *Journal of Colloid and Interface Science* 127(1) (1989) 189-204.
- [28] M. Graupe, M. Takenaga, T. Koini, R. Colorado, T.R. Lee, Oriented Surface Dipoles Strongly Influence Interfacial Wettabilities, *Journal of the American Chemical Society* 121(13) (1999) 3222-3223.
- [29] F.M. Fowkes, ATTRACTIVE FORCES AT INTERFACES, *Industrial & Engineering Chemistry* 56(12) (1964) 40-52.
- [30] Y. Liu, D. Tang, K. Zhang, P. Huang, Z. Wang, K. Zhu, Z. Li, L. Yuan, J. Fan, Y. Zhou, B. Song, Tuning Surface Energy of Conjugated Polymers via Fluorine Substitution of Side Alkyl Chains: Influence on Phase Separation of Thin Films and Performance of Polymer Solar Cells, *ACS Omega* 2(6) (2017) 2489-2498.
- [31] B. Tang, J. Liu, X. Cao, Q. Zhao, X. Yu, S. Zheng, Y. Han, Restricting the liquid-liquid phase separation of PTB7-Th:PF12TBT:PC71BM by enhanced PTB7-Th solution

- aggregation to optimize the interpenetrating network, *RSC Advances* 7(29) (2017) 17913-17922.
- [32] L. Krishnan Jagadamma, R.G.D. Taylor, Alexander L. Kanibolotsky, M.T. Sajjad, I.A. Wright, P.N. Horton, S.J. Coles, I.D.W. Samuel, P.J. Skabara, Highly efficient fullerene and non-fullerene based ternary organic solar cells incorporating a new tetrathiocin-cored semiconductor, *Sustainable Energy & Fuels* 3(8) (2019) 2087-2099.
- [33] T. Supasai, V. Amornkitbamrung, C. Thanachayanont, I.M. Tang, T. Sutthibutpong, N. Rujisamphan, Visualizing nanoscale phase morphology for understanding photovoltaic performance of PTB7: PC71BM solar cell, *Applied Surface Science* 422 (2017) 509-517.
- [34] O. Dyck, S. Hu, S. Das, J. Keum, K. Xiao, B. Khomami, G. Duscher, Quantitative Phase Fraction Detection in Organic Photovoltaic Materials through EELS Imaging, *Polymers* 7(11) (2015).
- [35] R. Pal, L. Bourgeois, M. Weyland, A.K. Sikder, K. Saito, A.M. Funston, J.R. Bellare, Chemical fingerprinting of polyvinyl acetate and polycarbonate using electron energy-loss spectroscopy, *Polymer Chemistry* 11(34) (2020) 5484-5492.
- [36] A.S. Dudnik, T.J. Aldrich, N.D. Eastham, R.P.H. Chang, A. Facchetti, T.J. Marks, Tin-Free Direct C–H Arylation Polymerization for High Photovoltaic Efficiency Conjugated Copolymers, *Journal of the American Chemical Society* 138(48) (2016) 15699-15709.
- [37] S.F. Hoefler, T. Rath, N. Pastukhova, E. Pavlica, D. Scheunemann, S. Wilken, B. Kunert, R. Resel, M. Hobisch, S. Xiao, G. Bratina, G. Trimmel, The effect of polymer molecular weight on the performance of PTB7-Th:O-IDTBR non-fullerene organic solar cells, *Journal of Materials Chemistry A* 6(20) (2018) 9506-9516.
- [38] W. Porzio, G. Scavia, L. Barba, G. Arrighetti, S. Milita, Depth-resolved molecular structure and orientation of polymer thin films by synchrotron X-ray diffraction, *European Polymer Journal* 47(3) (2011) 273-283.
- [39] A.L. Ayzner, C.J. Tassone, S.H. Tolbert, B.J. Schwartz, Reappraising the Need for Bulk Heterojunctions in Polymer–Fullerene Photovoltaics: The Role of Carrier Transport in All-Solution-Processed P3HT/PCBM Bilayer Solar Cells, *The Journal of Physical Chemistry C* 113(46) (2009) 20050-20060.
- [40] Z.-G. Zhang, H. Li, Z. Qi, Z. Jin, G. Liu, J. Hou, Y. Li, J. Wang, Poly(ethylene glycol) modified [60]fullerene as electron buffer layer for high-performance polymer solar cells, *Applied Physics Letters* 102(14) (2013) 143902.
- [41] A. Sperlich, M. Auth, V. Dyakonov, Charge Transfer in Ternary Solar Cells Employing Two Fullerene Derivatives: Where do Electrons Go?, *Israel Journal of Chemistry* n/a(n/a) (2021).
- [42] F. Carulli, G. Scavia, E. Lassi, M. Pasini, F. Galeotti, S. Brovelli, U. Giovanella, S. Luzzati, A bifunctional conjugated polyelectrolyte for the interfacial engineering of polymer solar cells, *Journal of Colloid and Interface Science* 538 (2019) 611-619.
- [43] C.H. To, A. Ng, Q. Dong, A.B. Djurišić, J.A. Zapien, W.K. Chan, C. Surya, Effect of PTB7 Properties on the Performance of PTB7:PC71BM Solar Cells, *ACS Applied Materials & Interfaces* 7(24) (2015) 13198-13207.
- [44] T. Vangerven, P. Verstappen, J. Drijkoningen, W. Dierckx, S. Himmelberger, A. Salleo, D. Vanderzande, W. Maes, J.V. Manca, Molar Mass versus Polymer Solar Cell Performance: Highlighting the Role of Homocouplings, *Chemistry of Materials* 27(10) (2015) 3726-3732.
- [45] N. Sary, F. Richard, C. Brochon, N. Leclerc, P. Lévêque, J.-N. Audinot, S. Berson, T. Heiser, G. Hadziioannou, R. Mezzenga, A New Supramolecular Route for Using Rod-Coil Block Copolymers in Photovoltaic Applications, *Advanced Materials* 22(6) (2010) 763-768.

Chapter 3

[46] R. Søndergaard, M. Helgesen, M. Jørgensen, F.C. Krebs, Fabrication of Polymer Solar Cells Using Aqueous Processing for All Layers Including the Metal Back Electrode, *Advanced Energy Materials* 1(1) (2011) 68-71.

Chapter 4

Investigation on two low band gap BDT-based polymers and on the middle band gap polymer PDCBT: synthesis, characterization, and perspectives

The content of this chapter was partially presented by Nicola Gasparini at the seminary “Status and perspective of organic photovoltaic: is it ready for commercialisation?”, 2nd December 2021, SCITEC-CNR, Milano (Italy).

4.1 Introduction

With the aim of producing sustainable organic solar cells (OSCs) with high efficiencies, and to improve the efficiency of the organic photovoltaic (OPV) devices fabricated from aqueous inks, we explored other semiconducting polymers as electron-donor materials. Particularly, we focused on two new low band gap (LBG) polymers and a medium band gap one.

The LBG polymers we chose consist of alternating 4,8-bis(5-(2-ethylhexyl)-4-fluorothiophen-2-yl)benzo[1,2-b:4,5-b']dithiophene (BDTTDF) and 2-ethylhexyl-3-fluorothieno[3,4-b]thiophene-2-carboxylate (FTTh) moieties, similarly to PTB7-Th (also known as PCE10),[1-5] with the main difference of two extra fluorine atoms on the electron-rich unit. Because the resulting polymer (hereafter PTB7-Th-F₂) presented solubility issues in the most common organic solvents, we decided to incorporate into the polymeric backbone an electron-withdrawing unit, namely a methyl ester-substituted thiophene.[6]. Besides to increase material solubility, the insertion of the methyl ester might lead to an improvement in the performance of the final device. In fact, it is reported in the literature that one of the main pathways to enhance the power conversion efficiency (PCE) of OPV devices is to broaden the absorption bandwidth of the photoactive layer to boost sunlight absorption. In this regard, the copolymerization of different building blocks is an effective method to optimize the electronic structure of the material, obtaining proper molecular energy levels, and thus improving the device performance.[7-9] Specifically, the ester group-substituted thiophene that we decided to include is able to increase the withdrawing property of the acceptor building block. Cui *et al.* adopted this approach, reaching a PCE of ~15% using non-fullerene acceptor (NFA) material in the photoactive layer.[6] Following their route, we will test the two BDT-based polymers as active donor material, in blend with both fullerene and NFA materials.

In recent years NFAs emerged as a very intriguing alternative to traditional fullerene molecules due to the possibility to tune their molecular energy levels, providing strong absorption capabilities and good electron mobilities. Thanks to these features, NFAs represent an excellent opportunity to develop OPV devices with PCEs surpassing those of fullerene-based devices.[10] In fact, NFAs are designed not only to match the electron accepting and transport properties typical of fullerenes, but also to bypass the poor optical properties, and long-term stability issues related to fullerene acceptors.[11] Similar to donor semiconducting polymers, most NFAs are characterized by push-pull hybridization, which

imparts strong absorption in both the visible and near-IR regions of the solar spectrum. Consequently, they can absorb a large number of photons, forming a lot of excitons and maximizing the photocurrent. A further peculiarity of NFAs is the inclusion of long alkyl chains or other steric hindrances to enhance their solubility and processability in the most common organic solvents, even in solvents considered “green”, such as tetrahydrofuran (THF). Several studies were published in which NFA molecules are employed in blend with electron-donor polymers to prepare water-processable nanoparticle (WPNP) aqueous suspensions, for a sustainable deposition of OSC active layers.[12, 13]

The last polymer we studied is the middle band gap poly [2,2'-(2,2'-bis[[[(2-butyloctyl)oxy]carbonyl][2,2':5,2''-quaterthiophene]-5,5''-diyl] (PDCBT), a polythiophene based on dialkyl-(2,2'-bithiophene-5,5'-diyl)-4,4'-dicarboxylate with the bithiophene as comonomer.[14] Poly(3-hexylthiophene) (P3HT) is the most studied material for OSCs as wide band gap absorber.[15-18] The P3HT attracted the interest of researcher thanks to its semicrystalline nature, which endows a high charge carrier mobility. Specifically, the regioregular P3HT was widely exploited in blend with phenyl-C₆₁-butyric acid methyl ester (PC₆₁BM), even if the corresponding OPV device has an efficiency limited by the relatively low open-circuit voltage (V_{OC}) (0.6 V), because of the low oxidation potential of the donor material. The insertion of electron-withdrawing ester side chains leads to the reduction of the highest occupied molecular orbital (HOMO) level, and to an increase in the oxidation potential.[19] Currently, PDCBT is already widely reported in the literature, since it is characterized by a better V_{OC} value (0.9 V) than P3HT, and it allows to achieve a PCE up to 7% when blended with phenyl-C₇₁-butyric acid methyl ester (PC₇₁BM).[14, 20] This variation in photovoltaic parameters could be related to the degree of aggregation, which significantly changes with the introduction of additional ester side chains, affecting energy levels, band gap, and thus final performances.[14, 21, 22]

Based on these considerations, we decided to synthesize the polymers discussed above to prepare aqueous inks in blend with fullerene and non-fullerene acceptor materials, for fabricating sustainable WPNP-based OPV devices.

4.2 Results and Discussion

4.2.1 Synthesis and Characterization of PTB7-Th-F₂ and PTB7-Th-F₂-Me ester

We synthesized a new LBG polymer whose molecular structure is very similar to the well-known PTB7-Th with the main difference that the electron-rich unit contains two extra

fluorine atoms.[2, 6, 23] The semiconducting polymer PTB7-Th-F₂ (**4**) was synthesized through a Stille coupling between the electron-rich monomer 2,6-bis(trimethyltin)-4,8-bis(5-(2-ethylhexyl)-4-fluorothiophen-2-yl)benzo[1,2-b:4,5-b']dithiophene (hereafter BDTTDFS_n) (**1**) and the electron-poor 2-ethylhexyl 4,6-dibromo-3-fluorothiopheno[3,4-b]thiophene-2-carboxylate (FTThBr) (**2**), as represented in **Scheme 4.1**. [24, 25] The resulting material is difficult to dissolve in the most common organic solvents, thus we tried the random insertion of a small amount (5% or 10%) of a thiophene derivative into the polymeric chain, with the aim to decrease the backbone rigidity, and to induce a higher conformational freedom in solution. We selected as thiophene derivative the methyl-2,5-dibromothiophene-3-carboxylate (methyl ester, **Figure 4.1a**) and the Krebs' ester (**Figure 4.1b**), already presented in Chapter 3.

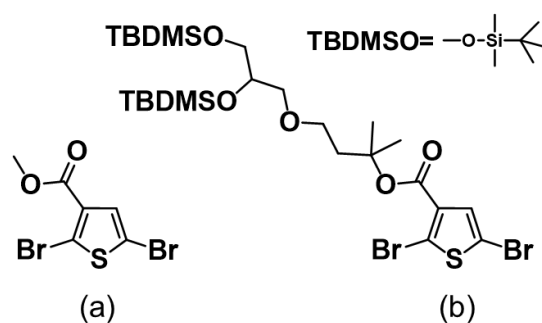
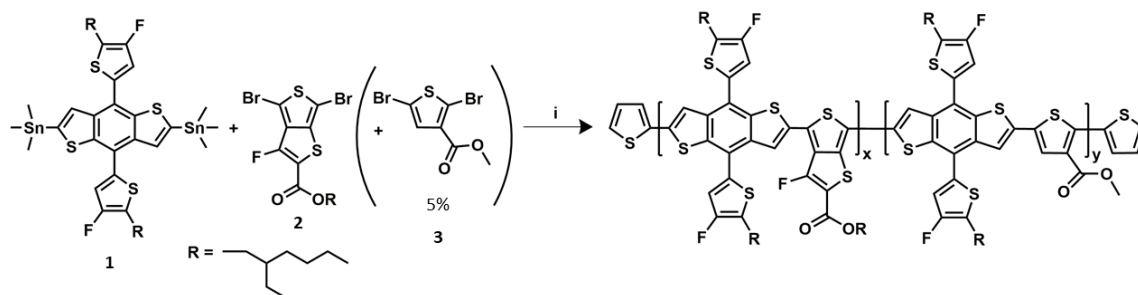


Figure 4.1 Chemical structure of **a**) methyl ester and **b**) Krebs' ester, selected to be inserted into the polymeric backbone of the PTB7-Th-F₂.

Matrix assisted laser desorption/ionization time of flight mass spectroscopy (MALDI-TOF MS) experiments, performed by Dr. Filippo Samperi (IPCB-CNR, Catania), revealed that insertion far from feeding is achieved using Krebs' ester. A similar result was observed including the 10% of methyl ester. Therefore, we considered only the polymer incorporating the 5% of the methyl ester-thiophene derivative, as it bears a short ester group, allowing insertion within the backbone, without important steric hindrance effects. In this manner, we gained a new LBG copolymer that we named PTB7-Th-F₂-Me ester (**5**). The feeding conditions to obtain the two materials are summarized in **Table 4.1**. Size exclusion chromatography (SEC) measurements were carried out by Dr. Stefania Zappia (SCITEC-CNR, Milano), and the achieved numerical molecular weight (M_n) and weighted molecular weight (M_w) values are illustrated in **Table 4.1**.



Scheme 4.1 Synthetic route for the polymers PTB7-Th-F₂ (x=1; y=0) and PTB7-Th-F₂-Me ester (x=0.95; y=0.05). Reaction conditions: i) Pd₂(dba)₃, P(*o*-tol)₃, 110 °C, 24 h.

Table 4.1 Feeding conditions adopted to obtain the polymers PTB7-Th-F₂ and PTB7-Th-F₂-Me ester. MWD data were obtained through SEC analysis.

Sample		x	y	M _n (g mol ⁻¹)	M _w (g mol ⁻¹)	M _w /M _n
PTB7-Th-F ₂	4	1.00	0	39780	84740	2.10
PTB7-Th-F ₂ -Me ester	5	0.95	0.05	47870	108800	2.30

We verified that the insertion of the methyl ester in the polymer chain leads to an improvement in solubility by means of tests conducted in a series of solvents (**Figure 4.2**). As a matter of fact, PTB7-Th-F₂-Me ester is more soluble than PTB7-Th-F₂ in the most common organic solvents. Remarkably, it dissolves more easily in non-halogenated ones (THF, toluene and xylene), even in solvents considered “green” as THF, while in chloroform it needs to be heated to totally dissolve. It is important to note the THF is considered “green” with respect to halogenated ones, but it is not without risk. 2-Methyltetrahydrofuran (Me-THF) is a more environmentally friendly and less toxic alternative to THF, hence it might improve the overall process economy.[26] Unluckily, the materials discussed in this chapter are not soluble in this solvent.

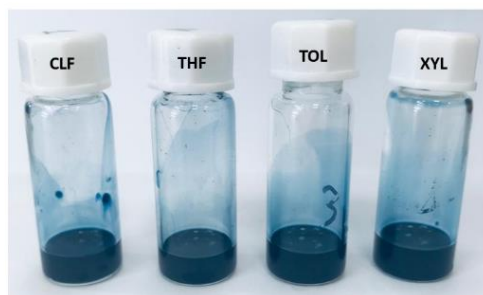


Figure 4.2 Solubility tests of the polymer PTB7-Th-F₂-Me ester in several solvents. From left to right the solutions in chloroform (CLF), tetrahydrofuran (THF), toluene (TOL) and *o*-xylene (XYL) (at the same concentration 5 mg ml⁻¹) are depicted.

The other difference between the two polymers resides in the absorption properties in solution. In fact, observing **Figure 4.3**, where the spectra of the two materials dissolved in toluene are shown, it is possible to notice that the maximum of the PTB7-Th-F₂-Me ester is red shifted compared to PTB7-Th-F₂ one. This behavior may be ascribable to dissimilar solubility in toluene, which leads to distinct aggregation mechanisms of the two materials. Indeed, we excluded that the different absorption was related to a different energy gap. In fact, cyclovoltammetry (CV) measurements were performed on films of PTB7-Th-F₂-Me ester and PTB7-Th-F₂, in collaboration with Dr. Nicola Gasparini (Imperial College, London). Particularly, both polymers exhibit the highest occupied molecular orbital (HOMO) and the lowest unoccupied molecular orbital (LUMO) levels of -5.5 eV and -3.3 eV, respectively. For organic semiconductors, HOMO represents the energy necessary to extract an electron from a molecule, thus implying an oxidation process, and LUMO is the energy required to inject an electron into a molecule, which is a reduction process.[27] These processes were measured for PTB7-Th-F₂ and PTB7-Th-F₂-Me ester by means of the redox potentials E_{red} and E_{ox} . **Figure 4.4a** and **b** display the oxidation and reduction curves of PTB7-Th-F₂ and PTB7-Th-F₂-Me ester, respectively, drop-casted directly onto a glassy carbon working electrode, and using ferrocene as the reference electrode. Ferrocene is used as standard reference to calculate the energy of the HOMO and LUMO levels, including the ferrocene value of -4.4 eV. Therefore, energy levels were calculated using the empirical Bredas' equations:[28] $E(\text{HOMO})=-e[E_{\text{ox,onset}}+4.4]$; $E(\text{LUMO})=-e[E_{\text{red,onset}}+4.4]$. The difference between HOMO and LUMO levels is the energy gap ($E_{\text{gap}}=\text{HOMO}-\text{LUMO}$). The obtained HOMO/LUMO and E_{gap} values are summarized in **Table 4.2**.

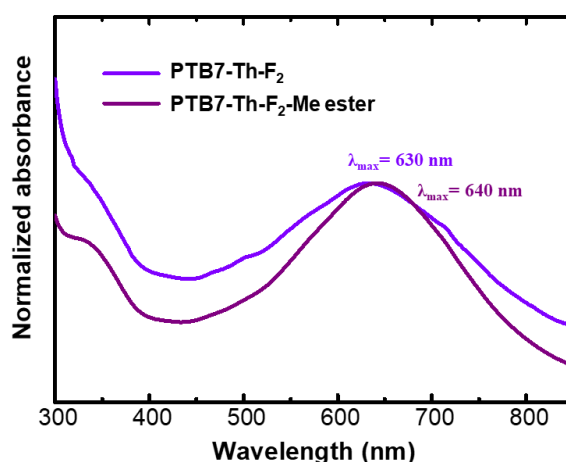


Figure 4.3 UV-Vis normalized spectra of PTB7-Th-F₂ and PTB7-Th-F₂-Me ester in toluene.

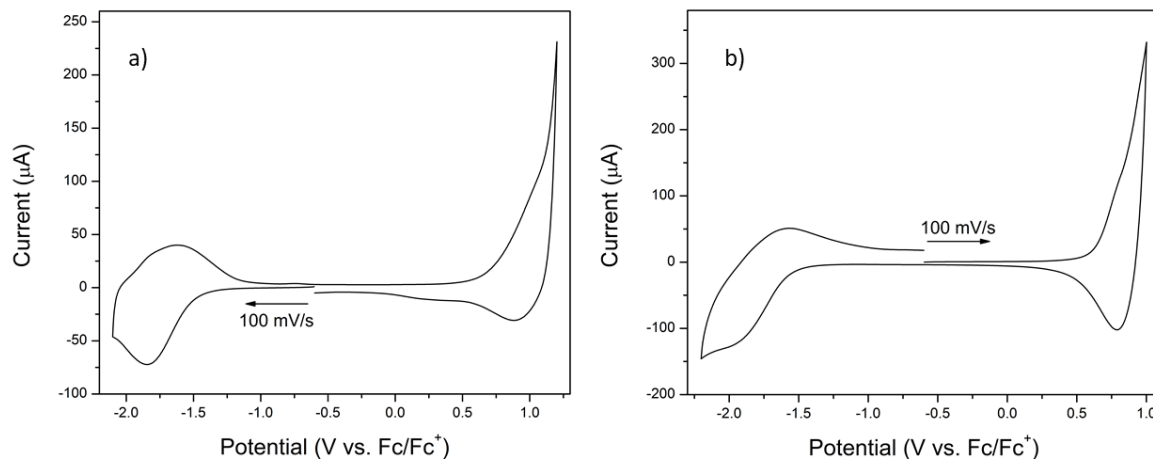


Figure 4.4 Oxidation and reduction curves of **a)** PTB7-Th-F₂: onset of reduction at -1.5 V vs. Fc/Fc⁺ (-3.3 eV); with a half-wave potential of -1.7 V (-3.1 eV); onset of oxidation at 0.7 V vs. Fc/Fc⁺ (-5.5 eV); **b)** PTB7-Th-F₂-Me ester: onset of reduction at -1.5 V vs. Fc/Fc⁺ (-3.3 eV); onset of oxidation at 0.7 V vs. Fc/Fc⁺ (-5.5 eV).

Table 4.2 HOMO/LUMO levels calculated from oxidation and reduction curves.

Sample	HOMO (eV)	LUMO (eV)	E _{gap} (eV)
PTB7-Th-F ₂	-5.5	-3.3	2.4
PTB7-Th-F ₂ -Me ester	-5.5	-3.3	2.4

In addition, proton nuclear magnetic resonance (¹H-NMR) and MALDI-TOF MS techniques were exploited to deeply investigate the polymeric structures, and in particular to understand the actual insertion of the thiophene derivative into the polymeric backbone of PTB7-Th-F₂-Me ester. As mentioned above, MALDI-TOF MS spectrum of PTB7-Th-F₂-Me ester confirms the feed, meaning that ~5% of copolymer with methyl ester was detected.

Also, differential scanning calorimetry (DSC) measurements were performed by Samperi's group. In the thermograms, exothermic peaks are observed in the first heating cycle between 90 °C and 160 °C, related to both PTB7-Th-F₂ and the PTB7-Th-F₂-Me ester, indicating that some reactions occur in this temperature range. Immediately afterwards an endothermic transition at ~170 °C is shown, denoting the polymer melting process. The thermograms of PTB7-Th-F₂ and PTB7-Th-F₂-Me ester are depicted in the Experimental Section (**Figure 4.9** and **Figure 4.10**), and they differ in shape and intensity of the exothermic peak. Further experiments are in progress to clarify the nature of the exothermic process and the origin of this different behavior of the two materials.

Lastly, contact angles and surface energy measurements were conducted by Dr. Nicola Gasparini (Imperial College, London). The insertion of the methyl ester influences the polymeric interactions with substrates. In fact, contact angle and surface energy measurements on both PTB7-Th-F₂ and PTB7-Th-F₂-Me ester revealed some slightly differences, as illustrated in **Table 4.3**. Contact angles were detected using water, ethylene glycol, and diiodomethane as test liquids.

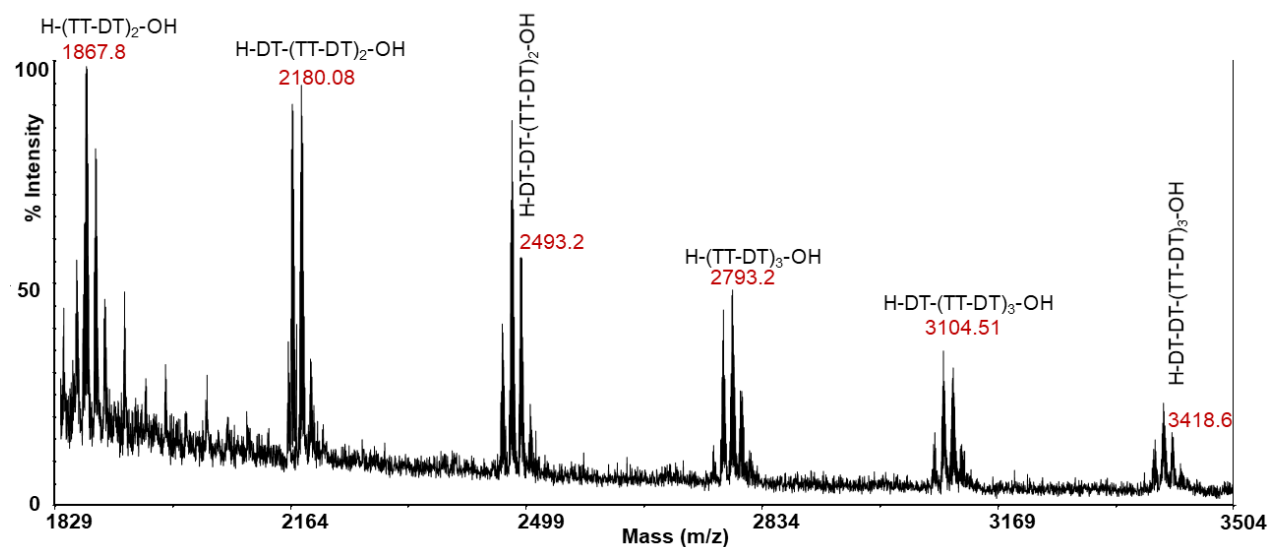


Figure 4.5 Enlarged section of the positive ions MALDI-TOF mass spectrum of the PTB7-Th-F₂ homopolymer recorded in reflectron mode using α -cyano as matrix.

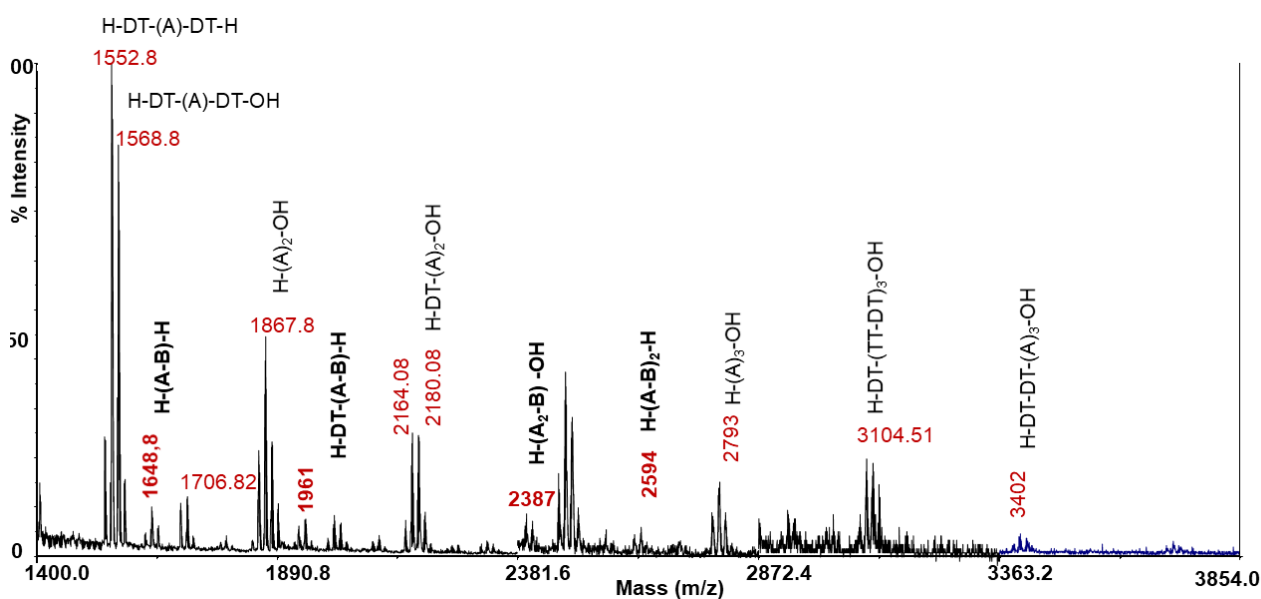


Figure 4.6 Enlarged section of the positive ions MALDI-TOF mass spectrum of the PTB7-Th-F₂-Me ester copolymer recorded in reflectron mode using α -cyano as matrix. (Copolymer species are labelled in bold).

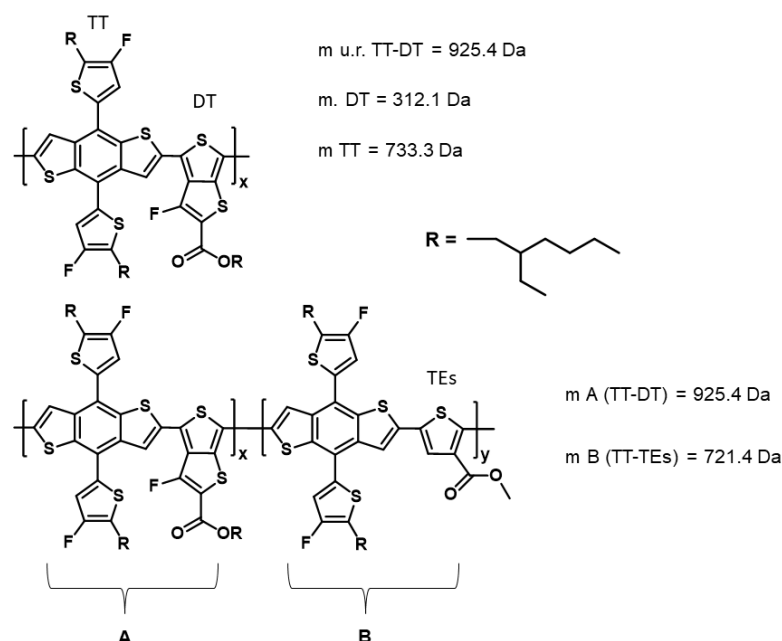


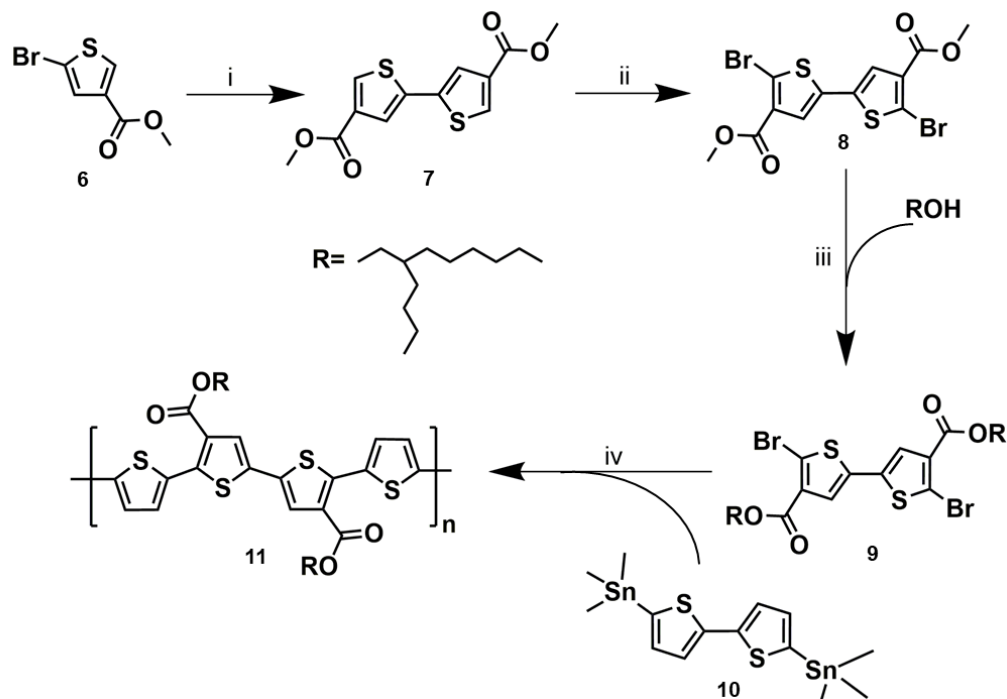
Chart 4.1 Structures of the PTB7-Th-F₂ and PTB7-Th-F₂-Me ester polymer chains detected by MALDI-TOF MS analysis (**Figure 4.5** and **Figure 4.6**, respectively).

Table 4.3 Contact angles of water (WAT), ethylene glycol (EG), and diiodomethane (DIM) on the PTB7-Th-F₂ and PTB7-Th-F₂-Me ester, and surface energy (γ) for the two samples.

Sample	Θ_{WAT} (°)	Θ_{EG} (°)	Θ_{DIM} (°)	γ (mN m ⁻¹)
PTB7-Th-F₂	98.0	22.9	49.5	43.7
PTB7-Th-F₂-Me ester	98.2	23.0	59.9	38.5

4.2.2 Synthesis and Characterization of PDCBT

The last material under study in this chapter is a middle band gap polymer based on thiophene and thiophene rings substituted by electron-withdrawing carboxylate side groups, already reported, and widely studied. Particularly, we synthesized the poly [2,2'''-bis[[2-butyl(octyl)oxy]carbonyl][2,2':5',2'':5'',2'''-quaterthiophene]-5,5'''-diyl] (PDCBT) (**11**) through a Stille coupling between bis(2-butyl(octyl) 5,5'-dibromo-[2,2'-bithiophene]-4,4'-dicarboxylate (**9**) and 2,5-bis(trimethylstannyl)thiophene (**10**), following the synthetic route represented in **Scheme 4.2**.^[14] We characterized the PDCBT from molecular and spectroscopical points of view. The ¹H-NMR spectrum is in accordance with that reported in literature,^[14] and the signals are listed in the Experimental Section. SEC analyses were performed by Dr. Stefania Zappia (SCITEC-CNR, Milano), and the MWD data are listed in **Table 4.4**. The acquired UV-Vis spectrum, depicted in **Figure 4.7**, shows the absorption maximum in the range typical of middle band gap polymers.



Scheme 4.2 Synthetic route for the PDCBT. Reaction conditions: i) Bis(pinacolato)diboron, $\text{Pd}_2(\text{dba})_3$, $t\text{-Bu}_3\text{PHBF}_4$, K_2CO_3 , room temperature, 16 h; ii) NBS, TFA, $0\text{ }^\circ\text{C}$, 16 h; iii) ZnTAC24, DMAP, $\text{MS4}\text{\AA}$, $110\text{ }^\circ\text{C}$, 16 h; iv) $\text{Pd}_2(\text{dba})_3$, PPh_3 , $115\text{ }^\circ\text{C}$, 24 h.

Table 4.4 MWD data of the PDCBT obtained through SEC.

Sample	M_n (g mol^{-1})	M_w (g mol^{-1})	M_w/M_n
PDCBT	16790	36540	2.2

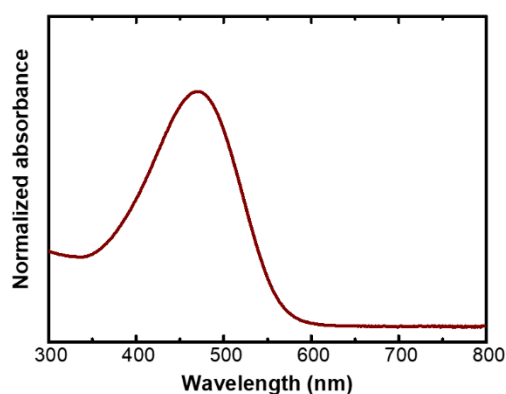


Figure 4.7 UV-Vis absorption spectrum of PDCBT in chloroform.

4.3 Conclusions and Perspectives

In conclusion, we synthesized and characterized two low band gap BDT-based polymers, namely the PTB7-Th-F₂ and the PTB7-Th-F₂-Me ester, and the middle band gap polymer PDCBT. These materials will be used for the preparation of aqueous inks through two different approaches: the miniemulsion method, and the surfactant-assisted nanoprecipitation, recently proposed by Xie *et al.*[12] We decided to focus on methods involving surfactants because the resulting nanoparticles (NPs) are more stable and easier to handle and store, enhancing the industrial scale-up process.

The surfactant-assisted nanoprecipitation is an adapted nanoprecipitation technique based on a micelle forming poloxamer, namely Pluronic F127 (the structure is shown in **Figure 4.8a**), selected to stabilize the NPs after the precipitation.[12, 29-31] Xie's group selected this surfactant because of its temperature-sensitive critical micelle concentration (CMC), enabling easy adjustment of excess through temperature. Specifically, the lowering the temperature to nearly 0 °C allows an increase in CMC to remove the excess of poloxamer, unbound to NPs, which thus remain surfactant-free, ready for the device processing. In a typical experiment both electron-donor and acceptor materials are dissolved in THF. Therefore, the organic solution is rapidly injected into an aqueous F127 solution under sonication, leading to the formation of a WPNP dispersion. Subsequently, the temperature is cooled to nearly 0 °C, and the excess F127 micelles are reconverted to linear poloxamers in water and are removed by centrifugal filtration (**Figure 4.8b**). This purification process requires low temperature because, as we can observe in **Figure 4.8c**, it is ineffective at room temperature. This evidence is highlighted by surface charge measurements conducted by the research group. The researchers noted that centrifuging the aqueous suspensions with all types of surfactants (including F127) at 25 °C, 5 to 6 washing steps are required before the surface charge starts to saturate. On the other hand, the stripping of F127 surfactant at 0 °C decreases the zeta potential after 2 to 3 times of washing to a significantly lower saturation value (about -10 mV) (**Figure 4.8d**). This developed approach enables the preparation of high purity NPs, minimizing the amount of residual surfactant in the aqueous medium, and providing the opportunity to deposit layers of high purity. This result is advantageous for the OPV device's final efficiency because of the higher crystallinity and reduced defect amount caused by surfactants. As a matter of fact, NFA:polymer based OSCs processed adopting this approach exceeded the charge transport and recombination limits generally affecting WPNP-based devices with conventional surfactants. Indeed, for

a *o*-IDTBR:P3HT (where *o*-IDTBR is the NFA 5*Z*,5'*Z*)-5,5'-((7,7'-(4,4,9,9-tetraoctyl-4,9-dihydro-*s*-indanoceno[1,2-*b*:5,6-*b'*])bithiophene-2,7-diyl)bis(benzo[*c*][1,2,5]thiadiazole-7,4-diyl))bis(methanylylidene))bis(3-ethyl-2-thioxothiazolidin-4-one) WPNP-based device, Xie gained a PCE comparable to devices processed from halogenated solvents (~5%).[12]

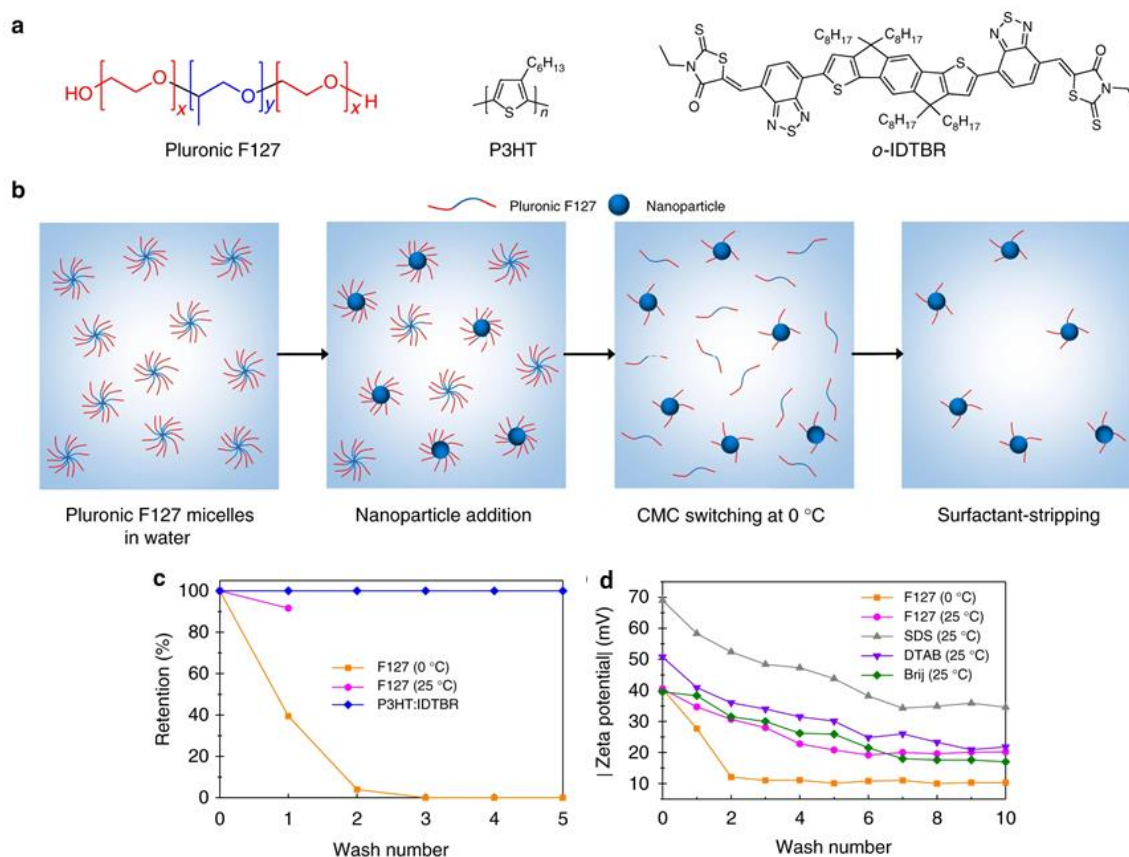


Figure 4.8 NFA:polymer NPs generated from surfactant-stripping technique. **a**) Chemical structure of polymer (P3HT), NFA (*o*-IDTBR), and surfactant (Pluronic F127) for NP preparation. **b**) Preparation and purification of NPs by temperature-mediated CMC-switching strategy. **c**) F127 retention as function of centrifugal washes at freezing and room temperature in water. **d**) Zeta potential of NP dispersions synthesized by various surfactants during centrifugal washes. Adapted with permission from reference [12]. Copyright © 2018, Springer Nature.

It is important to remark that for achieving stable aqueous suspensions, both electron-donor and acceptor materials must have good solubility in THF. For this reason, surfactant-assisted nanoprecipitation is a suitable method only for NFAs, while for fullerene materials a standard miniemulsion approach is more adequate. Early attempts were already done during the last period of my PhD, and WPNPs were produced by blending PTB7-Th-F₂-

Me ester with PC₇₁BM and *o*-IDTBR. The resulting aqueous suspensions are still under study and no results are yet available.

To select the most appropriate NFA material to blend with the donor polymer, we will consider five key factors: the HOMO and LUMO levels, the energy gaps of the acceptor and donor materials (E_g), the wavelength at which they exhibit their absorption maximum (λ_{max}), and the surface energy.[13] The importance of the last criterion was evidenced through an investigation conducted by Barr *et al.* In this study, they showed that the internal morphology of NPs is directly related to the surface energy difference between the blended active materials. In other words, the formation of the nanostructures is driven by the surface energy of the NFA with respect to the donor organic semiconductor material. In particular, a core-shell morphology is obtained if there is a significant difference between the two values. In fact, during NP formation, the higher energy material is driven towards the NP core, while the lower surface energy material is driven towards the NP shell, to lower the free surface energy. On the other side, to generate strongly intermixed donor-acceptor NPs, the matching of the surface energies of the materials is required to minimize the trend to phase separation in the NP formation process. Such a morphology, opposite to the core-shell nanostructure, assures efficient exciton dissociation and charge transport, so we will select NFA with surface energy comparable to that of polymers under consideration. Another parameter to consider, according to Khan *et al.*, is the quadrupole moment of the acceptor, which affects interfacial energy landscapes, causing differences in exciton quenching, charge dissociation efficiencies, and recombination losses.[32]

Lastly, the OPV device fabrication is ongoing in collaboration with Dr. Nicola Gasparini (Imperial College, London) and Dr. Nadia Camaioni (ISOF-CNR, Bologna), depositing the active layer from organic solvents, for now. The deposition from aqueous inks will take place after NP suspension preparation.

In addition to photovoltaic applications, on which this thesis is focused, the control over morphology and the possibility of obtaining nanostructures with a strongly intermixed donor/acceptor blend make NFA:polymer-based WPNPs good candidates for hydrogen evolution photocatalysts with greatly enhanced photocatalytic activity and increased hydrogen evolution rates.[33] Indeed, organic semiconductors offer several advantages over existing photocatalysts such as inorganic semiconductors, including lower toxicity, broader absorbance, and higher quantum efficiency. Moreover, the synthesis of polymer-based NPs, with the peculiar morphology discussed above, for photocatalytic hydrogen evolution on thin films also allows an increase in the interface area for the reaction

occurrence. A significant example is provided by the great result obtained by Kosco *et al.*, who prepared aqueous suspensions exploiting PTB7-Th as donor and the NFA EH-IDTBR as acceptor material. They obtained a photocatalyst that exhibited a H₂ evolution rate of over 60000 $\mu\text{mol h}^{-1} \text{g}^{-1}$ under 350 to 800 nm illumination, which is a value never reported in literature before.[34]

4.4 Experimental Section

4.4.1 Materials

All reagents were purchased from Sigma-Aldrich or Ossila and used as received. All solvents used for the chemical reactions were dried by standard procedures. All manipulations involving air-sensitive reagents were performed under dry nitrogen atmosphere. Purifications through flash chromatography were performed using Merck silica gel type 40-60 mesh. 1,2-Dideutero-1,1,2,2-tetrachloroethane (TCE-d₂) and deuteriochloroform (CDCl₃) used to collect ¹H-NMR spectra are TCI Chemicals products.

4.4.2 Synthetic Procedures

4.4.2.1 Synthesis of PTB7-Th-F₂ (4)

BDTTDFS_n (400 mg, 0.42 mmol) (**1**) and FTThBr (201 mg, 0.42 mmol) (**2**) were dissolved in 14 ml of toluene in a dry, oxygen-free Schlenk tube. After that, Pd₂(dba)₃ (15 mg, 0.017 mmol) and P(*o*-tol)₃ (41 mg, 0.134 mmol), dissolved in 3 ml of toluene, were added to the reaction mixture and five freeze-pump-thaw cycles were performed to remove any remaining oxygen. Therefore, the mixture was heated at 110 °C under stirring overnight. The color turns from burgundy to purple and subsequently to dark blue. After 24 hours 750 μl of degassed 2-bromothiophene was introduced to cap the stannyl terminal groups, together with additional catalyst. After another 24 hours at 110 °C, 750 μl of degassed 2-(tributylstannyl)thiophene and some catalysts were added to cap the bromide terminal groups. The mixture was heated again at 110 °C for 24 hours. At this point, ~150 mg of Scavenger resin (3-mercaptopropyl-functionalized silica gel) was added together with 3 ml of toluene and after about 2 hours under stirring at 110 °C, the mixture was filtered on Celite®, then poured into methanol, filtered, and extracted with Soxhlet apparatus in acetone, hexane, and chloroform, in sequence. The fraction extracted in chloroform was

dried by vacuum and the desired polymer was obtained as a dark blue solid (380 mg, Yield: 95%).

$^1\text{H-NMR}$ (TCE-d_2 , 400 MHz, ppm) δ : 8.00-7.25 (br, 2H, BDTTDF), 7.25-6.30 (br, 2H, BDTTDF), 4.23 (s, 2H, FTTh), 2.83 (s, 4H, BDTTDF), 1.85-1.65 (br, 3H, BDTTDF and FTTh, alkyl chains), 1.40-1.20 (br, 24H, BDTTDF and FTTh, alkyl chains), 1.05-0.80 (br, 18H, BDTTDF and FTTh, alkyl chains)

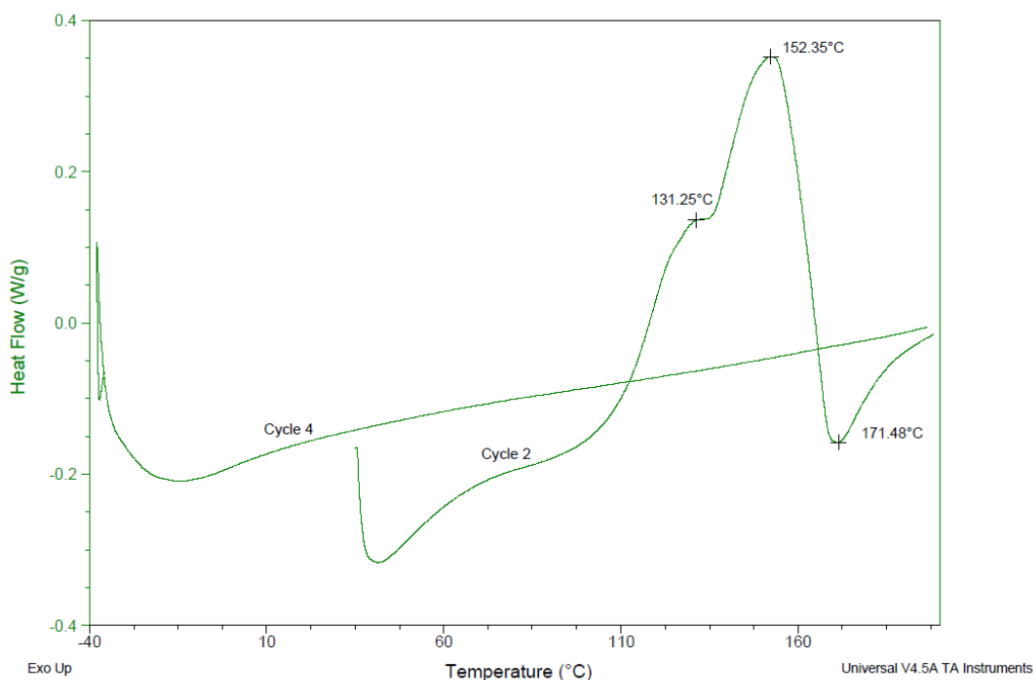


Figure 4.9 DSC thermogram of PTB7-Th-F₂.

4.4.2.2 Synthesis of PTB7-Th-F₂-Me ester (5)

BDTTDFS_n (400 mg, 0.42 mmol) (**1**), FTTh-Br (201 mg, 0.42 mmol) (**2**), and methyl-2,5-dibromothiophene-3-carboxylate (Me ester) (6 mg, 0.021 mmol) (**3**) were dissolved in 14 ml of toluene in a dry, oxygen-free Schlenk tube. After that, Pd₂(dba)₃ (15 mg, 0.017 mmol) and P(*o*-tol)₃ (41 mg, 0.134 mmol), dissolved in 3 ml of toluene, were added to the reaction mixture and five freeze-pump-thaw cycles were performed. The mixture was heated at 110 °C under stirring overnight. The reaction became quickly dark blue. After 24 hours 750 μl of degassed 2-bromothiophene was introduced, together with additional catalyst. After another 24 hours at 110 °C, 750 μl of degassed 2-(tributylstannyl)thiophene and some catalysts were added. The mixture was heated again at 110 °C for 24 hours. Therefore, ~150 mg of Scavenger resin (3-mercaptopropyl-functionalized silica gel) was added together with 3 ml of toluene and after about 2 hours under stirring at 110 °C, the mixture

was filtered on Celite®, then poured into methanol, filtered, and extracted with Soxhlet apparatus in acetone, hexane, and chloroform, in sequence. The fraction extracted in chloroform was dried by vacuum and the desired polymer was obtained as a dark blue solid (383 mg, Yield: 96%).

¹H-NMR (TCE-d₂, 400 MHz, ppm) δ: 8.00-7.25 (br, 2H, BDTTDF), 7.25-6.30 (br, 2H, BDTTDF), 4.23 (s, 2H, FTTh), 2.83 (s, 4H, BDTTDF), 1.85-1.65 (br, 3H, BDTTDF and FTTh, alkyl chains), 1.40-1.20 (br, 24H, BDTTDF and FTTh, alkyl chains), 1.05-0.80 (br, 18H, BDTTDF and FTTh, alkyl chains)

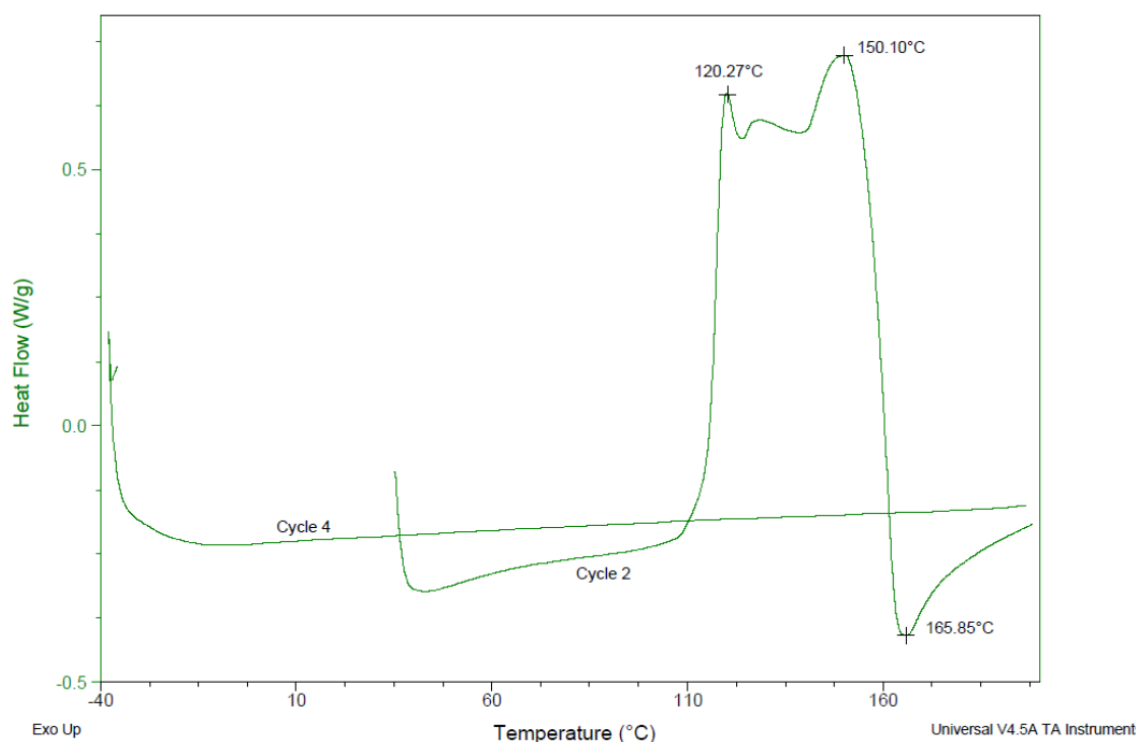


Figure 4.10 DSC thermogram of PTB7-Th-F₂-Me ester.

4.4.2.3 Synthesis of poly[2,2'''-bis[[2-butyl(octyl)oxy]carbonyl][2,2':5',2'':5'',2'''-quaterthiophene] -5,5'''-diyl] (PDCBT)

Synthesis of dimethyl [2,2'-bithiophene]-4,4'-dicarboxylate (7). Methyl 5-bromothiophene-3-carboxylate (8 g, 36.18 mmol) (**6**) and bis(pinacolato)diboron (5.4 g, 18.09 mmol) were dissolved in 160 ml of THF in a dry, oxygen-free Schlenk tube. A solution of potassium carbonate (20 g, 144.72 mmol) in MilliQ water (72 ml) was added. At this point, tri-tert-butylphosphonium tetrafluoroborate (626 mg, 2.16 mmol) and Pd₂(dba)₃ (512 mg, 0.56 mmol), dissolved in 40 ml of THF, were added and the reaction mixture was stirred overnight at room temperature. Diethyl ether was added to stop the

reaction, and the mixture was washed with water and brine. The water phase was then extracted several times with chloroform and the combined organic phases were dried over Na_2SO_4 , and after filtration the solvent was removed by vacuum. The crude material was purified through a short silica plug using dichloromethane as eluent. The product was obtained as white solid (1.8 g, Yield: 36%).

GC-MS (EI): 282 (M^+)

Melting point: $T_m=175\text{ }^\circ\text{C}$

$^1\text{H-NMR}$ (CDCl_3 , 400 MHz, ppm) δ : 8.01 (d, 2H), 7.59 (d, 2H), 3.89 (s, 6H)

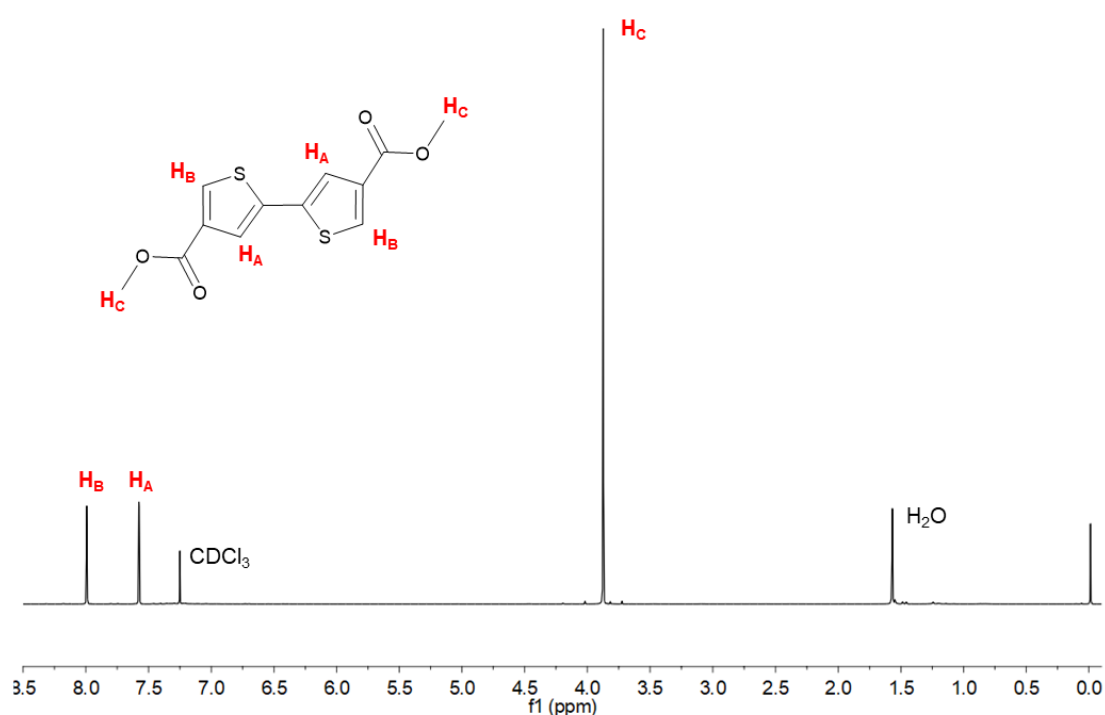


Figure 4.11 $^1\text{H-NMR}$ spectrum of dimethyl [2,2'-bithiophene]-4,4'-dicarboxylate (**7**) in CDCl_3 .

Synthesis of dimethyl 5,5'-dibromo-[2,2'-bithiophene]-4,4'-dicarboxylate (8).

Dimethyl [2,2'-bithiophene]-4,4'-dicarboxylate (1.00 g, 3.54 mmol) (**7**) was dissolved in 20 ml of chloroform in a dry, oxygen-free Schlenk tube. The solution was cooled to $0\text{ }^\circ\text{C}$ and 15 ml of trifluoroacetic acid was added. At this point, N-bromosuccinimide (1.44 g, 7.52 mmol) was added, and the reaction was stirred in the dark overnight, warming slowly to room temperature. The reaction was diluted with chloroform and dropped into water. The organic phase was washed with brine and the aqueous phase was extracted with chloroform. The combined organic phases were dried over Na_2SO_4 and after filtration the

solvent was removed by vacuum. The crude material was purified by flash column chromatography using dichloromethane as eluent. The product was obtained as white solid (717 mg, Yield: 48%).

GC-MS (EI): 439.9 (M^+)

$^1\text{H-NMR}$ (CDCl_3 , 400 MHz, ppm) δ : 7.39 (s, 2H), 3.92 (s, 6H)

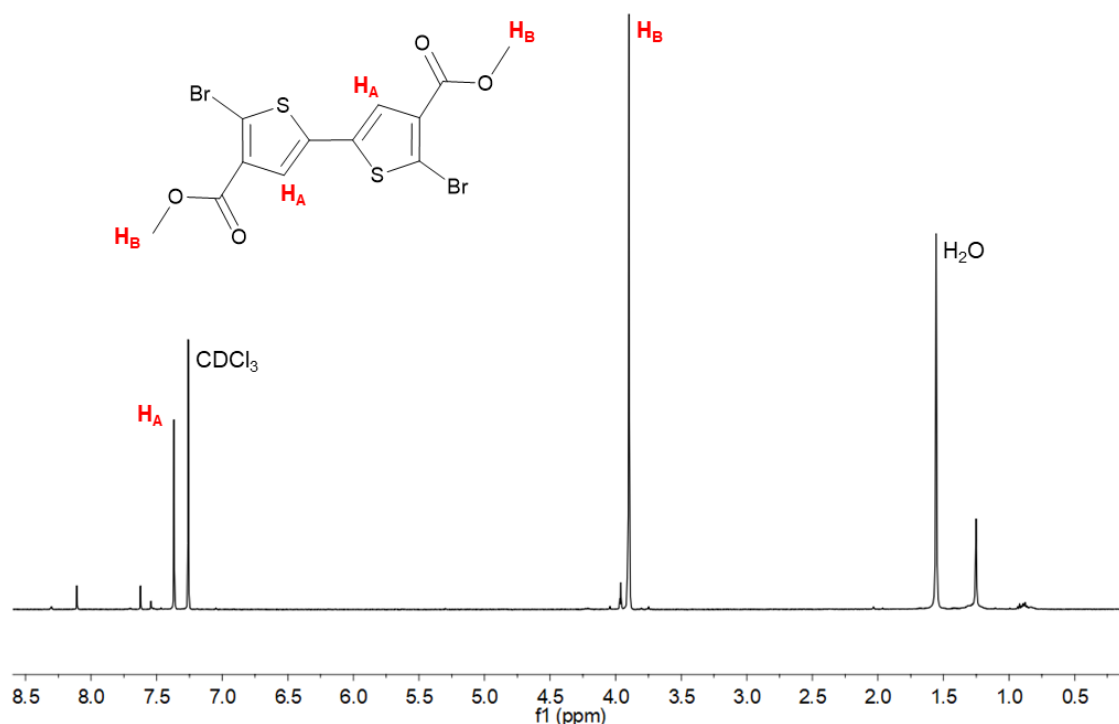


Figure 4.12 $^1\text{H-NMR}$ spectrum of dimethyl 5,5'-dibromo-[2,2'-bithiophene]-4,4'-dicarboxylate (**8**) in CDCl_3 .

Synthesis of bis(2-butyloctyl) 5,5'-dibromo-[2,2'-bithiophene]-4,4'-dicarboxylate (9).

In a dry, oxygen-free Schlenk tube dimethyl 5,5'-dibromo-[2,2'-bithiophene]-4,4'-dicarboxylate (715 mg, 1.63 mmol) (**8**), 4-dimethylaminopyridine (397 mg, 3.25 mmol) and oxo[hexa(trifluoroacetato)]tetrazinc (ZnTAC24^\circledR) (320 mg, 0.33 mmol) were introduced and dissolved in 21 ml of toluene. After that, 3.3 ml of degassed 2-butyloctanol (2.72 g, 14.62 mmol) was added, and 4 Å molecular sieves were introduced in the reaction mixture. The reaction Schlenk tube was heated at 110 °C under stirring overnight. Therefore, the reaction was cooled to room temperature and diluted with chloroform. After filtration, the solvent was removed by vacuum and the crude material was purified using flash column chromatography (silica, chloroform/hexane: 3:2) to obtain the product as a colorless oil (1.08 g, Yield: 90%).

$^1\text{H-NMR}$ (CDCl_3 , 400 MHz, ppm) δ : 7.38 (s, 2H), 4.26 (d, 4H), 1.73 (m, 2H), 1.53–1.33 (m, 32H), 0.95 (m, 12H).

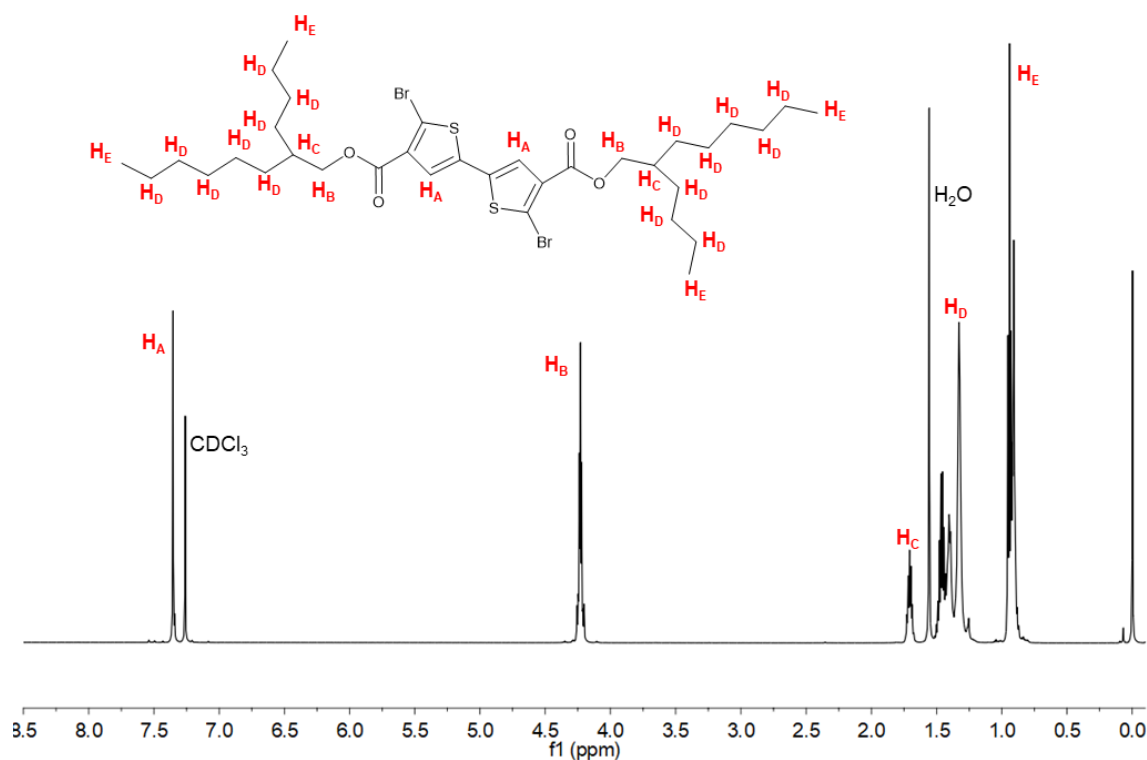


Figure 4.13 $^1\text{H-NMR}$ spectrum of bis(2-butyloctyl) 5,5'-dibromo-[2,2'-bithiophene]-4,4'-dicarboxylate (**9**) in CDCl_3 .

Synthesis of PDCBT (11). In a dry, oxygen-free Schlenk tube bis(2-butyloctyl) 5,5'-dibromo-[2,2'-bithiophene]-4,4'-dicarboxylate (115 mg, 0.15 mmol) (**9**), 2,5-bis(trimethylstannyl)thiophene (74 mg, 0.15 mmol) (**10**), PPh_3 (5 mg, 1.8×10^{-2} mmol), $\text{Pd}_2(\text{dba})_3$ (4 mg, 4.5×10^{-3} mmol) were introduced, 3.2 ml of toluene, and 0.3 ml of dimethylformamide were added. The color turns quickly from burgundy to yellowish and then to greenish. Five freeze-pump-thaw cycles were performed to remove any remaining oxygen, after which the mixture was heated to 115 °C under stirring overnight. The polymer was end capped with 150 μl of 2-(tributylstannyl)thiophene and 150 μl of 2-bromothiophene, heating to 115 °C for 2 hours after each addition. Therefore, ~150 mg of Scavenger resin (3-mercaptopropyl-functionalized silica gel) was added together with 2 ml of toluene, and after about 2 hours under stirring at 115 °C, the mixture was filtered on Celite®, then poured into methanol, filtered and extracted with Soxhlet apparatus in acetone, hexane, and chloroform, in sequence. PDCB was obtained as a reddish solid (75 mg, Yield: 66%).

$^1\text{H-NMR}$ (TCE- d_2 , 400 MHz, ppm) δ : 7.47-7.40 (m, 4H), 7.13-7.05 (m, 2H), 4.13 (d, 4H), 1.66 (s, 2H), 1.35-1.15 (br, 32H), 0.84-0.75 (br, 12H)

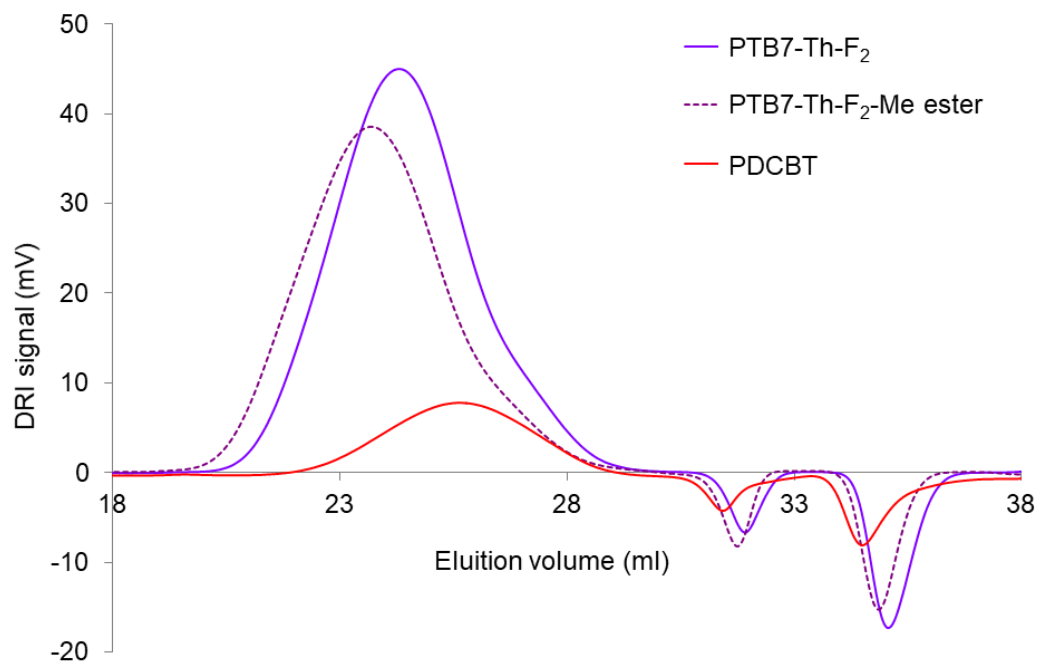


Figure 4.14 Concentration (DRI) signal comparison of the PTB7-Th-F₂, PTB7-Th-F₂-Me ester, and PDCBT samples.

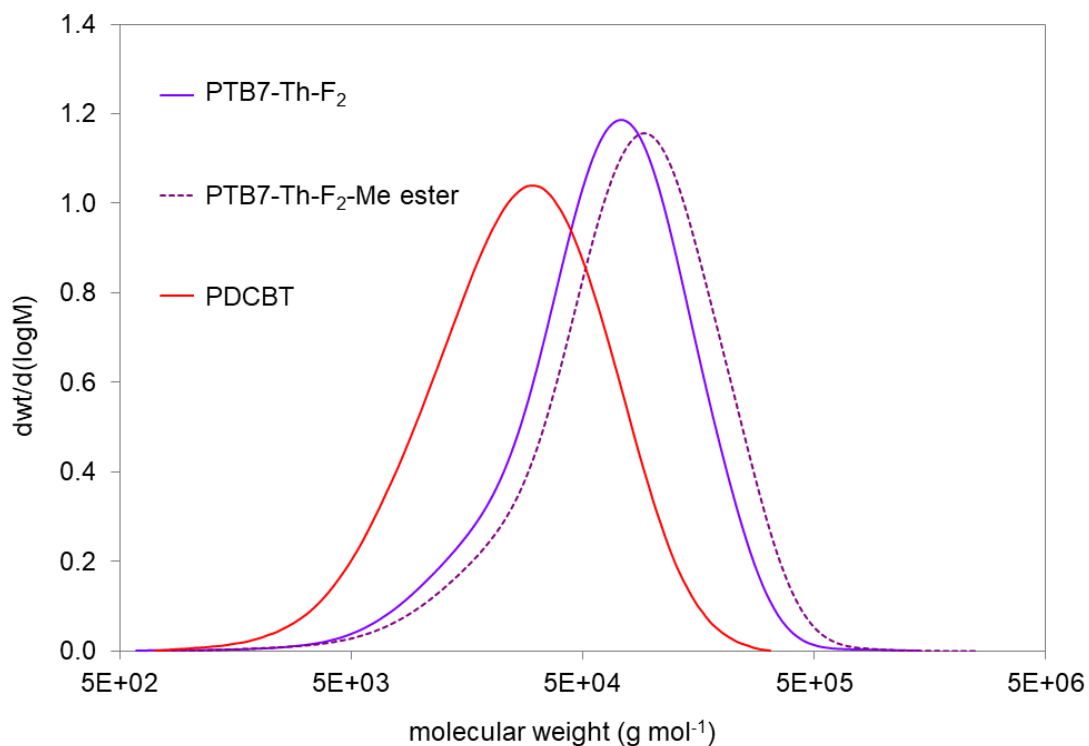


Figure 4.15 Comparison of differential MWD of the PTB7-Th-F₂, PTB7-Th-F₂-Me ester, and PDCBT samples.

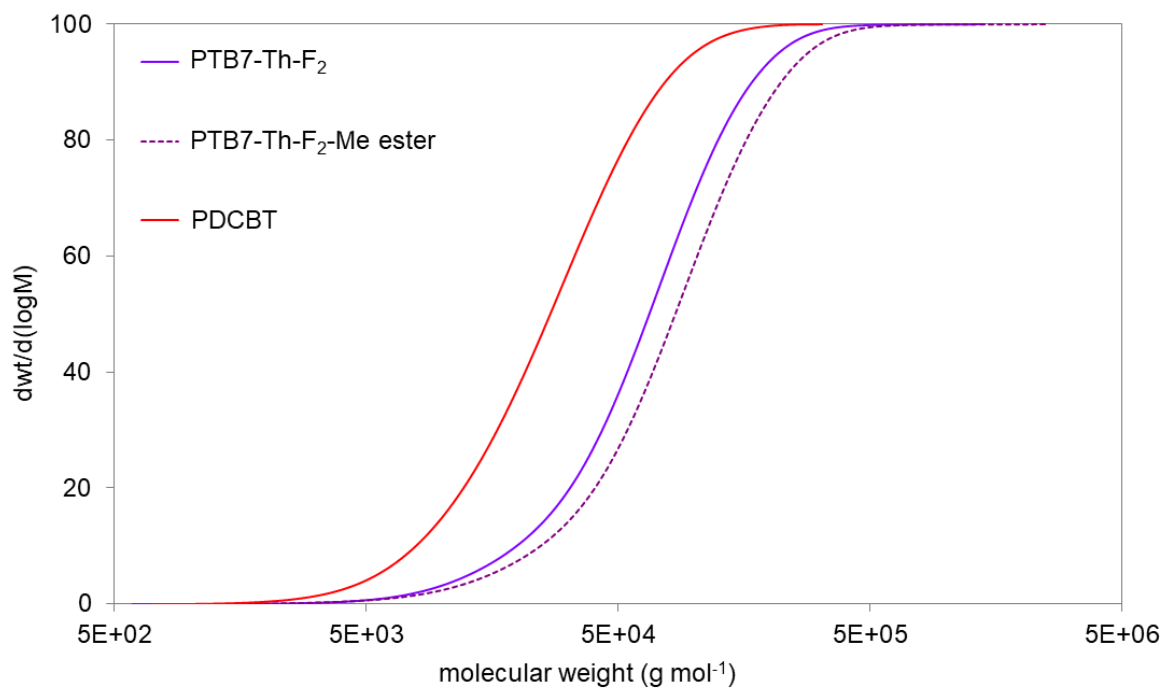


Figure 4.16 Comparison of Cumulative MWD of the PTB7-Th-F₂, PTB7-Th-F₂-Me ester, and PDCBT samples.

4.5 References

- [1] F. Bencheikh, D. Duché, C.M. Ruiz, J.-J. Simon, L. Escoubas, Study of Optical Properties and Molecular Aggregation of Conjugated Low Band Gap Copolymers: PTB7 and PTB7-Th, *The Journal of Physical Chemistry C* 119(43) (2015) 24643-24648.
- [2] Y. Lin, J. Wang, Z.-G. Zhang, H. Bai, Y. Li, D. Zhu, X. Zhan, An Electron Acceptor Challenging Fullerenes for Efficient Polymer Solar Cells, *Advanced Materials* 27(7) (2015) 1170-1174.
- [3] Q. Wan, X. Guo, Z. Wang, W. Li, B. Guo, W. Ma, M. Zhang, Y. Li, 10.8% Efficiency Polymer Solar Cells Based on PTB7-Th and PC71BM via Binary Solvent Additives Treatment, *Advanced Functional Materials* 26(36) (2016) 6635-6640.
- [4] Y. Qin, M.A. Uddin, Y. Chen, B. Jang, K. Zhao, Z. Zheng, R. Yu, T.J. Shin, H.Y. Woo, J. Hou, Highly Efficient Fullerene-Free Polymer Solar Cells Fabricated with Polythiophene Derivative, *Advanced Materials* 28(42) (2016) 9416-9422.
- [5] L. Fernandes, H. Gaspar, J.P.C. Tomé, F. Figueira, G. Bernardo, Thermal stability of low-bandgap copolymers PTB7 and PTB7-Th and their bulk heterojunction composites, *Polymer Bulletin* 75(2) (2018) 515-532.
- [6] Y. Cui, H. Yao, L. Hong, T. Zhang, Y. Xu, K. Xian, B. Gao, J. Qin, J. Zhang, Z. Wei, J. Hou, Achieving Over 15% Efficiency in Organic Photovoltaic Cells via Copolymer Design, *Advanced Materials* 31(14) (2019) 1808356.
- [7] K.-H. Kim, S. Park, H. Yu, H. Kang, I. Song, J.H. Oh, B.J. Kim, Determining Optimal Crystallinity of Diketopyrrolopyrrole-Based Terpolymers for Highly Efficient Polymer Solar Cells and Transistors, *Chemistry of Materials* 26(24) (2014) 6963-6970.
- [8] Y. Zhang, D. Deng, K. Lu, J. Zhang, B. Xia, Y. Zhao, J. Fang, Z. Wei, Synergistic Effect of Polymer and Small Molecules for High-Performance Ternary Organic Solar Cells, *Advanced Materials* 27(6) (2015) 1071-1076.
- [9] S. Chen, H.J. Cho, J. Lee, Y. Yang, Z.-G. Zhang, Y. Li, C. Yang, Modulating the Molecular Packing and Nanophase Blending via a Random Terpolymerization Strategy toward 11% Efficiency Nonfullerene Polymer Solar Cells, *Advanced Energy Materials* 7(21) (2017) 1701125.
- [10] Y. Qin, L. Ye, S. Zhang, J. Zhu, B. Yang, H. Ade, J. Hou, A polymer design strategy toward green solvent processed efficient non-fullerene polymer solar cells, *Journal of Materials Chemistry A* 6(10) (2018) 4324-4330.
- [11] A. Wadsworth, M. Moser, A. Marks, M.S. Little, N. Gasparini, C.J. Brabec, D. Baran, I. McCulloch, Critical review of the molecular design progress in non-fullerene electron acceptors towards commercially viable organic solar cells, *Chemical Society Reviews* 48(6) (2019) 1596-1625.
- [12] C. Xie, T. Heumüller, W. Gruber, X. Tang, A. Classen, I. Schultes, M. Bidwell, A. Späth, R.H. Fink, T. Unruh, I. McCulloch, N. Li, C.J. Brabec, Overcoming efficiency and stability limits in water-processing nanoparticulate organic photovoltaics by minimizing microstructure defects, *Nature Communications* 9(1) (2018) 5335.
- [13] M.G. Barr, S. Chambon, A. Fahy, T.W. Jones, M.A. Marcus, A.L.D. Kilcoyne, P.C. Dastoor, M.J. Griffith, N.P. Holmes, Nanomorphology of eco-friendly colloidal inks, relating non-fullerene acceptor surface energy to structure formation, *Materials Chemistry Frontiers* 5(5) (2021) 2218-2233.
- [14] R. Heuvel, F.J.M. Colberts, M.M. Wienk, R.A.J. Janssen, Thermal behaviour of dicarboxylic ester bithiophene polymers exhibiting a high open-circuit voltage, *Journal of Materials Chemistry C* 6(14) (2018) 3731-3742.
- [15] M. Kobayashi, J. Chen, T.C. Chung, F. Moraes, A.J. Heeger, F. Wudl, Synthesis and properties of chemically coupled poly(thiophene), *Synthetic Metals* 9(1) (1984) 77-86.

- [16] S. Hotta, S.D.D.V. Rughooputh, A.J. Heeger, F. Wudl, Spectroscopic studies of soluble poly(3-alkylthienylenes), *Macromolecules* 20(1) (1987) 212-215.
- [17] P. Schilinsky, C. Waldauf, C.J. Brabec, Recombination and loss analysis in polythiophene based bulk heterojunction photodetectors, *Applied Physics Letters* 81(20) (2002) 3885-3887.
- [18] G. Li, V. Shrotriya, J. Huang, Y. Yao, T. Moriarty, K. Emery, Y. Yang, High-efficiency solution processable polymer photovoltaic cells by self-organization of polymer blends, *Nature Materials* 4(11) (2005) 864-868.
- [19] M. Zhang, X. Guo, Y. Yang, J. Zhang, Z.-G. Zhang, Y. Li, Downwards tuning the HOMO level of polythiophene by carboxylate substitution for high open-circuit-voltage polymer solar cells, *Polymer Chemistry* 2(12) (2011) 2900-2906.
- [20] Z. Zheng, S. Zhang, M. Zhang, K. Zhao, L. Ye, Y. Chen, B. Yang, J. Hou, Highly Efficient Tandem Polymer Solar Cells with a Photovoltaic Response in the Visible Light Range, *Advanced Materials* 27(7) (2015) 1189-1194.
- [21] M.-Y. Chang, Y.-H. Huang, Y.-K. Han, Aggregation, crystallization, and resistance properties of poly(3-hexylthiophene-2,5-diyl) solid films gel-cast from CHCl₃/p-xylene mixed solvents, *Organic Electronics* 15(1) (2014) 251-259.
- [22] F. Panzer, M. Sommer, H. Bässler, M. Thelakkat, A. Köhler, Spectroscopic Signature of Two Distinct H-Aggregate Species in Poly(3-hexylthiophene), *Macromolecules* 48(5) (2015) 1543-1553.
- [23] S. Zhang, L. Ye, W. Zhao, D. Liu, H. Yao, J. Hou, Side Chain Selection for Designing Highly Efficient Photovoltaic Polymers with 2D-Conjugated Structure, *Macromolecules* 47(14) (2014) 4653-4659.
- [24] S. Hedström, P. Henriksson, E. Wang, M.R. Andersson, P. Persson, Light-harvesting capabilities of low band gap donor-acceptor polymers, *Physical Chemistry Chemical Physics* 16(45) (2014) 24853-24865.
- [25] L. Li, W.-y. Lo, Z. Cai, N. Zhang, L. Yu, Donor-Acceptor Porous Conjugated Polymers for Photocatalytic Hydrogen Production: The Importance of Acceptor Comonomer, *Macromolecules* 49(18) (2016) 6903-6909.
- [26] Sigmaaldrich.com, Greener Solvent Alternatives - Brochure, 2010.
- [27] L. Leonat, G. Sbarcea, I.V. Branzoi, Cyclic voltammetry for energy levels estimation of organic materials, *UPB Sci Bull Ser B*, 2013, pp. 111-118.
- [28] J.L. Bredas, R. Silbey, D.S. Boudreaux, R.R. Chance, Chain-length dependence of electronic and electrochemical properties of conjugated systems: polyacetylene, polyphenylene, polythiophene, and polypyrrole, *Journal of the American Chemical Society* 105(22) (1983) 6555-6559.
- [29] Y. Zhang, M. Jeon, L.J. Rich, H. Hong, J. Geng, Y. Zhang, S. Shi, T.E. Barnhart, P. Alexandridis, J.D. Huizinga, M. Seshadri, W. Cai, C. Kim, J.F. Lovell, Non-invasive multimodal functional imaging of the intestine with frozen micellar naphthalocyanines, *Nature Nanotechnology* 9(8) (2014) 631-638.
- [30] Y. Zhang, W. Song, J. Geng, U. Chitgupi, H. Unsal, J. Federizon, J. Rzayev, D.K. Sukumaran, P. Alexandridis, J.F. Lovell, Therapeutic surfactant-stripped frozen micelles, *Nature Communications* 7(1) (2016) 11649.
- [31] Y. Zhang, D. Wang, S. Goel, B. Sun, U. Chitgupi, J. Geng, H. Sun, T.E. Barnhart, W. Cai, J. Xia, J.F. Lovell, Surfactant-Stripped Frozen Pheophytin Micelles for Multimodal Gut Imaging, *Advanced Materials* 28(38) (2016) 8524-8530.
- [32] J.I. Khan, M.A. Alamoudi, N. Chaturvedi, R.S. Ashraf, M.N. Nabi, A. Markina, W. Liu, T.A. Dela Peña, W. Zhang, O. Alévêque, G.T. Harrison, W. Alsufyani, E. Levillain, S. De Wolf, D. Andrienko, I. McCulloch, F. Laquai, Impact of Acceptor Quadrupole Moment on Charge Generation and Recombination in Blends of IDT-Based Non-Fullerene

Acceptors with PCE10 as Donor Polymer, *Advanced Energy Materials* 11(28) (2021) 2100839.

[33] N.P. Holmes, S. Chambon, A. Holmes, X. Xu, K. Hirakawa, E. Deniau, C. Lartigau-Dagron, A. Bousquet, Organic semiconductor colloids: From the knowledge acquired in photovoltaics to the generation of solar hydrogen fuel, *Current Opinion in Colloid & Interface Science* 56 (2021) 101511.

[34] J. Kosco, M. Bidwell, H. Cha, T. Martin, C.T. Howells, M. Sachs, D.H. Anjum, S. Gonzalez Lopez, L. Zou, A. Wadsworth, W. Zhang, L. Zhang, J. Tellam, R. Sougrat, F. Laquai, D.M. DeLongchamp, J.R. Durrant, I. McCulloch, Enhanced photocatalytic hydrogen evolution from organic semiconductor heterojunction nanoparticles, *Nature Materials* 19(5) (2020) 559-565.

Summary and Conclusions

Summary and Conclusions

In summary, my PhD project was focused on the development of polymer nanoparticle-based aqueous inks for optoelectronic and electronic applications. Specifically, the aim of my research work was the preparation of sustainable active layers of organic photovoltaic (OPV) devices processable in water. In fact, OPV technology was intensively investigated in the last decades as it represents an intriguing alternative for electrical power generation. Nevertheless, its market penetration is limited not so much by the lower power conversion efficiencies (PCEs) compared to inorganic devices, but rather by the use of huge amount of halogenated organic solvents, which are toxic and harmful, and thus they must be reduced. This goal was reached through water-processable nanoparticle (WPNP) aqueous suspensions, prepared from semiconducting polymers as electron-donor and acceptor materials. The aqueous inks were obtained through a modified miniemulsion method, which unlike the standard process does not imply the addition of any surfactant to ensure the colloidal stability. The adapted approach was developed by Dr. Stefania Zappia and Dr. Silvia Destri (SCITEC-CNR, Milano) before my arrival in the research group. They synthesized four amphiphilic rod-coil block copolymers (BCPs) to be exploited to prepare the polymer-based aqueous suspensions. Rod-coil BCPs are very intriguing for the photovoltaic community since their self-assembly ability is a powerful route to obtain ideal morphologies in bulk heterojunction (BHJ) solar cells, which require strongly interconnected donor and acceptor material phases with proper nanodomains. These BCPs are characterized by a rigid block (a p-type semiconducting polymer) covalently linked to a hydrophilic flexible segment able to interact with aqueous medium, stabilizing the aqueous/non-aqueous interfaces as long as it can coordinate acceptors molecules. Amphiphilic BCPs are able to self-assemble both neat and in blend with acceptor materials, leading to the formation of nanostructures consisting of domains with dimensions suitable for the charge percolation in the resulting active layer of the organic solar cell (OSC). In fact, the optimized design of BCPs allows to achieve nanoparticles (NPs) with an intermixed inner morphology, different from the core-shell one mainly obtained with the standard miniemulsion method, not optimal for the proper device working. Finally, mild thermal annealing processes on the WPNP-based films deposited on different substrates provided the photoactive layers.

Primarily, low band gap (LBG) polymers were considered as electron-donor materials to match the solar radiation absorption. Specifically, in **Chapter 2** the synthesis of four different poly[2,6-(4,4-bis-(2-ethylhexyl)-4*H*-cyclopenta[2,1-*b*;3,4-*b'*]dithiophene)-*alt*-4,7(2,1,3-benzothiadiazole)] (PCPDTBT)-based amphiphilic BCPs, with a tailored

segment of poly-4-vinylpyridine (P4VP) as coil, is presented. Four different aqueous inks each containing WPNPs of blends of a particular BCP with the [6,6]-phenyl-C₆₁-butyric acid methyl ester (PC₆₁BM) were prepared and used as active layers in solar cells. The four devices performed very differently depending on the length and composition of the coil segment. Namely, PCE varied from 2.5% for BCP5, comparable with that of a conventional BHJ device fabricated using chlorinated solvents, to 0.001% for BCP100. Therefore, the correlation between the internal morphology and composition of the nanostructures, and the dimensions of the donor/acceptor nanodomains with the OSC efficiency was investigated and presented in Chapter 2. Atomic force microscopy (AFM) of the active layers, transmission electron microscopy (TEM), and energy filtered TEM (EFTEM) analyses of WPNPs were performed, for clarifying film topology and NP morphology, respectively, and they are discussed. In the Chapter 2 pump-probe experiments, which shed the light on the charge separation dynamics in the WPNP-films, are also reported. The relevant performance of BCP5 is due to formation of many small PC₆₁BM-rich regions within each WPNP thank to its relatively short coil block. Therefore, the exciton efficiently dissociates at the donor/acceptor interface, ensuring good charge generation and collection. In Chapter 2 is also discussed the biological application of neat BCP2-based WPNPs, which are able to affect the human cellular metabolism upon illumination.

In a second time, we explored other LBG polymers endowed with a partial order to improve the effectiveness of our approach. Actually, a higher polymer crystallinity generally leads to better charge transport properties, and thus to increased performances of the OPV device. In **Chapter 3** the synthesis and the deep characterization of a new amphiphilic BCP based on the poly[[4,8-bis[(2-ethylhexyl)oxy]benzo[1,2-*b*:4,5-*b'*]dithiophene-2,6-diyl][3-fluoro-2-[(2-ethylhexyl)carbonyl]thieno[3,4-*b*]thiophenediyl]] (PTB7) as rigid block, and a coil segment of 15 repeating units of 4VP are described in detail. PTB7 is stiffer and has a greater order degree than PCPDTBT. WPNP preparation from the self-assembly of the PTB7-*b*-P4VP blended with the [6,6]-phenyl-C₇₁-butyric acid methyl ester (PC₇₁BM) is described in this chapter. The aqueous inks were characterized by means of UV-Vis spectroscopy, dynamic light scattering (DLS), TEM, and EFTEM. WPNPs are spherical and have an inner morphology Janus-like, which can promote free charge generation because enlarges the surface area between donor and acceptor with respect to a core-shell morphology, and their transport and collection as the segregate domains of the two materials are interconnected. The fabrication of OSCs in direct configuration using WPNPs is reported together with the analysis of active layers through AFM and grazing-incidence

wide-angle X-ray scattering (GIWAXS). The best gained OPV device exhibited a PCE of 0.85%, which is still very far from the benchmark, but it is higher than the efficiency of the corresponding BHJ device. In Chapter 3 a reasonable explanation of this low efficiency and the attempts to overcome the drawback are depicted. Unfortunately, these attempts did not result in improved efficiencies. In conclusion, in Chapter 2 and Chapter 3 I demonstrated that the use of amphiphilic rod-coil BCPs able of self-assembling is a tool for obtaining WPNPs with morphology far from the core-shell one and more adapt to the proper charge dissociation, transport and collection. Obviously, a careful molecular design is crucial to optimize the BCP molecular structures, enabling the nanostructure control in the fabrication of the WPNP-based OPV active layer. Currently, it is very difficult to pre-determine the organization inside the NPs as the internal morphology depends on several conditions and experimental parameters. Indeed, the ratio of rod and coil blocks in BCPs, the concentrations and ratio of donors and acceptor materials, the surface energy of BCPs and acceptors, and so on, play an important role in the nanostructure formation inside the NPs. As a consequence, the use of surfactants in the WPNP preparation modifying also the synthetic approach for fabricating NPs of donor/acceptor blend should be preferred. The resulting aqueous suspensions are more stable, easier to handle and store, enhancing the industrial scale-up process. Furthermore, I will explore the poloxamer Pluronic F127 as emulsifying agent because of its temperature-sensitive critical micelle concentration (CMC), which ensures an easy excess removal by temperature.

Additionally, I prepared other semiconducting polymers as electron-donor materials in the active blends. Particularly, in **Chapter 4** I focused on two new LBG semiconducting BDT-based polymers, and a medium band gap one. The synthesis and characterizations of these materials are reported in the chapter. These materials will be blended with fullerene and non-fullerene acceptor (NFA) materials to obtain aqueous inks that will be deposited as active layers of OSCs, similarly to previous materials.

In addition to OPV applications, the aqueous inks made of NPs with strongly intermixed donor/acceptor networks result in excellent candidates for the emerging application of hydrogen evolution photocatalysts. What is more, several works in which semiconducting polymer-based NPs are employed in biological applications are published. Specifically, semiconducting polymer-based nanomaterials were exploited *in vitro* and *in vivo* experiments, as photoactuators able to transform light stimuli into an alteration of the physiological functions, as it occurred in the case of BCP2-based WPNPs discussed in Chapter 2.

Acknowledgements: this research work was funded by Eni Corporate University (ECU), and it was supported by National Council of Research (CNR) of Italy. I would like to thank Dr. Riccardo Po' for the collaboration during my PhD work.

Table of congresses, seminary and publications

During my PhD, my research project was presented at subsequent development levels at congresses:

- Macrogiovani 2019, Napoli, 1-2.07.2019 (oral communication)
- CIS2019 (Chemistry Meets Industry and Society), Salerno, 28-30.08.2019 (poster contribution)
- Nanoday IV, Milano, 11-14.12.2019 (poster contribution)
- ENERCHEM_2, Padova, 12-14.02.2020 (poster contribution)
- International School of Chemistry (organized by SCI), 1-6.09.2020 (book of Abstracts).

Furthermore, the project was partially presented by Dr. Nicola Gasparini at the seminary “*Status and perspective of organic photovoltaic: is it ready for commercialisation?*”, 2nd December 2021, SCITEC-CNR, Milano (Italy).

Lastly, I was author or *co*-author of the following publications:

- Lucia Ganzer, Stefania Zappia, Mattia Russo, Anna Maria Ferretti, Varun Vohra, Marianna Diterlizzi, Maria Rosa Antognazza, Silvia Destri and Tersilla Virgili, “Ultrafast spectroscopy on water-processable PCBM:rod–coil block copolymer nanoparticles” *Phys. Chem. Chem. Phys.* 2020, 22, 26583-26591.
- Anna Maria Ferretti, Marianna Diterlizzi, William Porzio, Umberto Giovanella, Lucia Ganzer, Tersilla Virgili, Varun Vohra, Eduardo Arias, Ivana Moggio, Guido Scavia, Silvia Destri and Stefania Zappia, “Rod-coil block copolymer:fullerene blend water-processable nanoparticles: how molecular structure addresses morphology and efficiency in NP-OPVs” *Nanomaterials* 2022, 12, 84-101.
- Marianna Diterlizzi, Anna Maria Ferretti, Guido Scavia, Roberto Sorrentino, Silvia Luzzati, Antonella Boccia, Riccardo Po, Eleonora Quadrivi, Stefania Zappia, Silvia Destri, “Amphiphilic PTB7-based rod-coil block copolymer for water-processable nanoparticles

Summary and Conclusions

as active layer for sustainable organic photovoltaic: a case study” *Polymers* 2022, 14, 1588.
<https://doi.org/10.3390/polym14081588>.

➤ Federico Gobbo, Marianna Diterlizzi, Anna Maria Ferretti, Silvia Destri, Stefania Zappia and Maria Rosa Antognazza, “PCPDTBT-based nanoparticles as smart photoactive transducers in cellular metabolism” in preparation.

Appendix

Characterization Methodologies

A.1 Nuclear magnetic resonance (NMR)

NMR experiments were carried out on a Bruker 500 MHz DM spectrometer operating at 11.7 T, equipped with a 5 mm probe and gradient unit on z, and thermostated at 330K. ^1H acquisition parameters: 90° pulse 9.10 μs , spectral width, 5240 Hz; number of transient, 1024. All chemical shifts were reported in the standard notation of parts per million (ppm) using the peak of residual proton signal of CDCl_3 ($\delta^1\text{H}=7.26$) and TCE- d_2 ($\delta^1\text{H}=5.94$). NMR spectra were recorded at room temperature in CDCl_3 and at 333 K in TCE- d_2 .

Diffusion-ordered spectroscopy (DOSY) seeks to separate the NMR signals of different species basing on their diffusion coefficient. A set of spin echo spectra is measured with different pulsed field gradient strengths, and the signal decays are analyzed to extract a series of diffusion coefficients allowing to summarize the diffusion domain of the spectrum.[1] Particularly, the spins are gradient-encoded by their z-position in the NMR tube. After a brief diffusion time (Δ) the spins are decoded. If a molecule remains within the same slice of the NMR tube, it will appear at full intensity, but if it diffuses to another slice, its signal will be attenuated as a function of the distance it has diffused. A simplified pulse sequence is shown in **Figure A.1**.

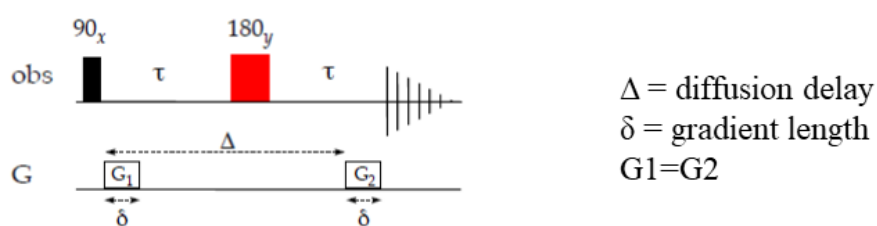


Figure A.1 Pulse sequence representation of DOSY experiment. Typical set values: $\Delta = 50\text{-}100$ ms; $\delta = 2\text{-}4$ ms

There are two different kind of DOSY: the low resolution DOSY to solve mixtures of molecules with high differences in sizes, and the high resolution DOSY for investigating complex mixtures which may contain molecules of very similar sizes.

DOSY experiments on PTB7-*b*-P4VP (Chapter 3) were performed with a pulsed-gradient stimulated echo sequence, using bipolar gradient.

Sequence delays were $\Delta=100$ ms, and a LED delay of 50 ms. For each experiment rectangular PFGs, with a duration of 1 ms and a recovery delay of 100 μs , were applied. The z axis gradient strength was logarithmically incremented in 32 steps from 2% up to 98% of its maximum value. After Fourier transformation and baseline

correction, the experiments were processed using the Bruker TopSpin software package (4.0.6 version).

2D TOCSY experiment (Total Correlation Spectroscopy) was acquired applying a Bruker library sequence phase sensitive, using Echo/Antiecho-TPPI gradient selection, and a TOCSY spinlock mixing time of 90 ms.

A.2 Size exclusion chromatography (SEC)

Two different instruments were used for the molecular characterization of the samples reported in this thesis.

In particular, the SEC measurements using THF:DMF=80:20 and pure DMF as mobile phase were carried out using a modular system HPLC/SEC Alliance 2695 Waters (USA) with degasser, pump, injector and column oven. The system was equipped with two on-line detectors: *i*) a differential viscosimeter; *ii*) a differential refractometer (DRI) as concentration detector. A Diode Array UV 996 to register the UV spectrum (λ da 200-800 nm) was added to the HPLC/SEC system.[2] The samples were prepared through dilution with the mobile phase at a proper concentration. Then the solutions were filtered at room temperature with PTFE 0.20 μm syringe filters before the injection in the system.

The SEC measurements using *ortho*-dichlorobenzene (*o*-DCB) as mobile phase at high temperature were carried out by using an integrated GPCV2000 SEC system. The system was equipped with two on-line detectors: *i*) a differential viscosimeter; *ii*) a differential refractometer (DRI) as concentration detector.[2] In order to avoid the thermal degradation and the formation of aggregates, the samples were prepared with an optimized procedure, as follows:

- protection with butylated hydroxytoluene (BHT) antioxidant (0.05%);
- samples solubilization in oven at 160 °C for about one hour;
- filtration with sintered metal filters of 0.5 μm pores size;
- insertion of the samples in the injection compartment of the system at 135 °C.

The other experimental conditions are reported in **Table A.1**, **Table A.2** and **Table A.3** referred to Chapter 2, Chapter 3 and Chapter 4, respectively. For the sake of the comparison of the different sample sets, each sample set was analyzed within the same sample run.

Table A.1 SEC experimental conditions related to Chapter 2.

Sample	Mobile Phase	Column Set	Flow Rate (ml min ⁻¹)	Temperature (°C)
Macromer, Coil100 BCP15, BCP100	THF:DMF (80:20)	3 PLgel (2 Mixed C+100Å) PL	0.6	50
Macroinitiator BCP2, BCP5	THF+0.25% TBAB	2 PLGel Mixed C PL	0.8	35

Table A.2 SEC experimental conditions related to Chapter 3.

Sample	Mobile Phase	Column Set	Flow Rate (ml min ⁻¹)	Temperature (°C)
PTB7	THF:DMF (80:20) +0.05M LiBr	Resipore PL	0.8	35
P4VP(15)	DMF+0.05M LiBr	2 Resipore PL	0.8	50
PTB7-<i>b</i>-P4VP	THF:DMF (80:20) +0.05M LiBr	2 Resipore PL	0.8	35

Table A.3 SEC experimental conditions related to Chapter 4.

Sample	Mobile Phase	Column Set	Flow Rate (ml min ⁻¹)	Temperature (°C)
PTB7-Th-F₂ PTB7-Th-F₂-Me ester PDCBT	<i>o</i> -DCB	806M-805-804 from Showa Denko (Japan)	0.8	135

In all cases, a relative calibration curve was used $\text{Log}(M)=f(V)$ with M =molecular weight and V =volume elution. A polynomial calibration curve (3order) was constructed with fifteen narrow MWD polystyrene standards and peak molecular weight (M_p) ranging from 3,280,000 g mol⁻¹ and 162 g mol⁻¹.

The HPLC/SEC chromatographic software for data acquisition and elaboration was Empower Pro 1.0 from Waters (Milford, USA).

A.3 Matrix assisted laser desorption/ionization time of flight mass spectroscopy (MALDI-TOF MS)

MALDI-TOF MS measurements were carried out in reflectron mode to record spectra by means of a 4800 Proteomic Analyzer (Applied Biosystems) MALDI-TOF/TOF instrument equipped with a Nd:YAG laser at a wavelength of 355 nm with <500 ps pulse and 200 Hz firing rate. The accelerating voltage was 15 kV. External calibration was performed using an Applied Biosystems calibration mixture consisting of polypeptides with different molar

mass values. The irradiance was maintained slightly above the threshold, to obtain a mass resolution of about 6000-8000 fwhm in the mass range between 500 and 4000 Da and 4000-7000 Da, respectively. Mass accuracy was about 50 ppm. The best mass spectra were recorded using as a matrix 2-methyl-2-propenylidene]malononitrile (DCTB) for PTB7 (Chapter 3), and alpha-Cyano-4-hydroxycinnamic acid for PTB7-Th-F₂ and PTB7-Th-F₂-Me ester (Chapter 4).

A.4 Gas chromatography mass spectroscopy (GC-MS)

GC-MS analyses were carried out using GC Agilent 7890A combined with detector Agilent 5975C MSD and electron ionization source.

A.5 Differential scanning calorimetry (DSC)

DSC measurements were performed by means of a TA Instrument Q100 DSC, calibrated with melt purity indium standard (156.6 °C and 28.45 J g⁻¹). Before any experiment, the baseline was recorded using empty aluminium pan (reference and sample). About 3-4 mg samples were used. Each sample was analysed under nitrogen atmosphere (flow rate of 50 ml min⁻¹) using the following runs:

- for PTB7-*b*-P4VP (Chapter 3): (a) heating at 10 °C/min from -50 to 200 °C; (b) cooling at 50 °C/min from 160 to -90 °C; (c) heating at 10 °C/min from -50 to 200 °C. Three repeated cycles were performed to verify the reproducibility of thermal transitions. The glass-transition (T_g) temperatures measured in the second heating run were computed by the midpoint method;
- for PTB7-Th-F₂ and PTB7-Th-F₂-Me ester (Chapter 4): (a) heating at 10 °C/min from -40 to 200 °C; (b) cooling at 50 °C/min from 200 to -90 °C; (c) heating at 10 °C/min from -40 to 200 °C. Three repeated cycles were performed to verify the reproducibility of thermal transitions.

A.6 Melting point measurements

Mettler 820 differential scanning calorimetry was used for the melting point of the samples equipped with an optical microscope Nikon Eclipse TE2000-U. The samples were prepared grinding the powder in a mortar, then the samples were put on a microscope slide and covered with a glass slide for the characterization.

A.7 UV-Vis spectroscopy

UV-visible absorption spectra were recorded with a Perkin Elmer Lambda 900 spectrometer. Optical characterizations were performed on polymers dissolved into a suitable organic solvent, on WPNP aqueous suspensions both in water and deposited onto a glass substrate, and on the device active layers.

A.8 Fourier transform infrared spectroscopy (FTIR)

FTIR experiments were performed by a Perkin-Elmer Spectrum One FTIR spectrometer equipped with a DTGS (deuterated triglycine sulphate) detector. The spectral resolution used for all experiments were 4 cm^{-1} . For attenuated total reflectance (ATR) measurements, the internal reflection element (IRE) was a three bounce 4-mm-diameter diamond microprism. Cast films were prepared directly onto the internal reflection element, by depositing the solution of interest ($\sim 5\ \mu\text{l}$) on a KBr disk and allowing the solvent to evaporate completely.

A.9 Contact angle and surface energy measurements

PTB7 and PTB7-*b*-P4VP films (Chapter 3) were deposited by blade coating ($v=10\text{ mm s}^{-1}$, $50\text{ }^\circ\text{C}$) on glass substrates from 8 mg ml^{-1} and 2 mg ml^{-1} in chlorobenzene solutions respectively. After the deposition the films were subjected to annealing treatment at $120\text{ }^\circ\text{C}$ for 5 minutes. Contact angles (CA) were measured using a KRUSS-Drop Shape Analyzer–DSA30 in sessile static mode.[3] About 10 independent drops of solvent were dropped on each substrate and left and right contact angle values were extrapolated by a circle fitting algorithm. For each drop, 15 CA estimations were performed, and the average value was calculated.

Contact angle measurements were performed on PTB7-Th-F₂ and PTB7-Th-F₂-Me ester samples (Chapter 4) with a Ossila contact angle goniometer. Polymer surface free energies were calculated from water, ethylene glycol and diiodomethane using the Owens-Wendt-Rabel and Kaelble model.[4]

A.10 Photoluminescence (PL)

PL spectra of BCP5-based bWPNPs (Chapter 2) were collected with a SPEX 270 M monochromator equipped with a nitrogen cooled charge-coupled device excited with a monochromated 450 W Xe lamp. Spectra are corrected for the instrument response.

PL spectra of PTB7 and PTB7-*b*-P4VP (Chapter 3) were measured with a Horiba Fluorolog 3 spectrofluorometer and collected perpendicular to the 380 nm exciting radiation. The setup consists of a 450 W OF Xenon lamp coupled to a double monochromator for excitation and a single monochromator for emission (iHR320) with holographic grating 150 gr mm^{-1} . The spectra were recorded using a Peltier cooled Synapse CCD detector (Horiba). In order to correct for temporal fluctuations of the stabilized Xenon lamp source, the emission signal was divided by the signal of a reference diode monitoring the lamp output. All emission spectra were corrected for dark counts from the detector (blank correction) and for the instrument specific contribution (emission correction) from files provided and updated by the manufacturer and obtained by calibrated lamps. The spectra were also scaled to the materials absorption value registered at the chosen excitation lambda.

A.11 Grazing incidence wide angle X-ray scattering (GIWAXS)

GIWAXS measurements were performed at the X-ray Diffraction beamline 5.2 at the Synchrotron Radiation Facility Elettra in Trieste (Italy). The X-ray beam emitted by the wiggler source on the Elettra 2 GeV electron storage ring was monochromatized by a Si(111) double crystal monochromator, focused on the sample and collimated by a double set of slits giving a spot size of $0.2 \times 0.2 \text{ mm}$. The beam was monochromatized at 1.4 \AA . The samples were oriented by means of a four-circle diffractometer with a motorized goniometric head. A diffractometer allowed sample surface alignment in the horizontal plane containing the X-ray beam by means of laser light reflection. For every sample, seven images at variable incidence (from -0.1° to 0.2° , step 0.05°) were taken, each one by rotating the sample of 360° around the normal to the surface in 60 s of exposition to the beam. The bidimensional diffraction patterns were recorded with a 2M Pilatus silicon pixel X-ray detector (DECTRIS Ltd., Baden, Switzerland) positioned perpendicular to the incident beam, at a distance of 350 mm from the sample. Patterns were calibrated by means of a LaB6 standard and integrated using the software fit2d, obtaining powder-like patterns, corrected for geometry, Lorentz and beam polarization effects, in the azimuthal region

between 70° and 110° for OOP signal and in that between 170° and 180° for IP signal. Peaks positions were extracted by means of the program Win Plot. Bidimensional images representing intensity as a function of q_{xy} and q_z , where q is the reciprocal lattice vector (or transferred momentum) expressed in \AA^{-1} were obtained with the software GIDVis.

A.12 Dynamic light scattering (DLS)

Hydrodynamic diameter, polydispersity, and ζ -potential of WPNPs were determined through DLS using a Brookhaven 90 Plus size analyzer. The apparatus is equipped with a He-Ne laser emitting light at $\lambda=632.8$ nm and a detector recording intensity at a fixed scattering angle $\theta=90^\circ$. All measurements were performed at room temperature. Samples for the measurements were prepared properly diluting the original WPNP suspensions with MilliQ water.

ζ -potential is parameter to define the charge on the surface of nanoparticles in solution.[5] As shown in **Figure A.2**, a charge on the NP surface attracts an opposite charged thin layer of ions on the surface. These two electric layers together is called double layer. The electric potential between the particle surface and the boundary of the double layer is defined as ζ -potential. This value indicates the property of NP surface and in particular it allows to predict the stability of the suspension.

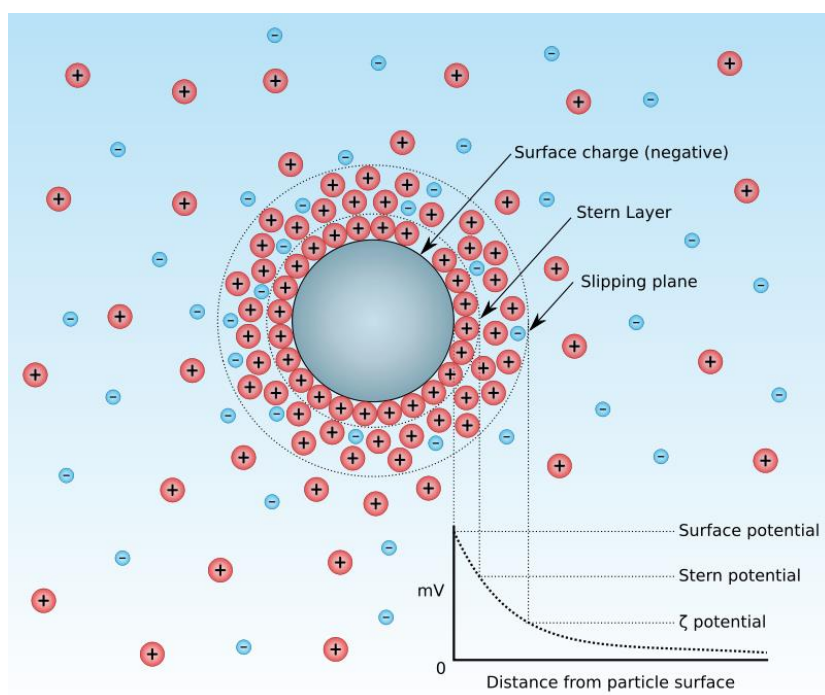


Figure A.2 Representation of the ionic concentration and potential difference as a function of the distance from the charged surface of a NP suspended in a dispersion medium.

A.13 Transmission electron microscopy (TEM)

TEM and EFTEM images were collected by means of a 200 kV ZEISS LIBRA 200 FE microscope equipped (Carl Zeiss Microscopy, Oberkochen, Germany) with a second-generation column W filter, and the EFTEM images were recorded by centering the energy selecting slit at 22 eV and 30 eV with a ± 2 eV range. The samples were prepared following this procedure: the mother solution was properly diluted with MilliQ water, then a 7 μl drop of WPNP suspension was dropped on a copper grid covered by a SiO film pre-treated with a plasma cleaner; the excess of water was blotted with filter paper after 1 min. The estimation of the WPNP diameter measurement was performed using TEM Imaging Platform Olympus and $d_m = \sum d_i n_i / \sum n_i$, where $\sum n_i$ is the number of particles of dimension d_i . [6]

A.14 Atomic force microscopy (AFM)

AFM was performed with a commercial equipment (AFM NTMDT NTEGRA) in tapping mode with a cantilever NSG10 operating at a typical resonance frequency of 140–390 kHz. The samples were prepared using glass slides properly treated with plasma etching for 10 minutes before the depositions of the aqueous WPNP suspensions. Samples discussed in Chapter 2 were dried at 60 °C in air and then annealed at 90 °C for 20 minutes in nitrogen flux, while the measurements on the samples reported in Chapter 3 were performed before and after annealing at 90 °C for 20 minutes in air. Active layer of the devices was also analyzed through AFM.

A.15 Pump and probe

Pump–probe experiments were performed with a fraction of the output light of a Ti:sapphire laser (Libra, Coherent) characterized by 100 fs pulse duration, 1 kHz repetition rate and 800 nm central wavelength. Pump excitation wavelengths of 600 nm were used for the characterization of the blend sample. The 600 nm light came from a non-collinear optical parametric amplifier. The broadband probe extending in the visible region resulted from white light continuum generation in a 3 mm-thick sapphire plate pumped with 800 nm light. The delay between pump and probe pulses was controlled by a translation stage and the pump beam was modulated by a mechanical chopper with a 500 Hz frequency. The differential transmission (DT/T) of the probe was measured as a function of probe

wavelength and pump–probe delay through an SP2150 Acton spectrometer from Princeton Instruments. The pump energy was adjusted to a fluence around $45 \mu\text{J cm}^{-2}$. Measurements were performed with parallel polarizations between pump and probe beams.

A.16 Cell cultures

The cells used in Chapter 2 belong to the line HEK-293 (Human embryonic Kidney), derived from the kidney of an aborted human fetus in 1973, transfected with adenovirus 5 DNA in order to avoid cell apoptosis. HEK cells were kept in T-25 Culture flask in an incubator (temperature $37 \text{ }^\circ\text{C}$, CO_2 level 5%). They were grown in Dulbecco's Modified Eagle Medium (DMEM, Sigma Aldrich), with 10% fetal bovine serum (FBS, Sigma Aldrich), 2 mM glutamine (Sigma Aldrich), 100 U ml^{-1} streptomycin (Sigma Aldrich) and 100 U ml^{-1} penicillin (Sigma Aldrich). When they reached 80% confluence in the flask, they were detached by adding 0.5% trypsin-0.2% EDTA (Sigma Aldrich) and leaving them in the incubator for 5 minutes. Detached cells were rinsed with fresh DMEM and by means of centrifugation they were separated from the trypsin. The pellet was diluted in fresh DMEM and the cells were plated on circular glass coverslip (18 mm diameter). All these procedures were carried out under a laminar flow hood. Glass substrates were previously cleaned in an ultrasonic bath with subsequent cycles of 10 minutes in deionized water, acetone and isopropanol, and then dried with a N_2 gun and thermally sterilized for 2 hours in an oven at $120 \text{ }^\circ\text{C}$. To promote cell adhesion, they were treated with 2 mg ml^{-1} of fibronectin (from bovine plasma, Sigma Aldrich) deposited on the surface and incubated for 30 minutes at $37 \text{ }^\circ\text{C}$.

A.17 Viability assay

The cytotoxicity of the NPs (Chapter 2) was tested with a viability assay carried out with Alamar Blue (ThermoFisher). Cells were plated on glass coverslips (18 mm), half of the sample were administered with NPs at a proper concentration. Cells were then rinsed with KRH and incubated for 3 hours in the Alamar Blue solution at $37 \text{ }^\circ\text{C}$ in sterile conditions. Then, the fluorescence of the solution was measured by means of a plate reader (Tecan Spark 10 M Plate Reader, excitation wavelength 540 nm, emission wavelength 590 nm). Cells were then washed and rinsed with their growing medium, until the successive treatment with the Alamar Blue. Experiment was performed on 6 samples, 3 of which

treated with NPs. Alamar Blue fluorescence was evaluated at two time points, corresponding to day 0 (the day after plating), and day 4 (4 days after plating).

A.18 Confocal microscopy

In the study of the internalization of NPs in HEK cells (Chapter 2) the Nikon A1 HD25 confocal microscope was used. The excitation beam is provided by a LU/N4 laser unit (Nikon), which is equipped with four lasers (405 nm, 488 nm, 561 nm and 640 nm), coupled to the microscope by an optical fibre. The excitation beam is then reflected by a dichroic mirror and focused on the sample. Fluorescent beam then passes through the pinhole aperture and is focalized at the detector. Four different detectors are present, two Si PMTs and two GaAsP PMTs, each one associated to a particular optical path. Filtering blocks are put along the optical path before the light reaches the detector, namely: 450/50 nm, 525/50 nm, 590/50 nm and 700/75 nm (the second number indicates the bandwidth of the filter). A GaAsP PMT measures the intensity on narrower spectral intervals separated by a grating (wavelength resolution 2.5 nm) and reconstructs the PL spectrum. Images can be acquired with different objectives: 10x, 20x, 40x and 60x; the latter is an oil immersed objective, while the others operate in air.

A.19 Staining procedure

Samples were analyzed at the confocal microscope (HEK-293 cells treated with PCPDTBT-*b*-P4VP NPs) after being fixed in paraformaldehyde. The procedure adopted to prepare the samples is the following: HEK-293 cells were plated on circular glass coverslips (18 mm diameter) copiously washed and treated with fibronectin. NPs were administered to them after 24 hours and during plating phase at a proper concentration. 48 hours after plating, cells were rinsed twice with PBS. Then, they were incubated for 15 minutes in paraformaldehyde solution (4% paraformaldehyde and 4% sucrose in 0.12 M sodium phosphate buffer, pH=7). Then cells were rinsed three times in PBS and incubated for 30 minutes with gelatin dilution buffer (GDB: 0.02 M sodium phosphate, pH=7.4, 0.45 M NaCl, 0.2% w/v gelatin), containing 0.3% (v/v) Triton X-100. Then they were incubated in a solution containing phalloidin for 1 hour and 30 minutes. The last step was the incubation for 10 minutes in DAPI (1mM in PBS), for nuclei staining. Then samples were washed in PBS for 10 minutes. Once the staining procedure was concluded, glass coverslips

were attached with mowiol to larger glass substrates suitable to be inserted in the sample holder of the confocal microscope.

A.20 Reactive Oxygen Species (ROS) imaging

Experiments regarding the intracellular production of ROS were carried out with a standard fluorescent microscope (Nikon Eclipse Ti). The instrument is equipped with an Analog-WDM Camera (Cool Snap Myo, Photometrics). The microscope is equipped with a LED system, made of a 660 nm (ThorLabs) source for the NP excitation and a 470 nm (ThorLabs) for the excitation of the probe. HEK-293 cells were plated on circular glass coverslips (18 mm, the procedure being explained in paragraph 2.8), and NPs were administered during plating phase or after 24 hours at a proper concentration. ROS experiments in both cases were carried out 24 hours after the administration of NPs. Samples were rinsed two times with KRH and incubated for 30 minutes in H₂DCF-DA diluted in KRH at a concentration of 25 μ M. After the incubation, samples were rinsed twice with KRH. Fluorescence of H₂DCF-DA was recorded with a standard FITC configuration of the filters, namely excitation/emission wavelengths 470/520 nm. Fluorescence images of H₂DCF-DA were acquired illuminating the sample with the blue LED at 470 nm and collecting an image with the camera immediately after the illumination onset (integration time 500 ms). Images were acquired before and immediately after the excitation of the NPs. They were excited by a continuous illumination lasting 3 minutes by the 660 nm LED (power density 16 mW mm⁻²). Images were acquired with the 20x objective. Statistical analysis of the fluorescence intensity over Regions of Interest (ROI) covering single cells area was carried out with the software ImageJ and data were analyzed with OriginPro 9.

A.21 Ca²⁺ imaging

Ca²⁺ imaging was carried out on the Nikon Eclipse Ti fluorescence microscope by means of a fluorescent probe (Fluo-4, Life Technologies, ex/em = 494/516 nm) that selectively binds to the intracellular Ca²⁺ ions. To evaluate the dynamic of the Fluo-4 fluorescence intensity, the CCD camera acquired frames for 3 minutes every 100 ms (with an integration time equal to 400 ms for each single image). Samples of HEK-293 cells, treated with NPs, were prepared as described in paragraph A.19 and, after 2 rinses in KRH, were incubated for 30 minutes in a Fluo-4 solution 1 μ M. Then samples were rinsed for 15 minutes in KRH

before measurement. Fluorescence images with the FITC configuration of filters were acquired before and during the illumination with the red LED, both for control samples and for cells treated with nanoparticles.

A.22 Current density-voltage (J-V) characteristics

The J-V characteristics of the OPV devices based on BCP2, BCP5, BCP15 and BCP100 (Chapter 2) were measured under simulated sunlight (AM1.5G, 100 mW cm⁻²) using a Keithley 2401 source meter. The photovoltaic parameters presented in this study correspond to the average of 4 devices and exhibited a minor deviation below 5%.

The device measurements described in Chapter 3 were carried out directly in the glovebox. J-V measurements were performed with a Keithley 2602 source meter, under AM 1.5G solar simulator (ABET 2000). The incident power, measured with a calibrated photodiode (Si cell + KG5 filter), was 100 mW cm⁻².

A.23 Cyclic Voltammetry (CV)

CV analyses were performed by means of Metrohm mStat-i 400. 10 µl of solution of PTB7-Th-F₂ (2.2 mg ml⁻¹) and PTB7-Th-F₂-Me ester (2.6 mg ml⁻¹) were drop-casted directly onto a glassy carbon working electrode (Chapter 4). The measurements were carried out using ferrocene as the reference.

References

- [1] H. Barjat, G.A. Morris, S. Smart, A.G. Swanson, S.C.R. Williams, High-Resolution Diffusion-Ordered 2D Spectroscopy (HR-DOSY) - A New Tool for the Analysis of Complex Mixtures, *Journal of Magnetic Resonance, Series B* 108(2) (1995) 170-172.
- [2] R. Mendichi, A. Giacometti Schieroni, Use of a multi-detector size exclusion chromatography for characterization of complex polymers, *Trends in Polymer Science*, 2001, pp. 17-32.
- [3] H.Y. Erbil, The debate on the dependence of apparent contact angles on drop contact area or three-phase contact line: A review, *Surface Science Reports* 69(4) (2014) 325-365.
- [4] D. Janssen, R. De Palma, S. Verlaak, P. Heremans, W. Dehaen, Static solvent contact angle measurements, surface free energy and wettability determination of various self-assembled monolayers on silicon dioxide, *Thin Solid Films* 515(4) (2006) 1433-1438.
- [5] J. Lyklema, *Fundamentals of Interface and Colloid Science*, 1995, pp. 3-208.
- [6] A. Borodziński, M. Bonarowska, Relation between Crystallite Size and Dispersion on Supported Metal Catalysts, *Langmuir* 13(21) (1997) 5613-5620.